Electrochemical Reduction of Nitrite and CO_2, and Oxidation of Organic Fuels

By

Jasmeen Akther

A thesis submitted to the School of Graduate Studies in partial fulfillment of the
requirements for the degree of Doctor of Philosophy

Department of Chemistry
Memorial University of Newfoundland

September 2023

St. John's Newfoundland and Labrador

Abstract

In today's world, the need for sustainable technology is more crucial than ever. With the continuous growth in demand for resources and energy, the environment is under severe strain due to climate change, depletion of natural resources, and environmental degradation. Electrochemical techniques offer a promising solution for sustainable development. One such approach is using carbon dioxide as a renewable, non-fossil-based feedstock to produce fuels and value-added chemicals via electrochemical processes that use renewable energy sources. In addition, coelectrolysis of carbon dioxide with environmental pollutants such as NO_2^-, NO_3^-, and NO has shown promising results for producing of sustainable fuels, commodity chemicals, and fertilizers while reducing environmental pollutants.

Our research focuses on coreduction of CO_2 with nitrite (NO_2^-) to produce ammonia and urea simultaneously using renewable power sources. Among the effective catalysts for this process, metallophthalocyanines (M-Pc) have been shown to be successful, especially iron-based phthalocyanine, with a high current efficiency. We investigated the electrochemical coreduction of NO_2^- and CO_2 at carbon-supported iron-based phthalocyanine electrocatalysts to produce ammonia and urea under ambient conditions. To understand the electrochemical behavior of the electrodes, we used both cyclic voltammetry and chronoamperometry in 0.1 M $NaHCO_3$ and 5 mM $NaNO_2$ solution under N_2 and CO_2 environments. The produced ammonia and urea concentrations were determined using two different spectrophotometric techniques, and secondary analytical techniques, liquid-chromatography-mass spectrometry (LC-MS) and proton nuclear magnetic resonance spectrometric (^{1}H-NMR), were used to confirm the accuracy of the results.

Our results indicate that it is possible to produce urea at low overpotentials at various iron-based phthalocyanine electrocatalysts in $NaHCO_3$ as an electrolyte. However, our experiments revealed that ammonia was the primary electrolysis product when using carbon-supported iron phthalocyanine (FePc/C) as an electrocatalyst. At a potential of -0.347 V vs RHE, 85% of the current was used for NH_3 production, while only 4.1% was utilized for urea production. Nevertheless, we observed a significant amount of urea production at FePc/C, with a maximum yield of 5.8% at the lowest overpotential (-0.047 V vs RHE).

We also observed that carbon supported sulfonated iron(III) phthalocyanine (FeTSPc/C) produced the highest faradaic yield (54.8%) of urea at a potential of +0.053 V vs RHE, with 25% coproduction of NH_3. In a PEM electrolysis cell, the FePc/C catalyst demonstrated the potential to produce urea and ammonia simultaneously using very low NO_2^- concentrations. The faradaic efficiency for urea was increased from 2.8% to 15.9% compared to the normal three-electrode cell.

In addition to producing commodity chemicals, research has also focused on developing electrocatalysts for fuel cell applications. PtBi/C and PtPb/C catalysts were prepared by the surface decoration of a commercial Pt/C catalyst, and their catalytic activities for electrochemical oxidation of formic acid, methanol and ethanol were compared. It was found that the currents at 0 V vs SCE for formic acid oxidation at the PtBi/C and PtPb/C catalysts were ~ 6 and ~ 2 times higher, respectively, compared to the unmodified Pt/C catalyst. In addition, the PtBi/C catalyst also showed slightly higher activity for ethanol oxidation at low potentials compared to the unmodified Pt/C.

Acknowledgements

Completing this thesis would not have been possible without the support and contributions of several individuals and organizations whom I would like to express my deepest gratitude. First and foremost, I extend my heartfelt appreciation to my supervisor, Prof. Peter Pickup, for his continuous guidance, expertise, and unwavering support throughout my academic journey. His mentorship has been invaluable to me, and I am immensely grateful for his contributions.

I would also like to thank the members of my supervisory committee, Prof. Christina Bottaro and Prof. Yuming Zhao, for their insightful comments and valuable feedback that helped me refine my research path.

Furthermore, I would like to express my gratitude to my colleagues at Prof. Pickup's lab, Hui (Ph.D., 2022), Diala (Ph.D., 2022), and Ahmed Ali (Ph.D. candidate), for their support, collaboration, and camaraderie. I am also grateful to Dr. Jane Stockmann and her group for the wonderful experiences we shared.

My deepest appreciation goes to my parents, siblings, and friends for their unwavering love, support, and encouragement. I am forever grateful for everything that you have done for me.

I would also like to acknowledge the financial support of the School of Graduate Studies of Memorial University, the Natural Sciences and Engineering Research Council and NRCan Canada, and the Dr. Liqin Chen Scholarships in Chemistry, which enabled me to pursue my research goals.

Lastly, I want to express my gratitude to Dr. Céline Schneider, Dr. Stefana Egli, Nicholas Ryan, and all the staff and academics in the Chemistry Department for providing me with the necessary resources and facilities to carry out my research. Your support and contributions have made my academic journey a memorable and fulfilling one.

Table of contents

Chapter 2. Experimental Methods…………………………………………………………79

Chapter 5. Electrochemical synthesis of urea and ammonia in a proton-exchange membrane (PEM) electrolysis cell under ambient conditions………………………………………... 139

List of tables

List of figures

List of appendices

List of figures:

List of tables:

List of figures:

List of figures:

List of Abbreviation and Symbols

A	Ampere
C	Coulomb
℃	Degree Celsius
ca.	Approximately
CFP	Carbon fiber paper
CO_2 RR	Carbon dioxide reduction reaction
DEMS	Differential electrochemical mass spectroscopy
DHE	Dynamic hydrogen electrode
DFT	Density functional theory
e^-	Electron
E	Potential
E^o	Standard potential
eV	Electron volt
EASA	Electrochemically active surface area
EDX	Energy dispersive X-ray analysis
EOR	Ethanol oxidation reaction
F	Faraday constant
FE	Faradic efficiency
FAOR	Formic acid oxidation reaction
G_f^0	Standard Gibbs energy of formation
H_f^0	Standard entropy of formation

h	Hour
I	Current
J	Current density
IRRAS	In situ infrared reflection-absorption spectroscopy
MEAs	Membrane electrode assemblies
MOR	Methanol oxidation reaction
min	Minute
m/z	Mass to charge ratio
µM	Micromol
NO_2^-RR	Nitrite reduction reaction
PEM	Proton exchange membrane
Q	Charge
RHE	Reversible hydrogen electrode
s	Second
SCE	Saturated calomel electrode
SHE	Standard hydrogen electrode
SEM	Scanning electron microscopy
t	Time
TEM	Transmission electron microscopy
TGA	Thermogravimetric analysis
V	Voltage (volts)
XRD	X-ray diffraction

Chapter 1

Introduction

1. Introduction

1.1 Electrochemistry for sustainable technology

As the world's nations continue to develop, their urbanization, industrialization, and growing population will require ever-increasing amounts of energy and commodities. According to the International Energy Agency (IEA), global energy consumption is projected to rise by 50% from 2021 to 2040 [1]. For decades, fossil-based resources have been used as primary energy sources and feedstocks for commodity chemicals worldwide. Unfortunately, fossil fuels are not renewable, and their availability is steadily declining. Even their present consumption levels have raised serious concerns about the guarantee of their future supply [2].

Greenhouse gases and other pollutants are to blame for environmental degradation and climate change, which seriously threaten humanity's and our ecosystem's survival. Burning fossil fuels for energy generation and utilizing fossil-based feedstocks in the manufacturing of industrial goods has resulted in significant anthropogenic emissions of greenhouse gases, such as carbon dioxide and methane, as well as other environmental pollutants over the past several decades. Fortunately, society has now recognized the importance of addressing climate change and in this regard, world leaders and the international community have made significant commitments to limit CO_2 emissions in order to establish a sustainable future. According to the 2022 Global Carbon Budget [3], the global atmospheric CO_2 concentration reached an average of 414.71 ± 0.1 ppm. Meanwhile, 350 ppm is the consensus limit for achieving a 1.5 ℃ increase in global temperature over pre-industrial levels and avoiding catastrophic climate change [4]. Sustainable technologies with novel carbon-neutral or carbon-negative strategies are necessary to achieve this aim.

Many nations are exploring new strategies and alternative sustainable technologies to maintain economic growth by ensuring a sustainable energy supply and environmental protection

[5]. Electrochemistry has a significant role to play in these types of strategies to achieve sustainable development. In the last century, there has been a remarkable development in the energy sector to produce sustainable power from electrochemical sources. Electrochemical power sources, such as fuel cells [6] and batteries [7], are efficient, clean, and unaffected by meteorological conditions [8]. Among them, fuel cells have received significant attention in this area due to their unique properties, such as high energy efficiency (98% in theory) [9] and use of renewable reactants (e.g., H_2, CH_3OH, C_2H_5OH, and HCOOH). Moreover, they can function for extended periods as long as reactants are supplied and have significantly higher energy densities than batteries. Thus, pure electric power can be generated at high efficiency in fuel cells, or electrical energy can be stored in batteries electrochemically. These power sources can be used in electrically powered vehicles or as stationary power devices. Recent breakthroughs in battery technology have also enabled the commercialization of electric and hybrid cars [10].

Chemical manufacturing is another sector where electrochemistry can play a significant role. As we intend to move towards sustainable development, this also requires substantial changes in our manufacturing sectors through developing new green processes that can reduce greenhouse gases and waste production. Electrosynthesis is an alternative to many conventional thermochemical processes for commodity chemical production, which uses electrons as green reactants instead of potentially hazardous chemicals and allows to use of renewable energy sources [11]. The environmental benefits of electrosynthesis, such as waste minimization, the use of non-fossil/renewable feedstocks, and the option of on-demand chemical production, are important considerations for sustainable chemical production [12]. CO_2 is one of the greenhouse gases that can be utilized as a sustainable non-fossil carbon-based feedstock. It is now most widely explored for producing value-added chemicals electrochemically [13-18]. The conversion of CO_2 to carbon monoxide has been demonstrated at scale using an electrochemical cell, and this technology is now moving toward commercialization to supply a renewable syngas (synthesis gas) component [19-21].

In addition to the greenhouse gases, another public health concern is pollutants from industrial and agricultural wastes that can leach into the main water stream. Electrochemical processes can also be used to treat industrial or municipal wastes and, in some cases, can be used to convert these wastes into valuable chemicals. For example, agricultural wastes such as NO_2^-, NO_3^-, and NO can be electrochemically converted into necessary commodity chemicals such as ammonia [22-24]. Other approaches, such as the co-electrolysis of CO_2 with environmental pollutants (e.g., NO_2^-, NO_3^-, and NO), utilize both pollutants simultaneously to address ecological concerns while producing sustainable fuels, commodity chemicals, and fertilizers [25-27]. Our research focuses primarily on the coreduction of CO_2 with nitrite (NO_2^-) to simultaneously produce two essential commodity chemicals, ammonia and urea, that can utilize renewable power sources.

However, despite all these advancements in electrochemistry, further and continuous improvements are required to make this technology viable. Achieving sustainability in the energy and manufacturing industries requires a collaborative effort from academia and industry, involving expertise in electrochemistry, electrocatalysts, electrolytes, and process engineering.

1.2 CO_2 reduction reaction (CO_2 RR) process

1.2.1 Introduction

Exploring non-fossil-based alternative carbon sources is crucial for building a sustainable manufacturing sector for carbon-based chemicals and products. Biomass is one of the widely accessible carbon sources and can be utilized as an alternative [28-30]. Renewable fuels such as methane, methanol, ethanol, and other carbon-based products can be produced from biomass [31]. While biomass is superior to fossil fuels, some drawbacks limit its use as a source of carbon-based products. First, biomass is primarily used for food production, land conservation, and landfills; only a limited amount of biomass can be used for other purposes. Second, burning biomass can be harmful to public health and is a source of pollution [32].

Alternatively, utilizing CO_2 as a carbon source is a promising solution for generating carbon-based compounds while addressing environmental concerns. Both thermochemical and electrochemical processes can convert CO_2 into fuels and other value-added chemicals. The thermochemical process involves reacting CO_2 with H_2 at high pressure and temperature to produce carbon-based compounds, such as long-chain hydrocarbons, through the Fischer-Tropsch reaction [33] or smaller molecules like methane synthesis [34]. The main challenge of this process is the sustainable and cost-effective sources of H_2 and energy. Currently, most hydrogen and energy are produced from fossil fuels, which results in significant greenhouse gas emissions [35].

The electrochemical conversion of CO_2 into fuels and other value-added chemicals utilizing energy produced from a renewable source (e.g., wind and solar) could end the use of fossil-based resources [36]. This conversion process has several advantages, including electrical energy can be stored from intermittent sources indefinitely as chemical fuels using surplus electricity generated during off-peak hours [37]. Later, electric power can be produced from these fuels by internal combustion engines or electrochemically through fuel cells when the energy production from wind or solar plants dips. Additionally, carbon-based chemicals and products can also be produced in this way to replace those that are currently produced from fossil-based feedstocks [9].

However, the viability of using CO_2 as a feedstock for fuels and chemical production depends on several factors, the most important of which are cost and scale [38]. The price of electricity is a significant cost related to CO_2 reduction, and in this regard, the high voltage needed for CO_2 RR is a primary concern. Therefore, lowering the amount of electrical energy required for this process is a keyway to reduce costs. Only an effective electrocatalyst can improve the energy efficiency of the process by decreasing the overpotential, which is the excess electrical energy (voltage) required (beyond the thermodynamic potential) to drive the reduction process. Unfortunately, an ideal electrocatalyst for CO_2 conversion has yet to be found, so research into electrocatalysts to improve reaction selectivity and overcome cost is crucial. Additionally, the production rate is essential when considering processes that can replace traditional fossil-based feedstocks [38]. To meet demand, an alternative to fossil-based feedstocks must have a high production rate. Electrolysis processes such as chlor-alkali [39] and aluminum refining [40] are in industrial operation and producing on a large scale, demonstrating that this type of electrochemical process can meet large-scale demand.

1.2.2 CO_2 reduction reaction

Currently, CO_2 reduction reaction (CO_2 RR) is the most intensively explored [41], focusing on strategies to improve its energy efficiency by controlling various essential parameters, such as selectivity, production rates, and reaction cell configuration. The voyage of the electrochemical CO_2RR began in 1954 when Teeter and Rysselberghe discovered this reaction for the first time [42], but until 1980, research mainly focused on synthesizing carbon monoxide, formate, and oxalate. A major breakthrough happened in 1985 when Hori et al. [43] discovered that methane and ethylene were the major products when using copper metal as an electrocatalyst. Since then, research on CO_2 RR has been growing and producing a variety of renewable chemical compounds while parallelly developing efficient electrolysis cell designs. Some of these products have the potential to be scaled up and commercialized [38].

In the CO_2 RR process, the main electrochemical reactions are water oxidation and reduction of CO_2. Thus, the two half-cell reactions are as follows (eq.1.1 and 1.2):

At the anode, H_2O is oxidized (oxygen evolution reaction, OER):

$$2H_2O \rightarrow 4H^+ + 4e^- + O_2 \quad (1.1)$$

At the cathode, CO_2 is reduced (CO_2 rection reaction, CO_2RR):

$$xCO_2 + yH^+ + ne^- \rightarrow C_xH_yO_z + H_2O \quad (1.2)$$

The sum of two electrochemical half-cell reactions (eq. 1.3)

$$xCO_2 + yH_2O \rightarrow C_xH_yO_z + zO_2 \quad (1.3)$$

Equation 1.3 is written in a general form to demonstrate that various carbon-containing products can be produced. The actual observed products depend on several factors, but the most important is the cathode material (catalyst) that plays the most significant role. Common products from electrochemical conversion of CO_2 and their standard potentials are given in Table 1.1 [44].

The first step of the CO_2 RR process, in which one electron transfers to form the $CO_2^{\bullet-}$ intermediate, poses the main energy barrier. This step requires overcoming a large negative potential of -1.90 V vs the standard hydrogen electrode (SHE). CO_2, being a thermodynamically stable, inert, and fully oxidized gas, is difficult to activate [44, 45]. However, proton-coupled-electron transfer steps are more thermodynamically favorable and require less-negative potential than the one-electron transfer step. In these steps, CO_2 must first absorb on the electrode's surface and undergo a proton and /or electron transfer process. As illustrated in equation 1.3, these multiproton-coupled-electron transfer steps can lead to various products with complex reaction mechanisms. The most common products are two-electron transfers to carbon monoxide and formic acid or formate ($HCOOH$ or $HCOO^-$). Other organic compounds such as methanol (6-electron transfer), methane (8-electron transfer), and ethylene and ethanol (12-electron transfer) can also be produced, depending on the cathode materials. The water reduction reaction (HER) can also occur at the same potential (-0.42 V vs SHE) as CO_2 RR. Thus, competitive HER is also a concern for CO_2 RR performance, which reduces the energy efficiency of the process.

Table 1.1. The standard potentials for CO_2 reduction to C_1 and C_2 products in aqueous solution at 25 ℃ [44].

Half reactions for CO_2 reduction	**Standard potentials E^0 (V vs SHE)**
$2CO_2 + 12H^+ + 12e^- \rightarrow C_2H_5OH + 3H_2O$	-0.33
$2CO_2 + 12H^+ +12e^- \rightarrow C_2H_4 + 4H_2O$	-0.35
$2CO_2 + 6H^+ + 6e^- \rightarrow CH_3OH + H_2O$	-0.38
$2H^+ + 2e^- \rightarrow H_2$	-0.42
$CO_2 + 4H + 4e^- \rightarrow HCHO + H_2O$	-0.51
$CO_2 + 2H^+ + 2e^- \rightarrow CO + H_2O$	-0.53
$CO_2 + 2H^+ + 2e^- \rightarrow HCOOH$	-0.61
$CO_2 + e^- \rightarrow CO_2^{\bullet -}$	-1.90

1.2.3 The state of art electrocatalysts for CO_2 RR

As was previously mentioned, the study of CO_2 reduction made significant progress when Hori et al. [16] revealed that the primary products from a copper metal electrocatalyst were ethylene and methane. Since then, a number of studies have investigated and compared the activity of different transition metals [46-49]. They found that the CO_2 RR products are dependent on the binding energy of CO at transition metals catalysts. Researchers believed CO is the crucial reaction intermediate in reducing CO_2 at catalysts prepared with transition metals [46]. The CO and other intermediate products produced during CO_2 RR easily poison the metal catalyst's surface. The metal catalysts that bind CO strongly, produced few CO_2RR products because of CO poisoning and hydrogen is the major product at those surfaces due to the competitive H_2O reduction reaction. On the other hand, metal catalysts that weakly bind CO only produce CO as a product because when CO_2 is reduced to CO, the CO is released quickly from the surface and does not continue to form further reduced products like alcohols and hydrocarbons. Among all these metal catalysts, Cu has an intermediate binding energy for CO, which is believed to be the reason for the formation of more reduced products that require more than a 2-electron reduction [50]. Currently, Cu and Cu-based materials are the only electrocatalysts capable of producing alcohols and hydrocarbons [41].

While the majority of studies have focused on transition metals, a number of other materials have also been studied. The activity of organic compounds, such as pyridinium-based catalysts, have also been studied, and among them, pyridine has shown selectivity for methanol at low potential, a product that is not favored for metal catalysts [51]. Various non-noble metallophthalocyanines have also been explored using gas diffusion electrodes (GDE), and crystalized copper-phthalocyanine has demonstrated selectivity for ethylene with 25% faradaic efficiency [52]. Recently, using ionic liquids in place of aqueous electrolytes was shown to decrease the overpotential necessary for CO_2 RR, where CO was their primary product; however, the current density under these conditions was low [53, 54]. The activity of a few metal-free catalysts, such as tetraalkylammonium salts, aromatic esters, and nitriles, has been reviewed [55] [28]. Carbon monoxide dehydrogenase (CODH), a protein, has been shown to convert CO_2 to CO at the reversible potential [56]. A Ni-CODH coated pyrolytic graphite "edge" (PGE) electrode has been demonstrated to exhibit electrocatalytic activity for both CO oxidation and CO_2 reduction. This electrode has two active sites, namely a [Ni4Fe-5S] cluster and Ni-CODH/acetyl-CoA synthase (ACS) and can function in both directions.

Unfortunately, none of the materials investigated so far for CO_2 RR catalysis have the required activity to be applied commercially. An ideal catalyst would work with a high current density at low overpotential and produce selectively only the desired product. A good understanding of the CO_2 RR mechanism and other factors influencing the reaction is needed to guide the research for catalysts that meet these requirements.

1.2.4 Electrolysis cells configuration for CO_2 RR

Currently, there is no widely accepted standard protocol for electrolysis cell configuration for CO_2 RR. Many research groups design and customize their electrolysis cells based on their specific goals. However, in addition to the high-performance cathode and anode materials, a reaction cell with low ohmic resistance and adequate mass transport capabilities are critical for achieving a highly efficient CO_2 RR process [57, 58].

While some CO_2 RR investigations have been conducted using simple one-compartment electrochemical cells [59], this type of cell is not preferred due to the possibility of products of

CO_2 RR forming at the working electrode, then diffusing to the cathode and becoming reoxidized. Despite this drawback of this system, this approach has been used successfully in several experiments [59].

A more popular CO_2 electrolysis cell is a H-type cell (Figure 1.2). This cell uses a separator, such as a glass frit or solid membrane, between the working and counter electrode compartments to prevent the diffusion of products from the cathode to the anode and vice versa. Due to their simple design and ease of operation, H-type cells are beneficial for mechanistic studies and electrolysis experiments that run over long periods of time. However, this cell also has some limitations. This system requires a large electrolyte volume, making it more challenging to get high concentrations of liquid phase products, making them difficult to detect and quantify. Another drawback of the H-cell is its low current density due to the limited CO_2 solubility (33 mM at 25 °C) in aqueous electrolytes [41, 60]. Despite these drawbacks, H-type cells are still widely used in CO_2 RR experiments due to their availability and have been used successfully in many experiments [60].

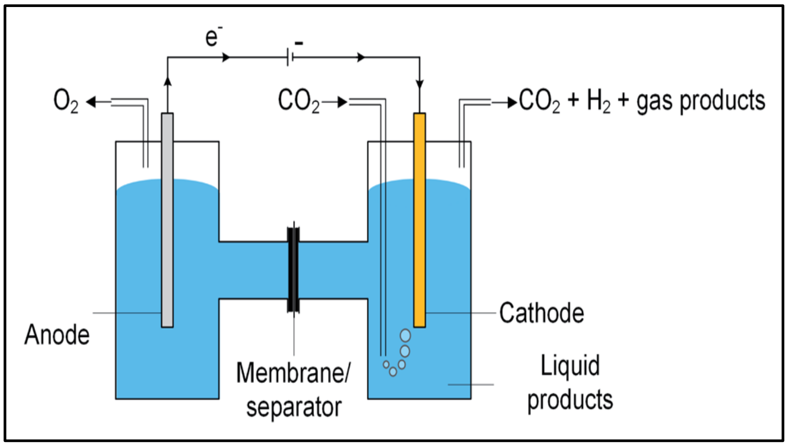

Figure 1.1. Schematic of a laboratory electrochemical H-cell [62]. Reprinted with permission, Copyright (2020), Journal of Materials Chemistry A.

Recently, to overcome the limitations of H-type cells, a flow cell system was developed for CO_2 RR [61, 62]. This system continuously supplies gas and liquid feeds to the cell, which provides high mass transport of CO_2 to the electrode surface. However, the constant flow of electrolytes in the flow cell dilutes liquid phase products formed during electrolysis, making them difficult to detect and quantify unless they are present in high concentrations. A modified flow cell system, called a membrane electrode assembly (MEA) flow cell, was later developed (Figure 1.2). This design uses a membrane to separate the counter and working electrode sides, allowing for the use of different electrolytes. Specifically, ionic liquids have been used on the working electrode side to perform CO_2 RR [63].

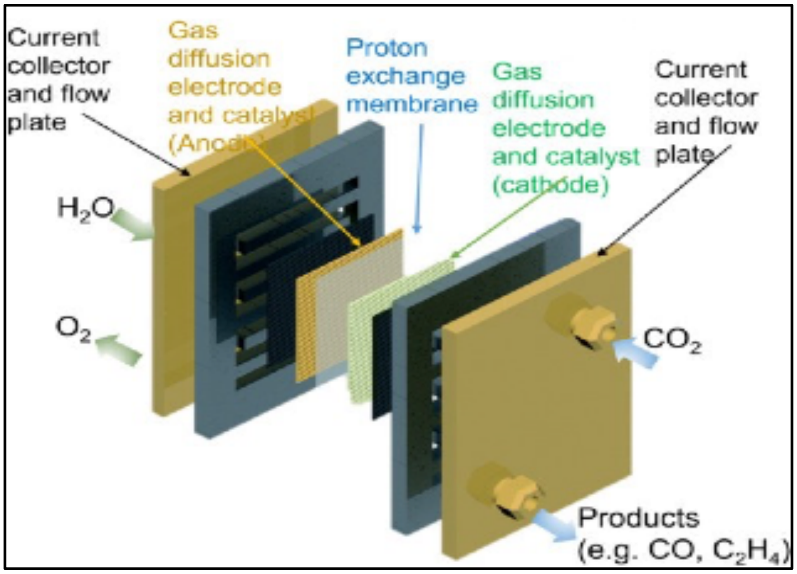

Figure 1.2. Schematic of a membrane electrode assembly (MEA) electrolysis cell [64]. Reprinted with permission, Copyright (2021), Acta Physico-Chimica Sinica.

The MEA-flow cell concept is similar to proton exchange membrane (PEM) based water electrolysis cells [64] and fuel cells, except that fuel cells operate in the opposite direction [65].

These types of cells have low cell resistance and good mass transport properties. However, attempts to run a CO_2 reduction reaction (CO_2 RR) using Nafion membranes, which create a very acidic environment where hydrogen evolution reaction (HER) dominates, have yet to be successful. Many research groups have used anion exchange membranes (AEMs) to allow the flow of OH^- and water between the cathode and anode in CO_2 RR [64]. However, these AEM-flow cells also have some limitations. The efficiency of the cell gradually decreases due to the accumulation of excess water and flooding on the cathode side [66]. This is caused by the inability of the OH^- exchange to keep up with the CO_2 input due to membrane carbonation. Additionally, the crossover of reactant (CO_2) via the cathode-to-anode transport of CO_3^{2-} /HCO_3^- and liquid products through the membrane is also an issue in all MEA-based electrolysis cells [40].

Another approach that differs from the rest is to couple an electrolysis cell directly to a mass spectrometer. This approach is known as a differential electrochemical mass spectrometer (DEMS). DEMS has the advantage that products can detect as the potential is scanned, reducing data collection times and allowing for the observation of transient electrochemical processes [68]. The disadvantage is the difficulty of setting up the DEMS system, requiring extensive calibrations, and the inability to detect low-volatility products. Furthermore, this technology is only suitable for laboratory-scale investigations.

Despite the development of advanced designs for CO_2 RR cells, their performance still lags behind that of current PEM water electrolysis cells. Apart from catalyst design, more efforts should be made to improve CO_2 RR performance through electrode configuration, ion exchange membrane, ionomer, mass transfer as well as process engineering.

1.3 Nitrite reduction reaction (NO_2 RR)

Effluents released from agricultural and industrial activities have led to significant environmental pollution. Nitrate, nitrite, and nitric oxide are the major nitrogen pollutants found in these effluents. Among them, nitrite is more toxic, and its presence in water systems is a major environmental challenge. Nitrite contamination of groundwater in many areas of Europe as well as in the United States and Canada has reached severe levels exceeding the nominal limits set by the European Standards. According to these standards, only 0.05 mg L^{-1} of nitrite is the maximum allowable level in potable water. Excessive nitrite exposure can have devastating effects on human health, such as respiratory deficiencies [69].

Various methods have been used for the treatment of nitrite in wastewater, such as biological [70], catalytical [71], ion exchange [72], and suspended solid removal by sedimentation [73]. Researchers have also investigated the electrochemical treatment of nitrite for wastewater [74, 75]. In addition, the electrochemical reduction of NO_2^- has also been extensively researched to produce N_2 and value-added chemicals while mitigating NO_2^- pollution in recent decades. Since 2020, it has become a potential research area as it considers a more reactive N-source to produce useful products with high faradaic efficiency. Figure 1.3 shows all possible pathways of electrochemical reduction of nitrite (NO_2 RR) to produce various useful products [76]. However, the main challenge of the NO_2 RR process is the selectivity of the products because of the complexity of the reduction reaction process as it involves multiple protons and electrons transfers (Figure 1.3). Thus, electrocatalysts are crucial to developing effective reaction systems with high efficiency and selectivity. This review will focus on the NO_2 RR to two useful products, nitrogen and ammonia.

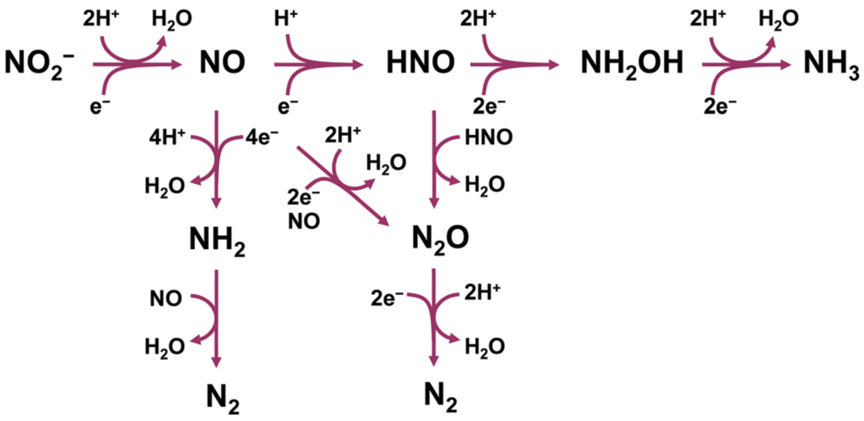

Figure 1.3. Different pathways of electrochemical reduction of nitrite (NO_2 RR) to useful products [76]. Reprinted with permission, Copyright (2022), Chemical Communications.

1.3.1 Electrochemical production of nitrogen from nitrite

Selective electrochemical reduction of nitrite to N_2 has been a topic of significant research due to its importance in maintaining the nitrogen cycle balance [77]. Recently, Koper et al. [78] studied the NO_2 RR to N_2 at a Pt(100) electrode in an alkaline environment. They found that the Pt(100) electrode had a unique reactivity and selectivity for this process, which requires $8H^+$ and $6e^-$ transferred to convert NO_2^- to N_2, as described in eq. 1.4 [79].

$$2NO_2^- + 8H^+ + 6e^- \longrightarrow N_2 + 4H_2O, \qquad E^0 = 1.52 \text{ V vs SHE} \qquad (1.4)$$

E^0 is the standard electrode potential vs. Standard Hydrogen Electrode (SHE).

The team used in-situ Fourier transform infrared (FTIR) and online mass spectrometry (OLEMS) experiments to reveal the origin of the unique reactivity of Pt(100) sites. The in-situ FTIR experiment showed that $NH_{2(ad)}$ and $NO_{(ad)}$ coexist near the N_2 evolution potential window. $NH_{2(ad)}$ was found to be dominant when E < 0.55 V, while $NO_{(ad)}$ was dominant when E > 0.55 V, with both overlapping in the potential region of 0.3-0.5 V. The involvement of both species was confirmed by the OLEMS experiment.

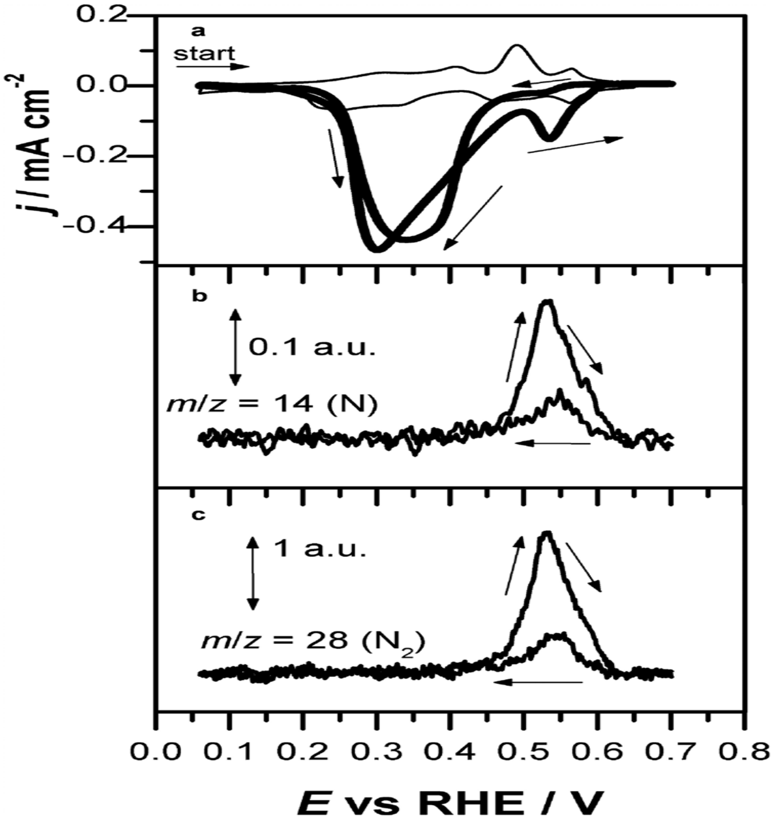

Figure 1.4: Cyclic voltammetry during OLEMS measurements (a) and ion current profiles for m/z = 14 (b) and m/z = 28 (c) in 0.1 M NaOH containing 2 mM $NaNO_2$ [78]. Reprinted with permission, Copyright (2010), American Chemical Society.

Figure 1.4 (a) shows the cyclic voltammograms obtained during OLEMS measurements in 0.1 M NaOH containing 2 mM $NaNO_2$. A sharp peak at around 0.55 V vs. RHE corresponds to NO_2^- reduction to N_2. The production of N_2 was confirmed by the detection of masses 14 and 28 m/z as shown in Figures 1.4 (b) and (c). The team proposed that the coexistence of $NO_{(ad)}$ and $NH_{2(ad)}$ led to the formation of N_2 through a Langmuir Hinshelwood recombination (eq. 1.5).

$$NH_{2(ad)} + NO_{(ad)} \longrightarrow N_2 + H_2O \qquad (1.5)$$

Additionally, the team suggests that achieving 100% selectivity in the conversion of NO_2^- to N_2 could be possible through the ($NH_{2(ad)}$ + $NO_{(ad)}$) mechanism. This is because it involves the participation of two highly adsorbed intermediates (NO and NH_2) [78], which can lead to more efficient catalysis compared to the traditional stepwise mechanism, which requires multiple steps involving the transfer of more than two electrons as described in eq. 1.6-1.8 [80]. However, the precursor N_2O in the stepwise pathway reaction can easily escape from the catalytic sites as it is a weakly ligating molecule, resulting in poor selectivity to N_2 [81].

$$NO_2^- + 2H^+ + e^- \longrightarrow NO_{(ads)} \qquad (1.6)$$

$$NO_{(ads)} + 2H^+ + 2e^- \longrightarrow N_2O_{(ads)} \qquad (1.7)$$

$$N_2O_{(ads)} + 2H^+ + 2e^- \longrightarrow N_2 \qquad (1.8)$$

Nishimura et al. [82] also studied the nitrite reduction reaction at a porous platinum electrode in acidic media and coupled it with online differential electrochemical mass spectrometry (DEMS) analysis. Unlike the results reported by Koper et al., they observed the simultaneous formation of NO, N_2, and N_2O during the voltammetry. They proposed that N_2 was being formed electrochemically from N_2O through the reaction of eq. 1.9.

$$N_2O + 2H^+ + 2e^- \longrightarrow N_2, \qquad E^0 = 1.77 \text{ V vs SHE} \qquad (1.9)$$

Similarly, the formation of N_2O during nitrite reduction was also confirmed by Bae et al. [83] at Pt using FTIR spectroscopy, and they also suggested that N_2 was being formed electrochemically from N_2O through a reaction similar to eq. 1.9. However, in contrast, He et al. recently investigated the reduction of NO_2^- to N_2 at oxo-molybdenum sulfide (oxo-MoS_X) in neutral media and reported a low faradaic efficiency of only 13.5% for N_2 generation, indicating that the process follows a stepwise reaction mechanism [80].

1.3.2 Electrochemical production of ammonia from nitrite

The electrocatalytic nitrite reduction to produce value-added commodity chemicals, like ammonia, is a potential area of research. Several research groups have investigated the selective electrochemical conversion of nitrite to ammonia, which is a challenging process due to the complexity of the $8H^+$ and $6e^-$ transferred reaction, as shown in eq. 1.10 [79]. The NO_2 RR generates various products, as shown in Figure 1.3, the most common of which is N_2, but NH_3 is actually easier to form than N_2 from a catalytic standpoint because no N-N bond is required though it is a thermodynamically favorable product [79]. However, converting nitrite to ammonia with high efficiency remains a challenge, and the development of catalysts with high activity and selectivity is needed for this process.

$$NO_2^- + 8H^+ + 6e^- \longrightarrow NH_4^+ + 2H_2O, \qquad E^0 = 0.897 \text{ V vs SHE} \qquad (1.10)$$

Dinuclear metal complexes, such as the ruthenium complex $\{(TpRu)_2\ (\mu\text{-pz})\}$ [(Tp = trispyrazolylborate and pz = pyrazole] have been studied for their ability to selectively catalyze the six-electron reduction of nitrite to ammonia [84]. Arikawa et al. proposed a three-step mechanism for this process (Figure 1.5). The first step for nitrite reduction was initiated by the $2H^+/e^-$ conversion of a nitrito ligand to a NO ligand, which was further reduced to a nitrido and a H_2O ligand through a $2H^+/5e^-$ process. Finally, the parent nitrito ligand could be recovered by the consumption of $3H^+$ and $3e^-$ in the presence of a nitrite ion, thereby releasing NH_3 and completing the cycle.

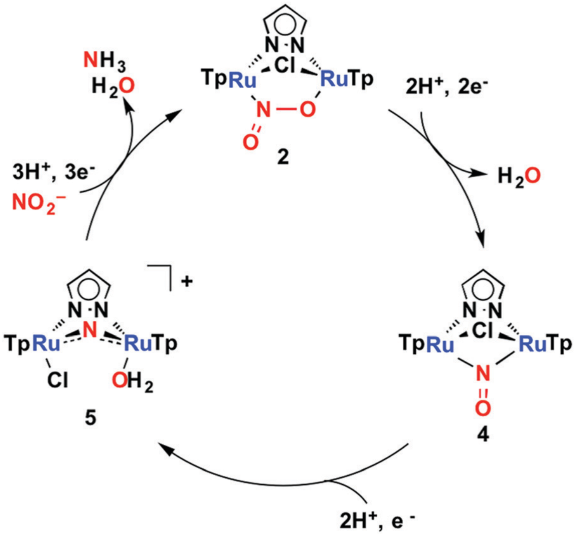

Figure 1.5: Nitrite reduction to ammonia on a dinuclear ruthenium complex [84]. Reprinted with permission, Copyright (2018), American Chemical Society.

Furthermore, the tripeptide GlyGly-HisA (CoGGH)-coordinated cobalt complex has also demonstrated high catalytic activity for the selective NO_2 RR to NH_3 with faradaic efficiency of 90% at 0.9 V vs. Ag/AgCl [85]. This catalyst also selectively converted two reaction intermediates, hydroxylamine and nitric oxide, to ammonium, limiting the simultaneous accumulation of by-products during NO_2RR to ammonia.

Chebotareva et al. have also studied nitrite reduction on glassy carbon electrodes modified with various metallophthalocyanine (M-Pc) complexes in an alkaline solution. They found that the Cu-Pc complex was the most active, producing mainly ammonia. They also reported that nitrite reduction to ammonia is much higher in basic media than in acidic media [86].

Recently, Wang et al. have demonstrated that Ni nanosheet arrays with Ni vacancies (Ni-NSA-VNi) exhibited excellent electrocatalytic performance for the selective NO_2 RR to NH_3, with a faradaic efficiency of 95.5% and a selectivity of 98.0% [87]. They identified nitric oxide (NO) as the reaction intermediate by online DEMS measurement. Through DFT calculation, they found that the addition of Ni vacancies decreased the surface electron cloud density in NiNSA-VNi, which improved the adsorption and activation of nitrite as well as the desorption of ammonia, leading to enhanced electrocatalytic performance. Additionally, they replaced the sluggish oxygen evolution reaction (OER) with value-added semi-dehydrogenation of tetrahydroisoquinolines by using NiNSA-VNi as an anode catalyst, which showed a high FE of 95.5% and a selectivity of 98.0%. The Ni-NSA-VNi ‖ Ni-NSA-VNi two-electrode system also exhibited excellent stability and high selectivity for the simultaneous production of ammonia and dihydroisoquinoline. This work showed that combining the beneficial anode reaction with nitrite reduction can result in efficient energy utilization and enhance economic benefits.

The electrocatalytic reduction of nitrite is a promising area of research for both wastewater treatment and the production of value-added products. This area is growing and has enormous prospects and challenges. Catalyst with high selectivity towards a specific product is crucial for practical applications. Rational catalyst design and reproducible and consistent performances are important. The development of effective electrocatalysts for selective nitrite reduction requires rational catalyst design, in-situ characterization, and theoretical studies to understand the reaction mechanism and intermediates.

1.4 Coreduction of nitrite and CO_2 to urea

1.4.1 Introduction

Electrochemical urea synthesis by coreduction of CO_2 and N-containing compounds, such as nitrogen, nitrite, nitrate, or nitrous oxide [88] is regarded as more sustainable than traditional urea production methods, as it eliminates the need for high temperatures and pressures, as well as reducing the consumption of fossil fuels.

Traditionally, urea is synthesized from the reaction between ammonia (NH_3) and carbon dioxide (CO_2) under harsh conditions such as high temperature (150-200 ℃) and pressure (150-250 bar) [88]. Currently, more than 95% of NH_3 is produced using the century-old Haber-Bosch process (HBP), where N_2 is reduced at high temperature and pressure using H_2 (eq. 1.11), which is mainly produced through the steam reforming of fossil fuels [89].

$$N_2 + 3H_2 \underset{\text{150-200 atm}}{\overset{\text{400-500 °C}}{\rightleftarrows}} 2NH_3 \tag{1.11}$$

$$\Delta G_f^0 = -16.4\ \text{kJ mol}^{-1},\ \Delta H_f^0 = -45.9\ \text{kJ mol}^{-1}$$

Where ΔG_f^0 is the standard Gibbs free energy of formation and ΔH_f^0 is the standard enthalpy of formation.

The electrochemical reduction of CO_2 and NO_2^- is an extensively studied area for urea synthesis, as NO_2^- is considered a highly active nitrogen source [26, 90-95]. This technique simultaneously removes two pollutants from the environment while producing urea as a valuable fertilizer. However, the formation of urea from coupling carbon dioxide and nitrite is challenging due to the complexity of the simultaneous reduction process. It involves multiple proton-coupled electron-transfer steps and chemical steps. The challenge is further complicated by the need to activate CO_2 and NO_2^- within the same potential window while competing with the water reduction reaction, resulting in low urea faradaic efficiency and complex product distribution. Highly active catalysts are desired to improve urea production with high efficiency. Unfortunately, an ideal electrocatalyst for converting CO_2 and NO_2^- to urea with high efficiency and production rate has yet to be discovered. Therefore, extensive research on electrocatalysts is crucial to improve the selectivity of both NO_2^- and CO_2 reduction towards urea and reduce side reactions.

1.4.2 Proposed reaction mechanism of coreduction of nitrite and CO_2 to urea

Electrochemical coreduction of NO_2^- and CO_2 to produce urea has been accomplished with a wide variety of catalysts [26,90-95]. Shibata et al. [90] first demonstrated the electrochemical synthesis of urea from CO_2 and NO_2^- using a Cu-loaded gas diffusion electrode in 1995, achieving the highest faradaic efficiency of 37% at -0.75 V vs RHE. The authors believed that adsorbed CO (CO*) and adsorbed NH_2 (NH_2*) are the two major reaction intermediates responsible for producing urea. They proposed that the formation of urea depends upon the catalyst's ability to convert CO_2 to CO*-type and NO_2^- to NH_2*-type intermediates simultaneously at the same potential window (eq. 1.12-1.13). Then the adjacent intermediate CO* and NH_2* help to form the C–N bond through Langmuir-Hinshelwood mechanism to produce urea (eq. 1.14) [96]. In this cathodic process a total of 14 protons and 12 electrons are consumed to produce one molecule of urea (eq. 1.15).

$$CO_2\,(g) + 2e^- + 2H^+\,(aq) \longrightarrow CO^*\,(\text{intermediate}) + H_2O \qquad (1.12)$$

$$NO_2^-\,(aq) + 5e^- + 6H^+\,(aq) \longrightarrow NH_2^*\,(\text{intermediate}) + 2H_2O \qquad (1.13)$$

$$CO^*\,(\text{intermediate}) + 2NH_2^*\,(\text{intermediate}) \longrightarrow NH_2CONH_2\,(aq) \qquad (1.14)$$

Overall cathodic reaction

$$CO_2\,(g) + 2NO_2^-\,(aq) + 12e^- + 14H^+\,(aq) \longrightarrow NH_2CONH_2\,(aq) + 5H_2O \qquad (1.15)$$

This group established their mechanism through control experiments by replacing either CO_2 with CO or NO_2^- with NH_3 and found no urea was produced under these conditions. These results confirmed that urea was directly produced from NH_2*-like and CO*-like intermediates, which were produced from the reductions of NO_2^- and CO_2.

Recently, Meng et al. [91] proposed a different type of reaction mechanism as described in eq. 1.16-1.18, when they investigated the coreduction of nitrite and CO_2 at oxygen vacancy-rich ZnO porous nanosheets (ZnO-V). This group was the first to establish their proposed mechanism by characterizing the surface intermediates with in-situ techniques, leading to an alternative C-N coupling mechanism.

$$NO_2^- (aq) + 6e^- + 6H^+ (aq) \longrightarrow NH_2^* \text{ (intermediate)} + 2H_2O \qquad (1.16)$$

$$CO_2 (g) + H^+ (aq) + e^- \longrightarrow COOH^* \text{ (intermediate)} \qquad (1.17)$$

The final cathodic reaction:

$$COOH^* + 2NH_2^* + H^+ (aq) + e^- \longrightarrow NH_2CONH_2 (aq) + H_2O + CO \qquad (1.18)$$

They have predicted the reaction pathway on the basis of the catalytic surface, which contains oxygen vacant sites in ZnO. The schematic illustration profile of the CO_2 reduction reaction and the NO_2^- reduction reaction at ZnO-V is represented in Figure 1.6.

According to the authors' proposed mechanism, the process begins with the oxygen atom in NO_2^- attacking the oxygen-vacant sites of the catalyst. This is followed by the reduction of NO_2^- to the intermediate NH_2* through a series of proton-coupled electron transfer reactions. At the same time, oxygen atom in CO_2 is also attacked into the vacant sites and reduced to COOH* through a single proton-coupled electron transfer reaction. The final step involves coupling the NH_2* and COOH* intermediates, leading to the formation of urea. The authors supported their proposed mechanism with the in-situ infrared absorption spectroscopy (FTIR) experiments under reaction conditions. Their IR spectra showed a strong band for COOH* intermediate at 1360 cm^{-1} when NO_2^- was absence then in the presence of both CO_2 and NO_2^-, indicating the consumption of

COOH* during urea formation. Additionally, an absorption band at 1440 cm^{-1} was found in the presence of both CO_2 and NO_2^-, indicating the present of a C-N bond as a result of urea formation.

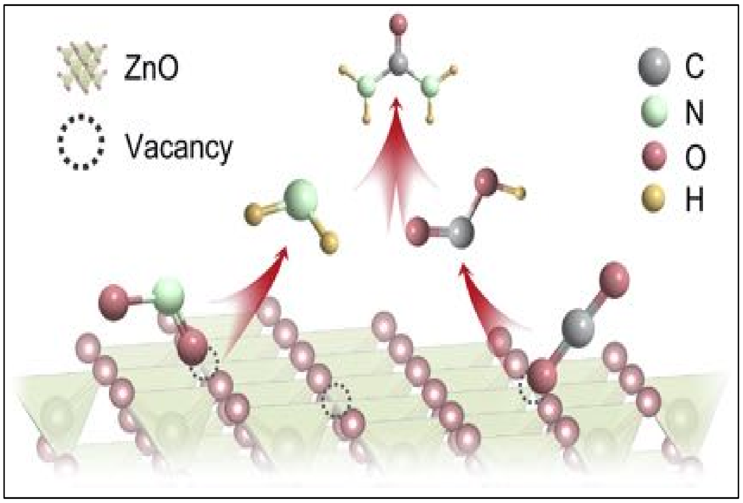

Figure 1.6. The schematic illustration profile of the CO_2 reduction reaction and the NO_2^- reduction reaction at ZnO-V surface. Reprinted with permission [91], Copyright (2021), Physical Science.

1.4.3 State of the art electrocatalysts for coreduction of nitrite and CO_2 to urea

As was previously mentioned, that the first report on the electrochemical synthesis of urea from the coreduction of CO_2 and NO_2^- was published by Shibata et al. in 1995 [90]. After then, this group has investigated various transition metal-loaded gas diffusion electrodes and found that the highest urea faradaic efficiency of 55% was achieved with a Cd electrode at -1.0 V vs RHE [92]. Later in 2001, further findings were reported by the same group that metal phthalocyanine (M-Pc) catalysts could be a potential electrocatalyst to produce urea by the coreduction of CO_2 and NO_2^- [93]. The presence of multiple active sites such as the metal center, pyridinic nitrogen, and pyrrolic nitrogen groups in M-Pc can greatly enhance the selective reduction of NO_2^- and CO_2 to produce urea, where the choice of metal ions is very important, which significantly influence the reaction's selectivity and efficiency [97-98]. They found that, except Al and Ge, all metal phthalocyanines from groups 8-14 were capable of producing urea. The most effective were Zn, Cu, Pd, Fe, Co, and Ni phthalocyanines, which produced urea at high faradaic efficiency of 20-42% at negative potentials range from -0.75 to -1.6 V vs RHE.

Since Shibata's work, there has been limited progress in developing effective and selective electrocatalysts. However, recent studies have shown promise. In a study by Cao et al. [26], the authors explored TiO_2 based materials and successfully synthesized an oxygen vacancy Cu-doped TiO_2 electrocatalyst. This electrocatalyst was able to produce urea with an excellent yield rate (20.8 $\mu M\ h^{-1}$) and high faradaic efficiency (43.1%) at a low overpotential (-0.4 V vs RHE). The oxygen vacancy Cu-doped TiO_2 played the role of a synergistic site, which could efficiently catalyze the reduction of CO_2 into CO* intermediate on the copper dopants site and the reduction of NO_2^- to NH_2* intermediate on Ti^{3+} defect site, resulting in high efficiency urea production.

In another study by Meng et al. [91], the authors used electrochemical reduction to create oxygen vacancies in synthesized ZnO porous nanosheets (ZnO-V). This electrocatalyst was able to convert nitrite and CO_2 to urea with a faradaic efficiency of 23.26% and a urea yield rate of 16.56 $\mu M\ h^{-1}$ at -0.79 V vs RHE. The authors were able to uncover the likely reactive intermediates and C-N coupling route for urea production through in-situ FTIR and DEMS. The preparation of oxygen vacancy-rich ZnO porous nanosheets involved a three-step steps, including the use of electrodeposition, calcination, and electrochemical CV reduction. In the first step, carbon cloth was used as the substrate to grow $Zn_4SO_4(OH)_6 \cdot 5H_2O$ nanosheet precursors through electrodeposition. Next, the $Zn_4SO(OH)_6 \cdot 5H_2O$ nanosheets were calcinated at 650 ℃ in air to create ZnO porous nanosheets. Finally, ZnO is converted into ZnO-V through electrochemical CV reduction.

In a study by Feng et al. [94], Te-doped Pd nanocrystals were prepared using a wet chemical method. The authors used Pd(acac)$_2$ and H_6TeO_6 as metal precursors and *N, N*-dimethylacetamide as the solvent and reducing agent, and NH_4HCO_3 and polyvinylpyrrolidone (PVP) as additional components in the synthesis process. The resulting electrocatalyst showed efficient electrochemical performance, with a faradaic efficiency of 12.2% for converting CO_2 and NO_2^- to urea at a high negative potential of -1.1 V vs RHE.

A very recent study conducted by Liu et al. [95] has shown that noble metal alloy AuCu self-assembled nanofibers (SANFs) are highly stable during long-term electrolysis. This catalyst has been found to have the capability to produce urea at a relatively high rate of 64.8 $\mu M\ h^{-1}$ with a faradaic efficiency of 24.7%. The authors attribute the success of this catalyst to the presence of rich structural defects in AuCu SANFs, which provide a large number of highly active catalytic sites. This allows the simultaneous reduction of CO_2 and NO_2^- to produce urea at a high rate.

1.5 Product analysis from coreduction of nitrite and CO_2

The performance of electrocatalytic coreduction of nitrite and CO_2 is directly determined by the amount of product produced during electrolysis. Therefore, product quantification methods are critical and should be highly sensitive, selective, accurate, and reproducible. Due to the diverse experimental conditions used, several detection techniques have been used to quantify products. This section will focus on discussing the most commonly used analytical techniques for measuring urea and ammonia, which are typically the primary commodity products produced during the coreduction of nitrite and CO_2.

1.5.1 Analysis of urea

Recently, Li et al. [99] provided a comprehensive overview and comparison of analytical techniques employed to quantify urea produced from coreduction of diverse carbon and nitrogen sources, including seven studies from coreduction of nitrite and CO_2. According to the report, around 58% of studies quantified urea using spectrophotometric techniques, of which 28% used indophenol blue method after hydrolysis/digestion with urease and 30% used the diacetyl monoxime method. In constant, only 24%, 16%, and 2% used ^{1}H-NMR, HPLC, and FTIR techniques, respectively.

Urea measurement using the urease method [26] mainly refers to the decomposition of urea by urease to ammonia (eq. 1.19), and the urea concentration is indirectly calculated by difference, by analyzing the total amount of ammonia following decomposition as described in eq. 1.20.

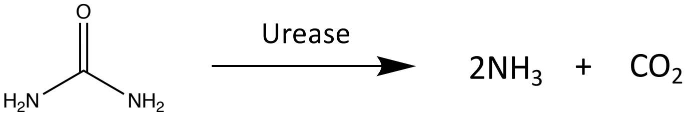

(1.19)

Total number of moles of urea = $[[NH_3]$ after digestion - $[NH_3]$ before digestion$]/2$ (1.20)

Here, $[NH_3]$ before digestion is the initial concetation of NH_3 in the sample and $[NH_3]$ after digestion is the total concetation of NH_3 in the sample after urea was digested with urease.

The indophenol blue method (or the salicylate method modification of the indophenol blue method) is widely used for the quantification of ammonia after the decomposition of urea to ammonia due to its low detection limit, stable color development, good reproducibility, and low cost [100]. Additionally, a few studies have also reported the use of ion-chromatography (IC) [101-102] for the quantification of ammonia. The indophenol blue method follows the Berthelot reaction (eq. 1.21), involving the reaction of ammonia with phenol and hypochlorite in an alkaline solution to generate a blue-colored indophenol product. Sodium nitroprusside is used as a catalyst to intensify the color change in the indophenol reaction, with citrate buffer used to stabilize the pH of the reaction solution [103].

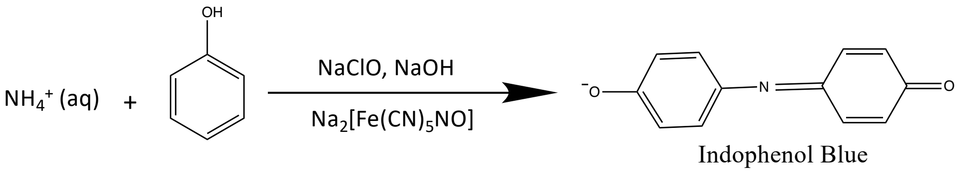

(1.21)

Unfortunately, this method is highly sensitive to various factors such as pH, reaction time, and reagent concentrations [103]. Additionally, the presence of certain metal ions (Fe^{2+}, Fe^{3+}, Na^+, Ca^{2+}, Cu^{2+}, Mg^{2+}), various anions, and especially N-containing compounds can adversely impact in the formation of the chromophores and accuracy of the ammonia measurement [102, 104,105].

Studies have shown that the presence of NO_2^- can suppress the formation of the indophenol blue, leading to the underestimation of the NH_4^+ formation, which in turn lowers the calculated urea concentration [8]. The influence of NH_4^+ on urea detection is also investigated extensively, since NH_4^+ is one of the inevitable by-products in the urea electrosynthesis system. It has been found that low concentrations of NH_4^+ (below 10 ppm) have low interference with urea measurement, with a relative error within 10%. However, higher concentrations of NH_4^+ (above 35 ppm) can significantly impact the accuracy of urea measurement, resulting in a relative error typically exceeding 30% [99, 105].

It is clear that the sample's matrix greatly influences the accuracy of urea quantification by the urease method. Therefore, it is crucial to match exactly the solution components and concentrations used to acquire the standard calibration data with those used in the coreduction process. However, due to the reaction process's complexity, many unknown products and intermediates can be produced during the electrolysis, making it very challenging to match the calibration standard composition with the actual sample's matrix. Additionally, Huang et al. [105] also noted other potential difficulties with using the urease method for urea quantification beside the sample's matrix, such as variations in urease activity between batches, potential loss of NH_4^+ during the digestion process, and inhibition of colorimetric determination of NH_4^+ by high urease concentrations. Therefore, the author recommended paying extra attention to the details of the experiment when the urease method is used, especially when urea is produced with a high amount of ammonia.

On the other hand, IC with appropriate chromatography columns can provide the advantages of a much lower detection limit, excellent reproducibility and accuracy, and direct determination of multiple ions. However, Li^+ and Na^+ containing electrolytes are unsuitable due to their shorter retention time, and ionic liquid and organic electrolytes are also incompatible [101, 102].

Compared to the urease method mentioned earlier, the diacetyl monoxime (DAM) method is a more straightforward detection approach based on the absorbance of the pink-red complex produced by the reaction between DAM and urea. Additionally, it has the advantage of a very low detection limit. For instance, the detection of 1.2 nM urea in seawater has been reported [106]. First, diacetyl monoxime is hydrolyzed and breaks down into diacetyl during the reaction in the presence of strong acid and heat (eq. 1.22). Diacetyl and urea then react in the same medium to form the yellow-colored diazine product and water. Diazine is stabilized by thiosemicarbazide and converted to a pink-red colored complex product with a stronger absorbance at 520 nm in the presence of metal ions such as Fe^{3+} (eq. 1.23) [107].

Step: 1

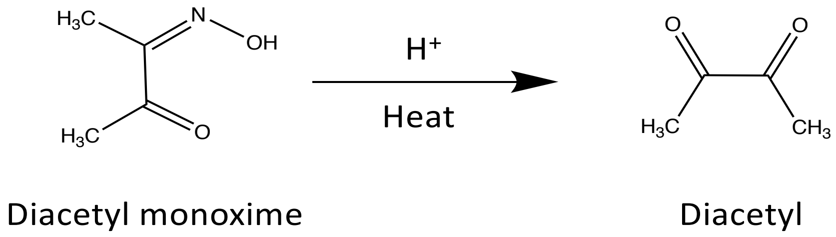

(1.22)

Step: 2

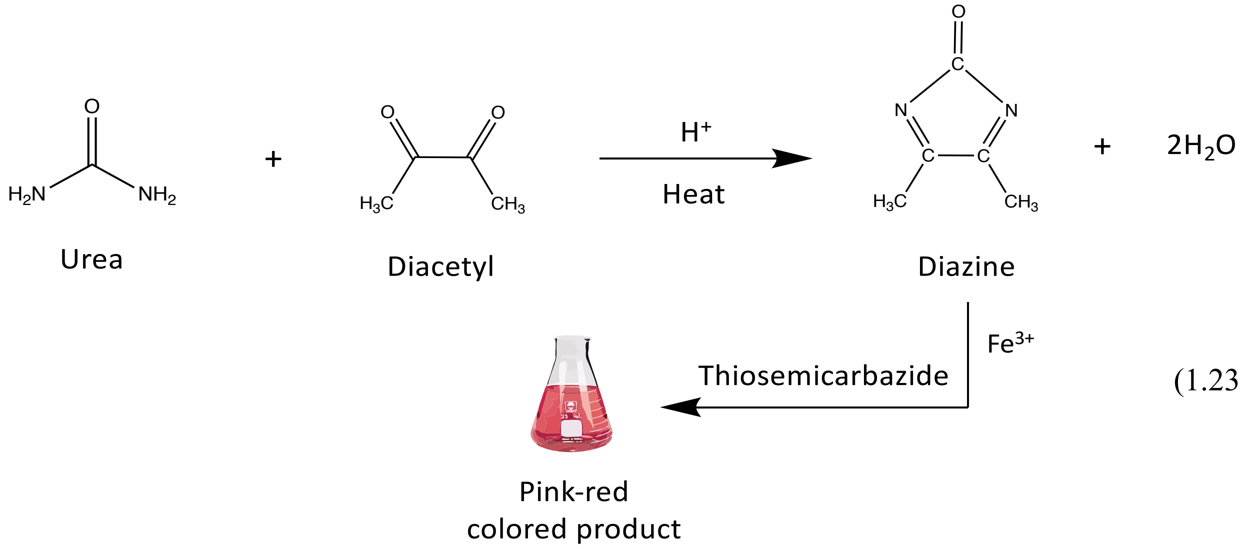

(1.23)

Chen et al. [106] reported that this method is highly sensitive to reagent stability, pH, and reaction temperature and time. Additionally, Li et al. found that the presence of metal ions at low concentration does not affect the detection of urea; however, various carbon and nitrogen containing reactants, sacrificial agents, and electrolytes do have a negative impact on the formation of the chromophores (Figure 1.7), which can lead to unreliable results [99].

The urea concentration measured in most experiments showed quantitative discrepancies, with all components except NH_4OH having a positive interference. More importantly, the addition of 0.1 M KNO_2 resulted in the inability to detect urea. Further experiments by decreasing the concentration of C/N-containing components revealed that, except for KNO_2, all components had a concentration-independent quantitative error. Significant quantitative inconsistencies happened when the KNO_2 concentration exceeded 0.1 mM, and no urea was detected above the concentration 10 mM. These results indicate that the DAM method is not suitable for systems containing NO_2^-.

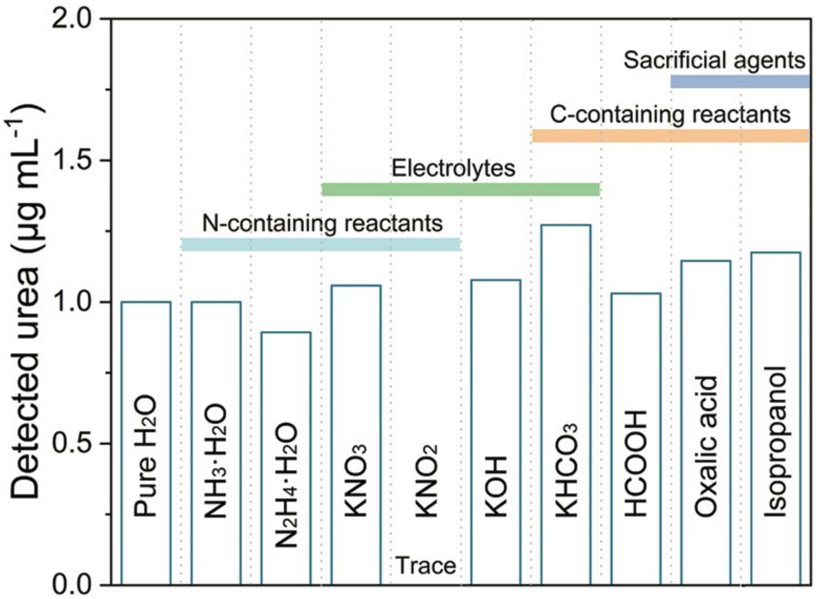

Figure 1.7. The urea concentration (theoretical value: 1 μg mL^{-1}) detected under different interferences (After added N/C-containing reactants before reaction ($NH_3.H_2O$ and NH_2OH: 1% v/v), sacrificial agents (oxalic acid: 1% w/v; HCOOH and isopropanol: 1% v/v), or electrolytes (0.1 mol L^{-1})) [99]. Reprinted with permission, Copyright (2022), Small Methods.

Compared to the spectrophotometric techniques, NMR is a non-destructive and isotope-sensitive technique that has been successfully employed to measure the urea and isotopic-labeled urea [99, 105, 108]. ^{1}H-NMR can easily differentiate $^{12}CO(^{14}NH_2)_2$ from $^{12}CO(^{15}NH_2)_2$ based on the spin difference between ^{14}N and ^{15}N. The interaction between ^{1}H and ^{15}N in $^{12}CO(^{15}NH_2)_2$

produces a doublet (two symmetric signals) with a coupling constant $^1J_{N\text{-}H}$ of 89.94 Hz. In contrast, the interaction between ^1H and ^{14}N in $^{12}CO(^{15}NH_2)_2$ produces a broad signal (singlet) instead of a triplet (three symmetric signals) due to the quadruple relaxation effect as seen in Figure 1.8. The amount of $^{12}CO(^{14}NH_2)_2$ or $^{12}CO(^{15}NH_2)_2$ produced during coreduction of $^{14}NO_2^-$/$^{15}NO_2^-$ and CO_2 can be quantified by making an external calibration curve or adding an internal standard. However, this technique is less sensitive than the spectrophotometric techniques (urease and DAM methods). The lowest detection limit (LOD) reported is 0.54 ppm [105].

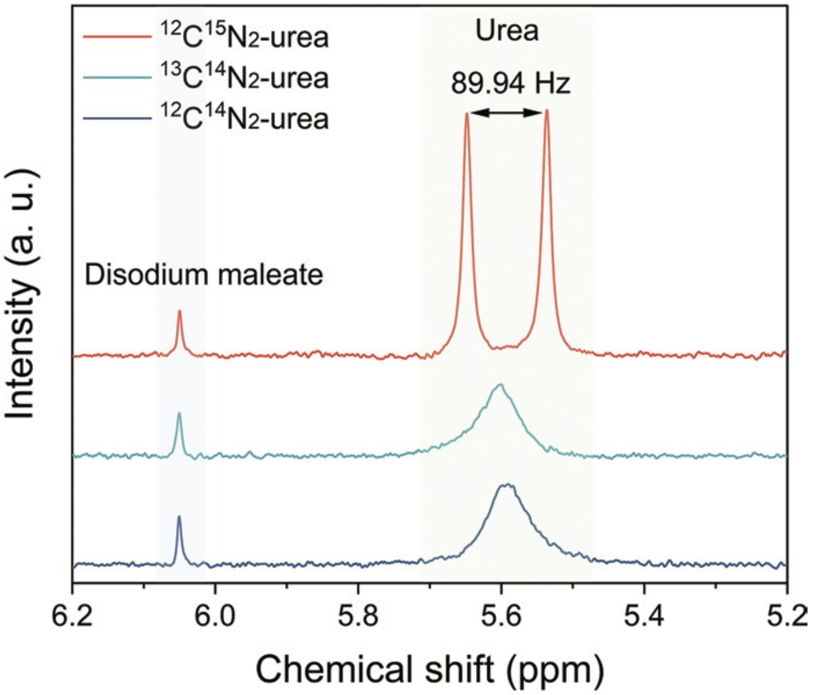

Figure 1.8. ^1H-NMR spectra of non-isotope and isotope-labeled urea (10 μg mL^{-1}) [99]. Reprinted with permission, Copyright (2022), Small Methods.

Recently Huang et al. [109] used the ^1H-NMR to effectively measure urea produced from the coreduction of NO and CO_2 at ZnO nanosheets (ZnO NSs). They achieved a yield rate and faradaic efficiency of 15.13 mM g^{-1} h^{-1} and 11.26% at -0.92 V vs RHE, respectively. However, they also emphasize the importance of proper sample preparation, signal acquisition, and processing procedures for obtaining accurate results with NMR. Additionally, the presence of reaction by-products and metal ions can have a negligible impact on urea quantification using ^{1}H-NMR due to the distinct chemical environment of hydrogen atoms. However, using ^{1}H-NMR to measure urea requires a cryoprobe-equipped NMR spectrometer, as well as an appropriate water suppression pulse sequence, to differentiate between urea (5.6 ppm) and H_2O (~4.7 ppm), as seen in Figure 1.9. This process can be time-consuming, costly and requires expertise, which makes it less accessible for widespread use.

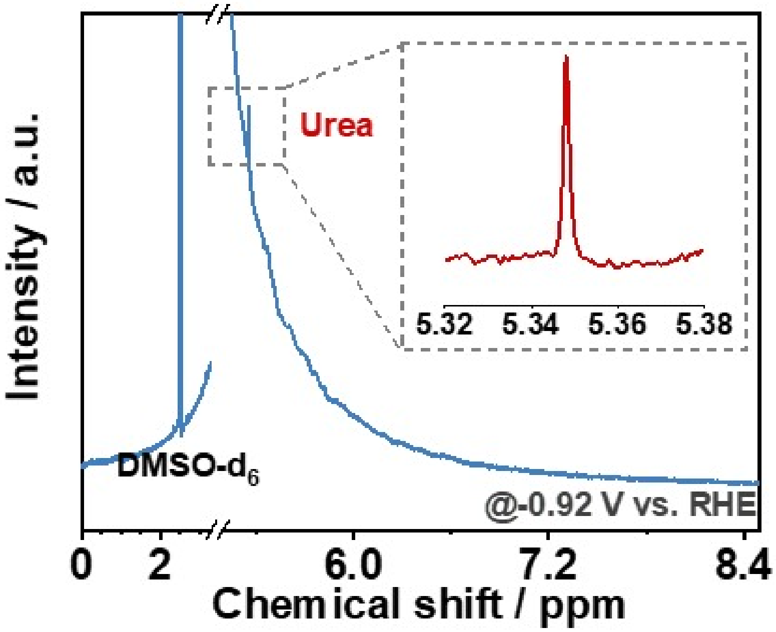

Figure 1.9. Typical ^{1}H-NMR spectrum of electrolyte extracted after electrolysis experiments [109]. Reprinted with permission, Copyright (2021), ACS.

In addition to NMR, mass spectrometry is another isotope sensitive technique that can accurately identify and quantify both urea and isotopic-labeled-urea [110, 111]. This technique is able to differentiate between the two based on their molecular mass differences. Mass spectrometry is highly selective and sensitive compared to other techniques. The use of electrospray ionization (ESI) in a mass spectrometer is very useful for the analysis of non-polar or semi-polar small molecules due to its soft ionization capabilities. In positive polarity mode, the molecular ion peaks of urea can be identified in MS spectra as a [Urea + H]$^+$ as seen in Figure 1.10. This method is particularly very useful when urea is produced at very low concentration levels, such as in the micromole or nanomole range concertation.

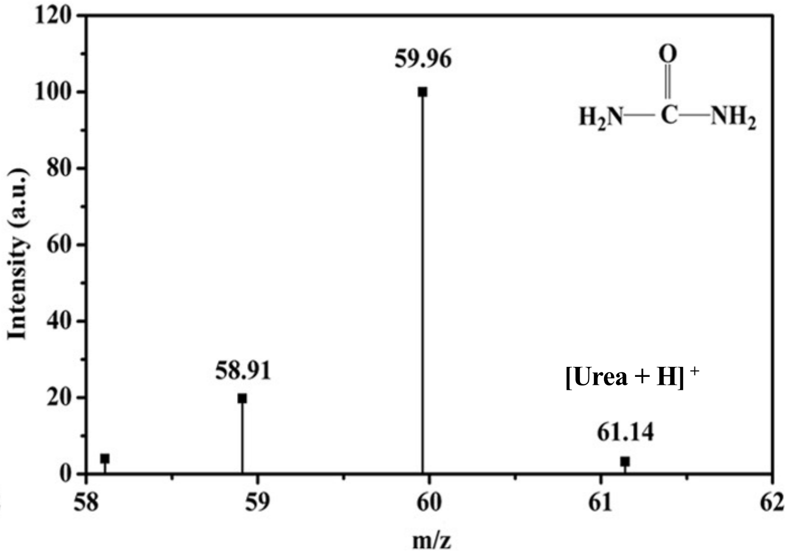

Figure 1.10. The molecular ion peaks and fragment ion peaks of urea [$^{12}CO(^{14}NH_2)_2$] [110]. Reprinted with permission, Copyright (2021), ACS.

Several research groups have successfully used the liquid-chromatography mass spectrometry (LC-MS) technique to identify urea produced from coreduction CO_2 and various N-sources [26,105,108]. Maimaiti et al. [110] recently used LC-MS to detect isotopically labeled urea produced from photocatalytic reduction of N_2 and CO_2, using an Fe-core-supported Ti^{3+}-TiO_2

composite as a catalyst. They found that Ti^{3+} sites and oxygen vacancies on TiO_2 were the active centers for N_2 and CO_2 reduction, respectively. To confirm that urea was produced from the coreduction of N_2 and CO_2, they conducted several controlled experiments using isotope labeling. Using LC-MS, they were able to identify the production of both $CO(^{15}NH_2)_2$ and $^{13}CO(^{14}NH_2)_2$ when using $^{15}N_2/CO_2$ and $N_2/^{13}CO_2$ as the feeding gases. Figures.1.11 (a) and (b) show the MS spectra, in negative polarity mode, of the molecular ion and fragment ion peaks of 61.04 and 59.86 m/z for $CO(^{15}NH_2)_2$, and 60.02 and 58.9 m/z for $^{13}CO(^{14}NH_2)_2$, respectively.

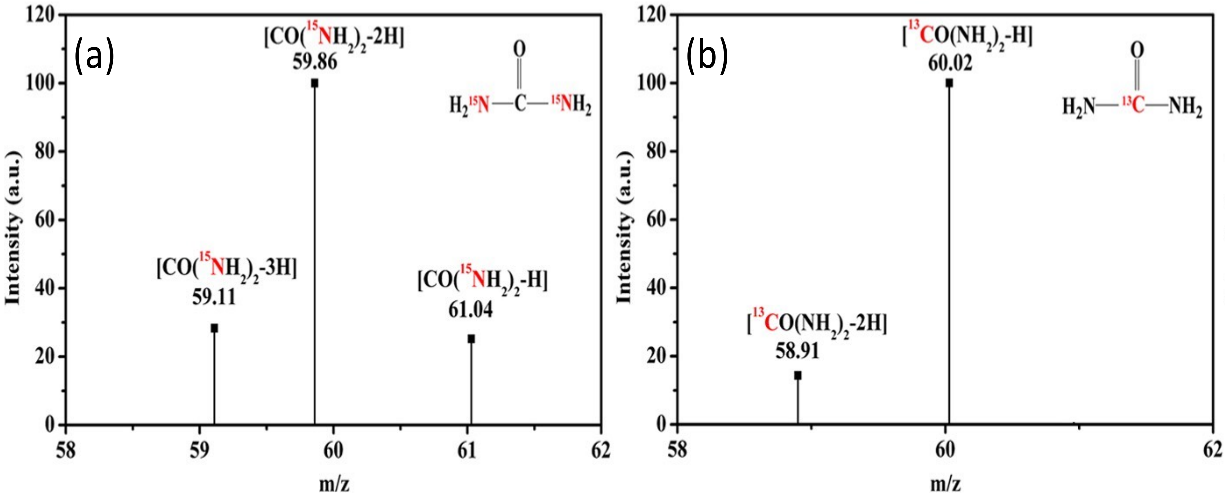

Figure 1.11. The molecular ion peaks and fragment ion peaks of (a) $CO(^{15}NH_2)_2$ and (b) $^{13}CO(^{14}NH_2)_2$ when used $^{15}N_2/CO_2$ and $N_2/^{13}CO_2$ as the feeding gases [110]. Reprinted with permission, Copyright (2021), ACS.

1.5.2 Analysis of ammonia

In addition to the indophenol blue method, as described in Section 1.5.1, NMR is also used to measure ammonia as it is a quick and convenient isotope sensitive method [112, 113]. This technique is commonly used by the nitrogen reduction community to verify that ammonia is produced from nitrogen reduction, rather than from contamination, by conducting isotopic-labeled experiments. For $^{15}NH_3$ measurement, ^1H-NMR is typically used instead of ^{15}N-NMR. ^1H-NMR can easily differentiate $^{15}NH_3$ from $^{14}NH_3$ by the spin difference between ^{14}N and ^{15}N. The interaction between ^1H and ^{15}N in $^{15}NH_4^+$ produces a doublet (two symmetric signals), while the interaction between ^1H and ^{14}N in $^{14}NH_4^+$ produces a triplet (three symmetric signals). However, due to quadruple relaxation effect, the ^{14}N splitting of the ^1H signal is not always observed, but when N is in a highly symmetrical environment, like $^{14}NH_4^+$, the ^{14}N splits the ^1H signal into a triplet. Hence, proper sample preparation and signal acquisition and optimizing of the method are very important for obtaining accurate results. Figure 1.12 shows overlaid ^1H-NMR spectra for $^{15}NH_4^+$ and $^{14}NH_4^+$, where a doublet with a coupling constant $^1J_{N\text{-}H}$ of 73.1 Hz was identified when $^{15}NH_4Cl$ was used as a standard, while a triplet with a coupling constant $^1J_{N\text{-}H}$ of 52.2 Hz was found when $^{14}NH_4Cl$ was used as a standard [112].

Andersen et al. [112] proposed a rigorously controlled experimental protocol for consistent and accurate measurement of ammonia produced from electrochemical nitrogen reduction. They conducted several controlled experiments and isotope-labeled experiments under different conditions to verify their protocol and presented a thorough comparison of ammonia measurement results. Two techniques, ^1H-NMR and a spectrophotometric method (indophenol blue), were used to measure ammonia and the results are presented in Table 1.2. The concentrations of NH_3 measured by ^1H-NMR and the indophenol blue method were 0.65 ± 0.08 and 0.56 ± 0.10 mM, respectively, when $^{14}N_2$ was used and 0.49 ± 0.05 and 0.61 ± 0.16 mM respectively, when $^{15}N_2$ was used. These results demonstrated that if the control experiments are executed carefully, similar amounts of NH_3 can be produced using $^{15}N_2$ as well as using $^{14}N_2$ as the feeding gas.

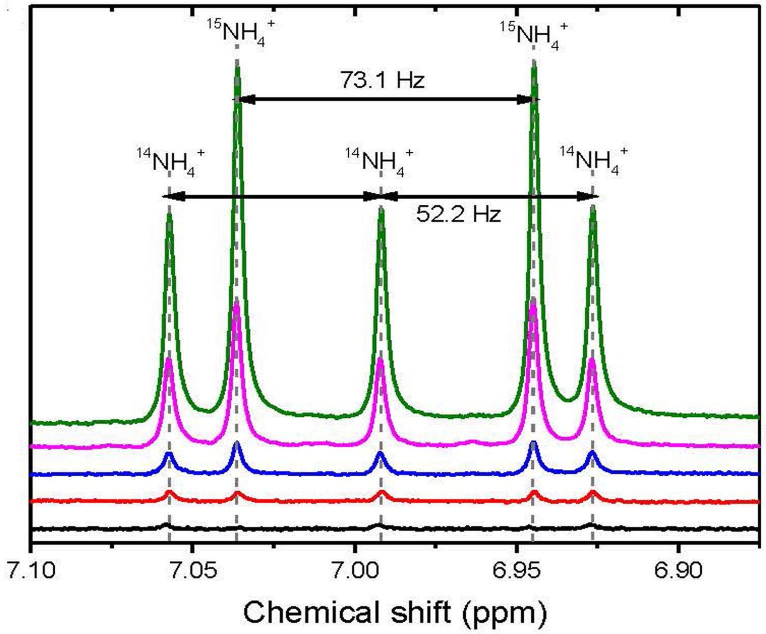

Figure 1.12. Overlaid ^{1}H-NMR spectra for $^{14}NH_4^+$ and $^{15}NH_4^+$ (solutions contain 0, 3,10, 50 and 100 μM L^{-1} of $^{14}NH_4Cl$ and $^{15}NH_4Cl$) [112]. Reprinted with permission, Copyright (2019), Nature.

Table 1.2: Average concentration, average faradaic efficiency (%FE), and average yield rate of NH_3 produced from N_2 reduction at -3.1 V vs RHE under ambient conditions.

Feeding gas	Indophenol blue			^{1}H-NMR		
	Average %FE	Average yield rate μM $h^{-1}cm^{-2}$	Average NH_3 (mM)	Average %FE	Average yield rate μM $h^{-1}cm^{-2}$	Average NH_3 (mM)
$^{14}N_2$	7.5 ± 1.1	0.8 ± 0.10	0.65 ± 0.08	6.5 ± 1.4	0.7 ± 0.20	0.56 ± 0.10
$^{15}N_2$	7.0 ± 2.2	0.7 ± 0.20	0.61 ± 0.16	5.7 ± 0.70	0.6 ± 0.10	0.49 ± 0.05

Additionally, Hu et al. [113] published a study on electrochemical N_2 reduction using a Mo_2N/Ti catalyst, where they achieved a high faradaic efficiency of 42.3% at -0.05 V vs RHE and a yield rate of 1.99 μg h^{-1} mg_{cat}^{-1}. However, when they slightly changed their applied potential from -0.05 V to -0.15 V, they found that faradaic efficiency dropped drastically from 42.3% to 1.93%. Initially, they believed that NH_3 was produced from electrochemically reduced N_2. An isotope-labeling experiment was performed to confirm the N_2 sources of their produced NH_3 using $^{15}N_2$ as a feeding gas. They analyzed the products with ^{1}H-NMR, and surprisingly, no doublet was observed in the spectra, which indicates that no $^{15}NH_3$ was produced in their isotopic labeled experiment. Further investigation using Ar-based electrochemical electrolysis revealed that NH_3 was formed due to the decomposition of the nitride catalyst. The isotope-labeling study thus proved that the Mo_2N/Ti catalyst does not have any catalytic ability to produce NH_3 from N_2.

1.6 Performance evaluation of the electrocatalytic coreduction of nitrite and CO_2

The performance of an electrocatalytic process can be evaluated using several fundamental parameters, including faradaic efficiency, reaction rate (yield rate), onset potential, current density, energy efficiency, and stability. However, this section will specifically focus on two key parameters, the faradaic efficiency and reaction rate, as both are far behind the practical expectations.

i. **Faradaic efficiency:** Faradaic efficiency implies the selectivity of the product in electrolysis. It measures how much of the total charge that flows through the cell is used for the desired reaction. The faradaic efficiency is expressed as a percentage and is calculated as the ratio of the charge consumed for the production of a specific product to the total charge that flows through an electrolysis cell as described in eq. 1.24 [114]. A faradaic efficiency of 100% would mean that all of the current is used for the desired reaction, and none is used on any side reactions.

$$Faradaic\ efficency\ (\%) \quad = \quad \frac{[C_i] * n_i * F}{Q_{total}} \text{ x } 100 \qquad (1.24)$$

Where Q_{total} is the quantity of the charge consumed in the reduction (C), n_i is the number of electrons transferred to form product i, $[C_i]$ is the concentration of product i (mol L^{-1}) and F is the Faraday constant (96485 C mol^{-1}).

ii. **Experimental reaction rate ($r_{i_{(exp)}}$):** The experimental reaction rate is a measure of the actual amount of a specific product that is formed during electrolysis. Production of a specific product per unit time and area (or per unit time and mass of the catalyst) is a direct parameter to evaluate the performance of catalysts. Based on the unit time and area, the reaction rate of a specific product can be calculated from the eq. 1.25 [112].

$$Reaction\ rate\ (r_{i_{(exp)}}): \quad = \quad \frac{[C_i] * V}{t\ * A} \quad (\text{mol s}^{-1}\text{ cm}^{-2}) \qquad (1.25)$$

where $[C_i]$ is the concentration of product i (mol L^{-1}), t is the electrolysis time (s), V is the total volume of electrolyte (L), and A is the electrode surface area (cm^2).

iii. **Theoretical reaction rate ($r_{i_{(theo)}}$):** The theoretical reaction rate is a measure of the maximum amount of a specific product that could be formed during electrolysis. It can be calculated from the current flow during the electrolysis using the eq. 1.26 [112].

$$Reaction\ rate\ (r_{i_{(exp)}}): \quad = \quad \frac{I}{\text{A} \ * \text{F} \ * \ n_i} \quad (\text{mol s}^{-1}\text{ cm}^{-2}) \qquad (1.26)$$

where, I is the current flow (A), n_i is the number of electrons transferred to form product i, A is the electrode surface area (cm^2), and F is the Faraday constant (96485 C mol^{-1}).

Based on the existing literature, the reported values of faradaic efficiency of urea from the reduction of nitrite and CO_2 under ambient conditions mostly fall within the range of 4-55 %, and the reaction rate is around 2-30 μM h^{-1}. In contrast, the faradaic efficiency of industrial urea production is typically about 85-95 %. This field is new and challenging, and is continuously improving, but for practical applications, the performance of the system is expected at least to be comparable to current state-of-the-art proton exchange membrane water electrolysis. However, recently published a noble-metal alloy catalyst such as AuCu has achieved a relatively high production rate of 64.8 μM h^{-1} with a faradaic efficiency of 24.7 % [95]. If this catalyst shows good stability, it could possibly be utilized in distributed applications, where a low quantity but continuous urea supply is needed.

1.7 Oxidation of small organic fuels

1.7.1 Introduction

Small organic fuels (SOF) such as formic acid, methanol, and ethanol are seen as promising sources of energy due to their high energy density [115, 116] and sustainable production [117]. Over the last several decades, the oxidation of SOF has been extensively researched in the field of electrochemistry. This research is important in order to understand the electrochemical oxidation reactions and guide the design of high-performance catalysts. This understanding is also crucial for the development of direct organic fuel cells (DOFC). Various techniques, such as cyclic voltammetry (CV), chronoamperometry (CA), CO stripping, Tafel plot, electrochemical impedance spectroscopy (EIS) have been using to investigate the electrocatalytic oxidation of SOF. Among them, cyclic voltammetry has been widely used to study this process using various metal catalysts. Through oxidation, these fuels can generate electrical power and they have high energy density (Table 1.3). Therefore, these fuels can be used in fuel cells, which can have applications across a variety of industries.

Table 1.3: Energy density of some organic fuels (E^0 is the standard potential of the reaction vs SHE) [115, 116].

Type of fuel	Anode reaction	Energy density (Wh L^{-1})	Energy density (Wh g^{-1})
Formic acid	$HCOOH \rightarrow CO_2 + 2H^+ + 2e^-$ $E^0 = -0.17$ V	1750	1630
Methanol	$CH_3OH + H_2O \rightarrow$ $CO_2 + 6H^+ + 6e^-$ $E^0 = 0.016$ V	4820	6073
Ethanol	$C_2H_5OH + 3H_2O \rightarrow$ $2CO_2 + 12H^+ + 12e^-$ $E^0 = 0.085$ V	6280	8028

1.7.2 Electrochemical oxidation of formic acid

Formic acid is a promising renewable fuel source that can be produced through sustainable methods such as from biomass [117] or electrochemical reduction of CO_2 [118]. It has several advantages as a fuel, including a high flash point of 69 ℃, making it less flammable than other fuels such as methanol (12 ℃) and ethanol (16.6 ℃). Additionally, it has 3.6 times greater proton storage capacity than compressed hydrogen (at 350 bar and by volume) [119] and low crossover properties through membranes [120]. Formic acid has a potential use as a fuel in direct formic acid fuel cells (DFAFC) [121].

Pt-based (or Pd-based) materials are typically used for formic acid oxidation in direct formic acid fuel cells (DFAFC). Capon et al. first proposed in 1973 that the oxidation of formic acid occurs through a dual-path mechanism [122, 123]. Initially, formic acid is adsorbed on the Pt surface. In the next step, it can be either dehydrogenated (eq. 1.27) to form CO_2 [124, 125] or it can be dehydrated (eq. 1.28) and blocks (poisons) sites on the Pt surface by adsorbed CO (CO_{ads}). CO_{ads} can be further oxidized to produce CO_2 (eq. 1.29) [124,126]. The dehydrogenation pathway is known as the direct pathway and dehydration as the indirect pathway.

$$HCOOH_{ads} \rightarrow CO_2 + 2H^+ + 2e^- \qquad (1.27)$$

$$HCOOH_{ads} \rightarrow CO_{ads} + H_2O \qquad (1.28)$$

$$CO_{ads} + H_2O \rightarrow CO_2 + 2H^+ + 2e^- \qquad (1.29)$$

1.7.2.1 Cyclic voltammetry of formic acid oxidation at a Pt electrode

The formic acid oxidation reaction (FAOR) is the most intensively investigated among other small organic molecules. Several research groups studied the FAOR mechanism by characterizing surface intermediates using various techniques, including in-situ, ex-situ, and online analysis of the electrode surface, and identified different intermediate and adsorbed species [127]. Figure 1.13 shows the cyclic voltammetry (CV) of 0.1 M formic acid oxidation at a Pt electrode in 0.5 M H_2SO_4 [128].

The CV exhibits two peaks in the forward scan. Initially, at the potential ca. 0.4 V vs RHE, the current slowly increases and reaches a plateau at ca 0.6 V vs RHE (1st peak). This is followed by an increase in current at ca. 0.7 V vs RHE, which peaks at ca. 0.9 V vs RHE (2nd peak). At low potentials, formic acid was oxidized through the direct pathway with the simultaneous formation of absorbed CO (CO_{ads}) through dehydration of adsorbed formic acid. At these potentials, in-situ ATR-FTIR analysis has identified the presence of both adsorbed formic acid ($HCOOH_{ads}$) and bridge-bonded formate ($HCOO*_b$) [129, 130]. However, of these species, weakly adsorbed $HCOOH_{ads}$ is considered a reactive intermediate directly oxidized to CO_2 [129], while $HCOO*_b$ is regarded as a site-blocking species [130]. Recent density functional theory (DFT) calculations suggested that $HCOO*_b$ acts as a catalyst for the direct oxidation of formic acid rather than being an active intermediate or a site-blocking species. This is because $HCOOH_{ads}$ (O-down) is difficult to oxidize to CO_2, while $HCOOH_{ads}$ (CH-down) can be oxidized to CO_2 when it presents near the adsorbed $HCOO*_b$ [131].

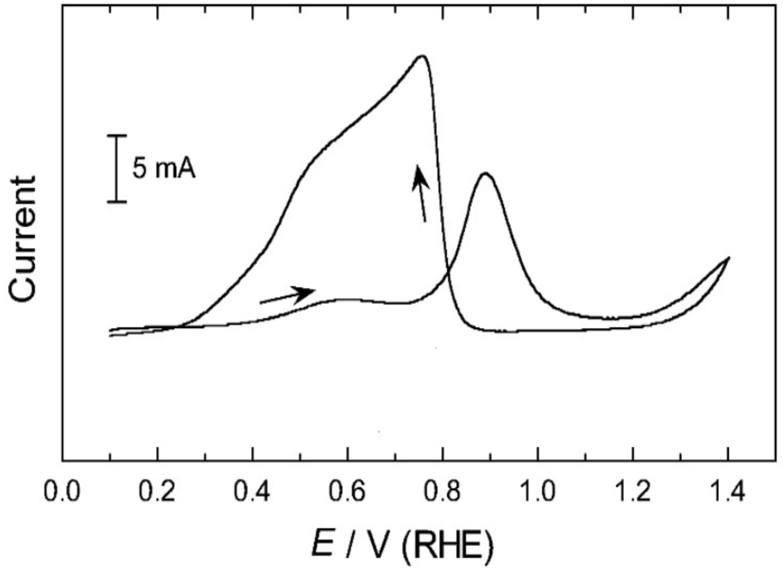

Figure 1.13. Cyclic voltammograms (scan rate 50 mV s^{-1}) for 0.1 M formic acid oxidation in 0.5 M H_2SO_4 (aq) at a Pt electrode [128]. Reprinted with permission, Copyright (2006), American Chemical Society.

However, as the potential increases, the coverage of CO_{ads} increases, the number of Pt sites available for the direct path decreases, and the rate of increase in the current decreases. The Pt surface is poisoned by CO_{ads}, which cannot be removed until water molecules are activated at higher potentials to give adsorbed hydroxyl groups at Pt sites nearby the CO_{ads}. At high potentials, Pt-OH becomes available to oxidize CO_{ads} [132, 133], and the current starts increasing, which results in a large current peak at ca. 0.9 V vs RHE (2nd peak). Therefore, electro-oxidation of formic acid on pure Pt proceeds predominantly via the indirect pathway.

In the reverse scan, a sharp increase in the FA oxidation current is observed. The current at ca. 0.4 V vs RHE is significantly higher than in the forward sweep because the reaction occurs at the electrocatalysts' freshly reduced, poison-free surface [128]. As the potential exceeds ca.1.1 V vs RHE, all adsorbed CO is oxidized, and the Pt surface regains its full activity as the oxide layer is reduced. Pulsed voltammetry has been used to investigate the electrooxidation of formic acid at Pt nanoparticles, revealing that in the backward scan, a large anodic peak is due to formic acid oxidation, which predominantly occurs via the direct oxidation pathway until the potential reaches around 0.5 V and lower, where CO adsorption begins [134]

1.7.3 Electrochemical oxidation of methanol

Methanol is a promising alternative fuel to hydrogen for use fuel cells (i.e, in direct methanol fuel cells (DMFC)), owing to its high energy density [135] and ability to be synthesized from various sources such as biomass, natural gas, coal, and oil [117, 136]. In DMFCs, methanol undergo reaction at the anode in the presence of water to produce six protons, six electrons and CO_2 (eq. 1.30).

$$CH_3OH + H_2O \rightarrow CO_2 + 6H^+ + 6e^- \qquad (1.30)$$

Breiter et al. [137] introduced the concept of a parallel pathway reaction mechanism for complete methanol oxidation at a Pt electrode in 1967. One pathway, known as an indirect path, involves the adsorption of methanol on the catalyst surface, followed by the production of absorbed CO (CO_{ads}), which is then oxidized to CO_2. The other pathway, known as a direct path/formate path, involves the production of CO_2 through the oxidation of formic acid and formaldehyde intermediates after the absorption of methanol. Both pathways require a catalyst to break the C-H bonds and facilitate the oxidation of intermediates to CO_2. Pt is the most effective catalyst for breaking the C-H bond and complete oxidation of methanol [138, 139].

Several research groups proposed that the process of methanol oxidation in acidic media begins with the adsorption of methanol at Pt sites (eq. 1.31), followed by a series of electrochemical dehydrogenation steps (eq. 1.32-1.35) [140, 141].

$$CH_3OH + Pt \rightarrow Pt - CH_3OH_{ads} \qquad (1.31)$$

$$Pt - CH_3OH_{ads} \rightarrow Pt - CH_3O_{ads} + H^+ + e^- \qquad (1.32)$$

$$Pt - CH_3O_{ads} \rightarrow Pt - CH_2O_{ads} + H^+ + e^- \qquad (1.33)$$

$$Pt - CH_2O_{ads} \rightarrow Pt - CHO_{ads} + H^+ + e^- \qquad (1.34)$$

$$Pt - CHO_{ads} + Pt - OH \rightarrow Pt - CO_{ads} + H_2O + Pt \qquad (1.35)$$

At high potentials, the CO intermediate at the Pt surface (Pt-CO_{ads}), can be oxidized to CO_2 as the final step (eq. 1.36 and 1.37) [142, 143]. This step is also known as oxidative removal of the adsorbed CO.

$$Pt - CO_{ads} + H_2O \rightarrow Pt + CO_2 + 2H^+ + 2e^- \qquad (1.36)$$

$$Pt - CO_{ads} + PtO \rightarrow 2Pt + CO_2 \qquad (1.37)$$

1.7.3.1 Cyclic voltammetry of methanol oxidation at a Pt electrode

The methanol oxidation reaction (MOR) is investigated with cyclic voltammetry coupled with various in-situ, ex-situ, and online analysis techniques and identifies different intermediate and adsorbed species [144, 145].

Recently, Lai et al. investigated the methanol oxidation reaction (MOR) using differential electrochemical mass spectrometry (DEMS) to analyze the reaction products. Figure 1.14 illustrates the cyclic voltammogram and corresponding mass spectrometric cyclic voltammograms (MSCVs) obtained for 1 M methanol oxidation at a carbon-supported Pt (Pt/C) electrode in 0.5 M H_2SO_4 [146].

The cyclic voltammogram (CV) exhibits two oxidation peaks, one in the forward scan and the other in the backward scan. During the forward scan, methanol oxidation commenced at around +0.3 V (vs Ag/AgCl) and peaked at +0.6 V, followed by a gradual decrease. At low potentials, methanol adsorbed onto the Pt surface and formed intermediates such as CO_{ads}, $HCHO_{ads}$, and COH_{ads} species via dehydration, as identified by various in-situ spectroscopic techniques [144], which subsequently led to CO_2 production. At higher potentials, a sharp increase in oxidation current was observed due to the formation of Pt-OH_{ads} and the increase in CO_{ads} oxidation, resulting in more Pt sites available for methanol adsorption, leading to a sharp peak at ca +0.9 V. At this potential, the presence of CO_2 (m/z = 44), HCOOH (m/z = 46), and $HCOOCH_3$ (m/z = 60), as well as methanol (m/z = 31) was observed [146].

During the reverse scan, an oxidation peak appeared at ca. +0.45 V. A study by Zhao et al. [147] investigated the oxidation peak of methanol electrooxidation on noble metal electrodes during negative potential scans. The authors proposed that the cathodic oxidation peak originated from the oxidation of freshly adsorbed methanol on the catalyst surface after the metal oxide layer was removed.

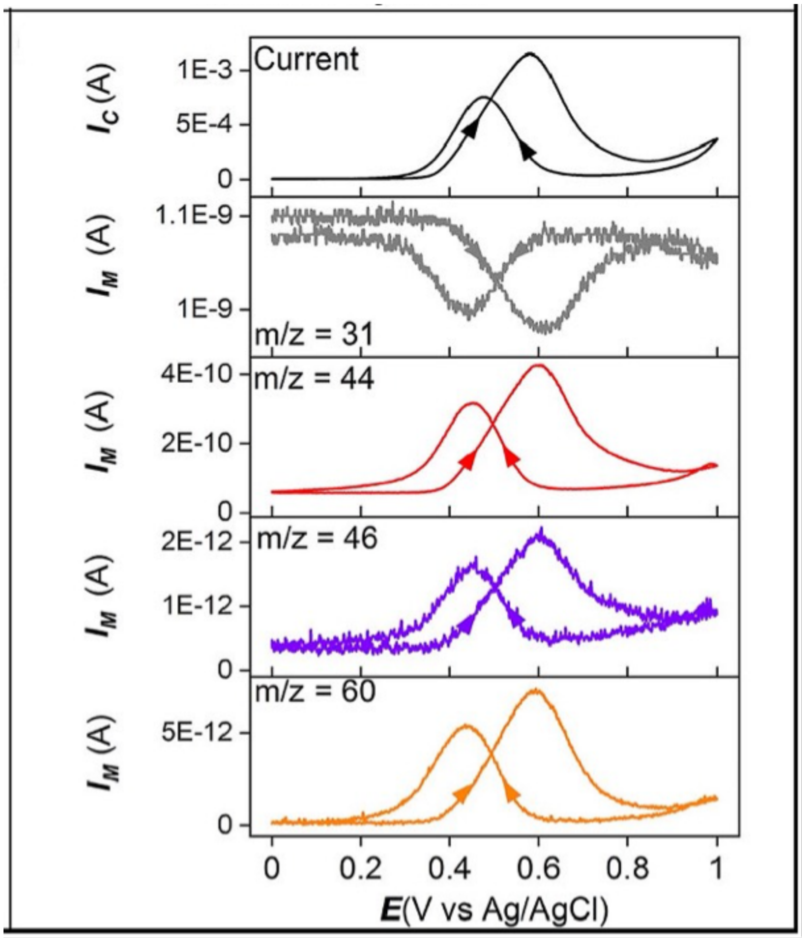

Figure 1.14. Cyclic voltammogram and corresponding mass spectrometric cyclic voltammograms for methanol oxidation on Pt/C in 1 M methanol and 0.5 M H_2SO_4 solution at the scan rate of 1 mV s^{-1} [146]. Reprinted with permission, Copyright (2021), Elsevier.

1.7.4 Electrochemical oxidation of ethanol

Compared to methanol, ethanol has a higher energy density (8.03 kWh kg^{-1} vs 6.1 kWh kg^{-1}) and is less toxic [115, 116]. It can be produced on a large scale from various biomass sources, including agriculture, forestry, and urban waste. Despite being widely studied as a liquid fuel for fuel cells, the oxidation reaction of ethanol is more complex than that of methanol, making the development of direct ethanol fuel cells (DEFC) a challenge. The ethanol oxidation reaction proceeds through multi-step reaction mechanisms, with the cleavage of the C-C bond in ethanol being the most challenging step [148]. Thus, finding more efficient catalysts becomes a critical issue for DEFC development.

The ethanol oxidation reaction mainly follows a dual-pathway mechanism, with one pathway being partial oxidation without C-C bond breaking, resulting in the formation of acetaldehyde by transferring two electrons and two protons (eq. 1.38) or acetic acid by transferring four electrons and four protons (eq. 1.39) [148, 149]. Later, acetaldehyde can be further oxidized to acetic acid. However, further oxidation of acetaldehyde to acetic acid is difficult [149].

$$CH_3CH_2OH \rightarrow CH_3CHO + 2H^+ + 2e^- \tag{1.38}$$

$$CH_3CH_2OH + H_2O \rightarrow CH_3COOH + 4H^+ + 4e^- \tag{1.39}$$

$$CH_3CH_2OH + 3H_2O \rightarrow 2CO_2 + 12H^+ + 12e^- \tag{1.40}$$

The other pathway of the dual-pathway mechanism is the complete oxidation of ethanol to carbon dioxide (eq. 1.40), which requires the transfer of twelve electrons and twelve protons. In this path, the C-C bond of ethanol must be broken for the reaction to occur, producing intermediate adsorbed species like $CH_{x,ads}$ and CH_yO_{ads} (eq. 1.41 and 1.42) [150]. These species can then be oxidized to carbon monoxide (CO_{ads}) through the transfer of electrons and protons. The further oxidation of CO_{ads} species to CO_2 occurs from the rection with hydroxyl species on Pt surfaces (eq. 1.43), which is the limiting step at low potentials [150, 151].

$$\text{Pt-O-CH}_2\text{CH}_3 \text{ or Pt-CH(OH)CH}_3 \rightarrow \text{Pt-CHx} + \text{Pt-CH}_y\text{O} + (5\text{-x-y})\ \text{H}^+ + (5\text{-x-y})\ \text{e}^- \quad (1.41)$$

$$\text{Pt-CH}_y\text{O or Pt-CH}_x \rightarrow \text{Pt-CO} + (\text{x or y})\ \text{H}^+ + (\text{x or y})\ \text{e}^- \quad (1.42)$$

$$\text{Pt-CO} + \text{Pt-OH} \rightarrow 2\text{Pt} + \text{CO}_2 + \text{H}^+ + \text{e}^- \quad (1.43)$$

1.7.4.1 Cyclic voltammetry of ethanol oxidation at a Pt electrode

Various spectroscopy techniques have been utilized to study the ethanol oxidation mechanisms at Pt surfaces [152]. Pt and Pt-based materials have been identified as the most effective catalysts for cleaving the C-C bond in ethanol, leading to fully oxidized products [153, 154].

Figure 1.15 shows the cyclic voltammetry of 0.1 M ethanol oxidation in 0.1 M $HClO_4$ at a Pt electrode studied by Shao et al. using surface-enhanced infrared absorption spectroscopy (SEIRAS) with attenuated total reflection (ATR) [155]. Similar to the oxidation of methanol, cyclic voltammetry of the ethanol oxidation reaction (EOR) also displays two oxidation peaks.

The initial step of EOR involves ethanol adsorption on the Pt surface, followed by its decomposition into intermediates such as CH_xCO, C_2H_X, CH_xO, CO, and CH_x species. In the forward scan, the first peak at +0.7 V (Ag/AgCl) is attributed to the oxidative removal of the adsorbed CO intermediate to CO_2, while the second peak arises from the overlapping current due to the removal of acetate and the formation of PtO. In the reverse scan, the oxide layer on Pt was removed and acetaldehyde/adsorbed acetyl was formed from fresh ethanol and a large oxidation peak is observed.

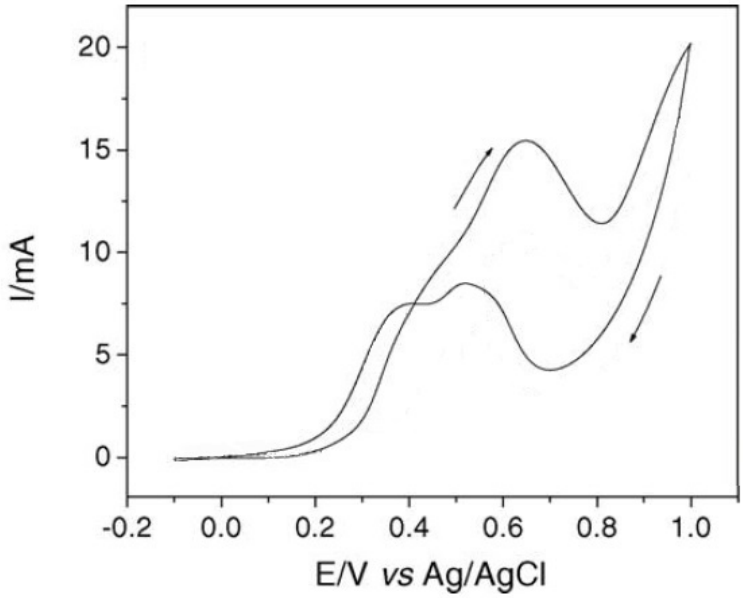

Figure 1.15. Cyclic voltammogram of 0.1 M ethanol oxidation in 0.1 M $HClO_4$ at a Pt electrode [155]. Reprinted with permission, Copyright (2005), Elsevier.

1.8 Pt-surface modification with adatoms for fuel cell application

The surface structure of an electrocatalyst is known to have a significant impact on its electrocatalytic activity and selectivity [156]. In order to improve performance for specific electrochemical reactions, various methods have been used to modify the surface of electrocatalysts. One effective approach is the modification of Pt surfaces by the adsorption of a sub-monolayer of foreign atoms, known as adatoms [157]. This modification can enhance electrocatalyst activity and reduce catalyst poisoning, which is a primary focus of current fuel cell catalyst research.

There are several effective methods used to modify the surface of Pt with adatoms, including solution deposition [158], electrochemical underpotential deposition [159], and irreversible adsorption of adatoms [160]. Various adatoms, such as Ru, Pd, Au, Sb, Se, As, Pb, and Bi, have been used to modify Pt surfaces, improving their activity and selectivity in oxidizing small organic fuels. Even a small coverage of these adatoms can significantly enhance catalytic activity for these reactions. The mechanisms behind the increased performance of adatoms on Pt can be attributed to several phenomena, including the third-body effect, electronic effect, and bifunctional effect [161]. However, the extent of the contribution may vary depending on various factors, such as the preparation of the catalysts, the shape of the Pt nanocrystals, their modification, and the resulting surface composition.

The third-body effect, also known to as the ensemble effect, results from inactive adatoms on the Pt surface that can enhance the oxidation current by blocking the formation of poisoning species, such as absorbed CO (CO_{ads}), and promoting the desorption of reactive intermediates species during the reaction. Many studies have reported that the third-body effect can effectively improve the catalytic activity for formic acid oxidation [162]. In this case, the adsorbed adatom divides the Pt surface into small domains that are large enough for the direct oxidation path but too small for the indirect oxidation path (which requires multiple adjacent Pt active sites for CO_{ads} formation) [163-165]. This provides higher activity through direct oxidation to CO_2. However, studies have shown that the third-body effect typically leads to a decrease in CO_2 selectivity for the oxidation of ethanol [166, 167]. This is because adatoms blocking active sites inhibit the cleavage of the C-C bond of ethanol, which prevents its complete oxidation to CO_2 due to the absence of multiple adjacent Pt active sites. Instead, the incomplete oxidation of ethanol to acetaldehyde and acetic acid is promoted, as fewer Pt active sites are required for these reactions.

Electronic effects can result from modifications to the electronic properties of surface. The adatoms lower the electron density of the 5d orbitals of Pt and changing the electronic properties of the Pt, resulting in a considerable decrease of the CO binding strength to Pt that helps CO to oxidize to CO_2 at low potential [168, 169].

The bifunctional effect involves two steps: promoting the formation of oxygen-containing species (OH) and facilitating removal of reaction intermediates. Modified surfaces have two types of sites with different roles. Pt site breaks the bonds in organic fuels and adatoms adsorb oxygen-containing species. Abundant oxygen-containing species can oxidize strongly adsorbed intermediates such as CO_{ads} to CO_2, resulting in improved cell efficiency by increasing voltage efficiency [170].

Numerous studies have demonstrated that Bi can act as an effective modifier of the Pt surface for formic acid oxidation [161]. Even very small coverages of Bi-adatoms have been shown to significantly improve activity through the direct path (dehydrogenation path), likely due to the electronic effect, third body affect as well as bifunctional mechanism [161].

For instance, Choi et al. [159] modified the surface of carbon-supported Pt (Pt/C) catalyst with Bi adatom to selectively promote formic acid oxidation. Irreversibly adsorbed Bi on the Pt/C surface, resulting in a significant increase in catalytic activity, with a 13-fold enhancement compared to Pt/C. This improvement was attributed to the third body effects, which makes Pt ensembles, preventing CO_{ads} poisoning, thereby increasing formic acid oxidation through direct pathways. They also noted that the performance enhancement is highly dependent on the surface structure of the decorated Pt NCs and the nature and coverage of the Bi adatom.

Additionally, Chen et al. [171] conducted a study on Pt nanocrystals for formic acid oxidation. They used tetra-hexahedral Pt nanocrystals (THH Pt NCs) and decorated their surface with Bi adatoms, which resulted in a significant increase in catalytic activity by up to 70 times when compared to bare THH Pt NCs. According to their findings, Bi-decorated THH Pt NCs hindered the indirect oxidation pathway through a third-body effect, preventing CO_{ads} poisoning. The Bi adatoms also improved the adsorption of OH species on adjacent Pt sites through electronic effects, promoting the oxidation of CO_{ads} through bifunctional mechanisms and making more Pt sites available for further adsorption, thus enhancing the catalytic activity.

Apart from Bi, several other groups investigated the use of Pb [172], Ti [173], Pd [174], Sb [175], and Au [176] adatoms to modified Pt nanoparticles (Pt NPs) for formic acid oxidation and in all cases, improved electrocatalytic activity was observed. However, the enhancement factor strongly depends on several factors such as the preparation method, surface structure of the substrate and coverage of the adatom [171]. The enhanced performance of Ti, Pd and Au-decorated octahedral Pt NPs was attributed to third-body effects. On the other hand, the systems such as Pb and Sb-decorated octahedral Pt NPs, the enhanced performance was attributed to both third-body and electronic effects [174, 175].

Additionally, Yang et al. [177] decorated octahedral Au NPs surface with Pt NPs to promote the formic acid oxidation. The researchers discovered that the electrocatalytic activity of formic acid oxidation was significantly improved through direct path when decreasing Pt coverages, particularly in the submonolayer range. The researchers found that a 0.05 monolayer of Pt NPs resulted in a mass activity of about 63 A mg Pt^{-1}, which was much higher than those obtained with 1 monolayer and with a commercial Pt/C catalyst. They explained the observed enhanced performance was not solely due to a third body effect, but also from the bifunctional effects of adjacent Pt-Au sites. The presence of Au NPs promoted the formation of oxygen-containing species at low potential, contributing to the improved CO_{ads} oxidation to CO_2.

Like formic acid, various adatom-decorated catalysts have also investigated for methanol and ethanol oxidation reactions [178 -182]. However, in most of the cases, negligible catalytic effects and predominantly inhibition effects have been observed for both methanol and ethanol oxidation in acidic medium.

One promising finding is that Ru-decorated THH Pt NPs have been shown to have a high tolerance to CO poisoning and a shift in onset potential to about 0.1 V towards more negative potentials for methanol oxidation reactions [178]. When compared to Ru-decorated Pt/C or commercial PtRu alloy nanoparticle catalysts, these Ru-modified THH Pt NPs exhibit higher activity in the low potential range. However, significant catalytic effects for methanol have been observed for Pb, and Bi decorated Pt NPs in alkaline medium [180]. In contrast, a study conducted by Rogero et al. [181] on ethanol oxidation with adatom decorated (Sn, Rh, Ru, and Pb) Pt NPs in both acidic and alkaline solutions showed that in acidic medium, only the Sn-decorated THH Pt NPs displayed slightly improved properties, which were dependent on the surface structure of the Pt NPs. However, the enhanced activity was also affected by the Sn coverage, potential region, and electrochemical method used. However, in alkaline solutions, none of the adatoms decorated Pt NPs provided significant enhancements of activity for ethanol oxidation. In contrast, a study conducted by Rogero et al. [182] on ethanol oxidation on adatom decorated (Sn, Rh, Ru, and Pb) Pt NPs in both acidic and alkaline solutions showed that in acidic medium, only the Sn-decorated THH Pt NPs displayed slightly improved properties, which were dependent on the surface structure of the Pt NPs. However, the enhanced activity was also affected by the Sn coverage, potential region, and electrochemical method used. However, in alkaline solutions, none of the adatoms decorated Pt NPs provided significant enhancements of activity for ethanol oxidation.

1.9 Objectives of the research

The scientific community has dedicated significant efforts to the development of alternative technologies that promote a sustainable future. Electrocatalysis is one of the critical areas of research in this field, with applications in electrolysis, electrosynthesis, and fuel cells.

Electrochemical processes are increasingly essential in meeting modern society's energy and chemical demands, and electrocatalysts play a pivotal role in enhancing their efficiency and sustainability. Continual efforts to develop and accurately evaluate the performance of new electrocatalysts will help advance these technologies, leading to more sustainable and efficient energy and chemical production processes. The above introductory chapter provides an overview of the history and necessity for alternative sustainable technologies.

Chapter 3 of this research aimed to develop effective methodologies for systematically evaluating the performance of various electrocatalysts used for coelectrolysis of CO_2 and nitrite. The objective was to establish reliable and accurate methods for assessing the performance of electrocatalysts by accurately determining their electrolysis products. To achieve this goal, various quantitative analytical techniques such as spectrophotometry, mass spectrometry, and ^{1}H-NMR techniques were developed and optimized to accurately measure and compare the performance of electrocatalysts. The influences of electrolyte and nitrite ion in the sample on the analysis results was investigated, and analysis procedures were optimized to develop appropriate methodologies for measuring urea and ammonia in the electrolysis solutions. These methodologies were crucial for accurately evaluating the performance of electrocatalysts and comparing their effectiveness.

Chapter 4 focused on the simultaneous synthesis of commodity chemicals such as ammonia and urea from coelectrolysis of CO_2 and nitrite using a highly effective electrocatalyst. The performance of the electrocatalysts was quantified using the quantitative method developed in Chapter 3.

In Chapter 5 aimed to establish a quick and straightforward methodology for screening electrocatalysts for co-electrolysis of CO_2 and nitrite ion using a proton-exchange membrane

(PEM) electrolysis cell. This method would be routinely used to comprehensively characterize, evaluate, and quantify the performance of both commercial and in-house catalysts. The method would be able to determine and compare the kinetic parameters such as yield rate and faradaic efficiency routinely. Chapter 6 focused on studying various surface-modified Pt/C catalysts used for fuel cells applications to obtain mechanistic information on the oxidation of formic acid, methanol, and ethanol by comparing the effects of various modifying metals on a commercial Pt/C catalyst. Here, cyclic voltammetry and chronoamperometry have been used to measure the effects of modifying Pt with Bi and Pb adatoms.

1.10 References

1. https://www.iea.org/reports/world-energy-outlook-2022
2. Center, B. P. (2020). Annual energy outlook 2002. Energy Information Administration, Washington, DC, 12, 1672-1679.
3. Friedlingstein, P., Jones, M. W., O'Sullivan, M., Andrew, R. M., Bakker, D. C., Hauck, J., & Zeng, J. (2022). Global carbon budget 2021. Earth System Science Data, 14, 1917-2005.
4. https://climate.ec.europa.eu/eu-action/international-action-climate-change/climate-negotiations/paris-agreement_en
5. Neef, H. J. (2009). International overview of hydrogen and fuel cell research. Energy, 34, 327-333.

6. Wang, Y., Chen, K. S., Mishler, J., Cho, S. C., & Adroher, X. C. (2011). A review of polymer electrolyte membrane fuel cells: Technology, applications, and needs on fundamental research. Applied Energy, 88, 981-1007.
7. Winter, M., & Brodd, R. J. (2004). What are batteries, fuel cells, and supercapacitors? Chemical Reviews, 104, 4245-4270.
8. Akinyele, D., Olabode, E., & Amole, A. (2020). Review of fuel cell technologies and applications for sustainable microgrid systems. Inventions, 5, 42.
9. Sharaf, O. Z., & Orhan, M. F. (2014). An overview of fuel cell technology: Fundamentals and applications. Renewable and Sustainable Energy Reviews, 32, 810-853.
10. Cano, Z. P., Banham, D., Ye, S., Hintennach, A., Lu, J., Fowler, M., & Chen, Z. (2018). Batteries and fuel cells for emerging electric vehicle markets. Nature Energy, 3, 279-289.
11. Bockris, J. (Ed.). (2013). Electrochemistry of cleaner environments. Springer Science & Business Media.
12. Clark, J. H., & Macquarrie, D. J. (Eds.). (2008). Handbook of green chemistry and technology. John Wiley & Sons.
13. Zhang, F., Zhang, H., & Liu, Z. (2019). Recent advances in electrochemical reduction of CO_2. Current Opinion in Green and Sustainable Chemistry, 16, 77-84.
14. Styring, P., Quadrelli, E. A., & Armstrong, K. (Eds.). (2014). Carbon dioxide utilisation: closing the carbon cycle. Elsevier.
15. Gao, F. Y., Wu, Z. Z., & Gao, M. R. (2021). Electrochemical CO_2 reduction on transition-metal chalcogenide catalysts: recent advances and future perspectives. Energy & Fuels, 35, 12869-12883.

16. Meylan, F. D., Moreau, V., & Erkman, S. (2015). CO_2 utilization in the perspective of industrial ecology, an overview. Journal of CO_2 Utilization, 12, 101-108.

17. Pei, Y., Zhong, H., & Jin, F. (2021). A brief review of electrocatalytic reduction of CO_2—Materials, reaction conditions, and devices. Energy Science & Engineering, 9, 1012-1032.

18. Jia, S., Ma, X., Sun, X., & Han, B. (2022). Electrochemical transformation of CO_2 to value-added chemicals and fuels. CCS Chemistry, 1-39.

19. Haldor Topsoe, https://www.topsoe.com/processes/carbon-monoxide.

20. Sheehan, S. W., Cave, E. R., Kuhl, K. P., Flanders, N., Smeigh, A. L., & Co, D. T. (2017). Commercializing solar fuels within today's markets. Chem, 3, 3-7.

21. Chen, C., Kotyk, J. F. K., & Sheehan, S. W. (2018). Progress toward commercial application of electrochemical carbon dioxide reduction. Chem, 4, 2571-2586.

22. Liu, Q., Liu, Q., Xie, L., Ji, Y., Li, T., Zhang, B., & Sun, X. (2022). High-performance electrochemical nitrate reduction to ammonia under ambient conditions using a FeOOH nanorod catalyst. ACS Applied Materials & Interfaces, 14, 17312-17318.

23. Liang, J., Deng, B., Liu, Q., Wen, G., Liu, Q., Li, T., & Sun, X. (2021). High-efficiency electrochemical nitrite reduction to ammonium using a Cu_3P nanowire array under ambient conditions. Green Chemistry, 23, 5487-5493.

24. Calatayud, M., Mguig, B., & Minot, C. (2004). Modeling catalytic reduction of NO by ammonia over V_2O_5. Surface Science Reports, 55, 169-236.

25. Saravanakumar, D., Song, J., Lee, S., Hur, N. H., & Shin, W. (2017). Electrocatalytic conversion of carbon dioxide and nitrate ions to urea by a titania–Nafion composite electrode. ChemSusChem, 10, 3999-4003.

26. Cao, N., Quan, Y., Guan, A., Yang, C., Ji, Y., Zhang, L., & Zheng, G. (2020). Oxygen vacancies enhanced cooperative electrocatalytic reduction of carbon dioxide and nitrite ions to urea. Journal of Colloid and Interface Science, 577, 109-114.

27. Huang, Y., Yang, R., Wang, C., Meng, N., Shi, Y., Yu, Y., & Zhang, B. (2021). Direct electrosynthesis of urea from carbon dioxide and nitric oxide. ACS Energy Letters, 7, 284-291.

28. Dodds, D. R., & Gross, R. A. (2007). Chemicals from biomass. Science, 318, 1250-1251.

29. Lv, P., Yuan, Z., Wu, C., Ma, L., Chen, Y., & Tsubaki, N. (2007). Bio-syngas production from biomass catalytic gasification. Energy Conversion and Management, 48, 1132-1139.

30. Sheldon, R. A. (2011). Utilisation of biomass for sustainable fuels and chemicals: Molecules, methods and metrics. Catalysis Today, 167, 3-13.

31. Badwal, S. P. S., Giddey, S., Kulkarni, A., Goel, J., & Basu, S. (2015). Direct ethanol fuel cells for transport and stationary applications–A comprehensive review. Applied Energy, 145, 80-103.

32. Field, C. B., Campbell, J. E., & Lobell, D. B. (2008). Biomass energy: the scale of the potential resource. Trends in Ecology & Evolution, 23, 65-72.

33. De Klerk, A. (2011). Fischer–Tropsch facilities at a glance. Fischer–Tropsch Refining, 1-20.

34. Klier, K. In Advances in Catalysis; D.D. Eley, H. P., Paul, B. W., Eds. (1982). Academic Press, Vol. Volume 31, p 243.

35. Midilli, A., & Dincer, I. (2007). Key strategies of hydrogen energy systems for sustainability. Int. Journal of Hydrogen Energy, 32, 511-524.

36. Kuhl, K. P., Cave, E. R., Abram, D. N., & Jaramillo, T. F. (2012). New insights into the electrochemical reduction of carbon dioxide on metallic copper surfaces. Energy & Environmental Science, 5, 7050-7059.

37. Nitopi, S., Bertheussen, E., Scott, S. B., Liu, X., Engstfeld, A. K., Horch, S., & Chorkendorff, I. (2019). Progress and perspectives of electrochemical CO_2 reduction on copper in aqueous electrolyte. Chemical Reviews, 119, 7610-7672.

38. Lin, R., Guo, J., Li, X., Patel, P., & Seifitokaldani, A. (2020). Electrochemical reactors for CO_2 conversion. Catalysts, 10, 473.

39. Kroschwitz, J. I., Howe-Grant, M., Kirk, R. E., & Othmer, D. F. (1996). Encyclopedia of chemical technology. John Wiley & Sons.

40. Guan, R. G., & Tie, D. (2017). A review on grain refinement of aluminum alloys: progresses, challenges and prospects. Acta Metallurgica Sinica (English Letters), 30, 409-432.

41. Lee, M. Y., Park, K. T., Lee, W., Lim, H., Kwon, Y., & Kang, S. (2020). Current achievements and the future direction of electrochemical CO_2 reduction: A short review. Critical Reviews in Environmental Science and Technology, 50, 769-815.

42. Teeter, T. E., & Van Rysselberghe, P. (1954). Reduction of carbon dioxide on mercury cathodes. Journal of Chemical Physics, 22, 759-760.

43. Hori, Y., & Suzuki, S. (1982). Electrolytic reduction of carbon dioxide at mercury electrode in aqueous solution. Bulletin of Chemical Society of Japan, 55, 660-665.

44. Xie, H., Wang, T., Liang, J., Li, Q., & Sun, S. (2018). Cu-based nanocatalysts for electrochemical reduction of CO_2. Nano Today, 21, 41-54.

45. Lim, H. K., & Kim, H. (2017). The mechanism of room-temperature ionic-liquid-based electrochemical CO_2 reduction: A review. Molecules, 22, 536.

46. Gattrell, M., Gupta, N., & Co, A. (2006). A review of the aqueous electrochemical reduction of CO_2 to hydrocarbons at copper. Journal of Electroanalytical Chemistry, 594, 1-19.

47. Vielstich, W., Lamm, A., & Gasteiger, H. (2003). Handbook of fuel cells. Fundamentals, technology, applications.

48. Jitaru, M., Lowy, D. A., Toma, M., Toma, B. C., & Oniciu, L. (1997). Electrochemical reduction of carbon dioxide on at metallic cathodes. Journal of Appl. Electrochem, 27, 875-889.

49. Peterson, A. A., Abild-Pedersen, F., Studt, F., Rossmeisl, J., & Nørskov, J. K. (2010). How copper catalyzes the electroreduction of carbon dioxide into hydrocarbon fuels. Energy & Environmental Science, 3, 1311-1315.

50. Yin, C., Li, Q., Zheng, J., Ni, Y., Wu, H., Kjøniksen, A. L., & Zhang, Y. (2022). Progress in regulating electronic structure strategies on Cu-based bimetallic catalysts for CO_2 reduction reaction. Advanced Powder Materials, 100055.

51. Barton Cole, E., Lakkaraju, P. S., Rampulla, D. M., Morris, A. J., Abelev, E., & Bocarsly, A. B. (2010). Using a one-electron shuttle for the multielectron reduction of CO_2 to methanol: kinetic, mechanistic, and structural insights. Journal of American Chemical Society, 132, 11539-11551.

52. Kusama, S., Saito, T., Hashiba, H., Sakai, A., & Yotsuhashi, S. (2017). Crystalline copper (II) phthalocyanine catalysts for electrochemical reduction of carbon dioxide in aqueous media. ACS Catalysis, 7, 8382-8385.

53. Rosen, B. A., Salehi-Khojin, A., Thorson, M. R., Zhu, W., Whipple, D. T., Kenis, P. J., & Masel, R. I. (2011). Ionic liquid–mediated selective conversion of CO_2 to CO at low overpotentials. Science, 334, 643-644.

54. García Rey, N., & Dlott, D. D. (2015). Structural transition in an ionic liquid controls CO_2 electrochemical reduction. The Journal of Physical Chemistry C, 119, 20892-20899.

55. Oh, Y., & Hu, X. (2013). Organic molecules as mediators and catalysts for photocatalytic and electrocatalytic CO_2 reduction. Chemical Society Reviews, 42, 2253-2261.

56. Parkin, A., Seravalli, J., Vincent, K. A., Ragsdale, S. W., & Armstrong, F. A. (2007). Rapid and efficient electrocatalytic CO_2/CO interconversions by Carboxydothermus hydrogenoformans CO dehydrogenase I on an electrode. Journal of American Chemical Society, 129, 10328-10329.

57. Ma, S., & Kenis, P. J. (2013). Electrochemical conversion of CO_2 to useful chemicals: current status, remaining challenges, and future opportunities. Current Opinion in Chemical Engineering, 2, 191-199.

58. He, J., & Janáky, C. (2020). Recent advances in solar-driven carbon dioxide conversion: expectations versus reality. ACS Energy Letters, 5, 1996-2014.

59. Barton, E. E., Rampulla, D. M., & Bocarsly, A. B. (2008). Selective solar-driven reduction of CO_2 to methanol using a catalyzed p-GaP based photoelectrochemical cell. Journal of American Chemical Society, 130, 6342-6344.

60. Li, C. W., & Kanan, M. W. (2012). CO_2 reduction at low overpotential on Cu electrodes resulting from the reduction of thick Cu_2O films. Journal of American Chemical Society, 134, 7231-7234.

61. Whipple, D. T., Finke, E. C., & Kenis, P. J. (2010). Microfluidic reactor for the electrochemical reduction of carbon dioxide: the effect of pH. Electrochemical and Solid-State Letters, 13, B109.

62. Garg, S., Li, M., Weber, A. Z., Ge, L., Li, L., Rudolph, V., & Rufford, T. E. (2020). Advances and challenges in electrochemical CO_2 reduction processes: an engineering and design perspective looking beyond new catalyst materials. Journal of Materials Chemistry A, 8, 1511-1544.

63. Feng, J., Zeng, S., Feng, J., Dong, H., & Zhang, X. (2018). CO_2 electroreduction in ionic liquids: A review. Chinese Journal of Chemistry, 36, 961-970.

64. Dunfeng, G., Pengfei, W., Hefei, L., Long, L., Guoxiong, W., & Xinhe, B. (2021). Designing electrolyzers for electrocatalytic CO_2 reduction. Acta Phys.-Chim. Sin, 37, 2009021.

65. Wang, Y., Pang, Y., Xu, H., Martinez, A., & Chen, K. S. (2022). PEM Fuel cell and electrolysis cell technologies and hydrogen infrastructure development: A Review. Energy & Environmental Science.

66. Peng, X., Kulkarni, D., Huang, Y., Omasta, T. J., Ng, B., Zheng, Y., & Mustain, W. E. (2020). Using operando techniques to understand and design high performance and stable alkaline membrane fuel cells. Nature Communications, 11, 1-10.

67. Larrazábal, G. O., Strøm-Hansen, P., Heli, J. P., Zeiter, K., Therkildsen, K. T., Chorkendorff, I., & Seger, B. (2019). Analysis of mass flows and membrane cross-over in CO_2 reduction at high current densities in an MEA-type electrolyzer. ACS Applied Materials & Interfaces, 11, 41281-41288.

68. Schouten, K. J. P., Qin, Z., Pérez Gallent, E., & Koper, M. T. (2012). Two pathways for the formation of ethylene in CO reduction on single-crystal copper electrodes. Journal of American Chemical Society, 134, 9864-9867.

69. Polatides, C., Dortsiou, M., & Kyriacou, G. (2005). Electrochemical removal of nitrate ion from aqueous solution by pulsing potential electrolysis. Electrochimica Acta, 50, 5237-5241.

70. Rossi, F., Motta, O., Matrella, S., Proto, A., & Vigliotta, G. (2014). Nitrate removal from wastewater through biological denitrification with OGA 24 in a batch reactor. Water, 7, 51-62.

71. Heck, K. N., Guo, S., Westerhoff, P., & Wong, M. S. (2018). Removing nitrates and nitrites through new catalysis chemistry. Water Conditioning & Purification, 3, 36-40.

72. Li, H., & Yang, C. (2015). Nitrite removal using ion exchange resin: batch vs. fixed bed performance. Separation Science and Technology, 50, 1721-1730.

73. Norton, S. (2014). Removal mechanisms in constructed wastewater wetlands. ONLINE: http://home. eng. iastate. edu/~ tge/ce421-521/stephen. pdf.

74. Jiang, X., Ying, D., Ye, D., Zhang, R., Guo, Q., Wang, Y., & Jia, J. (2018). Electrochemical study of enhanced nitrate removal in wastewater treatment using biofilm electrode. Bioresource Technology, 252, 134-142.

75. Zheng, J., Lu, T., Cotton, T. M., & Chumanov, G. (1999). Photoinduced electrochemical reduction of nitrite at an electrochemically roughened silver surface. Journal of Physical Chemistry B, 103, 6567-6572.

76. Zhang, X., Wang, Y., Wang, Y., Guo, Y., Xie, X., Yu, Y., & Zhang, B. (2022). Recent advances in electrocatalytic nitrite reduction. Chemical Communications, 58, 2777-2787.

77. Duca, M., & Koper, M. T. (2012). Powering denitrification: the perspectives of electrocatalytic nitrate reduction. Energy & Environmental Science, 5, 9726-9742.

78. Duca, M., Cucarella, M. O., Rodriguez, P., & Koper, M. T. (2010). Direct reduction of nitrite to N_2 on a Pt (100) electrode in alkaline media. Journal of American Chemical Society, 132, 18042-18044.

79. Rosca, V., Duca, M., de Groot, M. T., & Koper, M. T. (2009). Nitrogen cycle electrocatalysis. Chemical Reviews, 109, 2209-2244.

80. He, D., Li, Y., Ooka, H., Go, Y. K., Jin, F., Kim, S. H., & Nakamura, R. (2018). Selective electrocatalytic reduction of nitrite to dinitrogen based on decoupled proton–electron transfer. Journal of American Chemical Society, 140, 2012-2015.

81. Duca, M., & Koper, M. T. (2012). Powering denitrification: the perspectives of electrocatalytic nitrate reduction. Energy & Environmental Science, 5, 9726-9742.

82. Nishimura, K., Machida, K., & Enyo, M. (1991). On-line mass spectroscopy applied to electroreduction of nitrite and nitrate ions at porous Pt electrode in sulfuric acid solutions. Electrochimica Acta, 36, 877-880.

83. Bae, I. T., Barbour, R. L., & Scherson, D. A. (1997). In situ Fourier transform infrared spectroscopic studies of nitrite reduction on platinum electrodes in perchloric acid. Analytical Chemistry, 69, 249-252.

84. Arikawa, Y., Otsubo, Y., Fujino, H., Horiuchi, S., Sakuda, E., & Umakoshi, K. (2018). Nitrite reduction cycle on a dinuclear ruthenium complex producing ammonia. Journal of American Chemical Society, 140, 842-847.

85. Xu, S., Kwon, H. Y., Ashley, D. C., Chen, C. H., Jakubikova, E., & Smith, J. M. (2019). Intramolecular hydrogen bonding facilitates electrocatalytic reduction of nitrite in aqueous solutions. Inorganic Chemistry, 58, 9443-9451.

86. Chebotareva, N., & Nyokong, T. (1997). Metallophthalocyanine catalysed electroreduction of nitrate and nitrite ions in alkaline media. Journal of Applied Electrochemistry, 27, 975-981.

87. Wang, C., Zhou, W., Sun, Z., Wang, Y., Zhang, B., & Yu, Y. (2021). Integrated selective nitrite reduction to ammonia with tetrahydroisoquinoline semi-dehydrogenation over a vacancy-rich Ni bifunctional electrode. Journal of Materials Chemistry A, 9, 239-243.

88. Mei, Z., Zhou, Y., Lv, W., Tong, S., Yang, X., Chen, L., & Zhang, N. (2022). Recent progress in electrocatalytic urea synthesis under ambient conditions. ACS Sustainable Chemistry & Engineering, 10, 12477-12496.

89. Tang, C., & Qiao, S. Z. (2019). How to explore ambient electrocatalytic nitrogen reduction reliably and insightfully. Chemical Society Reviews, 48, 3166-3180.

90. Shibata, M., Yoshida, K., & Furuya, N. (1998). Electrochemical synthesis of urea at gas-diffusion electrodes: Part II. Simultaneous reduction of carbon dioxide and nitrite ions at Cu, Ag and Au catalysts. Journal of Electroanalytical Chemistry, 442, 67-72.

91. Meng, N., Huang, Y., Liu, Y., Yu, Y., & Zhang, B. (2021). Electrosynthesis of urea from nitrite and CO_2 over oxygen-vacancy rich ZnO porous nanosheets. Cell Reports Physical Science, 2, 100378.

92. Shibata, M., Yoshida, K., & Furuya, N. (1998). Electrochemical synthesis of urea at gas-diffusion electrodes: III. Simultaneous reduction of carbon dioxide and nitrite ions with various metal catalysts. Journal of Electrochemical Society, 145, 595.

93. Shibata, M., & Furuya, N. (2001). Electrochemical synthesis of urea at gas-diffusion electrodes: Part VI. Simultaneous reduction of carbon dioxide and nitrite ions with various metallophthalocyanine catalysts. Journal of Electroanalytical Chemistry, 507, 177-184.

94. Feng, Y., Yang, H., Zhang, Y., Huang, X., Li, L., Cheng, T., & Shao, Q. (2020). Te-doped Pd nanocrystal for electrochemical urea production by efficiently coupling carbon dioxide reduction with nitrite reduction. Nano Letters, 20, 8282-8289.

95. Liu, S., Yin, S., Wang, Z., Xu, Y., Li, X., Wang, L., & Wang, H. (2022). AuCu nanofibers for electrosynthesis of urea from carbon dioxide and nitrite. Cell Reports Physical Science, 3, 100869.

96. Yang, G. L., Hsieh, C. T., Ho, Y. S., Kuo, T. C., Kwon, Y., Lu, Q., & Cheng, M. J. (2022). Gaseous CO_2 coupling with N-containing intermediates for key C–N bond formation during urea production from coelectrolysis over Cu. ACS Catalysis, 12, 11494-11504.

97. Mukherjee, J., Paul, S., Adalder, A., Kapse, S., Thapa, R., Mandal, S., & Ghorai, U. K. (2022). Understanding the site-selective electrocatalytic co-reduction mechanism for green urea synthesis using copper phthalocyanine nanotubes. Advanced Functional Materials, 2200882.

98. He, C., Wu, Z. Y., Zhao, L., Ming, M., Zhang, Y., Yi, Y., & Hu, J. S. (2019). Identification of FeN_4 as an efficient active site for electrochemical N_2 reduction. ACS Catalysis, 9, 7311-7317.

99. Li, D., Xu, N., Zhao, Y., Zhou, C., Zhang, L. P., Wu, L. Z., & Zhang, T. (2022). A reliable and precise protocol for urea quantification in photo/electrocatalysis. Small Methods, 6, 2200561.

100. Tang, C., & Qiao, S. Z. (2019). How to explore ambient electrocatalytic nitrogen reduction reliably and insightfully. Chemical Society Reviews, 48, 3166-3180.

101. Zhao, Y., Wu, F., Miao, Y., Zhou, C., Xu, N., Shi, R., & Zhang, T. (2021). Revealing ammonia quantification minefield in photo/electrocatalysis. Angewandte Chemie, 133, 21896-21899.

102. Zhao, Y., Shi, R., Bian, X., Zhou, C., Zhao, Y., Zhang, S., & Zhang, T. (2019). Ammonia detection methods in photocatalytic and electrocatalytic experiments: how to improve the reliability of NH_3 production rates?. Advanced Science, 6, 1802109.

103. Searle, P. L. (1984). The Berthelot or indophenol reaction and its use in the analytical chemistry of nitrogen. A review. Analyst, 109, 549-568.

104. Ngo, T. T., Phan, A. P. H., Yam, C. F., & Lenhoff, H. M. (1982). Interference in determination of ammonia with the hypochlorite-alkaline phenol method of Berthelot. Analytical Chemistry, 54, 46-49.

105. Huang, Y., Wang, Y., Liu, Y., Ma, A., Gui, J., Zhang, C., & Zhang, B. (2023). Unveiling the quantification minefield in electrocatalytic urea synthesis. Chemical Engineering Journal, 453, 139836.

106. Chen, L., Ma, J., Huang, Y., Dai, M., & Li, X. (2015). Optimization of a colorimetric method to determine trace urea in seawater. Limnology and Oceanography: Methods, 13, 303-311.

107. Langenfeld, N. J., Payne, L. E., & Bugbee, B. (2021). Colorimetric determination of urea using diacetyl monoxime with strong acids. PloS One, 16, e0259760.

108. Chen, C., Zhu, X., Wen, X., Zhou, Y., Zhou, L., Li, H., & Wang, S. (2020). Coupling N_2 and CO_2 in H_2O to synthesize urea under ambient conditions. Nature Chemistry, 12, 717-724.

109. Huang, Y., Yang, R., Wang, C., Meng, N., Shi, Y., Yu, Y., & Zhang, B. (2021). Direct electrosynthesis of urea from carbon dioxide and nitric oxide. ACS Energy Letters, 7, 284-291.

110. Maimaiti, H., Xu, B., Sun, J. Y., & Feng, L. R. (2021). Photocatalytic synthesis of urea ($CO_2/N_2/H_2O$) on coal-based carbon nanotubes with the Fe-core-supported Ti^{3+}-TiO_2 composite catalyst. ACS Sustainable Chemistry & Engineering, 9, 6991-7002.

111. Meng, N., Huang, Y., Liu, Y., Yu, Y., & Zhang, B. (2021). Electrosynthesis of urea from nitrite and CO_2 over oxygen vacancy-rich ZnO porous nanosheets. Cell Reports Physical Science, 2, 100378.

112. Andersen, S. Z., Čolić, V., Yang, S., Schwalbe, J. A., Nielander, A. C., McEnaney, J. M., & Chorkendorff, I. (2019). A rigorous electrochemical ammonia synthesis protocol with quantitative isotope measurements. Nature, 570, 504-508.

113. Hu, B., Hu, M., Seefeldt, L., & Liu, T. L. (2019). Electrochemical dinitrogen reduction to ammonia by Mo_2N: catalysis or decomposition?. ACS Energy Letters, 4, 1053-1054.

114. Küngas, R. (2020). Electrochemical CO_2 reduction for CO production: comparison of low-and high-temperature electrolysis technologies. Journal of Electrochemical Society, 167, 044508.

115. Kamarudin, S. K., Achmad, F., & Daud, W. R. W. (2009). Overview on the application of direct methanol fuel cell (DMFC) for portable electronic devices. Int. Journal of Hydrogen Energy, 34, 6902-6916.

116. Demirci, U. B. (2007). Direct liquid-feed fuel cells: thermodynamic and environmental concerns. Journal of Power Sources, 169, 239-246.

117. Badwal, S. P. S., Giddey, S., Kulkarni, A., Goel, J., & Basu, S. (2015). Direct ethanol fuel cells for transport and stationary applications–A comprehensive review. Applied Energy, 145, 80-103.

118. Xie, H., Wang, T., Liang, J., Li, Q., & Sun, S. (2018). Cu-based nanocatalysts for electrochemical reduction of CO_2. Nano Today, 21, 41-54.

119. Eppinger, J., & Huang, K. W. (2017). Formic acid as a hydrogen energy carrier. ACS Energy Letters, 2, 188-195.

120. Rhee, Y. W., Ha, S. Y., & Masel, R. I. (2003). Crossover of formic acid through Nafion® membranes. Journal of Power Sources, 117, 35-38.

121. Fang, Z., & Chen, W. (2021). Recent advances in formic acid electro-oxidation: From the fundamental mechanism to electrocatalysts. Nanoscale Advances, 3, 94-105.

122. Vielstich, W., Gasteiger, H. A., & Yokokawa, H. (Eds.). (2009). Handbook of Fuel cells: Advances in electrocatalysis, materials, diagnostics and durability. John Wiley & Sons.

123. Capon, A., & Parsons, R. (1973). The oxidation of formic acid on noble metal electrodes: II. A comparison of the behaviour of pure electrodes. Journal of Electroanalytical Chemistry and Interfacial Electrochemistry, 44, 239-254.

124. Yu, X., & Pickup, P. G. (2008). Recent advances in direct formic acid fuel cells (DFAFC). Journal of Power Sources, 182, 124-132.

125. Briega-Martos, V., Solla-Gullón, J., Koper, M. T., Herrero, E., & Feliu, J. M. (2019). Electrocatalytic enhancement of formic acid oxidation reaction by acetonitrile on well-defined platinum surfaces. Electrochimica Acta, 295, 835-845.

126. Conway, B. E., & Bai, L. (1986). Determination of adsorption of OPD H species in the cathodic hydrogen evolution reaction at Pt in relation to electrocatalysis. Journal of Electroanalytical Chemistry and Interfacial Electrochemistry, 198, 149-175.

127. Fang, Z., & Chen, W. (2021). Recent advances in formic acid electro-oxidation: From the fundamental mechanism to electrocatalysts. Nanoscale Advances, 3, 94-105.

128. Samjeské, G., Miki, A., Ye, S., & Osawa, M. (2006). Mechanistic study of electrocatalytic oxidation of formic acid at platinum in acidic solution by time-resolved surface-enhanced infrared absorption spectroscopy. The Journal of Physical Chemistry B, 110, 16559-16566.

129. Chen, Y. X., Heinen, M., Jusys, Z., & Behm, R. J. (2006). Kinetics and mechanism of the electrooxidation of formic acid—spectroelectrochemical studies in a flow cell. Angewandte Chemie International Edition, 45, 981-985.

130. Chen, Y. X., Heinen, M., Jusys, Z., & Behm, R. J. (2006). Bridge-bonded formate: active intermediate or spectator species in formic acid oxidation on a Pt film electrode?. Langmuir, 22, 10399-10408.

131. Wang, H. F., & Liu, Z. P. (2009). Formic acid oxidation at Pt/H_2O interface from periodic DFT calculations integrated with a continuum solvation model. The Journal of Physical Chemistry C, 113, 17502-17508.

132. Luque, G. C., de Chialvo, M. R. G., & Chialvo, A. C. (2017). Kinetic study of the formic acid oxidation on steady state using a flow cell. Journal of Electrochemical Society, 164, H748.

133. Joo, J., Uchida, T., Cuesta, A., Koper, M. T., & Osawa, M. (2013). Importance of acid–base equilibrium in electrocatalytic oxidation of formic acid on platinum. Journal of American Chemical Society, 135, 9991-9994.

134. Grozovski, V., Solla-Gullon, J., Climent, V., Herrero, E., & Feliu, J. M. (2010). Formic acid oxidation on shape-controlled Pt nanoparticles studied by pulsed voltammetry. Journal of Physical Chemistry C, 114, 13802-13812.

135. Li, M., Kuttiyiel, K., Lu, F., Gang, O., & Adzic, R. R. (2019). Platinum monolayer electrocatalysts for methanol oxidation. Journal of Electrochemical Society, 166, F3300.

136. McNicol, B. D., Rand, D. A. J., & Williams, K. R. (1999). Direct methanol–air fuel cells for road transportation. Journal of Power Sources, 83, 15-31.

137. Breiter, M. W. (1968). Role of adsorbed species for the anodic methanol oxidation on platinum in acidic electrolytes. Discussions of Faraday Society, 45, 79-86.

138. Kariya, N., Fukuoka, A., Utagawa, T., Sakuramoto, M., Goto, Y., & Ichikawa, M. (2003). Efficient hydrogen production using cyclohexane and decalin by pulse-spray mode reactor with Pt catalysts. Applied Catalysis A: General, 247, 247-259.

139. Carrette, L., Friedrich, K. A., & Stimming, U. (2001). Fuel cells-fundamentals and applications. Fuel cells, 1.

140. Yang, M. L., Zhu, Y. A., Fan, C., Sui, Z. J., Chen, D., Zhou, X. G. (2011). DFT study of propane dehydrogenation on Pt catalyst: effects of step sites. Phys. Chem. Chem. Phys., 13, 3257-3267.

141. Wasmus, S., & Küver, A. (1999). Methanol oxidation and direct methanol fuel cells: a selective review. Journal of Electroanalytical Chemistry, 461, 14-31.

142. Cohen, J. L., Volpe, D. J.; Abruna, H. D. (2007). Electrochemical determination of activation energies for methanol oxidation on polycrystalline platinum in acidic and alkaline electrolytes. Phys. Chem. Chem. Phys., 9, 49-77.

143. Jiang, J., & Kucernak, A. (2005). Solid polymer electrolyte membrane composite microelectrode investigations of fuel cell reactions. II: voltammetric study of methanol oxidation at the nanostructured platinum microelectrode| Nafion® membrane interface. Journal of Electroanalytical Chemistry, 576, 223-236.

144. Yuda, A., Ashok, A., & Kumar, A. (2022). A comprehensive and critical review on recent progress in anode catalyst for methanol oxidation reaction. Catalysis Reviews, 64, 126-228.

145. Yaqoob, L., Noor, T., & Iqbal, N. (2021). Recent progress in development of efficient electrocatalyst for methanol oxidation reaction in direct methanol fuel cell. Int. Journal of Energy Research, 45, 6550-6583.

146. Lai, L., Yang, G., Zhang, Q., Yu, H., & Peng, F. (2021). Essential analysis of cyclic voltammetry of methanol electrooxidation using the differential electrochemical mass spectrometry. Journal of Power Sources, 509, 230397.

147. Zhao, Y., Li, X., Schechter, J. M., & Yang, Y. (2016). Revisiting the oxidation peak in the cathodic scan of the cyclic voltammogram of alcohol oxidation on noble metal electrodes. RSC Advances, 6, 5384-5390.

148. Wang, Y., Zou, S., Cai, W. B. (2015). Recent advances on electro-oxidation of ethanol on Pt-and Pd-based catalysts: From reaction mechanisms to catalytic materials. Catalysts, 5, 1507-1534.

149. Léger, J. M., Rousseau, S., Coutanceau, C., Hahn, F., Lamy, C. (2005). How bimetallic electrocatalysts does work for reactions involved in fuel cells? Example of ethanol oxidation and comparison to methanol. Electrochimica Acta, 50, 5118-5125.

150. Moghaddam, R. B., & Pickup, P. G. (2012). Support effects on the oxidation of ethanol at Pt nanoparticles. Electrochimica Acta, 65, 210-215.

151. Vigier, F., Coutanceau, C., Hahn, F., Belgsir, E., Lamy, C. (2004). On the mechanism of ethanol electro-oxidation on Pt and PtSn catalysts: Electrochemical and in situ IR reflectance spectroscopy studies. Journal of Electroanalytical Chemistry, 563, 81-89.

152. Colmati, F., Tremiliosi-Filho, G., Gonzalez, E. R., Berná, A., Herrero, E., & Feliu, J. M. (2009). The role of the steps in the cleavage of the C–C bond during ethanol oxidation on platinum electrodes. Physical Chemistry Chemical Physics, 11, 9114-9123.

153. Schmidt, V. M., Ianniello, R., Pastor, E., & González, S. (1996). Electrochemical reactivity of ethanol on porous Pt and PtRu: Oxidation/reduction reactions in 1 M $HClO_4$. Journal of Physical Chemistry, 100, 17901-17908.

154. Gootzen, J. F. E., Visscher, W., & Van Veen, J. A. R. (1996). Characterization of ethanol and 1, 2-ethanediol adsorbates on platinized platinum with Fourier transform infrared

spectroscopy and differential electrochemical mass spectrometry. Langmuir, 12, 5076-5082.

155. Shao, M. H., & Adzic, R. R. (2005). Electrooxidation of ethanol on a Pt electrode in acid solutions: in situ ATR-SEIRAS study. Electrochimica Acta, 50, 2415-2422.

156. Wang, C., Bai, S., & Xiong, Y. (2015). Recent advances in surface and interface engineering for electrocatalysis. Chinese Journal of Catalysis, 36, 1476-1493.

157. de Souza, M. B., Fernandez, P. S., & Solla-Gullón, J. (2018). Adatom decorated shape-controlled metal nanoparticles: advanced electrocatalysts for energy conversion. Current Opinion in Electrochemistry, 9, 121-128.

158. Yovanovich, M., Piasentin, R. M., Ayoub, J. M. S., Nandenha, J., Fontes, E. H., De Souza, R. F. B., & Da Silva, S. G. (2015). PtBi/C electrocatalysts for formic acid electro-oxidation in acid and alkaline electrolyte. Int. Journal Electrochem. Sci, 10, 4801-4811.

159. Sudha, V., & Sangaranarayanan, M. V. (2005). Underpotential deposition of metals–progress and prospects in modelling. Journal of Chemical Sciences, 117, 207-218.

160. El Sawy, E. N., Khan, M. A., & Pickup, P. G. (2016). Factors affecting the spontaneous adsorption of Bi (III) onto Pt and PtRu nanoparticles. Applied Surface Science, 364, 308-314.

161. Popović, K., & Lović, J. (2015). Formic acid oxidation at platinum-bismuth catalysts. Journal of Serbian Chemical Society, 80, 1217-1249.

162. Choi, M., Ahn, C. Y., Lee, H., Kim, J. K., Oh, S. H., Hwang, W., & Shin, W. (2019). Bi-modified Pt supported on carbon black as electro-oxidation catalyst for 300 W formic acid fuel cell stack. Applied Catalysis B: Environmental, 253, 187-195.

163. Lović, J. D., Obradović, M. D., Tripković, D. V., Popović, K. D., Jovanović, V. M., Gojković, S. L., & Tripković, A. V. (2012). High activity and stability of Pt_2Bi catalyst in formic acid oxidation. Electrocatalysis, 3, 346-352.

164. López-Cudero, A., Vidal-Iglesias, F. J., Solla-Gullón, J., Herrero, E., Aldaz, A., & Feliu, J. M. (2009). Formic acid electrooxidation on Bi-modified polyoriented and preferential (111) Pt nanoparticles. Physical Chemistry Chemical Physics, 11, 416-424.

165. Leiva, E., Iwasita, T., Herrero, E., & Feliu, J. M. (1997). Effect of adatoms in the electrocatalysis of HCOOH oxidation. A theoretical model. Langmuir, 13, 6287-6293.

166. Figueiredo, M. C.; Santasalo-Aarnio, A.; Vidal-Iglesias, F. J.; Solla-Gullón, J.; Feliu, J. M.; Kontturi, K.; Kallio, T., (2013). Tailoring properties of platinum supported catalysts by irreversible adsorbed adatoms toward ethanol oxidation for direct ethanol fuel cells. Applied Catalysis B: Environmental, 140, 378-385.

167. Altarawneh, R. M., Brueckner, T. M., Chen, B., & Pickup, P. G. (2018). Product distributions and efficiencies for ethanol oxidation at PtNi octahedra. Journal of Power Sources, 400, 369-376.

168. Lović, J. D., Stevanović, S. I., Tripković, D. V., Tripković, V. V., Stevanović, R. M., Popović, K. D., & Jovanović, V. M. (2014). Formic acid oxidation at platinum-bismuth clusters. Journal of Electrochemical Society, 161, H547.

169. De-los-Santos-Alvarez, N., Alden, L. R., Rus, E., Wang, H., DiSalvo, F. J., & Abruna, H. D. (2009). CO tolerance of ordered intermetallic phases. Journal of Electroanalytical Chemistry, 626, 14-22.

170. Roth, C., Papworth, A. J., Hussain, I., Nichols, R. J., & Schiffrin, D. J. (2005). A Pt/Ru nanoparticulate system to study the bifunctional mechanism of electrocatalysis. Journal of Electroanalytical Chemistry, 581, 79-85.

171. Chen, Q. S., Zhou, Z. Y., Vidal-Iglesias, F. J., Solla-Gullón, J., Feliu, J. M., & Sun, S. G. (2011). Significantly enhancing catalytic activity of tetrahexahedral Pt nanocrystals by Bi adatom decoration. Journal of American Chemical Society, 133, 12930-12933.

172. Perales-Rondón, J. V., Solla-Gullón, J., Herrero, E., & Sánchez-Sánchez, C. M. (2017). Enhanced catalytic activity and stability for the electrooxidation of formic acid on lead modified shape-controlled platinum nanoparticles. Applied Catalysis B: Environmental, 201, 48-57.

173. Busó-Rogero, C., Perales-Rondón, J. V., Farias, M. J., Vidal-Iglesias, F. J., Solla-Gullon, J., Herrero, E., & Feliu, J. M. (2014). Formic acid electrooxidation on thallium-decorated shape-controlled platinum nanoparticles: An improvement in electrocatalytic activity. Physical Chemistry Chemical Physics, 16, 13616-13624.

174. Vidal-Iglesias, F. J., López-Cudero, A., Solla-Gullón, J., Aldaz, A., & Feliu, J. M. (2012). Pd-modified shape-controlled Pt nanoparticles towards formic acid electrooxidation. Electrocatalysis, 3, 313-323.

175. Vidal-Iglesias, F. J., López-Cudero, A., Solla-Gullón, J., & Feliu, J. M. (2013). Towards more active and stable electrocatalysts for formic acid electrooxidation: antimony-decorated octahedral platinum nanoparticles. Angewandte Chemie, 125, 998-1001.

176. Liu, H. X., Tian, N., Brandon, M. P., Pei, J., Huangfu, Z. C., Zhan, C., & Sun, S. G. (2012). Enhancing the activity and tuning the mechanism of formic acid oxidation at

tetrahexahedral Pt nanocrystals by Au decoration. Physical Chemistry Chemical Physics, 14, 16415-16423.

177. Yang, S., & Lee, H. (2013). Atomically dispersed platinum on gold nano-octahedra with high catalytic activity on formic acid oxidation. ACS Catalysis, 3, 437-443.

178. Liu, H. X., Tian, N., Brandon, M. P., Zhou, Z. Y., Lin, J. L., Hardacre, C., and Sun, S. G. (2012). Tetrahexahedral Pt nanocrystal catalysts decorated with Ru adatoms and their enhanced activity in methanol electrooxidation. ACS Catalysis, 2, 708-715.

179. Campbell, S. A., & Parsons, R. (1992). Effect of Bi and Sn adatoms on formic acid and methanol oxidation at well-defined platinum surfaces. Journal of Chemical Society, Faraday Transactions, 88, 833-841.

180. Beden, B., Kadirgan, F., Lamy, C., & Leger, J. M. (1982). Oxidation of methanol on a platinum electrode in alkaline medium: effect of metal ad-atoms on the electrocatalytic activity. Journal of Electroanalytical Chemistry and Interfacial Electrochemistry, 142, 171-190.

181. Busó-Rogero, C., Solla-Gullon, J., Vidal-Iglesias, F. J., Herrero, E., & Feliu, J. M. (2016). Adatom modified shape-controlled platinum nanoparticles towards ethanol oxidation. Electrochimica Acta, 196, 270-279.

182. Li, G., & Pickup, P. G. (2007). Decoration of carbon-supported Pt catalysts with Sn to promote electro-oxidation of ethanol. Journal of Power Sources, 173, 121-129.

Chapter 2

Experimental Methods

2.1 Chemicals and materials

The chemicals and materials used in the study were used as received. For a complete list of all the chemicals and materials used, please refer to Appendix D.

2.2 Nafion™ 117 membrane pre-treatment

Nafion™ 117 membranes (Ion Power, Inc) were used in proton exchange membrane electrolysis cells. Before usage, the commercial Nafion™ 117 membranes underwent the following pre-treatment process:

First, Nafion™ 117 membranes were cut into approximately 4.5 X 4.5 cm square pieces. Then these pieces were heated in a 3% H_2O_2 solution at 80 °C with continuous stirring for 1 h. The membranes were then rinsed with deionized water, then immersed in deionized water for 15-20 min at room temperature. Subsequently, they were heated in 1 M H_2SO_4 solution at 80 °C with continuous stirring for a 1 h. Finally, the membranes were again rinsed with deionized and heated in deionized water at 80 °C with stirring for 3 h, followed by rinsing and storage in deionized water.

2.3 Preparation of membrane electrode assemblies (MEAs) for proton-exchange membrane (PEM) electrolysis cells.

In order to prepare MEAs for PEM cells, cathodes were prepared by depositing catalyst ink on CFP discs (0.24 cm^2 or 5 cm^2) with a target catalyst loading of 1.5 mg cm^{-2}. The catalyst ink was prepared in a mixture of 150 μL of H_2O, 75 μL of 2-propanol, and 75 μL of 5% Nafion^{TM} solution. Electrodes were dried in a fume hood overnight. A 5 cm^2 commercial anode electrode was used, which consisted of 4 mg cm^{-2} Pt black loaded onto wet-proofed Toray^{TM} CFP

(TGP-H-090). During the cell assembly, an anode and a cathode were pressed onto each side of a treated Nafion^{TM} 117 membrane with a pressure of 1.5 MPa at ambient temperature.

2.4 Electrochemical measurement

An in-house custom-made three-compartment glass cell was used for the coreduction of nitrite and CO_2 study, as shown in Fig. 2.1. The cell anode and cathode chambers were separated by a porous glass frit. A catalyst-loaded CFP disc was used as the working electrode and held in place by a Ti clip. A Pt wire was used as the counter electrode (CE), and $Hg/HgSO_4$ in saturated potassium sulfate solution (Koslow; 658 mV vs. SHE) as the reference electrode (RE).

Cyclic voltammetry (CV) and electrolysis of CO_2 and NO_2^- (constant potential experiments) were performed using an EG&G model 273A Potentiostat/Galvanostat. Corrware software was used to control the instrument and process the data.

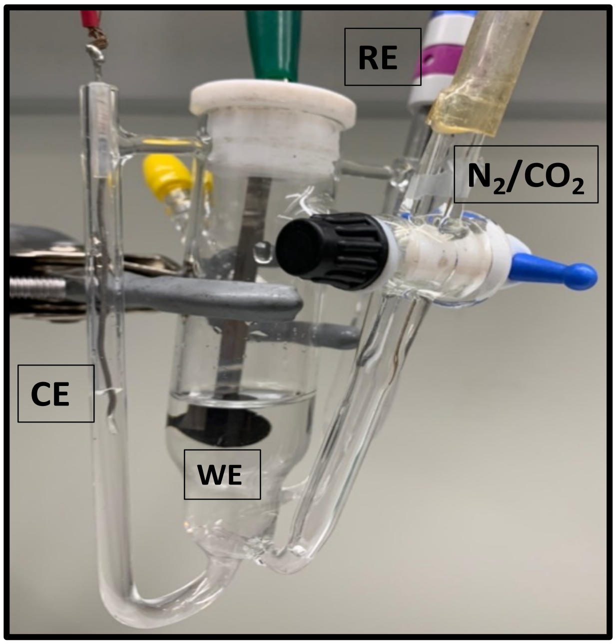

Figure 2.1. A photograph of a three-compartment glass electrochemical cell

In the proton-exchange membrane (PEM) electrolysis cell (Fig. 2.2), cyclic voltammetry and electrolysis of CO_2 and NO_2^- (or N_2) were performed using an EG&G model 273A Potentiostat/Galvanostat.

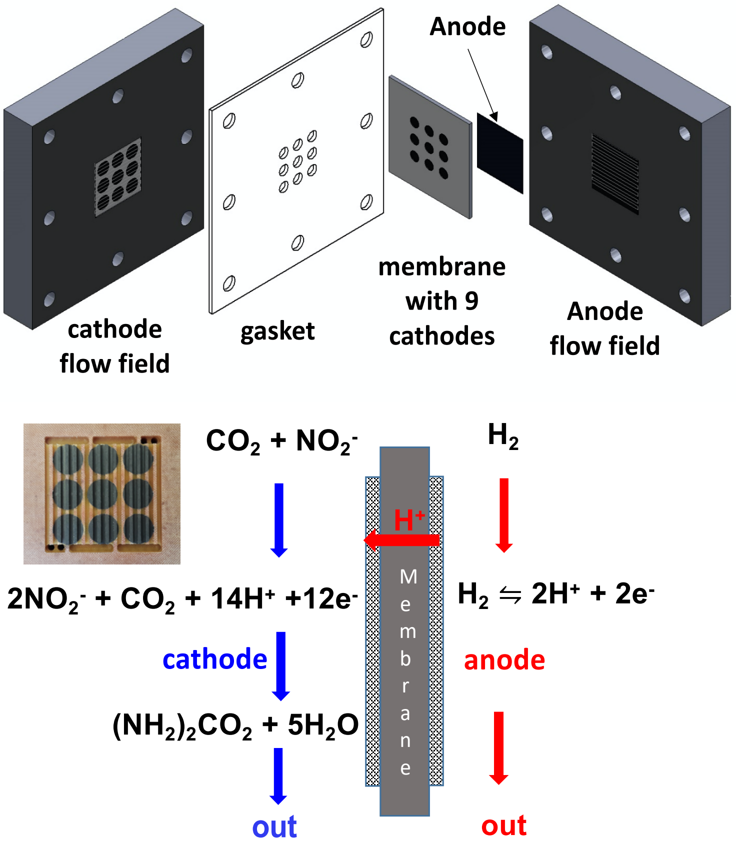

Figure 2.2. Schematic diagram of the PEM electrolysis cell (top) and the operation mode (bottom).

The PEM electrolysis cell was used with two different configurations; as a multi-cathode cell with nine 0.24 cm^2 cathodes, or with a single 5 cm^2 cathode. An electrolyte saturated with N_2, CO_2 or mixture of $N_2 + CO_2$ was pumped into the cathode flow field with a NE300 New Era Pump Systems syringe pump at a flow rate of 0.1 mL min^{-1} , while the anode was purged with 5% H_2 in N_2 at a flow rate of 4 mL min^{-1} as shown in Fig. 2.2 (bottom). The anode functions as a counter electrode as well as a reference electrode. The electrochemical reaction that occurs at the anode

(Pt black) is $H_2 \rightleftharpoons 2H^+ + 2e^-$, so the anode can be treated as a pseudo reference electrode (Dynamic hydrogen electrode).

2.5 Product analysis

Three analytical techniques were used to determine the concentrations of ammonia and urea produced from the electrolysis of nitrite and CO_2. For ammonia measurement, spectrophotometry and ^{1}H-NMR and for urea, spectrophotometry and mass spectrometry techniques were used.

2.5.1 Ultraviolet-visible (UV-Vis) spectrophotometry

UV-Vis spectrophotometry is an analytical method used to measure the transmission of light in the UV-Vis regions of the electromagnetic spectrum of a sample. The spectrum produced by the sample can be used to identify the presence of specific analytes and to determine the concentration of these analytes in the sample.

To measure the concertation of ammonia and urea, an Agilent Cary 100 UV-Vis spectrophotometer was used. The instrument uses a deuterium lamp as a light source and is capable of exciting samples with light across a wavelength range of 190 -1100 nm. The absorbed light was detected by a photodiode array (PDA) detector, which has a wavelength accuracy of within 1.5 nm and a 1 cm standard optical path length. Cary WinUV software was used to control and acquire the spectrum.

2.5.1.1 Salicylate method for ammonia analysis with standard addition of NH_3

The salicylate method was used to measure the concertation of ammonia, where aqueous NH_4^+ reacted with sodium salicylate and NaClO as an oxidizing agent in the presence of

$Na_2[Fe (CN)_5NO]$ as a catalyst to form an indophenol type blue (2,2-dicarboxy indophenol) as described in the eq. 2.1 [1]. The absorbance of 2,2-dicarboxy indophenol was measured at 655 nm against a reagent blank using Agilent Cary 100 UV-Vis Spectrophotometer. A detailed sample preparation and analysis procedure is described in Chapter 3, within the results and discussion section [1].

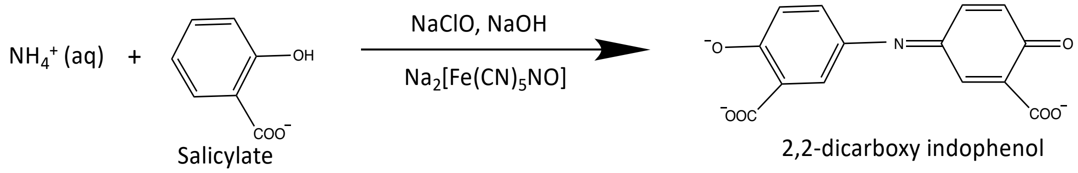

(2.1)

Figure 2.3. The Berthelot reaction; NH_4^+ reacts with salicylate to form 2,2-dicarboxy indophenol [2].

The ammonia concentration was calculated using equation 2.2 for multiple solutions with a constant total volume [3].

Standard addition equation:

$$A_{S+X} = A_X + \frac{A_X}{[X]_f}\,[S]_f \qquad (2.2)$$

Here, $[S]_f$, is the concentration of standard in the final solution, $[X]_f$ is the final concentration of analyte, A_X is the absorbance of the analyte and A_{S+X} is the absorbance of analyte plus standard.

A standard addition curve was constructed by plotting the absorbance of standard (NH_3) plus unknown (A_{S+X}) against the corresponding final concentrations of standard $[S]_f$. as shown in Figure 2.4. The x-intercept is the final concentration of unknown $[X]_f$, after dilution to the final sample volume. The initial concentration of unknown is calculated from the dilution that was applied to make the final sample.

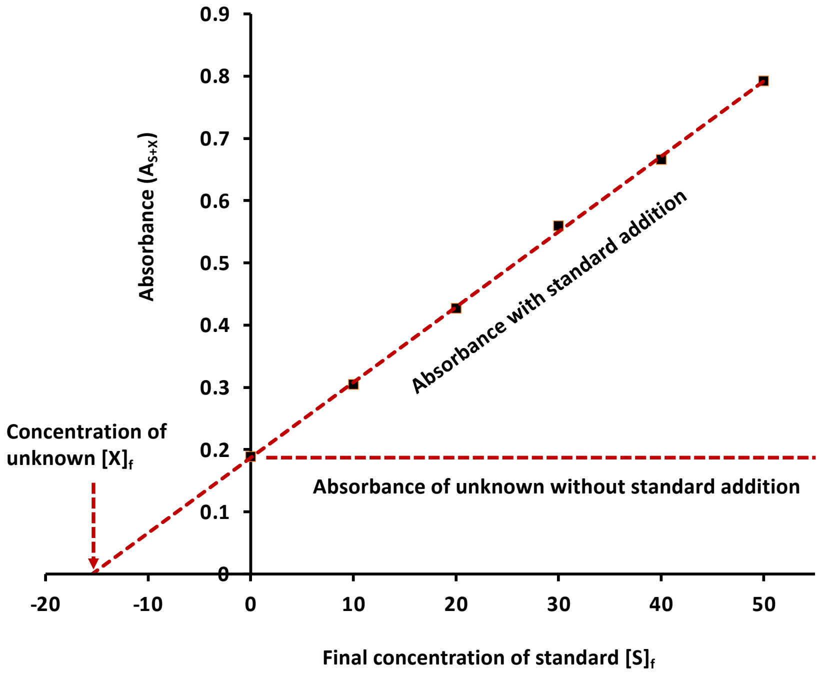

Figure 2.4. Graphical representation of standard addition analysis [2].

2.5.1.2 Salicylate method for urea analysis

Urea was measured by difference following its decomposition to ammonia with urease, as described in equation 1.19. Following the decomposition of the urea, the total number of moles of NH_3 present was measured by standard addition of NH_3 using the salicylate method as described in Section 2.5.1.1. A detailed analysis procedure is provided in Chapter 3 [1].

2.5.1.3 Diacetyl monoxime (DAM) method for urea analysis

The diacetyl monoxime (DAM) method was used to measure the concentration of urea produced, where urea reacted with diacetyl monoxime in an acidic media in the presence of thiosemicarbazide (TSC) and iron(III) sulfate hydrate ($Fe_2(SO_4)_3$) at high temperature [4, 5]. This reaction produced a pink-red colored complex, the absorbance of which was measured at 520 nm against a method blank. A detailed analysis procedure is provided in Chapter 3 [1].

2.5.2 Liquid chromatography–mass spectrometry (LC-MS) method for urea analysis

LC-MS is an analytical technique that involves the physical separation of target analytes followed by their mass-based detection. It is an extremely sensitive and selective analytical technique that can accurately determine the identities and concentration of analytes within a sample. First, targeted analytes in a sample are chromatographically separated in the LC system, then eluted analytes are introduced to a mass analyzer where analytes are ionized by electrospray ionization (ESI) or atmospheric pressure chemical ionization (APCI) source either in positive or negative polarity depending on the analytes. The charged analytes generated in the source are then analyzed by the mass analyzer based on their mass-to-charged (m/z) ratio.

Urea was quantified using the SCIEX triple TOF^{TM} 5600, a tandem quadrupole-time-of-flight (Q-TOF) based mass analyzer coupled with Agilent 1100 Series HPLC system. A detailed analysis procedure is provided in Chapter 3 [1].

2.5.3 Nuclear magnetic resonance (^{1}H-NMR) spectroscopy method for NH_3 analysis

NH_3 was analyzed using a Bruker AVANCE III HD spectrometer, which operated at a ^{1}H frequency of 500 MHz equipped with a 5 mm TCI CryoProbe (Bruker Biospin). The measurements were conducted at ambient temperature.

To determine the concentration of NH_3, the internal standard method was employed, with fumaric acid (FA) used as the internal standard. The spectra for NH_4^+ (7.23 ppm) and FA

(6.67 ppm) are presented in Fig. 2.6. The concentration of ammonia was calculated by comparing the peak intensity ratio of FA singlet and NH_4^+ triplet as described in eq. 2.3 [3]. A detailed analysis procedure is provided in Chapter 3 [1].

$$\frac{Signal\ from\ analyte}{Concentration\ of\ analyte} = F\frac{Signal\ from\ internal\ standard}{Concentration\ of\ internal\ standard} \tag{2.3}$$

Here F is the response factor, which was determined from the know concentration of analyte and internal standard and their respective signal intensity.

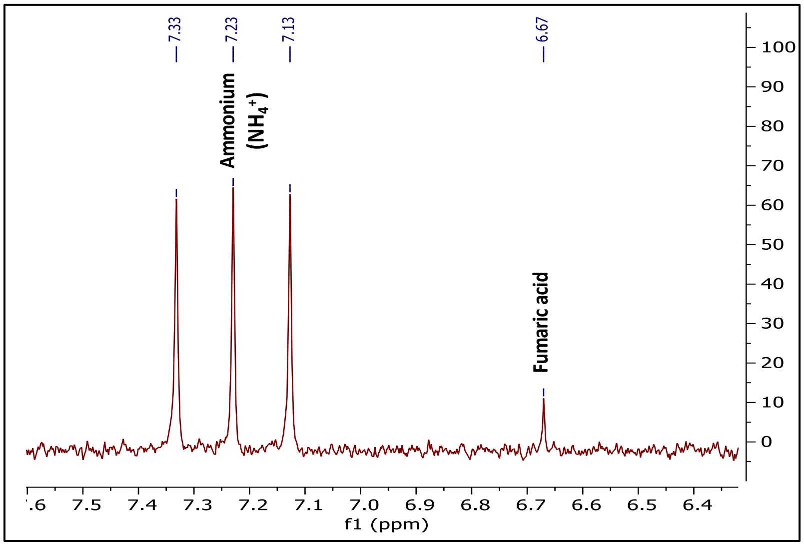

Figure 2.5. ^{1}H-NMR spectra for NH_4^+ and fumaric acid in 0.1 M $NaHCO_3$ and 5 mM $NaNO_2$ solution.

2.6 Deionization procedure of the electrolysis sample [6]

Prior to quantitative analysis, the electrolysis samples were deionized (clean-up) to eliminate interfering compounds, such as the NO_2^- or any ionic compound. A conical high-density polypropylene-based column (0.8 X 4 cm, Poly-Prep® Chromatography Columns; Bio-Rad) with a biotechnology grade AG® 501-X8 mixed bed ion exchange resin as a chromatographic media was used to deionize the sample (Figure 2.7). The resin was used as received, and approximately 0.6 g of resin was used for every 1 mL of column volume.

First, three-quarters of the column was filled with DI water, and then a very small amounts of resin were poured into the column until a total of 1 g of resin (~1.66 ml of a column volume) had been added. After the column was packed with resin, it was washed several times with deionized water. The sample was then carefully added to the reservoir above the resin and was eluted slowly (0.5 mL min^{-1}) through the column. First, 2 mL of eluent from a total of 5 mL of sample was discarded to avoid dilution of the sample with water present in the column, and then the rest of the eluent passed through the column twice and collected.

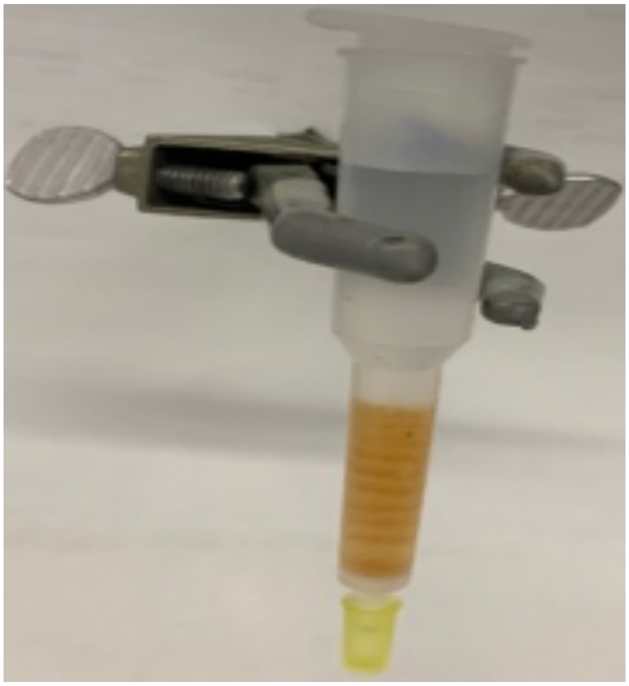

Figure 2.6. A photograph of a 1.66 mL (1 g) bed volume mixed-bed ion exchange chromatography column.

2.7 Catalyst characterization techniques

Four analytical techniques were used to characterize the catalysts: thermogravimetric analysis (TGA), scanning electron microscopy coupled with energy dispersive X-ray analysis (SEM-EDX), X-ray diffraction (XRD), and transmission electron microscopy (TEM).

2.7.1 Thermogravimetric analysis (TGA)

TGA is an analytical technique to characterize materials by measuring the mass of a sample as a function of temperature. The TGA experiments were carried out with a TA instruments Q500 thermogravimetric analyzer, and the data were processed using the Thermal Advantage software. The sample was loaded on a TGA platinum sample pan, which was stored in 3 M HCl solution. Before use, it was rinsed with deionized water and torched with a propane burner. The experiments were carried out under an airflow using a conventional ramp method, with a heating rate of 20 ℃ min^{-1} from ambient temperature to 800 ℃. During the analysis, the airflow was turned on when the temperature had reached at 300 ℃, and the final temperature (800 ℃) was held until the mass was constant. Once the airflow was turned on, the carbon contained in the sample of PtBi/C and PtPb/C started combustion as the temperature was increased above ca. 600 ℃. Metals like Pt, Bi, and Pb are thermally stable over the operating temperature range, and the residue of the combusted samples of PtBi/C and PtPb/C were assumed to be Pt and Bi or Pb. Therefore, the total percentage of metal loading of the prepared PtBi/C and PtPb/C catalysts can be easily obtained by TGA analysis.

2.7.2 Scanning electron microscopy coupled with energy dispersive X-ray analysis (SEM-EDX)

When SEM is coupled with an EDX system, both surface morphology and elemental composition of a sample can be obtained simultaneously. SEM is one kind of electron microscopy that generates high-resolution images of the surface by scanning a focused electron beam across the surface of the sample. When high-energy electrons are applied to the surface of a sample X- rays are produced as a result of the electrons ionizing the core shells of the atoms. The energies and intensities of these X-rays are measured, enabling the identification of different elements in the sample and providing semi-quantitative information.

For SEM-EDX analysis, the FePc/C catalyst was initially dispersed in a mixture of H_2O, 2-propanol, and Nafion and then deposited on a double-sided carbon adhesive film attached to an aluminum stub. The sample was allowed to dry at room temperature.

The SEM-EDX analysis was carried out using a Model FEI Quanta 400 scanning electron microscope equipped with a Bruker 4th generation XFlash SDD X-ray detector. This work was carried out under the supervision of Dr. David Grant at the Core Research Equipment and Instrument Training facility at the Memorial University of Newfoundland.

2.7.3 X-ray diffraction (XRD)

The X-ray diffraction (XRD) technique is a powerful tool used to determine a sample's crystalline properties. This method is based on the interaction between X-rays and the electrons in a sample, which results in the X-rays diffracting in various directions. The diffraction pattern produced can be analyzed to uncover the crystalline structures, size, and shape.

In order to determine the FePc/C, FePc, and carbon black (CB) crystalline properties, powder XRD measurements powder XRD measurements were performed using a Rigaku XtaLAB Synergy-S X-ray diffractometer with dual PhotonJet sources (Cu and Mo) and a HyPix-6000HE Hybrid Photon Counting detector. The X-ray powder diffraction was carried out from 20 to 90 degrees in 2θ at a scan rate of 1 degree per minute. The latest CrystAlisPro software was used for data collection and processing. The study was carried out by Dr. Jianbin Lin at the Core Research Equipment and Instrument Training facility at the Memorial University of Newfoundland.

2.7.4 Transmission electron microscopy (TEM)

Transmission electron microscopy (TEM) is a highly advanced analytical technique used to investigate the structure and properties of materials at the micro or nanoscale level. TEM is especially useful for analyzing samples' morphology and particle size and providing high-resolution images.

To obtain accurate results, sample preparation for TEM is a crucial step. TEM samples must be ultra-thin and electron-transparent so that electrons can pass through without being absorbed by the material. First, the catalyst (FePc/C) was dispersed evenly in deionized water through sonication. A drop of the sample solution was placed on a TEM grid and allowed to dry overnight, and then analyzed. The TEM analysis was conducted using a TecnaiTM Spirit scanning transmission electron microscope, and the work was carried out by Dr. Stephanie Tucker at the Memorial University of Newfoundland's Faculty of Medicine.

2.8 References

1. Akther, J., Song, C., Fatih, K., & Pickup, P. G. (2023). Electrochemical production of ammonia and urea from coreduction of nitrite and carbon dioxide at iron phthalocyanine electrodes and comparison of analytical methods. Journal of Electrochemical Society, 170, 026505.

2. Searle, P. L. (1984). The Berthelot or indophenol reaction and its use in the analytical chemistry of nitrogen. A review. Analyst, 109, 549-568.
3. Harris, Daniel C. Quantitative Chemical Analysis, Ninth Edition.
4. Li, D., Xu, N., Zhao, Y., Zhou, C., Zhang, L. P., Wu, L. Z., & Zhang, T. (2022). A reliable and precise protocol for urea quantification in photo/electrocatalysis. Small Methods, 6, 2200561.
5. Langenfeld, N. J., Payne, L. E., & Bugbee, B. (2021). Colorimetric determination of urea using diacetyl monoxime with strong acids. Plos One, 16, e0259760.
6. https://www.bio-rad.

Chapter 3

Electrochemical production of ammonia and urea from coreduction of nitrite and carbon dioxide at iron phthalocyanine electrodes and comparison of analytical methods.

Abstract

There is rapidly growing interest in the electrochemical reduction of both nitrite and carbon dioxide to mitigate environmental concerns and sustainably produce fuels, chemicals, and fertilizers. Ammonia and urea are key targets in this area and have been produced simultaneously by coreduction of NO_2^- and CO_2 at a variety of electrocatalysts. The salicylate spectrophotometric method is commonly employed to quantify both products, with urea determined by difference following decomposition with urease. However, this method can be influenced by numerous interferences and matrix effects. Here the electrochemical coreduction of NO_2^- and CO_2 at iron phthalocyanine electrodes has been investigated in order to accurately determine the ammonia and urea production. Urea concentrations were determined by salicylate, diacetyl monoxime and liquid-chromatography-mass spectrometry methods, while the salicylate method and nuclear magnetic resonance spectroscopy were used to determine ammonia. Urea was produced at low overpotentials, with a maximum faradaic yield of 5.8% at -0.047 V vs RHE, while a maximum 85% yield of ammonia occurred at -0.347 V. It is shown that the salicylate method can provide accurate ammonia and urea analyses when a standard addition method is employed, reaction conditions are carefully controlled, and the accuracy of calibration slopes are verified.

This chapter has been published as:

Akther, J., Song, C., Fatih, K., & Pickup, P. G. (2023). Electrochemical Production of Ammonia and Urea from Coreduction of Nitrite and Carbon Dioxide at Iron Phthalocyanine Electrodes and Comparison of Analytical Methods. Journal of The Electrochemical Society, 170, 026505.

Some modifications were made to the original paper for inclusion as a chapter in this thesis (e.g. the style of the references). The supporting information was incorporated into Appendix A.

The principal author (Jasmeen Akther) contributed to all aspects of the project as the main researcher including designing some of the experiments, performing all of the experiments, collecting, analyzing, presenting the data, and writing parts of the published manuscripts.

The corresponding author (Prof. Peter G. Pickup) was the principal investigator. He proposed the initial experiments, oversaw all aspects of the project, and contributed to several aspects of the project including experimental design, data analysis, writing and revision of the manuscripts, submission to the journals, and supervision of the principal author (Jasmeen Akther).

3.1 Introduction

Environmental concerns and the need to more sustainable production of fuel, commodity chemicals and fertilizers has prompted massive grow in research on the electrochemical reduction of N_2 and CO_2 [1] Electrochemical reduction of N_2 to produce NH_3 is particularly attractive, but also particularly challenging [2]. Although there are thousands of reports of NH_3 generation from N_2 at ambient temperature, the amounts produced are so small that it is difficult to separate the contributions from N_2 and the many other sources of N that have been identified [3, 4].

In light of the difficulties in reliably quantifying very small quantities of NH_3 generated from N_2, there has been increasing interest in the use of environmental pollutants as the N source. NH_3 has been successfully been generated from nitrate (NO_3^-), nitrite (NO_2^-), and nitrogen oxides by using a variety of electrocatalysts [5-8]. Since one of the main uses of NH_3 is for the manufacture of urea ($(NH_2)_2CO$) fertilizers, coreduction of CO_2 with these N sources is a particularly attractive process, and there are a growing number of studies that have demonstrated that urea can be produced in this way.

Shibata et al. [9] demonstrated in 1995 that urea could be generated by coreduction of CO_2 and NO_2^- under ambient conditions at Cu loaded gas diffusion electrodes. Subsequently, they showed that a wide variety of other metals were effective for this process [10], and that metallophthalocyanines could also produce substantial yields of urea [11]. $FeTiO_3$ nanoparticles [12], Cu doped TiO_2 [13], Te doped Pd [14], and ZnO nanosheets [15] have also been shown to produce urea from coreduction of CO_2 and NO_2^-. For example, a faradaic efficiency (yield) of 43% was reported at a rate of 21 μmol h^{-1} for Cu doped TiO_2 at -0.4 V vs RHE [13]. It has also been reported that urea can be produced by coreduction of CO_2 and N_2 [16-18], NO_3^- [9, 19], or nitric oxide (NO) [20].

The salicylate method (a modification of the indophenol blue method) [21], based on the Berthelot or indophenol reaction, is most commonly used for quantification of both ammonia and urea from electrochemical reduction of NO_2^- (or N_2) with or without CO_2 [10, 13, 14, 16]. Urea is determined by difference following its decomposition to ammonia with urease. However, the accuracy of this method can be influenced by many factors [21-25], which can lead to unreliable results, particularly for quantification (or even detection) of urea in the presence of excess ammonia. Of particular concern are the effects of electrolyte concentration [22], pH [25], and metal ions [22, 23].

Recently, Li et al. [26] have highlighted the need to confirm urea quantification using two different methods and reported a proton nuclear magnetic resonance (NMR) method. They compared results with analyses by a spectrophotometric method based on a reaction with diacetylmonoxime-thiosemicarbazide (DAM method), high-performance liquid chromatography, and ion chromatography following decomposition with urease. Notably, they reported that pH, metal ions, and high ammonia concentrations can lead to poor accuracy when urea is decomposed to ammonia for quantification.

We report here on the electrochemical coreduction of NO_2^- and CO_2 at iron phthalocyanine (FePc) electrodes and rigorous quantification of the production of urea and ammonia. Although this system has previously been reported to produce urea at gas-diffusion electrodes, current efficiencies for the formation of products were reported without supporting electrochemical data, such as current vs potential and time. The analytical method was identified only as "determined using a spectrophotometer" [11]. Here the electrochemistry of a carbon supported FePc catalyst in a hydrogen carbonate (bicarbonate) is reported, with and without NO_2^- under N_2 and CO_2, with production of urea and ammonia quantified using four different analytical methods. It was found that accurate urea analysis by the salicylate method could only be achieved by using standard addition, and that deionization of the samples was required for accurate analysis by the DAM method and a liquid-chromatography-mass spectrometry (LC-MS) method.

3.2 Experimental

3.2.1 Materials

Iron(II) phthalocyanine (FePc; 90%; Sigma-Aldrich), carbon black (Vulcan XC-72; Cabot), Nafion^{TM} solution (5.14 mass% in a mixture of lower aliphatic alcohols and 51.9% water; Dupont), 2-propanol (99.5% ACS grade; Caledon), carbon fiber paper (CFP; Toray), sodium hydrogen carbonate (99.7-100.3% ACS grade; BDH), sodium nitrite (≥99% ACS grade; BDH), ammonium chloride (99.5% ACS grade; BDH), sodium hypochlorite (reagent grade, available chorine 4.00-4.99%; Sigma-Aldrich), salicylic acid (≥99.0% ACS grade; Sigma-Aldrich), trisodium citrate dehydrate (reagent grade; Sigma-Aldrich), sodium hydroxide (97% ACS grade; BDH), sodium nitroprusside dihydrate (≥99% ACS grade; Sigma-Aldrich), urea (99.0-100.5% ASC grade; Sigma-Aldrich), diacetyl monoxime (DAM; 2,3-butanedione monoxime; 99%; Sigma-Aldrich), thiosemicarbazide (TSC; 98%, puriss. p.a; Sigma-Aldrich), $Fe_2(SO_4)_3$ (97%; Sigma-Aldrich), sulfuric acid (98%, ACS grade; Fisher Scientific), AG 501-X8 mixed bed resin (Bio-Rad Laboratories), acetonitrile (99.9% HiPerSolv CHROMANORM®, BDH), ammonium acetate (Sigma-Aldrich), acetic acid (Fisher Scientific), HPLC-grade water (Fisher Scientific), fumaric acid (≥99%, purum; Sigma-Aldrich), dimethyl sulfoxide-d_6 (DMSO-d_6; 99.9% reagent grade; Cambridge Isotope Laboratories, Inc), CO_2 (CD-50, Airgas) and nitrogen (Praxair, UHP, NI 5.0UH-T) gases were used as received. Urease, supplied as a glycerol solution (specific activity

500-800 units mL^{-1}; Sigma-Aldrich), was diluted by a factor of four with a 1% phosphate buffer (pH ~ 6.3). Deionized (DI; resistivity ≥17.9 MΩ)) water was used to prepare solutions.

3.2.2 Preparation of the carbon supported iron(II) phthalocyanine catalyst (FePc/C)

Carbon black (100 mg) and FePc (10 mg) were first dispersed in 5 mL and 1 mL of THF, respectively, under stirring followed by ultrasonication for 1 h, and then mixed together and sonicated for 4 h. The solvent was allowed to evaporate at room temperature overnight in a fume hood and the FePc/C catalyst was then dried at 60 ℃ in an oven for 30 min. Energy dispersive X-ray analysis (Appendix A, Figure A1) indicated that the Fe content of the catalyst was 0.85 mass%, which is close to the target value of 0.77%. Transmission electron microscopy (Appendix A, Figure A2) showed the typical structure of the carbon black [27], with no evidence of FePc particles, indicating that the FePc was well dispersed over the carbon surface. This conclusion was supported by X-ray diffraction (Appendix A, Figure A3), which did not show any evidence of crystalline FePc.

3.2.3 Electrode preparation

FePc/C (10.0 mg) was dispersed in a mixture of 150 μL of H_2O, 75 μL of 2-propanol and 75 μL of 5% Nafion^{TM} solution and sonicated for 3 h. The resulting catalyst ink (45 μL) was deposited onto a 1.0 cm^2 disc of CFP with a micropipette (in 2 μL aliquots) to give a catalyst loading of 1.5 mg cm^{-2} and left to dry overnight at ambient temperature. Figure A4 (Appendix A) shows a scanning electron microscopy image of an electrode.

3.2.4 Electrochemistry

A three-compartment glass cell (constructed in house) with a porous glass frit (ca. 1 mm X 0.2 cm^2; 10 μm porosity) separating the anode and cathode chambers was used at ambient temperature. A Pt wire (ca. 1 cm^2) was used as the counter electrode, with $Hg/HgSO_4$ in saturated potassium sulfate solution (Koslow; 658 mV vs SHE at 25 °C) as the reference electrode. All potentials are reported relative to the appropriate reversible hydrogen electrode (RHE), at -0.464 V vs SHE in 0.1 M $NaHCO_3$ under N_2 or -0.395 V vs SHE in 0.1 M $NaHCO_3$ under CO_2.

Cyclic voltammetry and chronoamperometry were performed using an EG&G model 273A Potentiostat/Galvanostat in 0.1 M $NaHCO_3$ and in a mixture of 0.1 M $NaHCO_3$ and 5 mM $NaNO_2$, under N_2 and CO_2. Before each measurement, the electrolyte solution was purged with N_2 or CO_2 for 30 min and then covered with the purge gas during measurements. Constant potential coreduction (electrolysis) of CO_2 and NO_2^- was performed for 2 h at each potential, with a new FePc/C electrode used at each potential.

3.2.5 Analysis of ammonia (salicylate method) [28]

Three reagent solutions were prepared as follows; The chromogenic reagent (A) was prepared by dissolving 5 g of salicylic acid and 5 g of sodium citrate in 100 mL of 1 M NaOH. An oxidizing solution (B) was prepared by diluting 7 mL of sodium hypochlorite solution (available chlorine 4.00-4.99 %) to 100 mL with DI water. The catalysis solution (C) was prepared by dissolving 1 g of sodium nitroferricyanide in 100 mL of DI water.

For analysis of NH_3 by standard addition, equal volumes (0.5 mL) of the unknown sample were pipetted into six volumetric flasks. Increasing volumes of a 1000 μmol L^{-1} standard solution of NH_4Cl were added to each flask. Then, 2 mL of the chromogenic solution (A), 1 mL of oxidizing solution (B) and 0.2 mL of catalyst solution (C) were added sequentially to each flask and diluted with deionized water to a final volume of 10 mL. Each reagent was added to all six flasks before addition of the next reagent without any delay. These solutions were then kept in the dark at ambient temperature for 2 h. The absorbance of each solution at 655 nm was measured using a double beam Agilent Cary 100 UV-Vis Spectrophotometer. A reagent blank, prepared with DI water in the same way as the samples, was used in the reference beam.

3.2.6 Analysis of urea (salicylate method) [19]

Urea was measured by difference following its decomposition to $CO_2 + 2NH_3$ by urease. In a sealed sample vial, 6 mL of the electrolysis solution was mixed with 3 mL of urease solution. The mixture was incubated for 1 h at 40 ℃ in a constant temperature water bath.

3.2.7 Diacetyl monoxime (DAM) method for urea analysis [26, 29]

Standard solutions of urea in a mixture of 0.1 M of $NaHCO_3$ and 5 mM of $NaNO_2$ were prepared daily, and freshly prepared DAM (50.0 g L^{-1}) and TSC (2.0 g L^{-1}) solutions in DI water were used. A $Fe_2(SO_4)_3$ (600 mg L^{-1}) solution was prepared by dissolving $Fe_2(SO_4)_3$ in a 5% H_2SO_4 solution (v/v) to avoid hydrolytic decomposition and was stored in an amber glass bottle at 4 ℃.

Prior to analysis of the urea, standard solutions and samples were first deionized using a conical 0.8 X 4 cm polypropylene column (Poly-Prep® Chromatography Columns; Bio-Rad) with 1.00 g (1.6 ml bed volume) of biotechnology grade mixed bed ion exchange resin (AG® 501-X8; Bio-Rad). Following deionization, 2 mL aliquots of the standards and samples from electrolyses were placed in 20 mL glass vials and freshly prepared solutions of DAM (0.225 mL), TSC (0.0375 mL), $Fe_2(SO_4)_3$ (0.0375 mL) and 50% H_2SO_4 (2 mL) were added sequentially. The resulting mixture was diluted to a final volume of 5 mL, heated for 30 min in a water bath at 90 ℃ and cooled to ambient temperature. The absorbance of the resulting red compound was measured at 520 nm against a reagent blank (prepared with DI water in the same way as the samples), was used in the reference beam.at room temperature using an Agilent Cary 100 UV-Vis Spectrophotometer.

3.2.8 Liquid chromatography-mass spectrometry (LC-MS) method for urea analysis [30, 31]

Standard solutions and samples were deionized, as described above for the DAM method, and then mixed with acetonitrile in a 1:4 volume ratio. Chromatographic separation was achieved using an Agilent 1100 Series HPLC system with a Poroshell 120 HILIC, 4.6 X 100 mm, 4 µm column (Agilent Technologies) with a KrudKatcher ULTRA HPLC in-line filter (2.0 µm, 0.004 in. ID, Phenomenex). The mobile phase was acetonitrile containing 10% HPLC-grade water 0.5 mM ammonium acetate and 0.2 mM acetic acid, at a flow rate of 0.5 mL min^{-1}. The injection volume was 10 µL and the column temperature was maintained at 30 ℃.

The eluant from the column was analyzed using a SCIEX triple TOF™ 5600 system (quadrupole time-of-flight (Q-TOF) mass analyzer) in multiple reaction monitoring (MRM) acquisition mode. The DuoSpray™ Source was used with an electrospray ionization probe in positive polarity. During analysis, the quadrupole mass analyzer (Q1) was operated in a mass filter mode to transmit only the precursor ion of interest for the mass of 61.03 m/z, then transmitted to the collision cell (Q2), where it undergoes fragmentation. TOF-MS acquired the MS/MS data from 15 to 1000 m/z in high sensitivity mode, and a multiple reaction monitoring (MRM) acquisition method was developed. Data was acquired using Analyst® TF software, and the extracted ion chromatograms (XIC) generated for fragment ions were processed with PeakView® software. A matrix-based calibration curve was prepared by plotting the integrated peak area of mass 61.03 m/z against the concentration of urea standard.

3.2.9 NMR method for ammonia analysis [3, 32]

A Bruker AVANCE III HD spectrometer operating at a ^{1}H frequency of 500 MHz equipped with a 5 mm TCI CryoProbe (Bruker Biospin) was used at ambient temperature. Electrolysis samples (75 µL) were mixed with 25 µL of 4 M H_2SO_4 in DMSO-d_6, 400 µL of DMSO-d_6, and 50 µL of 50 µM fumaric acid (FA) in DMSO-d_6 as an internal standard. The ratio of the integrated peak areas of the NH_4^+ triplet and FA singlet were used to calculate the ammonia concentration with calibration (a 4.5% correction) using a 0.200 mM standard solution of NH_4Cl in 0.1 M of $NaHCO_3$ + 5 mM of $NaNO_2$.

3.3 Results and Discussion

3.3.1 Quantification of ammonia and urea by the salicylate method

Based on the work of Shibata and Furuya [11] on the use of FePc for coreduction of CO_2 and NO_2^-, 0.1 M $NaHCO_3$ plus 5 mM $NaNO_2$ was selected as the electrolyte for this study. Due to concerns over the consistency of calibration curves [11], and possible changes in absorbance due to unknown species that may be present in samples following electrolysis (e.g., organic products from CO_2 reduction, ions from the electrodes, changes in pH) a standard addition method was used to quantify ammonia and urea. Figure 3.1 shows data for analysis of a standard solution containing 60 µM NH_4Cl and 40 µM urea. $\Delta C_{\mathrm{ammonia}}$ is the change in concentration following addition of NH_4Cl to other aliquots of the NH_4Cl + urea standard solution.

It can be seen from Figure 3.1 that the standard addition plots exhibited excellent linearity with very similar slopes, before and after decomposition of the urea. Table 3.1 shows averaged analytical results and slopes (with standard deviations) for six identical analyses performed in this way. The average NH_4Cl concentration of 60.0 ± 1.0 μM before urea decomposition is in agreement with the value of 60 μM in the standard. The ammonia (NH_4Cl plus NH_3 from urea) concentration following decomposition of the urea is also in good agreement with the expected value of 140 μM, resulting in a urea concentration of 41.0 ± 1.6 μM that is within experimental uncertainly of the true value.

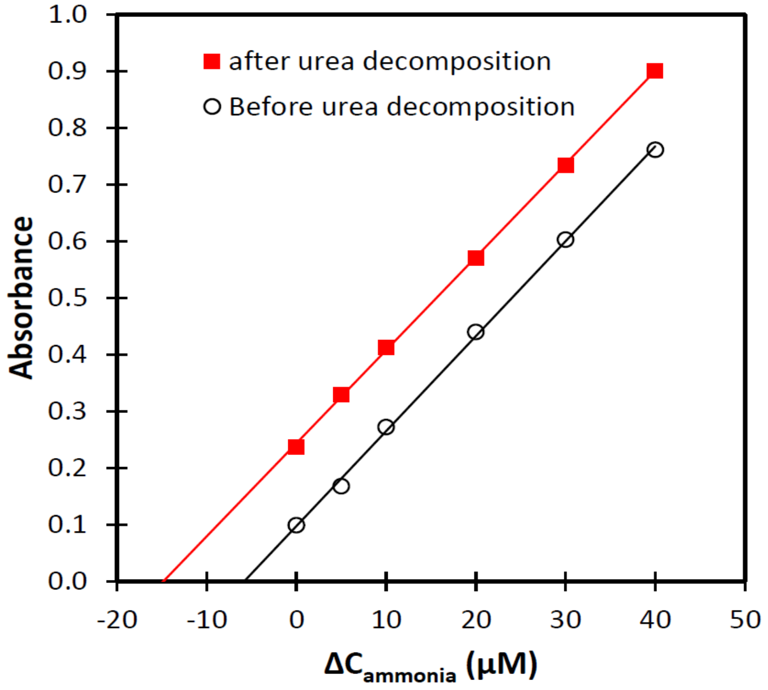

Figure 3.1. Standard addition analysis of 60 μM NH_4Cl and 40 μM urea in 0.1 M $NaHCO_3$ + 5 mM $NaNO_2$ using the salicylate method.

The average slopes of the standard addition plots before and after urea decomposition, reported as effective molar attenuation coefficients (ε* = absorbance/ (ammonia concentration x path length)) in Table 3.1, are close to a reported value of 17.7 mM^{-1} cm^{-1} in water [21]. It was found that without careful control of the experimental conditions during formation of the indophenol-type dye and decomposition of urea, and consideration of the instability of the dye, concentrations of urea determined by this method could be very inaccurate. Consequently, it was found to be essential to confirm that ε* was consistent, use quality control samples, and verify the accuracy of results with a second analytical method. Note that ε* is based on the concentration of ammonia after dilution, since it is based on the absorbance of the chromophore produced after the reagents have been added. It is independent of the dilution factor, whereas the slope of a calibration or standard addition plot (based in the initial ammonia concentration) varies with dilution.

Table 3.1. Concentrations and effective molar attenuation coefficients (ε*) (averages and standard deviations for six measurements) for analysis of 60 μM NH_4Cl and 40 μM urea in 0.1 M $NaHCO_3$ + 5 mM $NaNO_2$ using the salicylate method.

	$[NH_3]$ (μM)	**ε^* (mM cm^{-1})**	**[urea] (μM)**
Before urea decomposition	60.0 ± 1.0	17.4 ± 0.3	
After urea decomposition	142.0 ± 3.8	17.3 ± 0.2	41.0 ± 1.6

3.3.2 Quantification of urea by the diacetyl monoxime (DAM) method

The reaction of urea with diacetyl monoxime to form a red product is potentially better than the salicylate method for determining urea in the presence for ammonia because it avoids errors arising from the enzymatic urea decomposition step and subtraction of the ammonia concentration which may be much higher [26]. It can also provide a very low detection limit; detection of

1.2 nM urea in seawater has been reported [29]. However, interference by NO_2^- [26] makes the method unsuitable for the determination of urea from coreduction of CO_2 and NO_2^- without pre-treatment of samples to remove NO_2^- and other potential interferences.

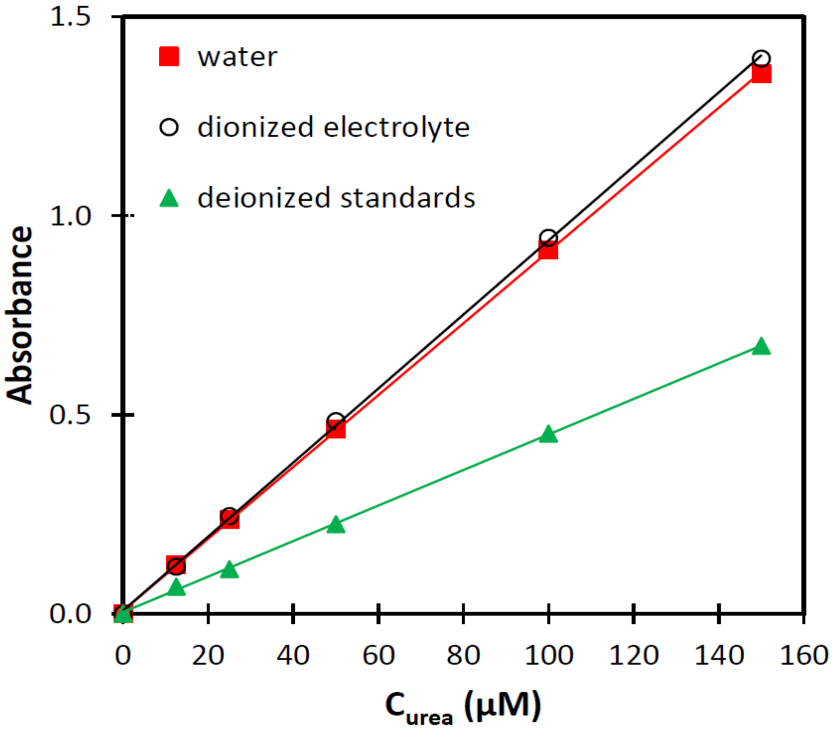

Figure 3.2. Calibration curves for analysis of urea in water, 0.1 M $NaHCO_3$ + 5 mM $NaNO_2$ (electrolyte) that had been deionized with a mixed bed ion-exchange resin, with urea added following deionization, and urea + 0.1 M $NaHCO_3$ + 5 mM $NaNO_2$ solutions (standards) that had been deionized.

An AG 501-X8 mixed bed ion-exchange resin was used here to remove both the $NaHCO_3$ electrolyte and $NaNO_2$. The efficacy of this deionization method is demonstrated in Figure 3.2, where a calibration curve for urea in water is compared with a calibration curve for urea added to a 0.1 M $NaHCO_3$ + 5 mM $NaNO_2$ solution that had been deionized with the mixed bed resin. Figure A5 (Appendix A) shows spectra for reagent blanks and 20 μM urea samples before and after deionization. It can be seen that the presence of the electrolyte prevents formation of the red product with urea (no peak at 520 nm) and produces a new peak at 480 nm. These effects were not seen in the absence of $NaNO_2$, but also occurred at $NaNO_2$ concentrations as low as 0.5 mM.

In order to employ this method for analysis of urea in samples from the co-reduction of CO_2 and NO_2^- it was necessary to account for the loss of urea during deionization by calibration with urea standards in 0.1 M $NaHCO_3$ + 5 mM $NaNO_2$ that had been deionized. This calibration curve is also shown in Figure 3.2, where it can be seen that the slope is ca. 50% lower due to adsorption of urea by the column. Nonetheless, the linearity of the calibration curve is excellent, the slope was reproducible with a second set of standards, and analysis of five 10 μM quality control samples gave an average urea concentration of 10.6 ± 0.4 μM.

3.3.3 Coreduction of NO_2^- and CO_2 at FePc/C electrodes

Figure 3.3 shows voltammograms for FePc/C electrodes in 0.1 M $NaHCO_3$, with and without 5 mM $NaNO_2$, under N_2 and CO_2. Under N_2, in the absence of $NaNO_2$, two main quasi- reversible redox waves are seen at formal potentials of +0.89 V ($\Delta E_p = 0.33$ V) and 0.00 V ($\Delta E_p = 0.18$ V) for the Fe(+3/+2) and Pc(-2/-3) (or Fe(+2/+1)) couples of the FePc, respectively [33]. Under CO_2 there are minor changes in these waves that are presumably due mainly to the change in pH from 8.3 to 6.8, and a significant increase in current at potentials below ca. -0.2 V due to CO_2 reduction [34]. The main product from CO_2 reduction at FePc is generally CO [34, 35]. Voltammograms were similar in the presence of $NaNO_2$ under N_2, but with enhanced cathodic currents below ca. 0 V due to reduction of NO_2^- [36].

When both NO_2^- and CO_2 were present there was a large increase in current at potentials below +0.1 V, with a cathodic peak at -0.21 V that was more than 3.5 times higher than the current at this potential for either NO_2^- and CO_2 alone. This suggests that there was substantial coreduction of NO_2^- and CO_2 in addition to their individual reduction processes. A previous report has demonstrated that urea is produced under similar condition, in addition to CO and NH_3 [11]. In that work, both NH_3 and urea produced from coreduction of NO_2^- and CO_2 at FePc "determined using a spectrophotometer", although the method was not specified. Urea was decomposed to NH_3 and determined by difference.

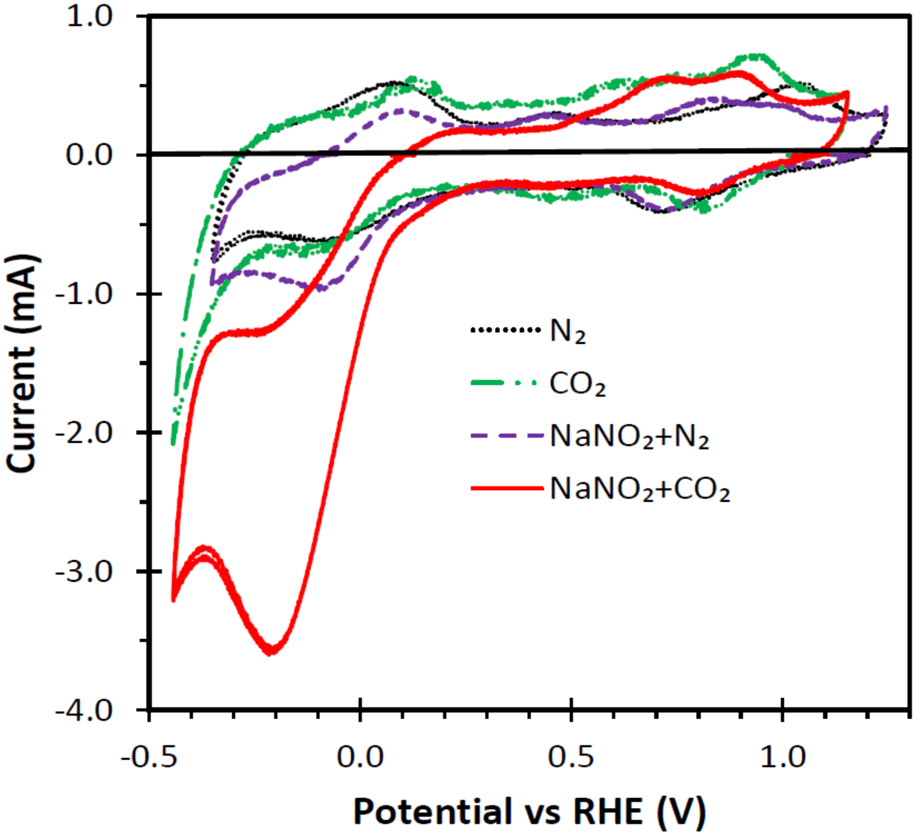

Figure 3.3. Cyclic voltammograms (10 mV s^{-1}) for FePc/C electrodes in 0.1 M $NaHCO_3$, with and without 5 mM $NaNO_2$, under N_2 and CO_2.

In order to verify that urea could be produced from the coreduction of NO_2^- and CO_2 at FePc, and quantify both urea and ammonia production, a series of 2 h constant potential electrolyses were conducted. As shown in Figure 3.4, the current was reasonably stable during electrolysis, with relatively small changes in the average current (Table 3.2) as the potential was changed (a range of 0.87 to 1.19 mA). The higher currents at -0.247 V and -0.447 V were reproducible with 2nd electrodes, and correspond approximately to the peak seen at ca. -0.21 V in cyclic voltammetry (Figure 3.3) and the onset of other reduction processes, such as reduction of water at -0.4 V seen in the voltammogram under N_2 in the absence of $NaNO_2$, respectively. The noise, spikes, and positive and negative variations/drift in the current vs time plots can be attributed to gases (e.g. NH_3, CO, N_2, H_2) formed within the electrode structure, since bubbles were visible on the electrode surface during electrolysis.

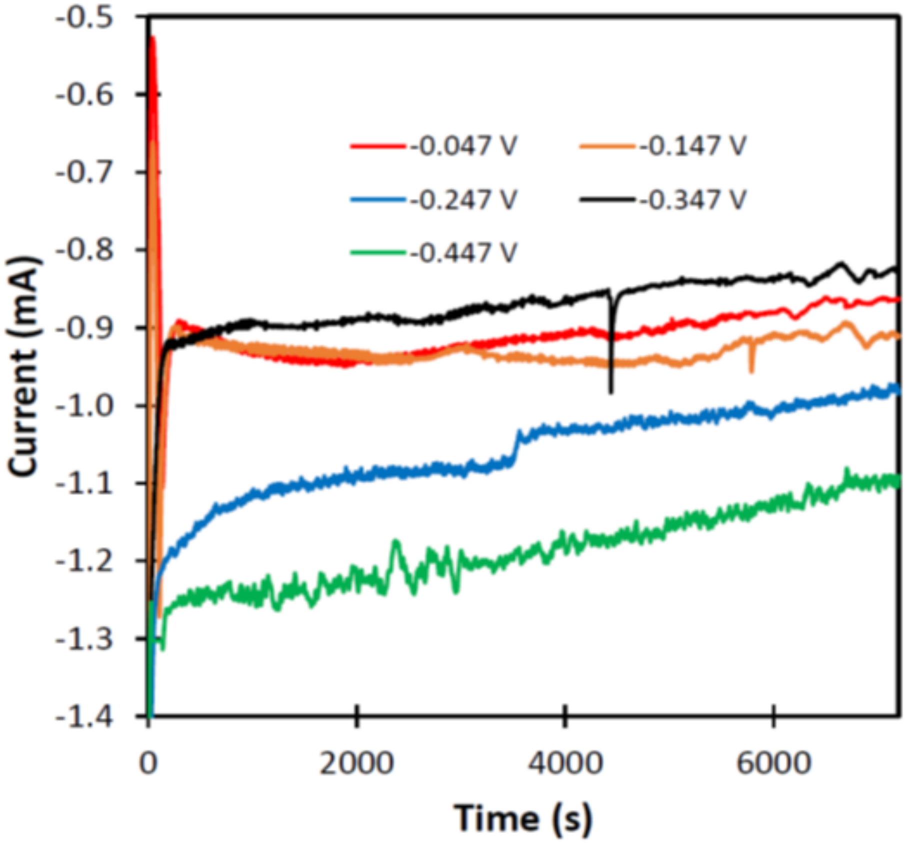

Figure 3.4. Current vs time at various potentials (vs RHE) for electrolysis of 5 mM $NaNO_2$ under CO_2 in 0.1 M $NaHCO_3$ at FePc/C electrodes.

Since initial attempts to quantify urea by the salicylate method produced inconsistent results, both the DAM and LC-MS methods were used to establish accurate values. The salicylate method was used to determine ammonia and verified by NMR. It can be seen from the analytical data in Table 3.2 that the urea concentrations from the DAM and LC-MS methods were in good agreement (average difference of 1.8%) and that the NH_3 concentrations from the salicylate and NMR methods were also in good agreement (average difference of 2.8%). Reproducibility at -0.047 V was assessed by running four electrolyses at different electrodes. Averages and standard deviation are reported in Table 3.2 (NMR was only used for one run). Relative standard deviations were 3.9%, 2.6%, 4.1%, 0.7% for the average current, DAM, LC-MS, and salicylate methods, respectively.

Table 3.2. Average currents and concentrations of urea and ammonia for electrolysis of 5 mM $NaNO_2$ in 0.1 M $NaHCO_3$ under CO_2 at FePc/C electrodes for 2 h. Averages and standard deviations are reported for four different electrodes at -0.047 V.

Potential (V) vs RHE	Average current (mA)	Urea concentration (μM)		NH_3 concentration (μM)	
		DAM	LC-MS	Salicylate	NMR
-0.047	-0.865 ± 0.034	20.7 ± 0.5	21.1 ± 0.9	501 ± 4	520
-0.147	-0.932	18.9	18.6	457	453
-0.247	-1.02	16.4	16.0	668	683
-0.347	-0.890	15.3	15.3	629	659
-0.447	-1.19	13.9	14.3	436	452

Following optimization of the salicylate standard addition method, and validation by NMR, it was used to determine urea produced in a separate set of electrolyses at -0.047 V. The average current of -0.859 ± 0.003 mA for three different electrodes agreed with the value of -0.865 ± 0.034 mA in Table 3.2, while the average urea concentration of 22.5 ± 0.9 µM was in reasonable agreement with the values from DAM and LC-MS in Table 3.2 (average of 20.9 ± 0.7 µM). Although this demonstrates that the optimized salicylate method can be reasonably accurate for urea analysis, great care is still required and it is important to verify accuracy.

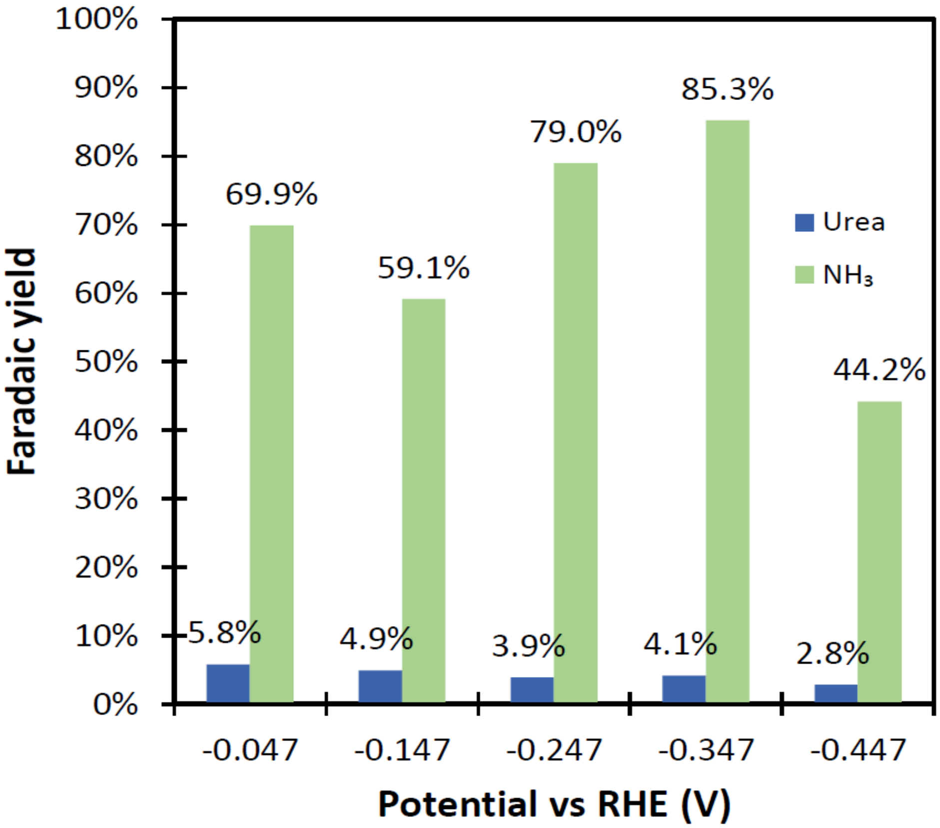

Figure 3.5. Faradaic yields of NH_3 and urea, calculated from the data in Table 3.2.

Faradaic yields of NH_3 and urea calculated from the salicylate and DAM data in Table 3.2 are reported in Figure 3.5. They show that the main product from the electrolyses was NH_3, with 85% of the current producing NH_3 at -0.347 V. However, there was significant production of urea, with a maximum yield of 5.8% at the lowest overpotential employed. The high yields of NH_3 relative to urea indicate that the large increase in current observed when NO_2^- was reduced under CO_2, relative to N_2, was due to primarily the effect of CO_2 on NO_2^- reduction rather than coreduction to produce urea. This is most likely due to the change in pH, and suggests that it may be possible to control the urea:NH_3 ratio by changing pH.

The yields of urea obtained in this work are significantly lower than the faradaic yield of 15% reported for coreduction of CO_2 and NO_2^- using a FePc based gas diffusion electrode at -1.5 V vs SCE (ca. -0.86 V vs RHE) [11]. There are many possible reasons for this, including the differences in potential, differences in concentrations (e.g. 20 mM vs 5 mM NO_2^-), gas phase vs dissolved CO_2, and FePc loading (not specified in [11]). Nonetheless, urea was produced at much lower overpotentials (less negative potentials) in this work (a 5.8% yield at -0.047 V vs RHE). Higher faradaic yields of urea have also been reported for Cu doped TiO_2 (43% at -0.4 V vs RHE) [13], Te doped Pd (12% at -1.1 V vs RHE) [14], and ZnO nanosheets (21% at -0.79 V vs RHE) [15].

The production of urea at FePc at less negative potentials than for other reported catalysts warrants further investigation and development to increase yields and production rates and take advantage of the higher energy efficiency arising from the lower cathode overpotential. In addition, other metallophthalocyanines should be investigated, such as CoPc which has been reported to be more selective for urea production [11].

3.4 Conclusions

Iron phthalocyanine has been shown to be an effective catalyst for coreduction of CO_2 and NO_2^- to produce urea at low overpotentials, although faradaic yields of urea (≤ 5.5%) were low relative to ammonia (≤ 85%). At -0.347 V vs RHE, 89% of the charge passed produced ammonia or urea, demonstrating very high efficiency for conversion of NO_2^- to high value products.

Although the salicylate method can be used for measuring both ammonia and urea from electrochemical coreduction of CO_2 and NO_2^-, great care must be taken to avoid inaccuracies due to interferences, matrix effects, variations in reaction condition, and instability of the chromophore. This is particularly important when urea is formed together with a large excess of ammonia. It is essential to confirm that the correct effective molar attenuation coefficient is consistently obtained for the electrolyte employed, and to monitor accuracy with quality control samples. It is recommended that analyses be conducted by standard addition, and verified by independent analytical methods.

3.5 References

1. Tang, C., Zheng, Y., Jaroniec, M., & Qiao, S. Z. (2021). Electrocatalytic refinery for sustainable production of fuels and chemicals. Angewandte Chemie International Edition, 60, 19572-19590.
2. Yang, B., Ding, W., Zhang, H., & Zhang, S. (2021). Recent progress in electrochemical synthesis of ammonia from nitrogen: strategies to improve the catalytic activity and selectivity. Energy & Environmental Science, 14, 672-687.

3. Andersen, S. Z., Čolić, V., Yang, S., Schwalbe, J. A., Nielander, A. C., McEnaney, J. M., & Chorkendorff, I. (2019). A rigorous electrochemical ammonia synthesis protocol with quantitative isotope measurements. Nature, 570, 504-508.
4. Choi, J., Suryanto, B. H., Wang, D., Du, H. L., Hodgetts, R. Y., Ferrero Vallana, F. M., & Simonov, A. N. (2020). Identification and elimination of false positives in electrochemical nitrogen reduction studies. Nature Communications, 11, 5546.
5. Wang, Y., Wang, C., Li, M., Yu, Y., & Zhang, B. (2021). Nitrate electroreduction: mechanism insight, in situ characterization, performance evaluation, and challenges. Chemical Society Reviews, 50, 6720-6733.
6. Xu, H., Ma, Y., Chen, J., Zhang, W. X., & Yang, J. (2022). Electrocatalytic reduction of nitrate–a step towards a sustainable nitrogen cycle. Chemical Society Reviews.
7. Ko, B. H., Hasa, B., Shin, H., Zhao, Y., & Jiao, F. (2022). Electrochemical reduction of gaseous nitrogen oxides on transition metals at ambient conditions. Journal of American Chemical Society, 144, 1258-1266.
8. Tran, N. Q., Le, B. T. N., Phan, B. T., Cho, Y., Liu, X., & Lee, H. (2022). Efficient ammonia synthesis via electroreduction of nitrite using single-atom Ru-doped Cu nanowire arrays. Chemical Communications, 58, 5257-5260.
9. Shibata, M., Yoshida, K., & Furuya, N. (1995). Electrochemical synthesis of urea on reduction of carbon dioxide with nitrate and nitrite ions using Cu-loaded gas-diffusion electrode. Journal of Electroanalytical Chemistry, 387, 143-145.
10. Shibata, M., Yoshida, K., & Furuya, N. (1998). Electrochemical synthesis of urea at gas-diffusion electrodes: IV. Simultaneous reduction of carbon dioxide and nitrate ions with various metal catalysts. Journal of Electrochemical Society, 145, 2348.

11. Shibata, M., & Furuya, N. (2001). Electrochemical synthesis of urea at gas-diffusion electrodes: Part VI. Simultaneous reduction of carbon dioxide and nitrite ions with various metallophthalocyanine catalysts. Journal of Electroanalytical Chemistry, 507, 177-184.

12. Siva, P., Prabu, P., Selvam, M., Karthik, S., & Rajendran, V. (2017). Electrocatalytic conversion of carbon dioxide to urea on nano-$FeTiO_3$ surface. Ionics, 23, 1871-1878.

13. Cao, N., Quan, Y., Guan, A., Yang, C., Ji, Y., Zhang, L., & Zheng, G. (2020). Oxygen vacancies enhanced cooperative electrocatalytic reduction of carbon dioxide and nitrite ions to urea. Journal of Colloid and Interface Science, 577, 109-114.

14. Feng, Y., Yang, H., Zhang, Y., Huang, X., Li, L., Cheng, T., & Shao, Q. (2020). Te-doped Pd nanocrystal for electrochemical urea production by efficiently coupling carbon dioxide reduction with nitrite reduction. Nano Letters, 20, 8282-8289.

15. Meng, N., Huang, Y., Liu, Y., Yu, Y., & Zhang, B. (2021). Electrosynthesis of urea from nitrite and CO_2 over oxygen vacancy-rich ZnO porous nanosheets. Cell Reports Physical Science, 2, 100378.

16. Kayan, D. B., & Köleli, F. (2016). Simultaneous electrocatalytic reduction of dinitrogen and carbon dioxide on conducting polymer electrodes. Applied Catalysis B: Environmental, 181, 88-93

17. Chen, C., Zhu, X., Wen, X., Zhou, Y., Zhou, L., Li, H., & Wang, S. (2020). Coupling N_2 and CO_2 in H_2O to synthesize urea under ambient conditions. Nature Chemistry, 12, 717-724.

18. Guo, Z. Y., Li, C. X., Gao, M., Han, X., Zhang, Y. J., Zhang, W. J., & Li, W. W. (2021). Inside cover: Mn-O covalency governs the intrinsic activity of Co-Mn spinel oxides for

boosted peroxymonosulfate activation (Angew. Chem. Int. Ed. 1/2021). Angewandte Chemie International Edition, 60, 2-2.

19. Saravanakumar, D., Song, J., Lee, S., Hur, N. H., & Shin, W. (2017). Electrocatalytic conversion of carbon dioxide and nitrate ions to urea by a titania-Nafion composite electrode. ChemSusChem, 10, 3999-4003.
20. Huang, Y., Yang, R., Wang, C., Meng, N., Shi, Y., Yu, Y., & Zhang, B. (2021). Direct electrosynthesis of urea from carbon dioxide and nitric oxide. ACS Energy Letters, 7, 284-291.
21. Giner-Sanz, J. J., Leverick, G., Perez-Herranz, V., & Shao-Horn, Y. (2021). Optimization of the salicylate method for ammonia quantification from nitrogen electroreduction. Journal of Electroanalytical Chemistry, 896, 115250.
22. Shi, L., Yin, Y., Wang, S., Xu, X., Wu, H., Zhang, J., & Sun, H. (2020). Rigorous and reliable operations for electrocatalytic nitrogen reduction. Applied Catalysis B: Environmental, 278, 119325.
23. Giner-Sanz, J. J., Leverick, G. M., Pérez-Herranz, V., & Shao-Horn, Y. (2020). Salicylate method for ammonia quantification in nitrogen electroreduction experiments: the correction of iron III interference. Journal of Electrochemical Society, 167, 134519.
24. Biswas, S. S., Saha, A., & Eswaramoorthy, M. (2022). Facts or artifacts: Pitfalls in quantifying sub-ppm levels of ammonia produced from electrochemical nitrogen reduction. ACS Omega, 7, 1874-1882.
25. Zhao, Y., Shi, R., Bian, X., Zhou, C., Zhao, Y., Zhang, S., ... & Zhang, T. (2019). Ammonia detection methods in photocatalytic and electrocatalytic experiments: how to improve the reliability of NH_3 production rates?. Advanced Science, 6, 1802109.

26. Li, D., Xu, N., Zhao, Y., Zhou, C., Zhang, L. P., Wu, L. Z., & Zhang, T. (2022). A reliable and precise protocol for urea quantification in photo/electrocatalysis. Small Methods, 6, 2200561.

27. Pérez-Rodríguez, S., Pastor, E., & Lázaro, M. J. (2018). Electrochemical behavior of the carbon black Vulcan XC-72R: Influence of the surface chemistry. Int. Journal of Hydrogen Energy, 43, 7911-7922.

28. Li, L., Tang, C., Xia, B., Jin, H., Zheng, Y., & Qiao, S. Z. (2019). Two-dimensional mosaic bismuth nanosheets for highly selective ambient electrocatalytic nitrogen reduction. ACS Catalysis, 9, 2902-2908.

29. Chen, L., Ma, J., Huang, Y., Dai, M., & Li, X. (2015). Optimization of a colorimetric method to determine trace urea in seawater. Limnology and Oceanography: Methods, 13, 303-311.

30. Krämer, M., Fry, H., & Kappenstein, O. (2021). Development and validation of two analytical methods for urea determination in compound feed, including pet food, and yeast using high-performance liquid chromatography coupled with fluorescence detection and tandem mass spectrometry. Food Additives & Contaminants: Part A, 38, 931-942.

31. Pitiranggon, M., Perzanowski, M. S., Kinney, P. L., Xu, D., Chillrud, S. N., & Yan, B. (2014). Determining urea levels in exhaled breath condensate with minimal preparation steps and classic LC-MS. Journal of Chromatographic Science, 52, 1026-1032.

32. Hodgetts, R. Y., Kiryutin, A. S., Nichols, P., Du, H. L., Bakker, J. M., Macfarlane, D. R., & Simonov, A. N. (2020). Refining universal procedures for ammonium

quantification via rapid ^{1}H NMR analysis for dinitrogen reduction studies. ACS Energy Letters, 5, 736-741.

33. Zagal, J. H., Griveau, S., Silva, J. F., Nyokong, T., & Bedioui, F. (2010). Metallophthalocyanine-based molecular materials as catalysts for electrochemical reactions. Coordination Chemistry Reviews, 254, 2755-2791.

34. Manbeck, G. F., & Fujita, E. (2015). A review of iron and cobalt porphyrins, phthalocyanines and related complexes for electrochemical and photochemical reduction of carbon dioxide. Journal of Porphyrins and Phthalocyanines, 19, 45-64.

35. Yang, S., Yu, Y., Gao, X., Zhang, Z., & Wang, F. (2021). Recent advances in electrocatalysis with phthalocyanines. Chemical Society Reviews, 50, 12985-13011.

36. D. Y. Hwang, J. M. Park and S. H. Kim, Bull. (1998). Korean Chem. Soc., 19, 795.

Chapter 4

High efficiency production of urea from electrochemical coreduction of carbon dioxide and nitrite at carbon supported iron(III) tetrasulfophthalocyanine under ambient conditions.

Abstract

Electrochemical coreduction of carbon dioxide with nitrite can potentially be used to remove two serious pollutants from the environment while producing urea as an essential fertilizer and valuable fuel. However, efficiencies are currently much too low due to the high overpotentials required and/or low faradaic efficiency (FE) for urea formation. Although metal phthalocyanine catalysts can provide reasonably high FE (≤ 42%), high negative potentials (≤-0.75 V vs RHE) are required. Here it is shown that a water soluble, sulfonated iron(III) phthalocyanine can produce a higher yield of urea (54%) at +0.053 V vs RHE, with 25% coproduction of NH_3. Urea production was measured by the diacetyl monoxime (DAM) method and verified by liquid chromatography–mass spectrometry. Electrodes prepared with a carbon black support and Nafion binder exhibited good stability in the 0.1 M $NaHCO_3$ electrolyte.

This chapter has been published as:

Akther, J., Song, C., Fatih, K., & Pickup, P. (2023). High Efficiency Production of Urea from Electrochemical Coreduction of Carbon Dioxide and Nitrite at Carbon Supported Iron(III) Tetrasulfophthalocyanine Under Ambient Conditions. ECS Advances.

Some modifications were made to the original manuscript for inclusion as a chapter in this thesis (e.g. the style of the references). The supporting information was incorporated into Appendix B.

The principal author (Jasmeen Akther) contributed to all aspects of the project as the main researcher including performing all of the experiments, collecting, analyzing, presenting the data, and writing draft of the manuscripts.

The corresponding author (Prof. Peter G. Pickup) was the principal investigator. He proposed the initial experiments, oversaw all aspects of the project, and contributed to several aspects of the project including experimental design, data analysis, writing and revision of the manuscripts, submission to the journals, and supervision of the principal author (Jasmeen Akther).

4.1 Introduction

Electrochemical production of urea by the coreduction of CO_2 with a variety of nitrogen sources [1, 2] is regarded as more sustainable than the use of ammonia from the Haber-Bosch process, which is energy intensive and produces high CO_2 emissions [3]. In addition, the use of nitrogen containing pollutants, such as nitrate and nitrite, can accomplish their simultaneous removal from the environment with CO_2 [4-7].

Nitrite in water systems is a major environmental challenge and can be mitigated by electrochemical reduction of the NO_2^- to N_2 and useful products such as NH_3, NO, N_2O, and NH_2OH [8]. Coupling of NO_2^- and CO_2 reduction to produce urea [9] is particularly attractive, and has been accomplished with a variety of catalysts, including metals and alloys [10, 11], metal phthalocyanines [12], $FeTiO_3$ [13], Cu doped TiO_2 [14], Te doped Pd [15], and ZnO_2 [16]. Cu, Fe, Co, and Ni phthalocyanines produced urea at faradaic efficiencies (current efficiencies) of 13-42% [12], while an efficiency of 43% was reported for Cu-doped TiO_2 [14] and a Cd metal catalyst gave an efficiency of ca. 55% [10].

Metallophthalocyanines are attractive for the electrochemical production of urea from NO_2^- and CO_2 because of their synthetic versatility and the wide range of ways in which they can be incorporated into electrode materials [17, 18]. Substituents can be used to control redox potentials and solubility, and to bind them to surfaces and polymers [17]. Fe(III) tetrasulfophthalocyanine (FeTSPc) has been shown to be effective for reduction of both CO_2 [19] and NO_2^- [20], and its water solubility makes it more versatile than unsubstituted iron phthalocyanine for incorporation into electrodes and control of the catalytic environment. We demonstrate here that it is highly effective for coreduction of NO_2^- and CO_2 to produce urea. A maximum faradaic efficiency of 54% was obtained at +0.053 V vs RHE.

4.2 Experimental

4.2.1 Materials

Fe(III) tetrasulfophthalocyanine (FeTSPc) (iron(III) phthalocyanine-4,4′,4″,4‴-tetrasulfonic acid, compound with oxygen, monosodium salt hydrate; Sigma-Aldrich), carbon black (Vulcan XC-72; Cabot), 5% Nafion^{TM} solution (5.14 mass% in a mixture of lower aliphatic alcohols and 51.9% water; Dupont), 2-propanol (Caledon), carbon fiber paper (CFP; Toray), sodium hydrogen carbonate (BDH), sodium nitrite (BDH), urea (Sigma-Aldrich), diacetyl monoxime (DAM; 2,3-butanedione monoxime; Sigma-Aldrich), thiosemicarbazide (TSC; Sigma-Aldrich), $Fe_2(SO_4)_3$ (Sigma-Aldrich), sulfuric acid (Fisher Scientific), AG 501-X8 mixed bed resin (Bio-Rad Laboratories), Acetonitrile (HiPerSolv CHROMANORM®, BDH), ammonium acetate (Sigma-Aldrich), acetic acid (Fisher Scientific), ammonium chloride (BDH), sodium hypochlorite (Sigma-Aldrich), salicylic acid (Sigma-Aldrich), sodium citrate (Sigma-Aldrich), sodium hydroxide (BDH), sodium nitroprusside dihydrate (Sigma-Aldrich), urease (specific activity 500-800 units/mL supplied as a glycerol solution; Sigma-Aldrich), and carbon dioxide (CD-50, Praxair Canada Inc.) and nitrogen (NI 5.0UH-T, Praxair Canada Inc.) gases were used as received. Deionized water was used to prepare all solutions.

4.2.2 Preparation of carbon supported FeTSPc electrodes

Carbon supported FeTSPc catalysts (3% FeTSPc/C and 10% FeTSPc/C) were prepared by depositing FeTSPc on Vulcan carbon black at mass loadings of 3% and 10%. FeTSPc in water (50 mg mL^{-1}) was added to 10 mg of carbon black dispersed in a mixture of 150 µL of H_2O, 75 µL of 2-propanol and 75 µL of 5% Nafion^{TM} solution, and the resulting ink was sonicated for 1 h. The ink was deposited onto a 1.0 cm^2 disc of CFP with a micropipette to give a FeTSPc/C loading of

1.5 mg cm^{-2}, and Nafion loadings of 0.44 and 0.42 mg cm^{-2} for the 3% FeTSPc/C and 10% FeTSPc/C electrodes, respectively.

4.2.3 Electrochemistry

Electrochemical measurements were made in 0.1 M $NaHCO_3$ at ambient temperature in a glass cell with a porous glass frit between the working and counter electrode compartments. A Pt counter electrode and $Hg/HgSO_4$/saturated Na_2SO_4 reference electrode (Koslow; 658 mV vs SHE) were employed. Potentials are reported relative to the appropriate RHE (reversible hydrogen electrode), at -0.464 V vs SHE under N_2 (pH = 8.30) or -0.395 V vs SHE under CO_2 (pH = 6.75).

4.2.4 Product analysis

Ammonia in electrolysis solutions was measured by the salicylate method [21]. Samples (0.5 mL) were mixed with solutions prepared with 5 g of salicylic acid and 5 g of sodium citrate in 100 mL of 1 M NaOH (2 mL), 7 mL of sodium hypochlorite solution (available chlorine 4.00-4.99 %) in 100 mL of water (1 mL), and 1 g of sodium nitroferricyanide in 100 mL of water (0.2 mL), and diluted to 10 mL with water. After 2 h in the dark at ambient temperature for 2 h, the absorbance of each solution was measured at 655 nm against a reagent blank, using an Agilent Cary 100 UV-Vis spectrophotometer. The UV- Vis spectra and calibration plot is shown as Figure B1 in Appendix B.

Urea was measured by the diacetyl monoxime (DAM) method [22, 23]. In order to avoid interference from NO_2^- [23], standards and samples were first deionized with a mixed bed ion exchange resin (AG® 501-X8; Bio-Rad) using a conical 0.8 X 4 cm polypropylene column (Poly-Prep® Chromatography Columns; Bio-Rad). DAM (0.225 mL; 50.0 g L^{-1}), TSC

(0.0375 mL; 2.0 g L^{-1}), $Fe_2(SO_4)_3$ (0.0375 ml; 600 mg L^{-1} in a 5% H_2SO_4) and 50% H_2SO_4 (2 mL) were added sequentially to 2 mL aliquots of the deionized solutions with dilution to a final volume of 5 mL. Following 30 min at 90 ℃, and cooling to ambient temperature, the absorbance of the resulting red compound was measured at 520 nm. The UV-Vis spectra and calibration curve is shown in Figure B2 in Appendix B.

To confirm accuracy [23], urea concentrations were also determined by liquid chromatography-mass spectrometry (LC-MS) [24, 25] using a SCIEX triple TOF^{TM} 5600 mass spectrometer coupled with an Agilent 1100 Series HPLC system with a Poroshell 120 HILIC, 4.6 X 100 mm, 4 µm column (Agilent Technologies) with a KrudKatcher ULTRA HPLC in-line filter (2.0 µm, 0.004 in. ID, Phenomenex). Deionized samples (as described for the DAM method) were diluted with acetonitrile in a 1:9 volume ratio and eluted using a mobile phase of acetonitrile containing 10% HPLC-grade water, 0.5 mM ammonium acetate and 0.2 mM acetic acid, at a flow rate of 0.5 mL min^{-1}. The injection volume was 10 µL and the column temperature was maintained at 30 ℃. A calibration curve (Figure. B3 in Appendix B) was prepared by plotting the integrated peak area of mass 61.03 m/z against the urea standard concentration.

4.3 Results and discussion

4.3.1 Coreduction of NO_2^- and CO_2 at FeTSPc/C electrodes

Figure 4.1 shows cyclic voltammograms of electrodes prepared with the 10% FeTSPc/C catalyst in 0.1 M $NaHCO_3$ with and without 5 mM $NaNO_2$, under N_2 and CO_2. Under N_2 in the absence of $NaNO_2$, three main redox waves are observed at formal potentials of +0.92 V ($\Delta E_p = 0.07$ V) for the Fe(+3/+2), and +0.06 V ($\Delta E_p = 0.02$ V) and -0.11 ($\Delta E_p = 0.15$ V) for the Fe(+2/+1)/TSPc(-2/-3) couples, which cannot be unambiguously assigned [26]. Addition of

$NaNO_2$ (under N_2) did not influence the Fe(+3/+2) wave significantly, but resulted in an enhanced cathodic peak at ca. +0.0 V due to the reduction of NO_2^-. The proximity of this peak to the wave at +0.06 V strongly suggests that the process is catalyzed by the Fe(+1) state, although there is likely involvement of the TSPc(-3) state [26].

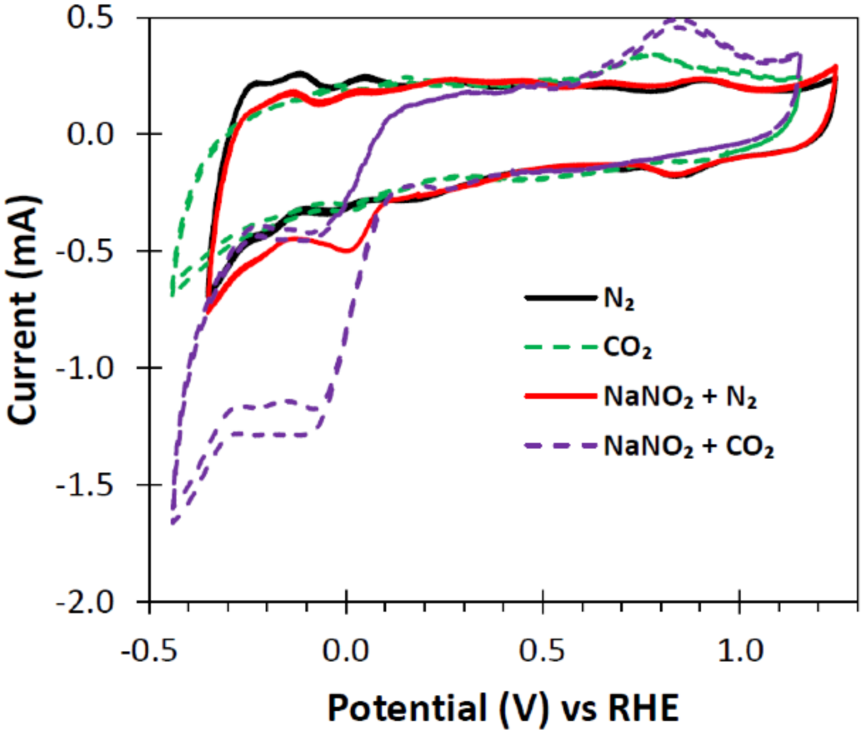

Figure 4.1. Cyclic voltammograms (10 mV s^{-1}) for 10% FeTSPc/C electrodes in 0.1 M $NaHCO_3$ with and without 5 mM $NaNO_2$ under N_2 and CO_2.

Under CO_2, in the absence of NO_2^-, the waves for all three couples became indistinct and shifted to higher potentials, presumably due to the decrease in pH from 8.30 to 6.75 due to the formation of H_2CO_3. An irreversible oxidation peak appeared at +0.78 V on the reverse scan, indicating that an oxidizable species was formed at low potentials, although there was no enhancement of the cathodic current to suggest that there was significant reduction of CO_2.

In the presence of both NO_2^- and CO_2, a large increase in the cathodic wave was observed with an onset potential of ca. +0.08 V. The cathodic peak at -0.075 V was more than 2.5 times higher than the peak observed at 0 V for NO_2^- reduction. This indicates that there was substantial coreduction of NO_2^- and CO_2 in addition to their individual reduction processes. Shibata and Furuya have reported that, in addition to CO and NH_3 (eqs. 4.1 and 4.2), there is a significant amount of urea produced from the coreduction of NO_2^- and CO_2 (eq. 4.3) at metallophthalocyanine catalysts [12].

$$CO_2\,(g) + 2e^- + 2H^+(aq) \longrightarrow CO\,(g) + H_2O \tag{4.1}$$

$$NO_2^-(aq) + 6e^- + 7H^+(aq) \longrightarrow NH_3\,(aq) + 2H_2O \tag{4.2}$$

$$CO_2\,(g) + 2NO_2^-(aq) + 12e^- + 14H^+(aq) \longrightarrow NH_2CONH_2\,(aq) + 5H_2O \tag{4.3}$$

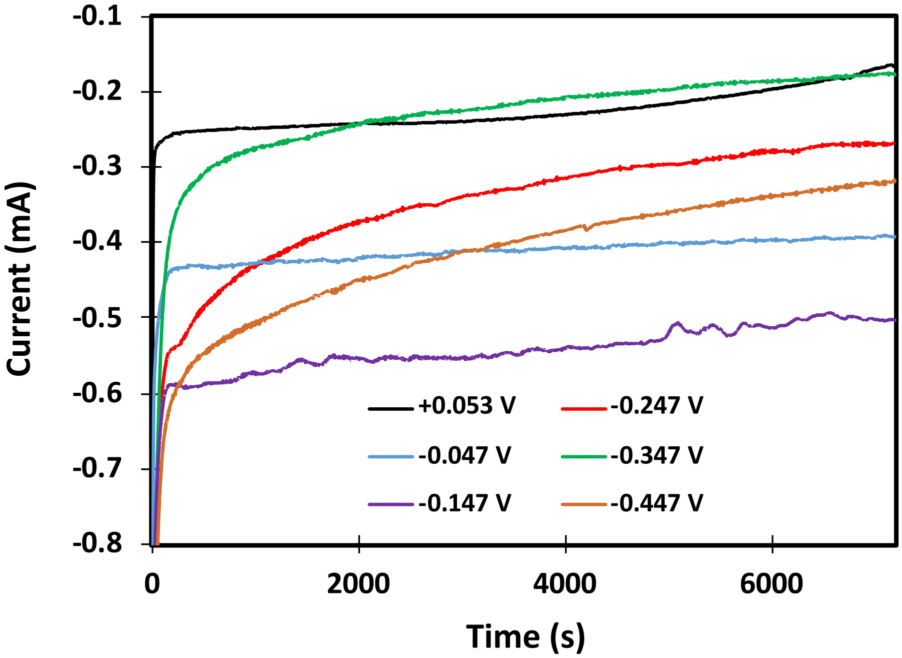

Figure 4.2. Current vs time at various potentials (vs RHE) for electrolysis of 5 mM $NaNO_2$ under CO_2 in 0.1 M $NaHCO_3$ at 3% FeTSPc/C electrodes.

In order to measure NH_3 and urea production, electrolysis of 5 mM $NaNO_2$ under CO_2 was performed in 0.1 M $NaHCO_3$ at various constant potentials, using the 3% FeTSPc/C catalyst. Figure 4.2 shows the current vs time data. It can be seen that during electrolysis, the current was quite steady at potentials ≥ -0.147 V while it decayed over time at lower potentials. The highest average current of -0.55 mA was observed at -0.147 V, which corresponds approximately to the peak seen at -0.075 V in cyclic voltammetry.

Table 4.1. Average currents, and concentrations and rates of urea and ammonia production for electrolysis of 5 mM NaNO in 0.1 M $NaHCO_3$ under CO_2 at 3% FeTSPc/C electrodes for 2 h.

Potential vs RHE (V)	**Average current (mA)**	**Urea concentration (µM)**		**NH_3 concentration (µM)**	**Production rate (µM h^{-1})**		**Urea: NH_3 mol ratio**
		DAM	**LC-MS**	**Salicylate**	**Urea**	**NH_3**	
+0.053	-0.228	50.0	51.3	47.9	0.381	0.359	1.06
-0.047	-0.415	40.3	39.3	107	0.310	0.803	0.37
-0.147	-0.547	37.8	36.9	185	0.281	1.39	0.20
-0.247	-0.353	34.8	35.2	174	0.263	1.31	0.20
-0.347	-0.237	31.0	31.1	91.4	0.233	0.686	0.34
-0.447	-0.422	28.2	28.0	88.1	0.211	0.661	0.32

Urea and ammonia production during electrolysis was measured using the DAM (UV-Vis spectra in Figure B4 in Appendix B) and salicylate methods (UV-Vis spectra in Figure B5 in Appendix B), respectively. Additionally, LC-MS was used to verify the urea concentrations

(LC-MS spectra Figure B6 in Appendix B), since the DAM method can be unreliable [23]. The results are shown in Table 4.1. Urea concentrations from the DAM and LC-MS methods were averaged for calculation of urea production rates and faradaic efficiencies.

The maximum amount of urea (50.7 µM) was produced at +0.053 V and there was a gradual decrease in urea production as the potential was decreased (increasing overpotential). NH_3 production initially increased as the potential was decreased, to a peak at -0.147 V, and then decreased. The maximum rate of urea production (0.381 µM h^{-1}) also occurred at +0.053 V, while the maximum rate for NH_3 (1.39 µM h^{-1}) occurred at -0.147 V.

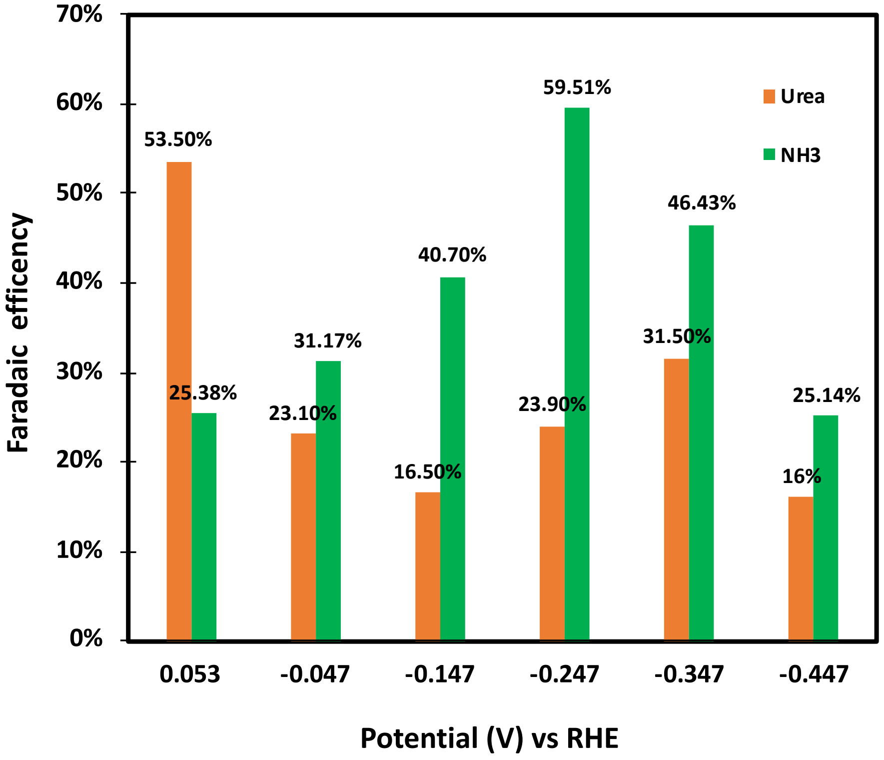

Figure 4.3. Faradaic efficiencies for NH_3 and urea production, calculated from the data in Table 4.1.

Figure 4.3 shows faradaic efficiencies for production of urea and NH_3. The maximum faradaic efficiency for urea (53.6%) was observed at 0.053 V, and 79% of the charge passed produced urea or NH_3 (25.4%) at this potential. As the potential was decrease, the yield of urea decreased and then increased to a peak at -0.347 V. In contrast the faradaic efficiency for NH_3 increased to a peak of 59.5% at -0.247 V as the potential was decreased, and then decreased. The resulting decrease in the urea:NH_3 mole ratio (Table 4.1), shows that the high currents seen in cyclic voltammetry at potentials below ca. 0 V were due to enhanced reduction of NO_2^- rather than coreduction of CO_2 to produce urea. This is presumably due to the lower pH when CO_2 is present.

Table 4.2. Average currents, potentials, and concentrations of urea (DAM method) for electrolysis of 5 mM $NaNO_2$ in 0.1 M $NaHCO_3$ under N_2 and CO_2 in control experiments.

Electrode	**Potential (V) vs RHE**	**Average current (mA)**	**Urea concentration (μM)**
FeTSPc/C (under CO_2)	OCP	0.0	0.0
FeTSPc/C (under N_2)	0.053	-0.03	1.0
Blank (carbon black) (under CO_2)	0.053	-0.004	0.0
	-0.447	-0.12	2.5

Control experiments were performed to determine whether there were other sources of urea, such as contamination and electrochemistry at the carbon support materials (carbon black and carbon fiber paper). Table 4.2 shows the concentrations of urea measured at the open circuit potential (OCP), and in the absence of CO_2 or FeTSPc. No urea was detected following 2 h at OCP in 0.1 M $NaHCO_3$ containing 5 mM $NaNO_2$ under CO_2, demonstrating that urea contamination was negligible. However, 1.0 μM urea was detected following electrolysis at +0.053 V in the absence of CO_2 (i.e. under N_2), indicating that coreduction of the $NaHCO_3$ electrolyte with NO_2^- produces small amounts of urea. No urea was detected at +0.053 V in the absence of the FeTSPc catalyst, indicating that the carbon support materials (CB and CFP) did not produce urea at this potential. However, significant urea production (2.5 µM) was observed at -0.447 V, corresponding to 8.9% of the amount measured in the presence of the FeTSPc catalyst.

4.3.2 Effect of FeTSPc loading and electrode stability

The 10% FeTSPc/C catalyst was used to increase the urea formation rate and also used to evaluate stability. Figure 4.4 shows 30 potential cycles for a 10% FeTSPc/C electrode in 0.1 M $NaHCO_3$ under N_2. The stability of the electrodes was good, with only gradual changes in the large background current due to the carbon support. Notably, the wave for the Fe(+3/+2) couple at +0.92 V was stable, indicating that there was not electrochemically significant leaching of the FeTSPc. However, a slight blue coloration of the electrolyte showed that there was some loss of the catalyst.

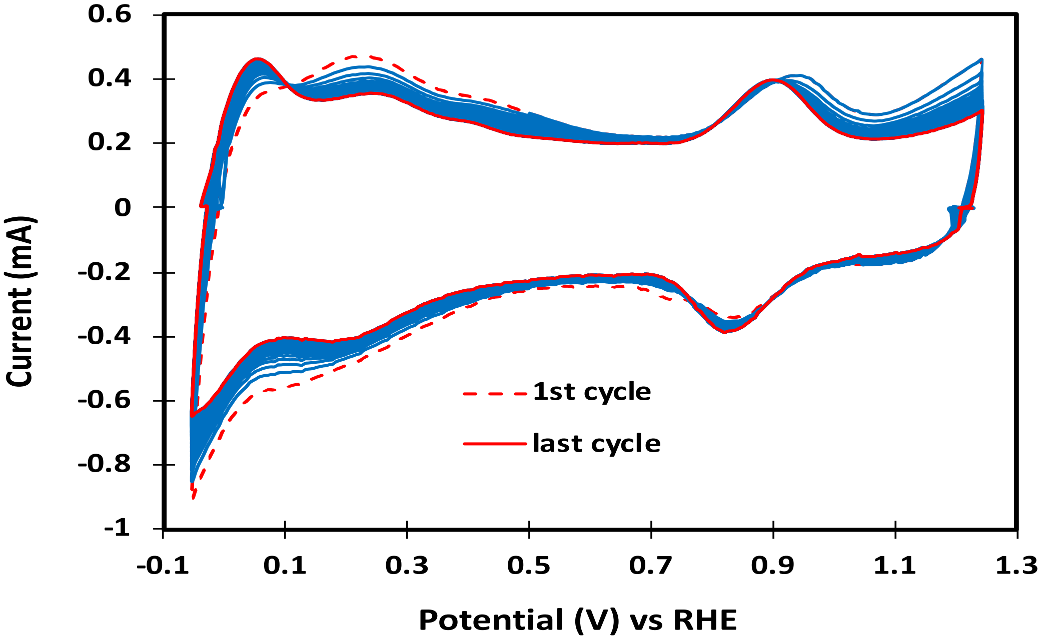

Figure 4.4. Cyclic voltammograms (30 cycles at 10 mV s^{-1}) for a 10% FeTSPc/C electrode in 0.1 M $NaHCO_3$ under N_2.

Figure 4.5 shows current vs time curves for two consecutive 2 h electrolyses of NO_2^- under CO_2 at 0.053 V, and Table 4.3 shows the average current, and concentrations, faradaic efficiencies, and production rates of urea and ammonia. Comparison with the data in Table 4.1 shows that increasing the FeTSPc loading from 3% to 10% increased the average current by 123% and also increased urea and ammonia production. It is worth noting that the rate of urea production increased by 120 % (to 0.86 μmol h^{-1}) without a significant decrease (~1%) in the faradaic efficiency. The average current during the second electrolysis (i.e. for the same electrode with fresh electrolyte) was 6.3% lower than in the first, and there was a decrease in the yield of urea from 52.6% to 47.7%, suggesting that there was some instability of the electrode.

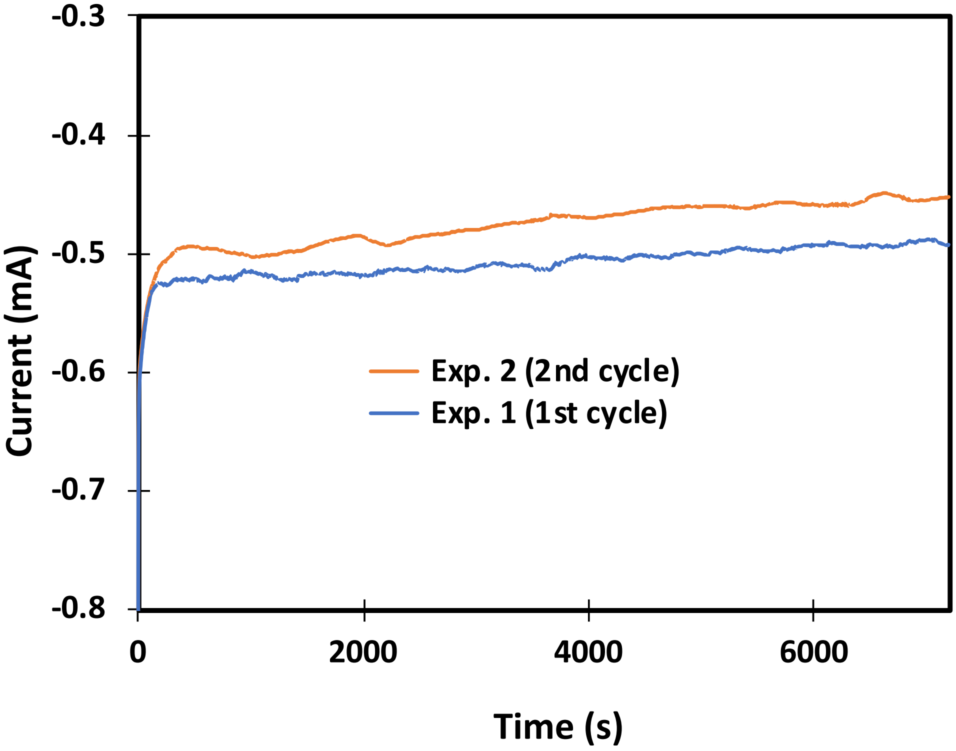

Figure 4.5. Current vs time curves at 0.053 V for electrolysis of 5 mM $NaNO_2$ under CO_2 in 0.1 M $NaHCO_3$ at a 10% FeTSPc/C electrode.

Table 4.3. Average currents, concentrations, faradaic efficiencies, and production rates of urea and ammonia for electrolysis of 5 mM $NaNO_2$ in 0.1 M $NaHCO_3$ under CO_2 at a 10% FeTSPc/C electrode for 2 h.

Sample ID	Average current (mA)	Urea concentration (μM)		NH_3 concentration (μM)	Faradaic efficiency		Production rate (μM h^{-1})	
		DAM	Salicylate		Urea	NH_3	Urea	NH_3
1st electrolysis	-0.509	114	112	90	52.6%	21.3%	0.857	0.68
2nd electrolysis	-0.477	106	100	85	47.7%	22.0%	0.790	0.64

Cyclic voltammograms recorded before electrolysis and after 2 h and 4 h of electrolysis at +0.053 V (Figure 4.6), show that the reduction current at potentials below -1.0 V increased notably after the first electrolysis, and that the activity of the electrode was still higher than the initial activity after the second electrolysis. These results indicate that the 10% FeTSPc electrode was quite durable for an extended period of electrolysis. However, blue coloration of the electrolyte during the first electrolysis indicated that there was some loss of FeTSPc from the electrode. Quantification of the FeTSPc in the electrolyte by electronic absorption spectrometry after each electrolysis revealed that there was a 14% loss of FeTSPc from the electrode during the 1st electrolysis. However, no FeTSPc was detected in the electrolyte after the 2nd electrolysis, indicating that the remaining FeTSPc was strongly bound or adsorbed. This implies that the electrodes should be stable for longer term use, once loosely bound, excess FeTSPc has been lost.

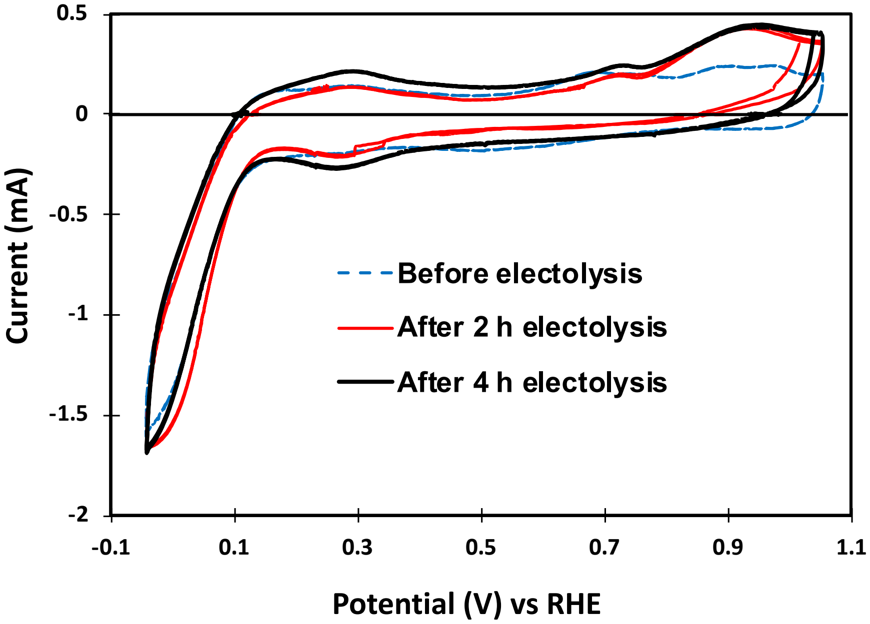

Figure 4.6. Cyclic voltammograms (10 mV s^{-1}) before, and after 2 and 4 h of electrolysis at a 10% FeTSPc/C electrode in 0.1 M $NaHCO_3$ containing 5 mM $NaNO_2$ under CO_2.

4.4.3 Discussion

The maximum faradaic yield of urea reported here, of 53.6% at +0.053 V vs RHE, is more than double the yield of ca. 25% at -0.75 V vs RHE reported by Shibata and Furuya for unsubstituted Fe phthalocyanine (FePc) [12], and was obtained at a much lower overpotential. These differences presumably arise in part from the effects of the hydrophilic and electron withdrawing sulfonyl substituents on solubility and the electronic structure of the Fe center and Pc π system [18]. Shibata and Furuya demonstrated that the yields of urea obtained with MPc catalysts depend on their efficiencies for reduction to both CO_2 to CO, and NO_2^- to NH_3 [12]. Their proposal that urea was formed by coupling of asdorbed –CO and –NH_2 species (Langmuir−Hinshelwood mechanism) [27] has received wide acceptance in more recent work on other types of catalysts [5, 11, 16].

Phthalocyanine complexes are well known for their ability of catalyze the reduction of CO_2 to CO [18], can reduce NO_2^- to NH_3 [12], and have two free axial sites for binding –CO and $-NH_2$ intermediates. However, coupling of −CO and $-NH_2$ species would require separate PcM−CO and PcM−NH_2 species in a cofacial arrangement. The solubility of FeTSPc would increase the probability of this occuring, relative to FePc adsorbed on a carbon surface. Alternatively, one of the adsorbed −CO or $-NH_2$ species could form on the carbon black support [28]. The observation in Table 4.2 that urea was formed in the absence of FeTSPc indicates that both urea precursors can be formed on the carbon support. In addition, urea formation could occur at a single Fe site by reaction of a Fe−NH_2 species with CO_2 (Eley−Rideal mechanism) [27].

Under the conditions employed here, the sulfonyl substituents shift the formal potential for the Fe(3+/2+) couple from +0.89 V for FePc (Figure B7 in Appendix B) to +0.92 V, while the second reduction wave shifts from 0 V to +0.06 V. Since the second reduction is responsible for urea production, the high activity and efficiency provided by FeTSPc can be attributed in part to the electron withdrawing effect of the sulfonyl substituents. In addition, the hydrophilicity of FeTSPc would make it more mobile within the catalyst layer than FePc, and increase the probability and rate for formation of adjacent −CO and $-NH_2$ species. However, this can also increase diffusion into the bulk solution and require methods for confinement or tethering of the FeTSPc catalyst.

4.3 Conclusions

Carbon supported FeTSPc is a highly active catalyst for NO_2^- and CO_2 coreduction to produce urea at high potentials (low overpotentials). The 53.6% faradaic yield of urea at +0.053 V vs RHE is comparable to the highest yield that has been reported (ca. 55% for a Cd catalyst at

-1.0 V vs RHE [10]), and the highest potential at which urea formation has been observed. Although some initial leaching of the water soluble FeTSPc catalyst was observed, high electrochemical activity and urea production was maintained, and longer term stability was good. However, further work on electrode design and composition is needed to improve the rate of urea production and ensure durability.

4.4 References

1. Kim, J. E., Choi, S., Balamurugan, M., Jang, J. H., & Nam, K. T. (2020). Electrochemical C-N bond formation for sustainable amine synthesis. Trends in Chemistry, 2, 1004-1019.
2. Tang, C., Zheng, Y., Jaroniec, M., & Qiao, S. Z. (2021). Electrocatalytic refinery for sustainable production of fuels and chemicals. Angewandte Chemie International Edition, 60, 19572-19590.
3. Driver, J. G., Owen, R. E., Makanyire, T., Lake, J. A., McGregor, J., & Styring, P. (2019). Blue urea: Fertilizer with reduced environmental impact. Frontiers in Energy Research, 7, 88.
4. Tao, Z., Rooney, C. L., Liang, Y., & Wang, H. (2021). Accessing organonitrogen compounds via C-N coupling in electrocatalytic CO_2 reduction. Journal of American Chemical Society, 143, 19630-19642.
5. Fu, J., Yang, Y., & Hu, J. S. (2021). Dual-sites tandem catalysts for C-N bond formation via electrocatalytic coupling of CO_2 and nitrogenous small molecules. ACS Materials Letters, 3, 1468-1476.

6. Mei, Z., Zhou, Y., Lv, W., Tong, S., Yang, X., Chen, L., & Zhang, N. (2022). Recent progress in electrocatalytic urea synthesis under ambient conditions. ACS Sustainable Chemistry & Engineering, 10, 12477-12496.

7. Liang, J., Liu, Q., Alshehri, A. A., & Sun, X. (2022). Recent advances in nanostructured heterogeneous catalysts for N-cycle electrocatalysis. Nano Research Energy, 1, e9120010.

8. Zhang, X., Wang, Y., Wang, Y., Guo, Y., Xie, X., Yu, Y., & Zhang, B. (2022). Recent advances in electrocatalytic nitrite reduction. Chemical Communications, 58, 2777-2787.

9. Amanullah, S., Saha, P., Nayek, A., Ahmed, M. E., & Dey, A. (2021). Biochemical and artificial pathways for the reduction of carbon dioxide, nitrite and the competing proton reduction: effect of 2nd sphere interactions in catalysis. Chemical Society Reviews, 50, 3755-3823.

10. Shibata, M., Yoshida, K., & Furuya, N. (1998). Electrochemical synthesis of urea at gas-diffusion electrodes: III. Simultaneous reduction of carbon dioxide and nitrite ions with various metal catalysts. Journal of Electrochemical Society, 145, 595.

11. Liu, S., Yin, S., Wang, Z., Xu, Y., Li, X., Wang, L., & Wang, H. (2022). AuCu nanofibers for electrosynthesis of urea from carbon dioxide and nitrite. Cell Reports Physical Science, 3, 100869.

12. Shibata, M., & Furuya, N. (2001). Electrochemical synthesis of urea at gas-diffusion electrodes: Part VI. Simultaneous reduction of carbon dioxide and nitrite ions with various metallophthalocyanine catalysts. Journal of Electroanalytical Chemistry, 507, 177-184.

13. Siva, P., Prabu, P., Selvam, M., Karthik, S., & Rajendran, V. (2017). Electrocatalytic conversion of carbon dioxide to urea on nano-$FeTiO_3$ surface. Ionics, 23, 1871-1878.

14. Cao, N., Quan, Y., Guan, A., Yang, C., Ji, Y., Zhang, L., & Zheng, G. (2020). Oxygen vacancies enhanced cooperative electrocatalytic reduction of carbon dioxide and nitrite ions to urea. Journal of Colloid and Interface Science, 577, 109-114.

15. Feng, Y., Yang, H., Zhang, Y., Huang, X., Li, L., Cheng, T., & Shao, Q. (2020). Te-doped Pd nanocrystal for electrochemical urea production by efficiently coupling carbon dioxide reduction with nitrite reduction. Nano Letters, 20, 8282-8289.

16. Meng, N., Huang, Y., Liu, Y., Yu, Y., & Zhang, B. (2021). Electrosynthesis of urea from nitrite and CO_2 over oxygen vacancy-rich ZnO porous nanosheets. Cell Reports Physical Science, 2, 100378.

17. Zagal, J. H., Griveau, S., Silva, J. F., Nyokong, T., & Bedioui, F. (2010). Metallophthalocyanine-based molecular materials as catalysts for electrochemical reactions. Coordination Chemistry Reviews, 254, 2755-2791.

18. Yang, S., Yu, Y., Gao, X., Zhang, Z., & Wang, F. (2021). Recent advances in electrocatalysis with phthalocyanines. Chemical Society Reviews, 50, 12985-13011.

19. Manbeck, G. F., & Fujita, E. (2015). A review of iron and cobalt porphyrins, phthalocyanines and related complexes for electrochemical and photochemical reduction of carbon dioxide. Journal of Porphyrins and Phthalocyanines, 19, 45-64.

20. Kudrik, E. V., Makarov, S. V., Zahl, A., & Van Eldik, R. (2003). Kinetics and mechanism of the cobalt phthalocyanine catalyzed reduction of nitrite and nitrate by dithionite in aqueous solution. Inorganic Chemistry, 42, 618-624.

21. Li, L., Tang, C., Xia, B., Jin, H., Zheng, Y., & Qiao, S. Z. (2019). Two-dimensional mosaic bismuth nanosheets for highly selective ambient electrocatalytic nitrogen reduction. ACS Catalysis, 9, 2902-2908.

22. Chen, L., Ma, J., Huang, Y., Dai, M., & Li, X. (2015). Optimization of a colorimetric method to determine trace urea in seawater. Limnology and Oceanography: Methods, 13, 303-311.

23. Li, D., Xu, N., Zhao, Y., Zhou, C., Zhang, L. P., Wu, L. Z., & Zhang, T. (2022). A reliable and precise protocol for urea quantification in photo/electrocatalysis. Small Methods, 6, 2200561.

24. Krämer, M., Fry, H., & Kappenstein, O. (2021). Development and validation of two analytical methods for urea determination in compound feed, including pet food, and yeast using high-performance liquid chromatography coupled with fluorescence detection and tandem mass spectrometry. Food Additives & Contaminants: Part A, 38, 931-942.

25. Pitiranggon, M., Perzanowski, M. S., Kinney, P. L., Xu, D., Chillrud, S. N., & Yan, B. (2014). Determining urea levels in exhaled breath condensate with minimal preparation steps and classic LC-MS. Journal of Chromatographic Science, 52, 1026-1032.

26. Alsudairi, A., Li, J., Ramaswamy, N., Mukerjee, S., Abraham, K. M., & Jia, Q. (2017). Resolving the iron phthalocyanine redox transitions for ORR catalysis in aqueous media. Journal of Physical Chemistry Letters, 8, 2881-2886.

27. Yang, G. L., Hsieh, C. T., Ho, Y. S., Kuo, T. C., Kwon, Y., Lu, Q., & Cheng, M. J. (2022). Gaseous CO_2 coupling with N-containing intermediates for key C-N bond

formation during urea production from coelectrolysis over Cu. ACS Catalysis, 12, 11494-11504.

28. Liu, X., Kumar, P. V., Chen, Q., Zhao, L., Ye, F., Ma, X., & Hu, C. (2022). Carbon nanotubes with fluorine-rich surface as metal-free electrocatalyst for effective synthesis of urea from nitrate and CO_2. Applied Catalysis B: Environmental, 316, 121618.

Chapter 5

Electrochemical synthesis of urea and ammonia in a proton-exchange membrane (PEM) electrolysis cell under ambient conditions.

Abtract:

The performance of a proton-exchange membrane (PEM) electrolysis cell was examined to investigate its potential for the coreduction of CO_2 and nitrite (and N_2) to produce urea. In this study, carbon-supported iron(II) phthalocyanine (FePc/C) and carbon-supported MoS_2 (MoS_2/C) catalysts were employed. The electrocatalytic activity of these catalysts for the co-reduction of CO_2 and nitrite (and N_2) was assessed using cyclic voltammetry and chronoamperometry techniques. The results revealed a significant enhancement in the faradaic efficiency of urea production, rising from 2.8% to 15.9% (~ -0.4 V), with the utilization of the FePc/C catalyst for the co-reduction of CO_2 and nitrite, compared to a conventional cell, even when a lower concentration of NO_2^- solution was employed. However, it was observed that MoS_2/C was unable to generate urea in H_2O through the co-reduction of CO_2 and N_2. Furthermore, the influence of different aqueous electrolytes on the electrochemistry of CO_2 and N_2 in the PEM cell was investigated. Dilute acetic acid, $NaHCO_3$, and sulfuric acid electrolytes were used for this purpose. It was found that the use of $NaHCO_3$ as an electrolyte resulted in a gradual deterioration in cell performance over time.

The principal author (Jasmeen Akther) contributed to all aspects of the project as the main researcher including literature review, performing all of the experiments, collecting, analyzing, presenting the data.

Prof. Peter G. Pickup was the principal investigator and provided the initial ideas for this project. He mentored the principal author (Jasmeen Akther) and supported her during the project. He reviewed all data analysis.

The raw data is provided in Appendix C.

5.1 Introduction

Converting greenhouse gas such as CO_2 and agricultural waste like NO_2^- to value-added products is a promising approach to counteract their negative impact on the environment and human health [1,2]. Compared to conventional thermochemical approaches, direct electrochemical controlled reactions are more targeted, economical in terms of energy consumption, and environmentally friendly [3]. These reactions can utilize sustainable energy sources such as wind, solar power, and fuel cells, as well as non-toxic and safe electrolytes. This leads to a reduction in greenhouse gas emissions and waste generation while also promoting a carbon-negative economy.

Co-electrolysis of CO_2 and various N-sources such as N_2, NO_2^-, NO_3^- and NO to convert them into commodity chemicals like ammonia and urea, is a desirable process [4-9]. However, this process poses a number of challenges, including the need for a highly efficient catalyst, accurate product quantification, and proper electrolysis cell configuration. Currently, there is no standard cell configuration for this application and most researchers customize their cells based on the research objectives. However, H-type cells are most commonly used, despite their low current density due to the low solubility of reagent gases [10, 11]. This type of cell is widely used because it is readily available off-the-shelf.

Several research groups have demonstrated that a flow cell system could improve current density and yield rate compared to conventional electrolysis cells [12, 13]. This is because the continuous supply of gas and liquid feeds at the electrocatalyst surface in a flow cell enhances mass transport efficiency. Additionally, the direct contact of the polymer electrolyte membrane with the catalyst surface and the use of appropriate electrocatalyst substrates all have an impact on the thermodynamics and kinetics of the reaction in a flow system [14]. However, for an ideal cell, it should be capable of producing high current density with efficient mass transport and low resistance, making it suitable for industrial applications without requiring further modification. Therefore, further research is necessary to optimize a more efficient cell design to address the challenges faced by conventional cells and improve current density and yield rate.

This chapter outlines an experimental method that utilizes a customized electrochemical cell with a solid electrolyte (Nafion) to address the common experimental challenges faced in conventional electrochemical cells. This method is suitable for conducting laboratory-scale experiments aimed to characterize catalyst performance as well as has the potential for use in industrial applications.

Using this customized cell, we investigated the performance of carbon-supported iron(II)phthalocyanine (FePc/C) in the coreduction of CO_2 in a low concentration of NO_2^- solution and compared its performance with conventional electrolysis. Additionally, we investigated the performance of a carbon-supported MoS_2 catalyst (MoS_2/C) in the coreduction of CO_2 and N_2 in an attempt to produce urea. We also investigated the effect of the electrolyte and flow conditions of reagent gases on the production of urea from the coreduction of N_2 and CO_2. The findings of our investigation will provide valuable insights for the development of advanced electrochemical cells to produce urea that can be utilized in both laboratory and industrial settings.

5.2 Experimental

5.2.1 Electrochemical cell setup

A proton-exchange membrane (PEM) electrolysis cell was used to conduct cyclic voltammetry (CV) and constant potential experiments using an EG&G model 273A Potentiostat/Galvanostat. The electrolysis cell is based on a commercial (ElectroChem Inc.) PEM fuel cell graphite plate flow field and hardware for the anode, and a Bakelite plate with embedded graphite rod current collectors and a similar flow field for the cathode [15]. The cathode and anode of the cell were arranged parallel to each other to maintain a uniform voltage, and a Nafion™ 117 membrane was used to separate the cathode and anode chambers. This allowed for the flow of ions while preventing the oxidation of reduced products. The cell had small volume capacity for both cathode and anode chambers and could be operated either as a multi-cathode cell with nine 0.24 cm^2 cathodes or with a single large 5 cm^2 cathode.

The cathodes were prepared by depositing catalyst ink on carbon fiber paper (CFP) discs aiming for a target catalyst loading of 1.5 mg cm^{-2}. The catalyst ink was prepared by mixing 150 μL of H_2O, 75 μL of 2-propanol, and 75 μL of 5% Nafion™ solution. A 5 cm^2 commercial Pt black anodes was used. Membrane electrode assemblies (MEAs) were prepared by pressing an anode and a cathode onto each side of a Nafion™ 117 membrane with a pressure of 1.5 MPa at ambient temperature.

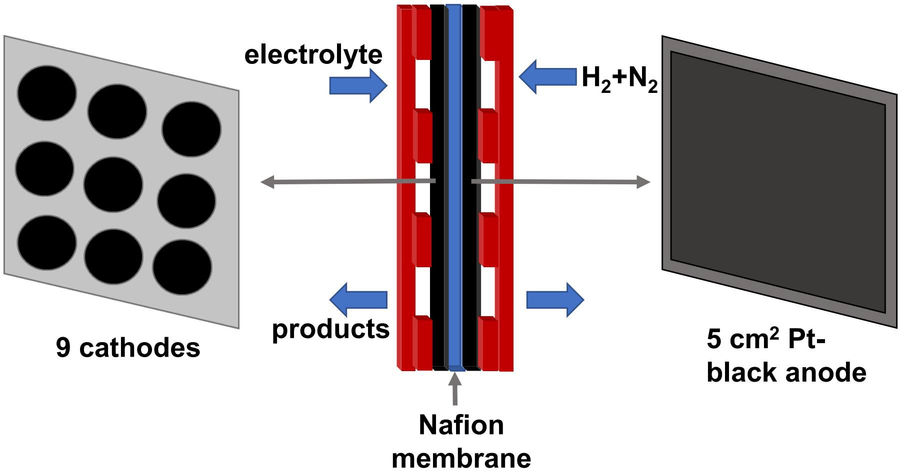

Figure 5.1: Schematic of a PEM electrolysis cell.

An electrolyte (or DI water) saturated with N_2, CO_2, or a N_2 + CO_2 mixture was pumped into the cathode flow field with a NE300 New Era Pump Systems syringe pump at a flow rate of

0.1 mL min^{-1}, while the anode was purged with 5% H_2 in N_2 at a flow rate of 4 mL min^{-1} as shown in Figure 5.1. Under these conditions, the anode functions as a counter electrode as well as a reference electrode (Dynamic hydrogen electrode) and provides a relatively stable reference potential. The small distance between the cathode and anode (as a reference electrode) in the cell reduces the uncompensated resistance (R_u).

5.3 Results and discussion

5.3.1 Coreduction of CO_2 and 1 mM $NaNO_2$ at carbon-supported iron(II)phthalocyanine (FePc/C) electrode in a PEM cell

The carbon supported FePc (FePc/C) catalyst was prepared based on our previous work, as reported in Chapter 3. The membrane electrode assemblies (MEAs) of the cell were prepared following the procedure described in Section 5.2.1. After assembling the cell, cyclic voltammograms (CVs) were performed using a 5 cm^2 FePc/C electrode in H_2O and 1 mM $NaNO_2$ under N_2 and CO_2 before electrolysis. Prior to performing the CVs, the cell cathode was flushed with H_2O for at least 10 min. Figure 5.2 displays the CVs obtained at the FePc/C electrode in H_2O with and without 1mM $NaNO_2$ under N_2 and CO_2. In the absence of 1mM $NaNO_2$, the CVs in H_2O under N_2 and CO_2 displayed comparable shapes with no distinct redox waves detected for the Fe(+3/+2) and Pc(-2/-3) couples of the FePc/C catalyst. However, when compared to N_2, a slightly enhanced cathodic current was observed in the potential region of ca. -0.1 to -0.6 V under CO_2. This increased current may be attributed to the reduction of CO_2 [16].

In the presence of 1mM $NaNO_2$ under N_2, the shape of the voltammogram exhibited a slightly distinct shape compared to that without $NaNO_2$ under N_2. Quasi-reversible redox waves were observed at the formal potential of -0.18 V for Fe(+3/+2) [16, 17] and an irreversible wave with a peak potential (E_P) of 0.7 V due to the NO_2^- reduction. When both NO_2^- and CO_2 were present, an increased cathodic current was observed with an onset potential of ca. -0.35 V. The cathodic current at -1.0 V was more than twice as high as the current observed for individual NO_2^- reduction at this potential. This result suggests a reasonable coreduction of NO_2^- and CO_2, in addition to their individual reduction processes [16, 7].

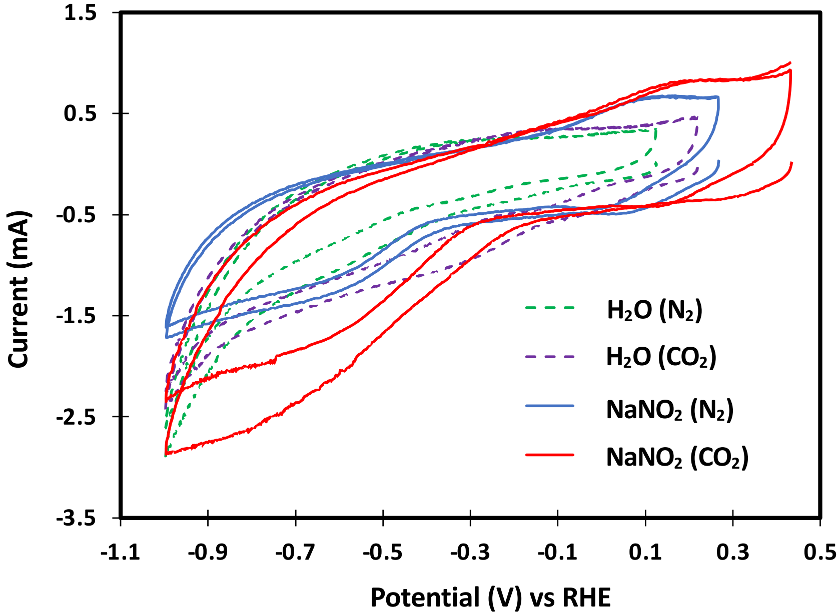

Figure 5.2. Cyclic voltammograms (10 mV s^{-1}) for a 5 cm^2 FePc/C electrode in H_2O and 1 mM $NaNO_2$ under N_2 and CO_2.

A series of constant potential experiments (electrolysis) were performed at a 5 cm^2 FePc/C electrode to investigate whether urea can be produced from the co-reduction of $NaNO_2$ (1 mM) with CO_2. The cathode solution was collected in a sealed vial for chemical analysis. These electrolyses were carried out by reusing the 5 cm^2 FePc/C electrode used for the CVs in Figure 5.2.

The current vs time profiles (electrolysis curves) are presented in Figure 5.3. It can be observed that the current remained relatively stable throughout each electrolysis, with only small changes in the average current (Table 5.1) as the potential was changed (a range of -0.12 to -0.50 mA). The highest average current of -0.50 mA was observed at -0.5 V and the lowest average current was -0.12 mA at -0.4 V. However, at -0.4 V, the electrolysis curve became somewhat noisy, which could be due to formation of gas bubbles on the electrode surface, which cover areas of the electrode until they grow large enough to be released, causing fluctuations in the current [15].

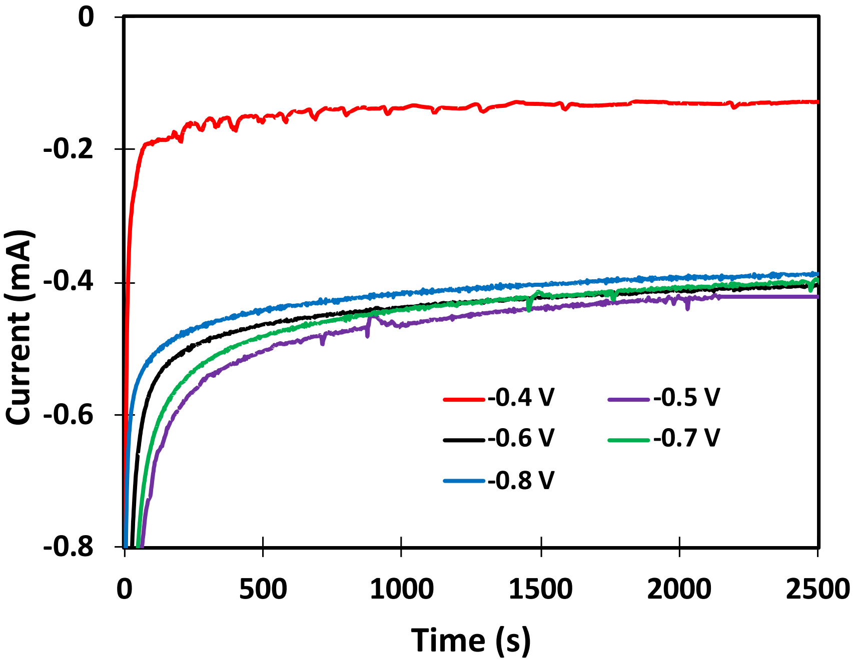

Figure 5.3. Current vs time at various constant potentials at FePc/C electrode for electrolysis of 1 mM $NaNO_2$ and CO_2.

The ammonia and urea produced during these electrolyses were analyzed using DAM, LC-MS, and salicylate methods based on our previous work, as described in Chapter 3 [16]. UV-Vis and LC-MS spectra for the urea and ammonia measurements are provided in Appendix-C (Figure. C1-C3)

Table 5.1 presents the average current and concentrations of urea and ammonia measured at various potentials using the 5 cm^2 FePc/C electrode. The analysis results show that the maximum urea (12.72 μM) was produced at -0.5 V vs RHE. Initially, urea production increased as the potential was decreased from -0.4 V, reaching a peak at -0.5 V, then decreased again. On the other hand, the maximum NH_3 (27 μM) was produced at -0.4 V and decreased as the potential was decreased further, then increased at -0.6 V and -0.7 V before decreasing once more.

Table 5.1. Average currents and concentrations of urea and ammonia for electrolysis of 1 mM $NaNO_2$ and CO_2 at FePc/C electrode at a flow rate of 0.1 mL min^{-1}.

Potential vs RHE (V)	Average current (mA)	Urea concentration (μM)		NH_3 concentration (μM)
		DAM	LC-MS	Salicylate
-0.4	-0.12	9.8	10.1	27
-0.5	-0.50	12.8	12.6	24
-0.6	-0.45	11.4	11.6	25
-0.7	-0.45	10.8	10.3	26
-0.8	-0.41	9.4	9.4	24

Figure 5.4 shows faradaic efficiencies for the production of urea and NH_3. The maximum faradaic efficiency for urea (15.9%) was observed at -0.4 V, and at this potential, 37.5% of the charge passed produced urea or NH_3. This represents a six-times improvement over the maximum faradaic efficiency of urea (2.8%) observed in a conventional cell at -0.44 V vs RHE, as reported

in Chapter 3 [16]. While the faradaic efficiency of urea decreased below 15.9% as the potential decreased, it remained comparable across all potentials. Similarly, the maximum faradaic efficiency for NH_3 (21.6%) was also observed at -0.4 V, although the current density at this potential was observed to be very low. As the potential was decreased, the faradaic efficiency of NH_3 decreased but remained similar across all potentials, similar to urea. Notably, the ratio of faradaic efficiencies for urea and NH_3 remained similar for all applied potentials at approximately a 1:1 ratio.

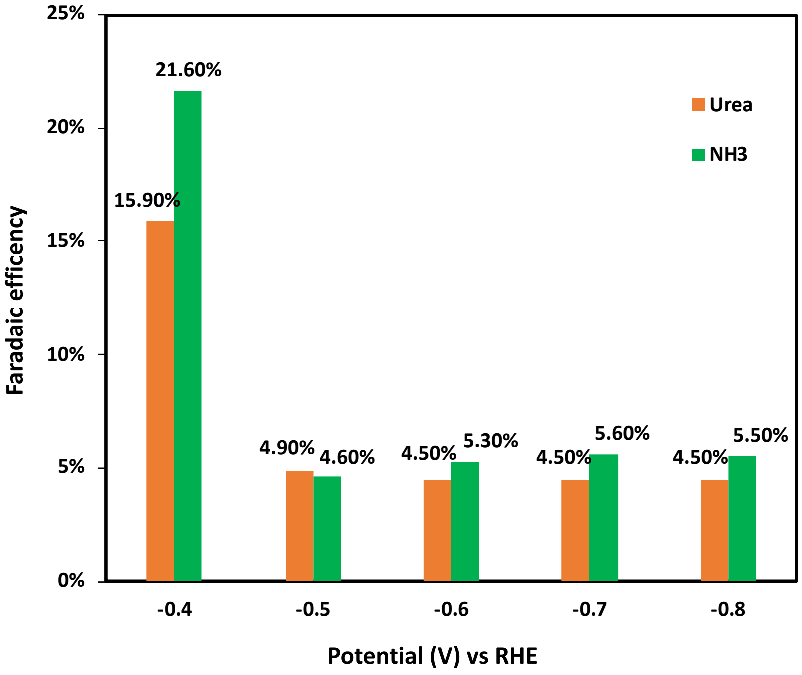

Figure 5.4: Faradaic efficiency of NH_3 and urea, calculated from the data in Table 5.1.

5.3.2 Attempted coreduction of N_2 and CO_2 at carbon supported MoS_2 (MoS_2/C) in a PEM electrolysis cell

The effectiveness of MoS_2 as a catalyst for N_2 reduction to produce ammonia has been reported in previous studies [18-20]. Based on these reports, we employed a MoS_2 catalyst mixed with a carbon black support (MoS_2/C) to investigate its potential for producing urea through the coreduction of N_2 and CO_2 in the PEM electrolysis cell.

To prepare the cathode, a catalyst ink was first prepared by mixing MoS_2 and carbon black (CB) in a 1:10 ratio with 150 µL of H_2O, 75 µL of 2-propanol, and 75 µL of 5% Nafion™ solution. The appropriate amount of ink was then loaded onto a 5 cm^2 CFP cathode to achieve a MoS_2 + CB loading of 1.5 mg cm^{-2}. Before conducting the electrolysis of N_2 and CO_2, cyclic voltammograms were recorded at a 5 cm^2 MoS_2/C electrode in H_2O under various gas flow conditions (purging and bubbling) of N_2, CO_2, and a mixture of N_2 + CO_2. The effects of these conditions on the electrochemistry were investigated, and the results are presented in Figures 5.5 and 5.7.

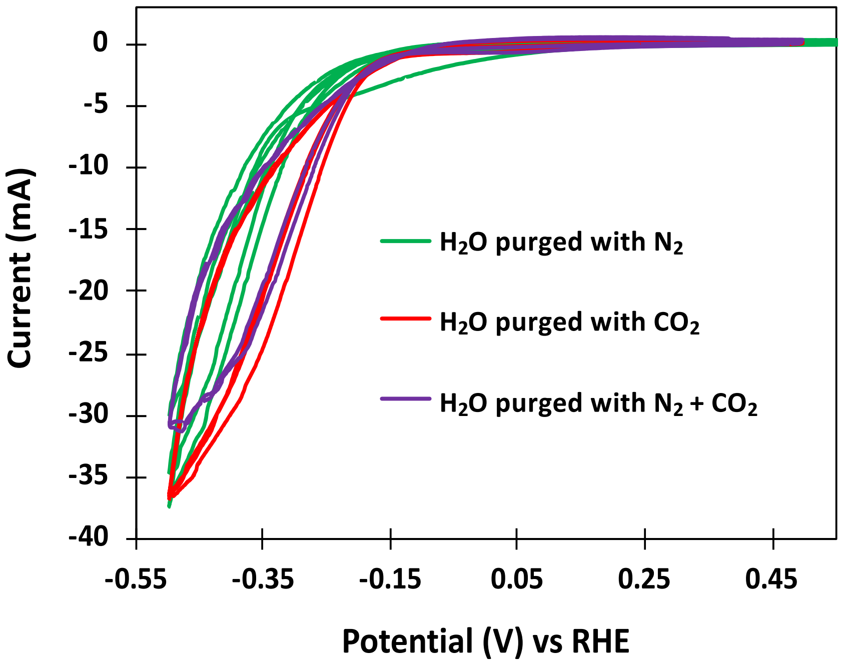

Figure 5.5. Cyclic voltammograms (10 mV s^{-1}) at a 5 cm^2 MoS_2/C electrode in H_2O under N_2, CO_2, and the mixture of N_2 and CO_2.

Figure 5.5 presents a comparison of cyclic voltammograms (CVs) obtained in H_2O under three different gas environments: N_2, CO_2, and a mixture of $N_2 + CO_2$ (1:1). Prior to performing the CVs, H_2O was purged with the gas in a sparger for 15 min. The purged H_2O was then pumped through the cathode field during the CV measurement. Under N_2 environment, a well-defined CV was observed, with a large cathodic current at potentials below -0.33 V. However, there were no distinct redox waves observed for the Mo(+4/+5) couple of MoS_2/C catalyst. This large cathodic current could be due to N_2 reduction to ammonia [14]. Under CO_2, the shape and current of the CVs were comparable to those under N_2, but the onset potential for CO_2 reduction was less negative than for N_2 reduction. When both N_2 and CO_2 were present, the onset potential for coreduction of N_2 and CO_2 was similar to that under CO_2, but the current was slightly lower than for individual N_2 or CO_2 reduction. Several research groups have reported that in addition to CO and NH_3 (eq. 5.1 and 5.2), urea could be produced from the coreduction of N_2 and CO_2 (eq. 5.3) using diverse electrocatalysts [21-25].

$$CO_2\,(g) + 2e^- + 2H^+\,(aq) \longrightarrow CO\,(g) + H_2O \qquad (5.1)$$

$$N_2\,(g) + 6e^- + 6H^+\,(aq) \longrightarrow 2NH_3\,(aq) \qquad (5.2)$$

$$CO_2\,(g) + N_2\,(g) + 6e^- + 6H^+\,(aq) \longrightarrow NH_2CONH_2\,(aq) + H_2O \qquad (5.3)$$

Figure 5.6 shows a schematic diagram of the PEM electrolysis cell and reagent gas setup used in this study. To investigate the impact of reagent gas flow on the electrochemical, cyclic voltammetry were conducted in H_2O under various gas conditions and shown in Figure 5.7. Three different gas flow conditions were tested: (1) H_2O was first purged with a $N_2 + CO_2$ mixture (1:1) in a sparger for 15 min before being pumped to the cathode field, (2) N_2 was bubbled into the solution at a flow rate of 10 mL min^{-1} while $N_2 + CO_2$ purged water was pumped to the cathode field, and (3) N_2 was bubbled into the solution while CO_2 purged water was pumped to the cathode field.

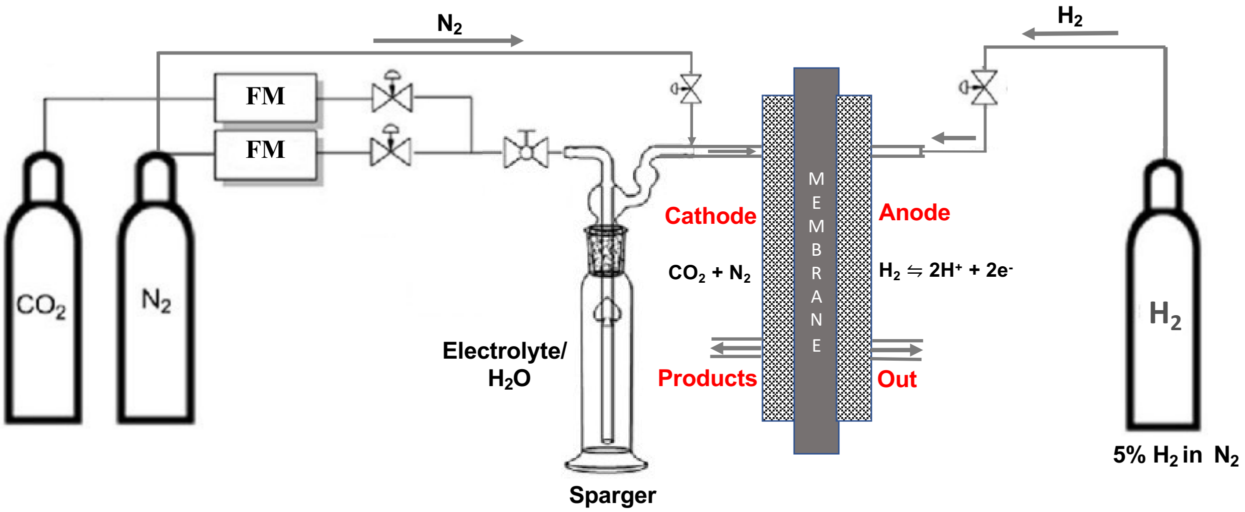

Figure 5.6. A schematic diagram of the PEM electrolysis cell and reagent gas flow setup, where FM refers to the flow meter

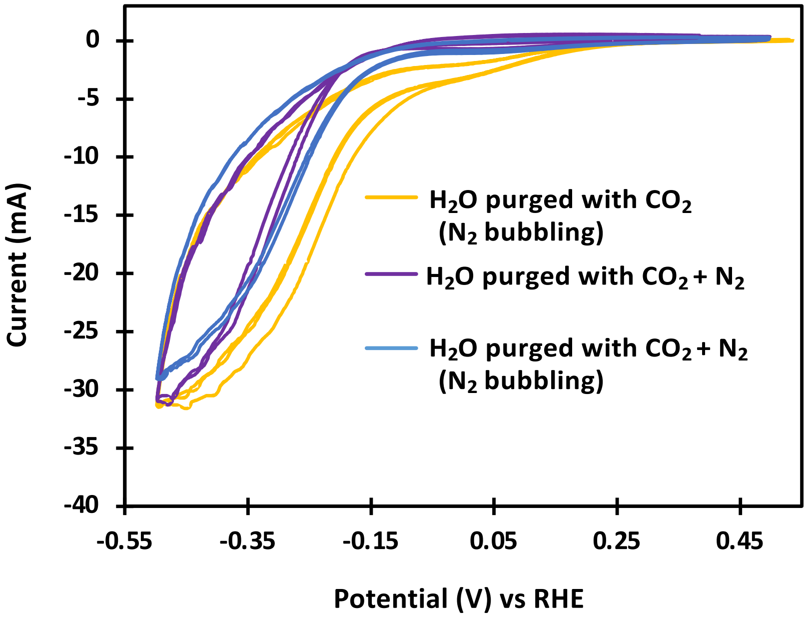

Figure 5.7. Cyclic voltammograms (10 mV s^{-1}) at a 5 cm^2 MoS_2/C electrode in H_2O under a mixture of N_2 and CO_2 in different gas flow conditions.

As observed in Figure 5.7, the shape and current of the CVs were comparable under the three conditions. However, the onset potential for N_2 + CO_2 coreduction was found to be significantly less negative (-0.02 V) when N_2 was bubbling in CO_2 purged H_2O as compared to the other two conditions. This suggests that under this condition, urea could be produced at a low overpotential from the coreduction of N_2 and CO_2 relative to the others two conditions.

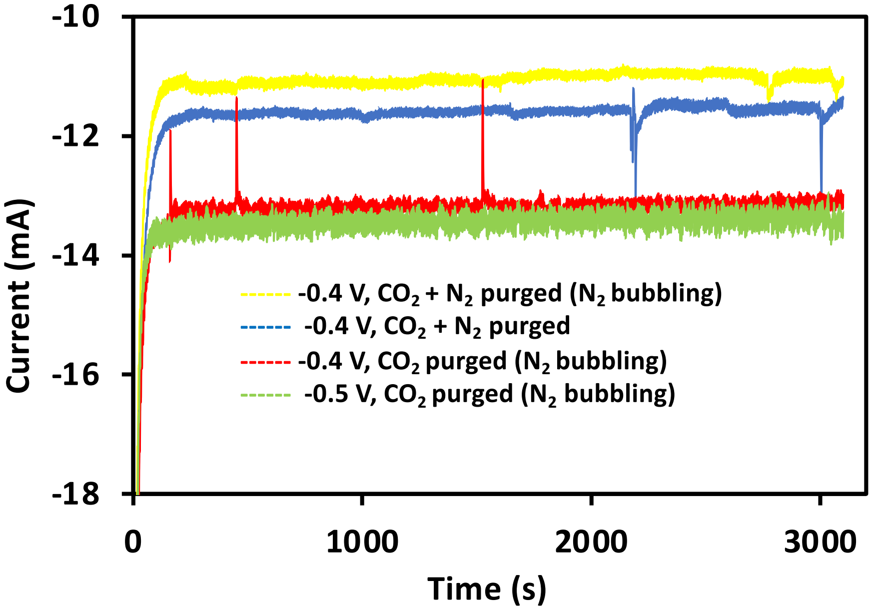

Figure 5.8. Current vs time at various constant potentials at MoS_2/C electrode for electrolysis of N_2 and CO_2 in H_2O under different gas flows.

Electrolysis was conducted to investigate whether urea could be produced through the co-reduction of N_2 and CO_2 at MoS_2/C, as well as to determine if the reagent gas flow has any effect on the yield. Figure 5.8 illustrates the electrolysis curves at a 5 cm^2 MoS_2/C electrode under a mixture of N_2 + CO_2 with different gas flow conditions (purging and bubbling).

Electrolysis at -0.4 V was performed under three different conditions: (1) H_2O was first purged with a N_2 + CO_2 mixture and pumped to the cathode field, (2) N_2 was bubbling into the solution while N_2 + CO_2 purged water was pumped to the cathode field, and (3) N_2 was bubbling into the solution while CO_2 purged water was pumped to the cathode field. The highest current was observed when CO_2-purged H_2O was pumped, and N_2 was bubbling into the CO_2 purged solution, which was also consistent with the current observed in CVs under these conditions. However, as the potential was decreased, the current slightly increased under this condition.

Table 5.2. Average currents and concentrations of urea produced from electrolysis of N_2 and CO_2 at a 5 cm^2 MoS_2/C and blank (carbon black, CB) electrode in water under various condition.

Catalyst	**Purged gas**	**Potential (V) vs RHE**	**Average current (mA)**	**Urea concentration (µM)**
MoS_2/C	$CO_2 + N_2$ (1:1)	-0.4	-11.7	1.11
	$CO_2 + N_2$ (1:1) (N_2 bubbling)	-0.4	-11.2	1.60
	CO_2 (N_2 bubbling)	-0.4	-13.3	1.65
	CO_2 (N_2 bubbling)	-0.5	-13.5	0.91
	$CO_2 + N_2$ (1:1) (N_2 bubbling)	-0.3	-6.3	0.45
	$CO_2 + N_2$ (1:1) (N_2 bubbling)	OCP	0.0	0.60
CB	$CO_2 + N_2$ (1:1) (N_2 bubbling	-0.4	-9.9	0.80
Blank H_2O	$CO_2 + N_2$ (1:1) (purged)	No electrolysis		0.45

The urea analysis was carried out using the DAM method based on our previous work without deionizing the samples with an ion exchange column [16]. Table 5.2 presents the concentrations and average current of urea measured at the open circuit potential (OCP) and at -0.4 and -0.5 V under different gas flow conditions, and for a blank analysis using deionized H_2O purged with the reagent gases (1:1) for 15 min. The results indicated that the highest urea concentration (1.6 μM) was achieved at -0.4 V, and that no significant differences were observed in urea production when the reagent gas conditions were altered. However, when the potential was changed to -0.5 V or -0.3 V, urea production decreased slightly.

However, the color that developed during the DAM reaction (Figure 5.9) was different from the color for the standards, and the absorbance spectra were significantly different (Figure 5.10). This shows that there were other chromophores present in the samples, which were largely responsible for the development of a pinkish-red color and absorbance at 520 nm.

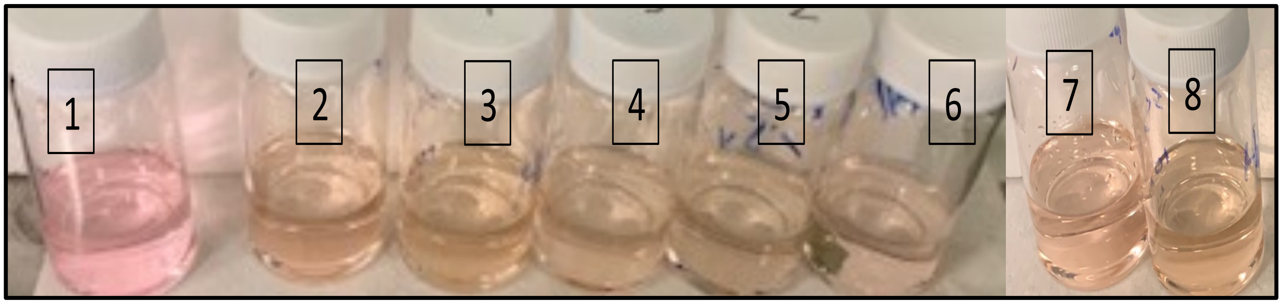

Figure 5.9: Photography of solution after DAM reactions for (1) 2 μM of urea standard in H_2O, (2) MoS_2/C @ -0.4 V (purged with N_2 + CO_2), (3) MoS_2/C @ -0.4 V (purged with N_2 + CO_2 and N_2 bubbling), (4) MoS_2/C @ -0.4 V (purged with CO_2 and N_2 bubbling), (5) MoS_2/C @ -0.5 V (purged with N_2 + CO_2 and N_2 bubbling), (6) MoS_2/C @ -0.3 V (purged with N_2 + CO_2 and N_2 bubbling), (7) CB @ -0.4 V (purged with N_2 + CO_2 and CO_2 bubbling), and (8) MoS_2/C @ OCP (purged with N_2 + CO_2 and N_2 bubbling).

This was confirmed by replicate experiments which revealed that the apparent production of urea was not reproducible, and by a control experiment at OCP and blank analysis (Table 5.2), which revealed that impurities in the reagent gases were partially responsible for the pinkish-red color. Based on these findings, it can be concluded that the MoS_2/C catalyst did not generate measurable quantities of urea.

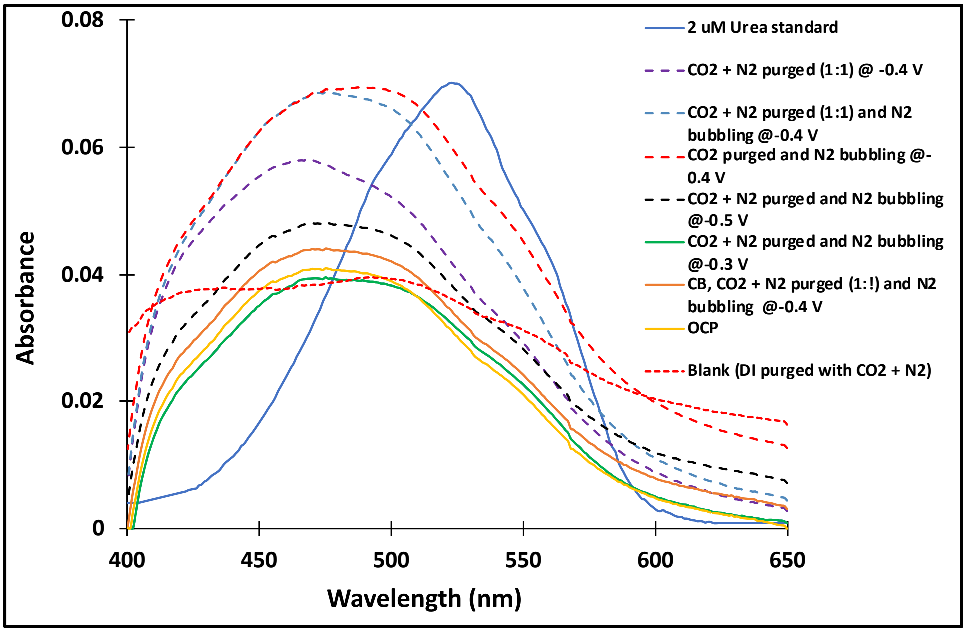

Figure 5.10. UV-Vis spectra for analysis of urea (DAM method) from electrolysis of CO_2 and N_2 at a 5 cm^2 MoS_2/C electrode under different gas flow conditions

5.3.2.1 Effect of electrolytes

The impact of various aqueous electrolytes on the electrochemistry of N_2 and CO_2 in the PEM cell was investigated by using dilute acetic acid, $NaHCO_3$ and sulfuric acid electrolytes. CVs were conducted at a 5 cm^2 MoS_2/C electrode in these electrolytes under N_2 and a mixture of N_2 + CO_2 to study their impact. Prior to each measurement, the electrolytes were purged with N_2 and a mixture of $N_2 + CO_2$ for 15 min and then pumped to the cathode field at a flow rate of 0.1 mL min^{-1}. The cathode was washed with the electrolyte for at least 10 minutes before performing the CVs.

Figure 5.11 presents a comparison of the CVs at the MoS_2/C electrode in 0.1 M acetic acid and H_2O under N_2 and a mixture of $N_2 + CO_2$. The CV conducted under N_2 in 0.1 M acetic acid (pH = 3) showed a similar profile to that performed in H_2O. However, the CV obtained under a mixture of $N_2 + CO_2$ in 0.1 M acetic acid had a similar shape to the CV obtained in H_2O, but the onset potential for the coreduction of $N_2 + CO_2$ was slightly more negative than that observed under H_2O. Despite this difference, the highest current at -0.5 V was similar to that obtained in H_2O. It appears that in acidic condition (pH = 3), the coreduction of $N_2 + CO_2$ was initiated at a more negative potential, leading to the production of urea at a higher overpotential when compared it to the conditions in H_2O.

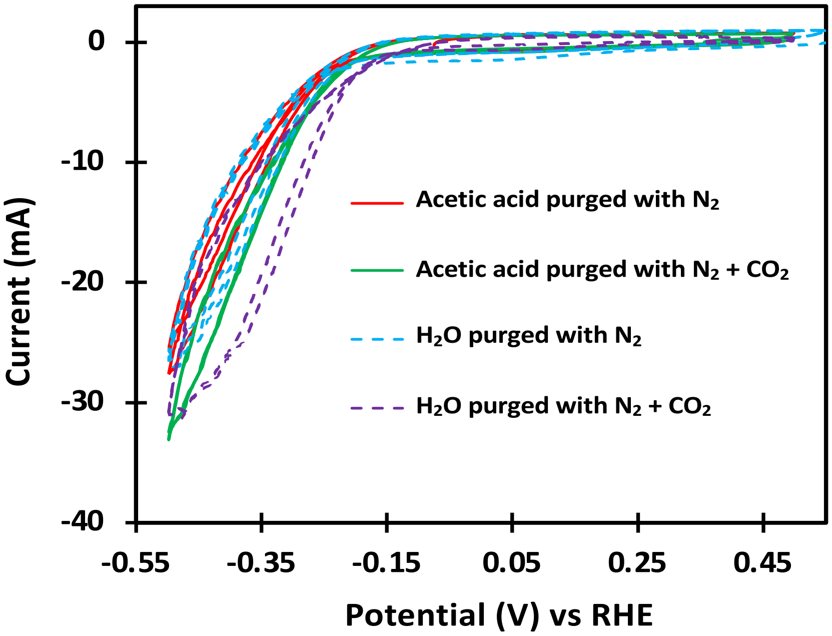

Figure 5.11. Comparison of cyclic voltammograms (10 mV s^{-1}) at MoS_2/C electrode in 0.1 M acetic acid and H_2O under N_2 and mixture of $N_2 + CO_2$.

When the 0.1 M acetic acid eletrolyte was replaced with a mixture of 0.1 M acetic acid + 0.2 M $NaHCO_3$ (1:1), the performance of the cell decreased over time. Figure 5.12 shows CVs obtained in 0.1 M acetic acid + 0.2 M $NaHCO_3$ (1:1) under N_2. During the initial run, a high anodic current was observed, which could be due to the oxidation of H_2O, while the cathodic current was low. By the fifth run, a well-defined CV with a similar shape and current to that of 0.1 M acetic acid was observed. However, the cell performance gradually declined over time, as evidenced by the significant decrease in the cathodic current, as illustrated in Figure 5.12 (10th run)

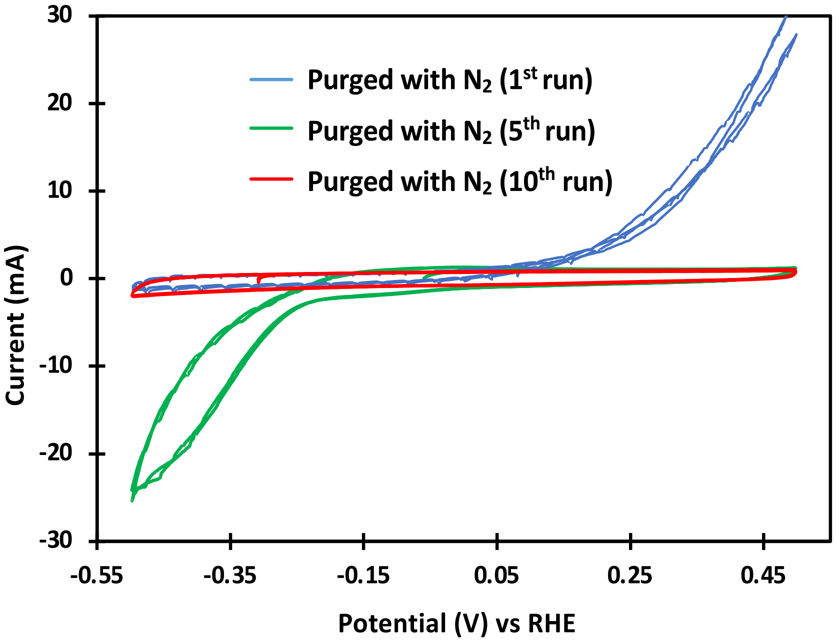

Figure 5.12. Cyclic voltammograms (10 mV s^{-1}) for MoS_2/C electrode in 0.1 M acetic acid + 0.2 M $NaHCO_3$ (1:1) under N_2.

In order to determine if the deactivated membrane could be regenerated, the 0.1 M acetic acid + 0.2 M $NaHCO_3$ electrolyte was replaced with 0.1 M H_2SO_4 (pH = 0.7). Figure 5.13 shows

CVs obtained after purging the 0.1 M H_2SO_4 with N_2 for 15 min, demonstrating highly reproducible electrochemistry after 20 cycles. Regeneration of the membrane in 0.1 M H_2SO_4 allowed for CVs similar to those run in H_2O due to the equilibrium in H^+ activity across the membrane being balanced again.

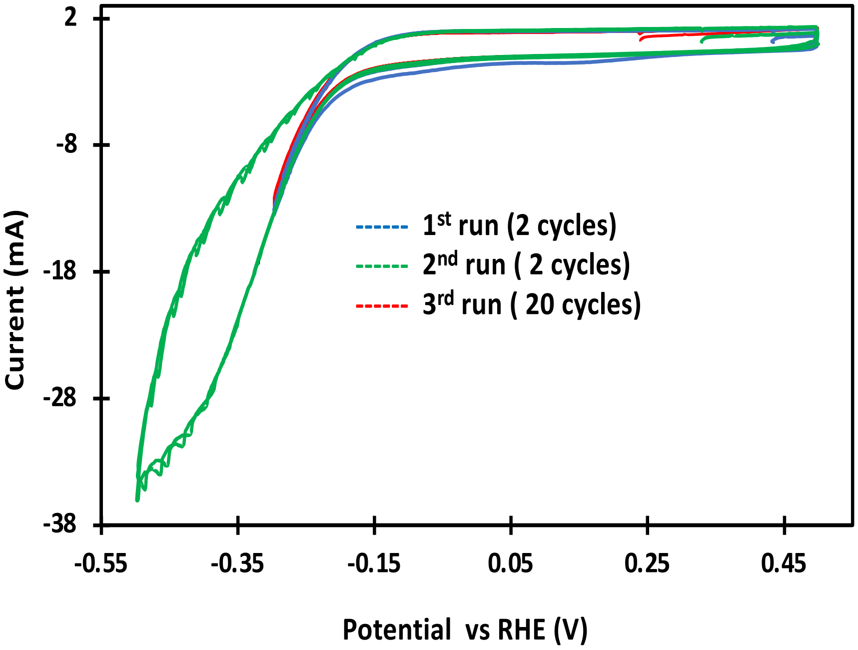

Figure 5.13. Cyclic voltammograms (10 mV s^{-1}) for MoS_2/C electrodes in 0.1 M H_2SO_4 under N_2.

To produce urea in 0.1 M H_2SO_4, a series of electrolyses of N_2 and CO_2 were performed and yielded similar results to those obtained with H_2O. However, during one electrolysis at -0.3 V, an interesting observation was made when N_2 gas was purged for 15 min, and both N_2 and CO_2 were continuously bubbling with a 1:1 ratio at a flow rate of 10 mL min^{-1}. Under these conditions, the DAM reaction showed the correct color (Figure 5.14 (5)) and the corresponding absorbance spectrum (Figure 5.15, red desh line), unlike the other two electrolysis conditions conducted at -0.3 V: one was purged with $N_2 + CO_2$ (1:1), and the other was bubbling with N_2 while purged with

CO_2 (Figure 5.14 (4 and 6)). This results suggests that urea can be produced with a gas phase mixture of N_2 and CO_2. However, due to the very trace production, the presence of interferenecs the concentration of urea could not be accuratly quantified. Therefore, further investigations are required to establish this result.

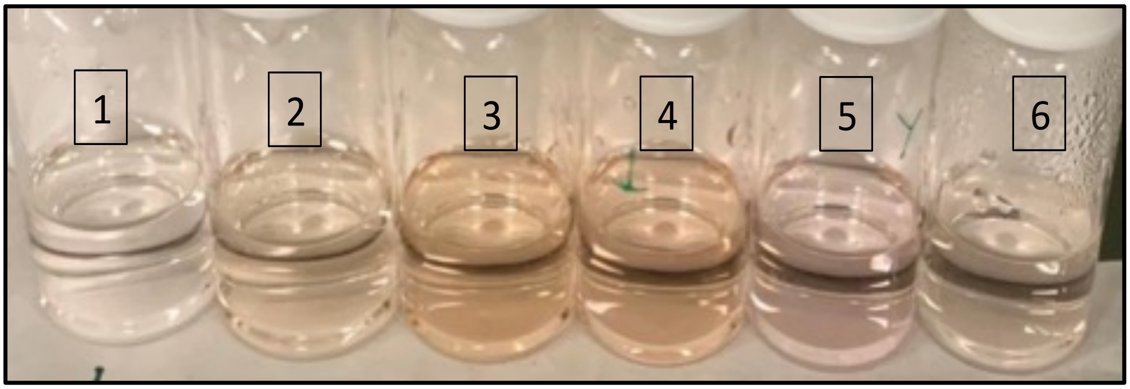

Figure 5.14: Photography of the solutions after DAM reactions for (1) 0.1 M H_2SO_4 (without purged gas), (2) 0.1 M H_2SO_4 (purged with N_2 + CO_2, 1:1 ratio), (3) electrolysis at a MoS_2/C @ -0.4 V (purged with N_2 + CO_2 (1:1) and N_2 bubbling), (4) electrolysis at a MoS_2/C @ -0.3 V (purged with N_2 + CO_2 (1:1) and N_2 bubbling), (5) electrolysis at a MoS_2/C @ -0.3 V (purged with N_2 and CO_2 + N_2 bubbling (1:1)), (6) electrolysis at a MoS_2/C @ -0.3 V (purged with N_2 and CO_2 bubbling).

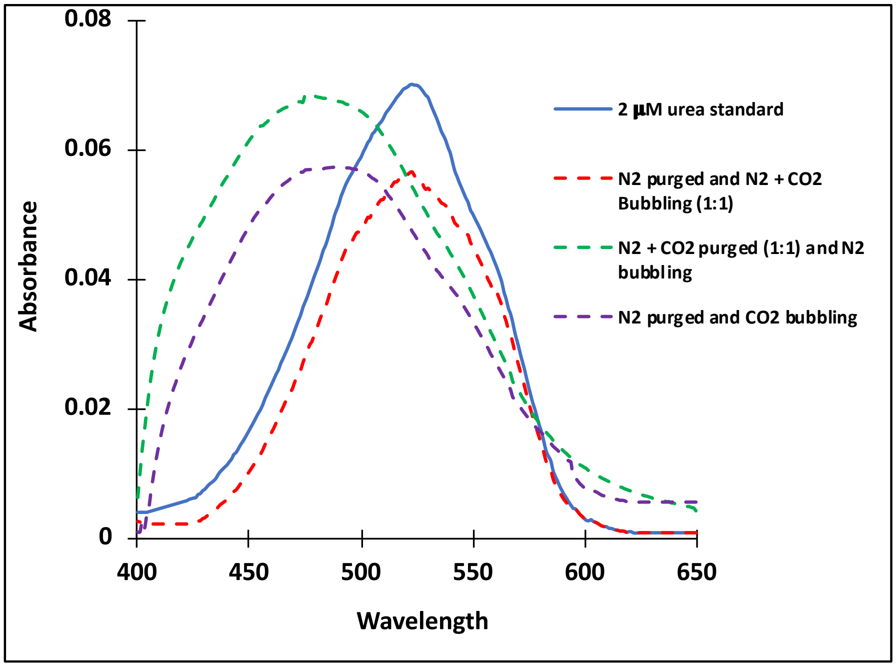

Figure 5.15: UV-Vis spectra for analysis of urea (DAM method) from electrolysis of CO_2 and N_2 in 0.1 M H_2SO_4 at a 5 cm^2 MoS_2/C electrode under different gas flow conditions.

5.4 Conclusions

In this study, the production of urea in a PEM electrolysis cell was investigated through the coreduction of CO_2 with NO_2^- in H_2O. The results demonstrated a significant increase in the faradaic efficiency of urea production from 2.8% to 15.9% (~ -0.4 V) at the FePc/C catalyst when compared to a conventional cell, even with a lower concentration of NO_2^- solution. On the other hand, MoS_2/C was explored as a potential catalyst for urea production through the coreduction of N_2 and CO_2 in a PEM electrolysis cell. However, the results showed that this catalyst was unable to produce urea in H_2O. Nevertheless, it was found that at MoS_2/C using 0.1 M H_2SO_4 as an electrolyte and having both reagent gases in the gaseous phase could potentially lead to the production of trace amount of urea.

In addition, the study found that the use of $NaHCO_3$ as an electrolyte caused a decline in the performance of the cell over time. This observation may limit the applicability of this technique, especially when dealing with complex samples. Therefore, it is crucial to carefully select the appropriate electrolyte for PEM electrolysis cells to ensure optimal performance.

5.5 References

1. Tugaoen, H. O. N., Garcia-Segura, S., Hristovski, K., & Westerhoff, P. (2017). Challenges in photocatalytic reduction of nitrate as a water treatment technology. Science of Total Environment, 599, 1524-1551.
2. Peter, S. C. (2018). Reduction of CO_2 to chemicals and fuels: a solution to global warming and energy crisis. ACS Energy Letters, 3, 1557-1561.
3. Clark, J. H., & Macquarrie, D. J. (Eds.). (2008). Handbook of green chemistry and technology. John Wiley & Sons.
4. Feng, Y., Yang, H., Zhang, Y., Huang, X., Li, L., Cheng, T., & Shao, Q. (2020). Te-doped Pd nanocrystal for electrochemical urea production by efficiently coupling carbon dioxide reduction with nitrite reduction. Nano Letters, 20, 8282-8289.
5. Mei, Z., Zhou, Y., Lv, W., Tong, S., Yang, X., Chen, L., & Zhang, N. (2022). Recent progress in electrocatalytic urea synthesis under ambient conditions. ACS Sustainable Chemistry & Engineering, 10, 12477-12496.
6. Chen, C., Zhu, X., Wen, X., Zhou, Y., Zhou, L., Li, H., & Wang, S. (2020). Coupling N_2 and CO_2 in H_2O to synthesize urea under ambient conditions. Nature Chemistry, 12, 717-724

7. Shibata, M., & Furuya, N. (2001). Electrochemical synthesis of urea at gas-diffusion electrodes: Part VI. Simultaneous reduction of carbon dioxide and nitrite ions with various metallophthalocyanine catalysts. Journal of Electroanalytical Chemistry, 507, 177-184.

8. Cao, N., Quan, Y., Guan, A., Yang, C., Ji, Y., Zhang, L., & Zheng, G. (2020). Oxygen vacancies enhanced cooperative electrocatalytic reduction of carbon dioxide and nitrite ions to urea. Journal of Colloid and Interface Science, 577, 109-114.

9. Meng, N., Huang, Y., Liu, Y., Yu, Y., & Zhang, B. (2021). Electrosynthesis of urea from nitrite and CO_2 over oxygen vacancy-rich ZnO porous nanosheets. Cell Reports Physical Science, 2, 100378.

10. Pei, Y., Zhong, H., & Jin, F. (2021). A brief review of electrocatalytic reduction of CO_2—materials, reaction conditions, and devices. Energy Science & Engineering, 9, 1012-1032.

11. C. Li, C. W., & Kanan, M. W. (2012). CO_2 reduction at low overpotential on Cu electrodes resulting from the reduction of thick Cu_2O films. Journal of American Chemical Society, 134, 7231-7234.

12. Lin, J., Yan, S., Zhang, C., Hu, Q., & Cheng, Z. (2022). Electroreduction of CO_2 toward high current density. Processes, 10, 826.

13. Li, Y. C., Zhou, D., Yan, Z., Gonçalves, R. H., Salvatore, D. A., Berlinguette, C. P., & Mallouk, T. E. (2016). Electrolysis of CO_2 to syngas in bipolar membrane-based electrochemical cells. ACS Energy Letters, 1, 1149-1153.

14. Weekes, D. M., Salvatore, D. A., Reyes, A., Huang, A., & Berlinguette, C. P. (2018). Electrolytic CO_2 reduction in a flow cell. Accounts of Chemical Research, 51, 910-918.

15. Brueckner, T. M., & Pickup, P. G. (2017). Kinetics and stoichiometry of methanol and ethanol oxidation in multi-anode proton exchange membrane cells. Journal of Electrochemical Society, 164, F1172.

16. Akther, J., Song, C., Fatih, K., & Pickup, P. G. (2023). Electrochemical production of ammonia and urea from coreduction of nitrite and carbon dioxide at iron phthalocyanine electrodes and comparison of analytical methods. Journal of Electrochemical Society, 170, 026505.

17. Alsudairi, A., Li, J., Ramaswamy, N., Mukerjee, S., Abraham, K. M., and Jia, Q. (2017). Resolving the iron phthalocyanine redox transitions for ORR catalysis in aqueous media. Journal of Physical Chemistry Letters, 8, 2881-2886.

18. Suryanto, B. H., Wang, D., Azofra, L. M., Harb, M., Cavallo, L., Jalili, R., & MacFarlane, D. R. (2018). MoS_2 polymorphic engineering enhances selectivity in the electrochemical reduction of nitrogen to ammonia. ACS Energy Letters, 4, 430-435.

19. Zhang, L., Ji, X., Ren, X., Ma, Y., Shi, X., Tian, Z., and Sun, X. (2018). Electrochemical ammonia synthesis via nitrogen reduction reaction on a MoS_2 catalyst: theoretical and experimental studies. Advanced Materials, 30, 1800191.

20. Chen, S., Liu, X., Xiong, J., Mi, L., & Li, Y. (2022). Engineering strategies for boosting the nitrogen reduction reaction performance of MoS_2 based electrocatalysts. Materials Today Nano, 100202.

21. Zhang, Z., & Guo, L. (2021). Electrochemical reduction of CO_2 and N_2 to synthesize urea on metal-nitrogen-doped carbon catalysts: a theoretical study. Dalton Transactions, 50, 11158-11166.

22. Zhu, X., Zhou, X., Jing, Y., & Li, Y. (2021). Electrochemical synthesis of urea on MBenes. Nature Communications, 12, 4080.

23. Giuffredi, G., Asset, T., Liu, Y., Atanassov, P., & Di Fonzo, F. (2021). Transition metal chalcogenides as a versatile and tunable platform for catalytic CO_2 and N_2 electroreduction. ACS Materials Au, 1, 6-36.

24. Bharath, G., Karthikeyan, G., Kumar, A., Prakash, J., Venkatasubbu, D., Nadda, A. K., & Banat, F. (2022). Surface engineering of Au nanostructures for plasmon-enhanced electrochemical reduction of N_2 and CO_2 into urea in the visible-NIR region. Applied Energy, 318, 119244.

25. Chen, C., Zhu, X., Wen, X., Zhou, Y., Zhou, L., Li, H., & Wang, S. (2020). Coupling N_2 and CO_2 in H_2O to synthesize urea under ambient conditions. Nature Chemistry, 12, 717-724.

Chapter 6

Oxidation of Formic Acid, Methanol, and Ethanol at Surface-Modified Pt/C Catalysts

Abstract

PtBi/C and PtPb/C catalysts were prepared by surface decoration of a commercial Pt/C catalyst, and their catalytic activities for electrochemical oxidation of formic acid, methanol and ethanol were compared. The electrocatalytic activity of these catalysts towards formic acid oxidation has been studied by both cyclic voltammetry and chronoamperometry. It was found that after addition of Bi or Pb, the catalytic activity of the Pt/C catalyst for formic acid oxidation increased greatly at low potentials. Bi in particular was found to greatly enhance oxidation of formic acid through the direct pathway in which absorbed CO is not formed, while it strongly inhibited methanol oxidation. It was found that the currents at 0 V vs SCE for formic acid oxidation at the PtBi/C and PtPb/C catalysts were ~ 6 and ~ 2 times higher, respectively compared to the unmodified Pt/C catalyst. In addition, the PtBi/C catalyst showed more stable activity relative to PtPb/C. The PtBi/C catalyst also showed slightly higher activity for ethanol oxidation at low potentials compared to the unmodified Pt/C.

This chapter has been published as:

Akther, J., & Pickup, P. G. (2020). Oxidation of Formic Acid, Methanol, and Ethanol at Surface-Modified Pt/C Catalysts. ECS Transactions, 97, 939.

Some modifications were made to the original paper for inclusion as a chapter in this thesis (e.g. the style of the references).

The principal author (Jasmeen Akther) contributed to all aspects of the project as the main researcher including performing all of the experiments, collecting, analyzing, presenting the data, and writing parts of the published manuscripts.

The corresponding author (Prof. Peter G. Pickup) was the principal investigator. He proposed the initial experiments, oversaw all aspects of the project, and contributed to several aspects of the project including experimental design, data analysis, writing and revision of the manuscripts, submission to the journals, and supervision of the principal author (Jasmeen Akther).

6.1 Introduction

Modification of Pt surfaces by adsorption of a sub-mono layer of foreign atoms (adatoms) is a powerful way to improve the activities of electrocatalysts [1-7]. Adatoms such as Bi and Pb have been widely applied to modify Pt surfaces to improve activity and selectivity for the oxidation of organic fuels such as formic acid [4, 5], methanol [8, 9], and ethanol [10, 11]. Bismuth especially, has received significant attention as a Pt surface modifier for formic acid oxidation. Various structures such as PtBi alloys [12], PtBi intermetallic [13], and surface modified systems [14] have been reported. Chemical deposition on carbon supported Pt (Pt/C) [14], under potential deposition [15] and irreversible adsorption [16] of Bi have been reported to produce excellent catalysts for formic acid oxidation, in terms of onset potential, activity, stability, and durability. The enhanced performance produced by adatoms on Pt towards formic acid oxidation can arise from various factors. It can be due to an ensemble/third body effect, where an adsorbed metal divides the Pt surface into small domains, which is favorable for direct oxidation of formic acid to CO_2 [17]. It can also be due to electronic/ligand effects, where the adsorbed metal decreases the CO binding strength by lowering the electron density of the Pt 5d orbitals [18].

In this study, we report the oxidation of small organic fuels on three different types of the electrode surface: PtBi/C, PtPb/C, and unmodified Pt/C catalysts. The primary objective of this work is to obtain mechanistic information on the oxidation of formic acid, methanol and ethanol by comparing the effects of various modifying metals on a commercial Pt/C catalyst. Here, cyclic voltammetry and chronoamperometry have been used to measure the effects of Bi and Pb adatom.

6.2 Experimental

6.2.1 Synthesis of the PtM/C (M = Bi or Pb) catalysts

PtM/C catalysts were prepared as previously reported [14]. Pt/C (100 mg) was dispersed in 100 mL of deionized (DI) water containing 10 drops of 10 M HNO_3 by stirring for 16 h. Then 3.9 mL of $Bi(NO_3)_3 \cdot 5H_2O$ (5 g L^{-1} dissolved in 5 M HNO_3) or 2.8 mL of $Pb(NO_3)_2$ (5 g L^{-1} dissolved in 5 M HNO_3) solution was added to give Pt:Bi and Pt:Pb mass ratios of 10:1 and 8:1, respectively. The mixture was then stirred for 0.5 h, followed by the addition of 5 M NaOH dropwise to raise the pH to 7.4. Next, 43.8 mL of 0.05 M $NaBH_4$ was added dropwise and stirred vigorously for 1 h. The catalyst was allowed to settle for 0.5 h, collected by filtration, washed with DI water and dried at 70 °C for 24 h.

The compositions of the prepared catalysts were determined by thermogravimetric analysis (TGA; TA instrument Q500 thermogravimetric analyzer) and energy dispersive X-ray spectroscopy (EDX; FEI Quanta 400 scanning electron microscope with a Xflash SDD energy dispersive X-ray spectrometer).

A SP-50 Potentiostat controlled by EC-Lab software (BioLogic) was used for cyclic voltammetry and chronoamperometry measurements with a three-compartment electrochemical cell at ambient temperature. A Pt wire was used as the counter electrode and a saturated calomel electrode (SCE) as a reference electrode. Before all measurements, the electrolyte solution was purged with ultrapure N_2 for 30 min to remove oxygen, and then covered with N_2 during measurements. To prepare the working electrodes, 2.0 mg of catalyst was dispersed in a mixture of 100 μL of H_2O, 60 μL of 1-propanol and 40 μL of 5% Nafion™ solution (DuPont) and sonicated for 3 h. Then, 3.0 μL of the resulting ink was deposited onto a 0.071 cm^2 glassy carbon electrode, that had been polished with 0.3 μm alumina and washed with DI water, and dried at room temperature.

6.3 Results and Discussion

6.3.1 Characterization of the catalysts

Figure 6.1 shows TGA profiles for the PtBi/C and PtBi/C catalysts. The residual mass was taken to be Pt and Bi or Pb. The results are shown in Table 6.1 and agree within experimentally uncertainty with the targeted values. Figure 6.2 shows EDX spectra of the catalysts. It can be clearly seen in the spectra that the catalysts consisted of Pt, M, and C. Table 6.2 summarizes the elemental compositions of both catalysts. The measured ratio of Pt:Pb was very close to the targeted ratio, whereas the ratio of Pt:Bi was a little higher.

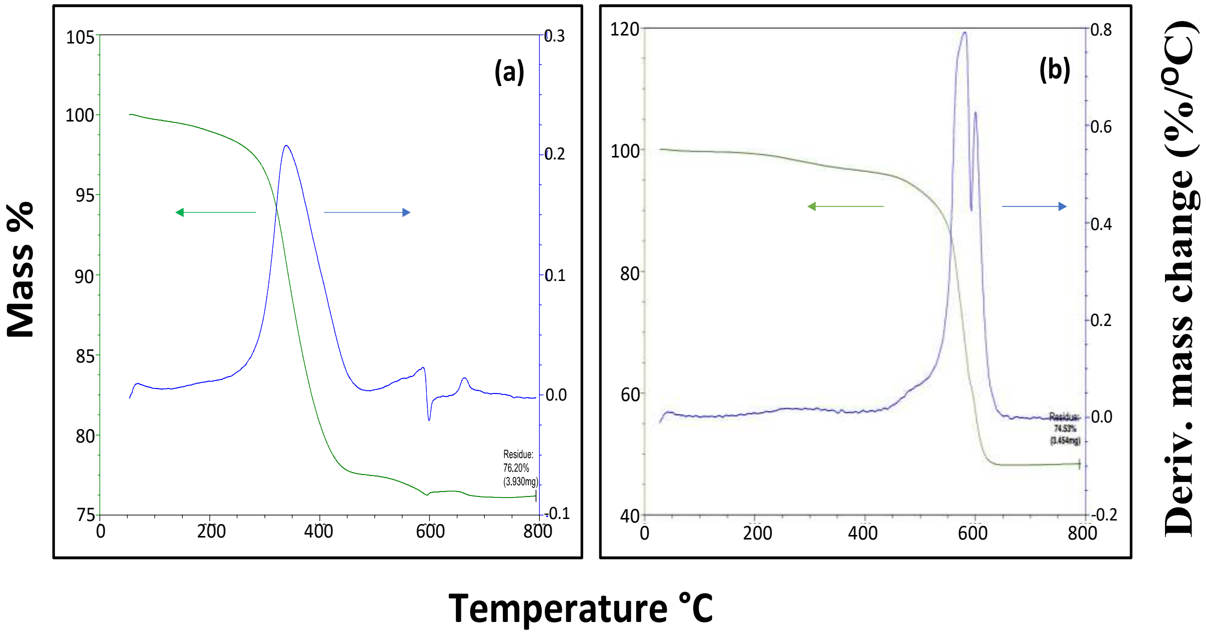

Figure 6.1. TGA profiles for the PtBi/C (a) and PtPb/C (b) catalysts.

TABLE 6.1. TGA Results of the PtM/C Catalysts.

PtM/C	Targeted mass %	Experimental mass %
PtBi/C	72	76
PtPb/C	72	75

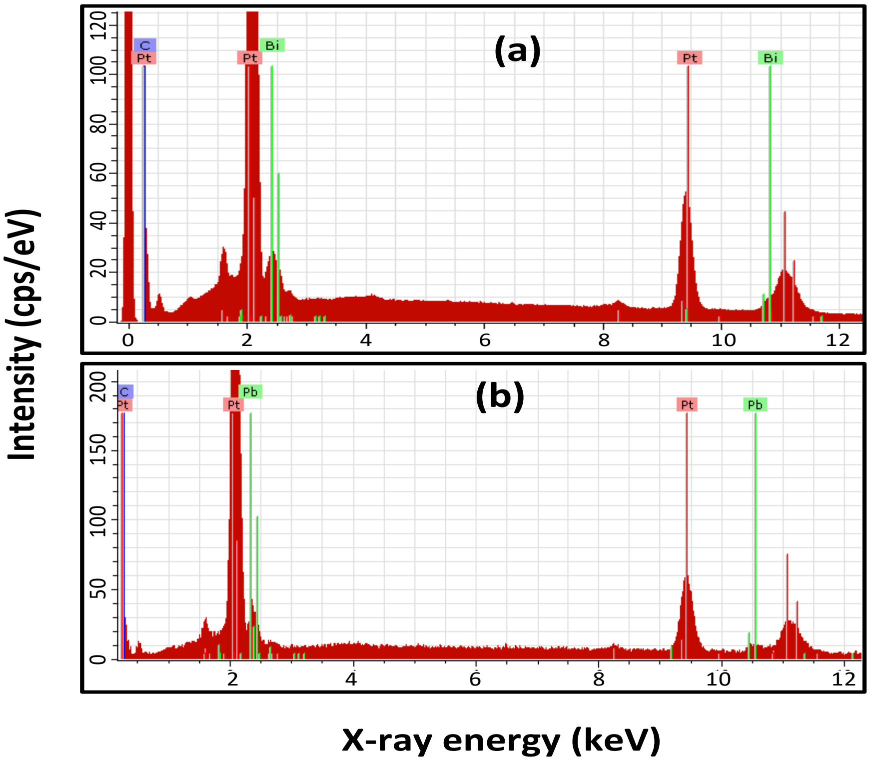

Figure 6.2. EDX spectra of the PtBi/C (a) and PtPb/C (b) catalysts.

TABLE 6.2. SEM-EDX Results

PtM/C	Pt:M ratio		Mass %			Atomic %		
	Target	Experimental	C	Pt	M	C	Pt	M
PtBi/C	10:1	7.0:1	20.0	70.0	10.1	79.2	18.2	2.6
PtPb/C	8:1	7.6:1	17.1	73.2	9.6	77.6	19.8	2.5

6.3.2 Formic acid oxidation

Figure 6.3 shows a cyclic voltammogram of the Pt/C catalyst in 0.5 M H_2SO_4. It shows the characteristic peaks of Pt in an acid medium [19], where the hydrogen desorption/adsorption peaks on the forward and reverse scans can be seen below ca. 0 V. Also, well established oxide formation/oxide reduction peaks can be seen at higher potentials, where oxide formation starts at ca. 0.5 V on the forward scan and there is an oxide reduction peak at ca. 0.45 V on the reverse scan.

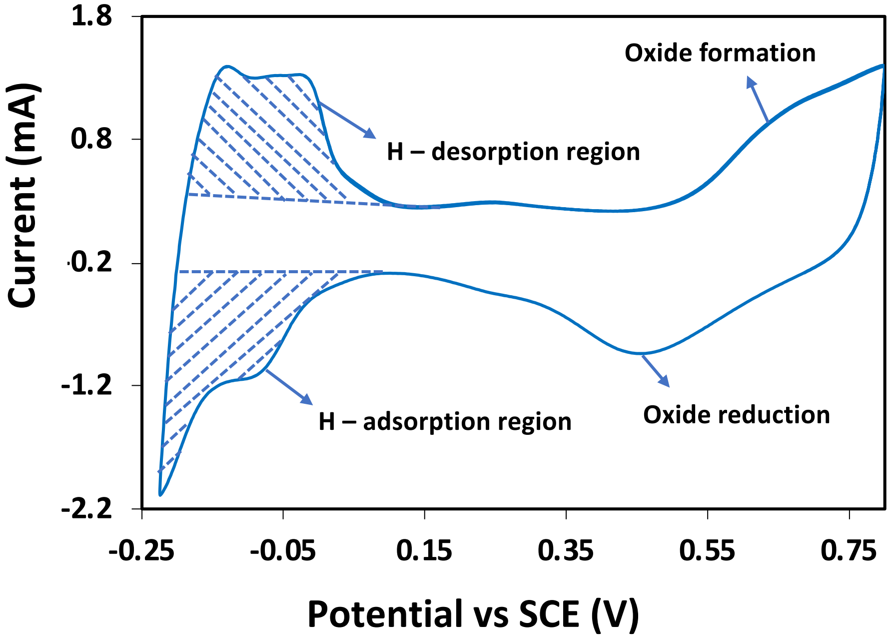

Figure 6.3. Cyclic voltammogram of the Pt/C catalyst in 0.5 M H_2SO_4 (aq) at a scan rate of 100 mV s^{-1}.

Figure 6.4 represents a cyclic voltammogram of formic acid oxidation in 0.5 M H_2SO_4 at the Pt/C catalyst. It shows well-established features for formic acid oxidation [20]. In the forward scan, the current began to increase at ca. 0.15 V and reached a shoulder at ca. 0.27 V, followed by an ascending current to a peak at 0.59 V. This is explained by the dual pathway mechanism. At low potentials, formic acid is oxidized through a direct, dehydrogenation pathway, with simultaneous formation of adsorbed CO (CO_{ads}) through dehydration of adsorbed formic acid. As the coverage of CO_{ads} increases, the number of Pt sites available for the direct pathway decreases, and the rate of increase in the current (due to the increasing potential) decreases. The poisoning of the Pt surface by CO_{ads} cannot be removed until water molecules are activated at higher potentials to give adsorbed hydroxyl groups. As the potential increases, Pt-OH becomes available to oxidize CO_{ads} [21] and the current increases more rapidly, which results in a large peak at 0.59 V.

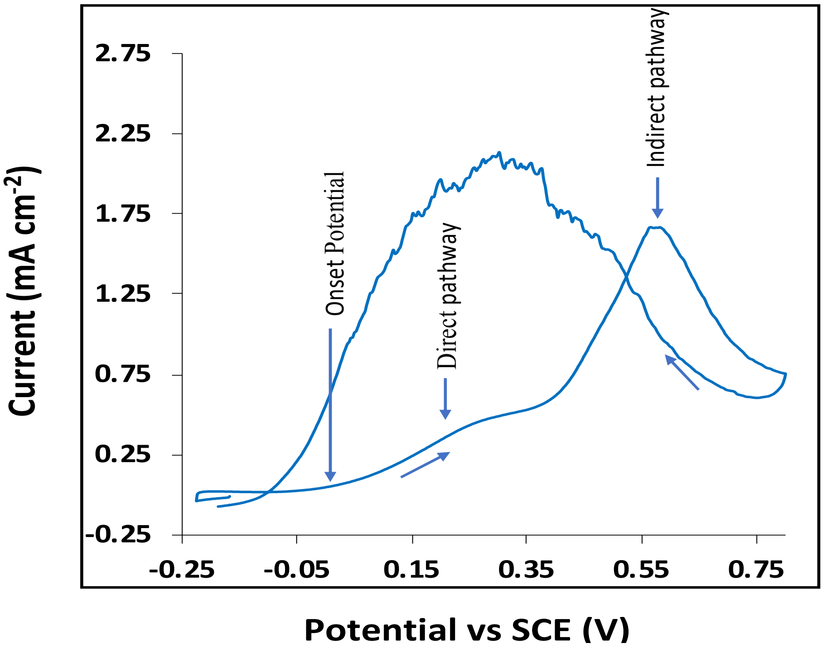

Figure 6.4. Cyclic voltammogram of the Pt/C catalyst in 0.5 M H_2SO_4 (aq) and 0.1 M formic acid at a scan rate of 10 mV s^{-1}.

In the reverse scan, a sharp increase in the formic acid oxidation current coincides with the reduction of Pt oxide. The peak current at ca. 0.27 V was higher than in the forward scan, because the reaction was occurring at a freshly reduced, poison-free Pt surface.

Figure 6.5 compares CVs of the Pt/C, PtBi/C, and PtPb/C catalysts in 0.5 M H_2SO_4. It can be seen that the areas under the hydrogen adsorption/desorption peaks of the PtBi/C and PtPb/C catalysts were smaller than for the Pt/C catalyst. This indicates that the presence of Bi or Pb on the Pt surface blocks adsorption sites for monatomic hydrogen [22]. The electrochemically active surface areas (ECSA) of the catalysts were calculated by integrating the areas under the hydrogen absorption peaks [23]. The values were 9.0 cm^2, 7.7 cm^2 and 5.6 cm^2, respectively, for the Pt/C, PtBi/C, and PtPb/C catalysts.

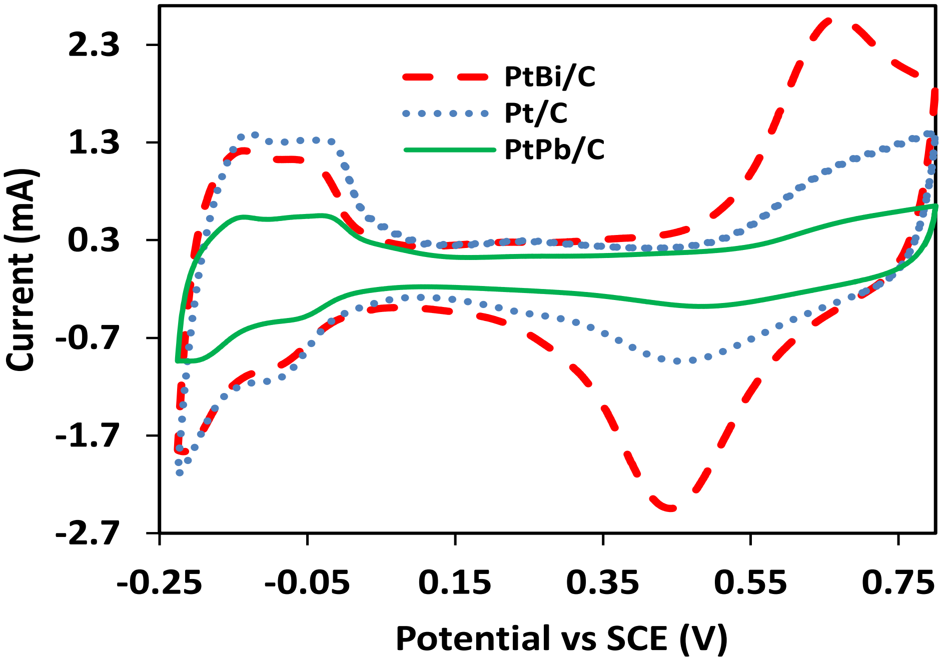

Figure 6.5. Cyclic voltammograms of the Pt/C and PtBi/C and PtPb/C catalysts in 0.5 M H_2SO_4 (aq) at a scan rate of 100 mV s^{-1}.

Figure 6.6 shows CVs of formic acid oxidation at the Pt/C, PtBi/C, and PtPb/C catalysts in 0.5 M H_2SO_4. All data were normalized based on the active surface area. It is seen that both the PtBi/C and PtPb/C catalysts exhibited significantly enhanced catalytic performances in terms of both onset potential and activity compared to the Pt/C catalyst.

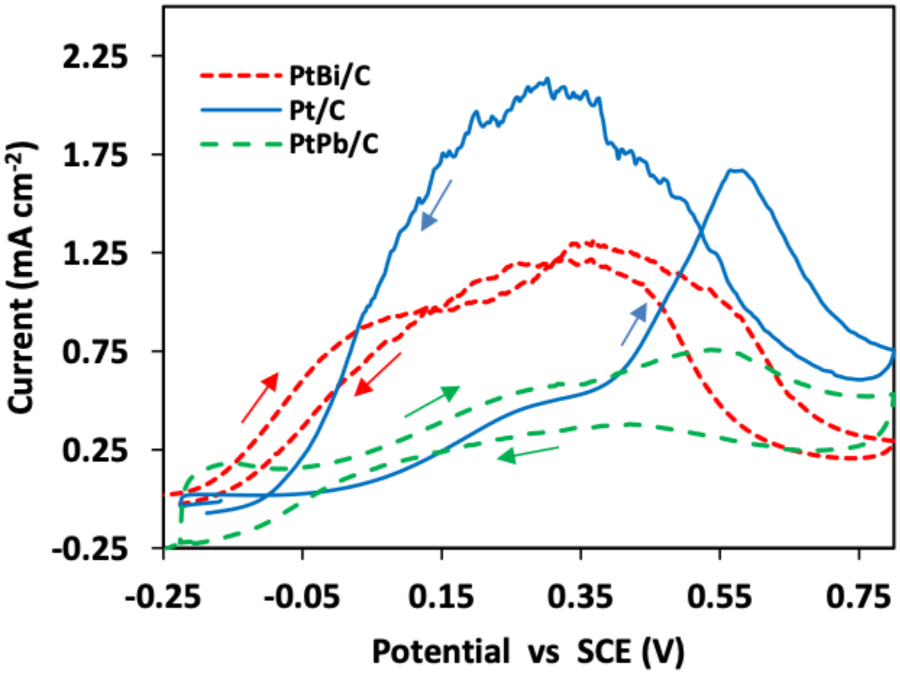

Figure 6.6. Cyclic voltammograms of the Pt/C, PtBi/C, and PtPb/C catalysts in 0.5 M H_2SO_4 (aq) and 0.1 M formic acid at a scan rate of 10 mV s^{-1}.

The onset potentials for the PtBi/C and PtPb/C catalysts are more negative and the currents at 0 V, are ~ 6 and 2 times higher, respectively, compared to the Pt/C catalyst. Since formic acid oxidation to CO_2 occurs via the direct pathway at such a low potential, this indicates that there was much less poisoning of the Pt sites by CO_{ads}. The shoulder at ca. 0.55 V for the PtBi/C catalyst in the forward scan, and small peak for the PtPb/C catalyst, correspond to the oxidation of formic acid via the indirect path, through oxidation of CO_{abs} to CO_2. Their lower currents relative to Pt/C indicate that formic acid oxidation at both the PtBi/C and PtPb/C catalysts proceeds primarily through the dehydrogenation pathway with dehydration occurring to a much lesser degree, particularly at PtBi/C.

Figure 6.7 shows staircase chronoamperometric curves for formic acid oxidation at the Pt/C, PtBi/C, and PtPb/C catalysts. For each catalyst, currents were recorded consecutively from 0 V to

0.5 V in 0.1 V steps. It can be seen that the currents at the PtBi/C and PtPb/C catalysts were much higher than for Pt/C at low potentials. At 0 V the currents at the PtBi/C and PtPb/C catalysts were five and two times higher, respectively, than at the Pt/C catalyst.

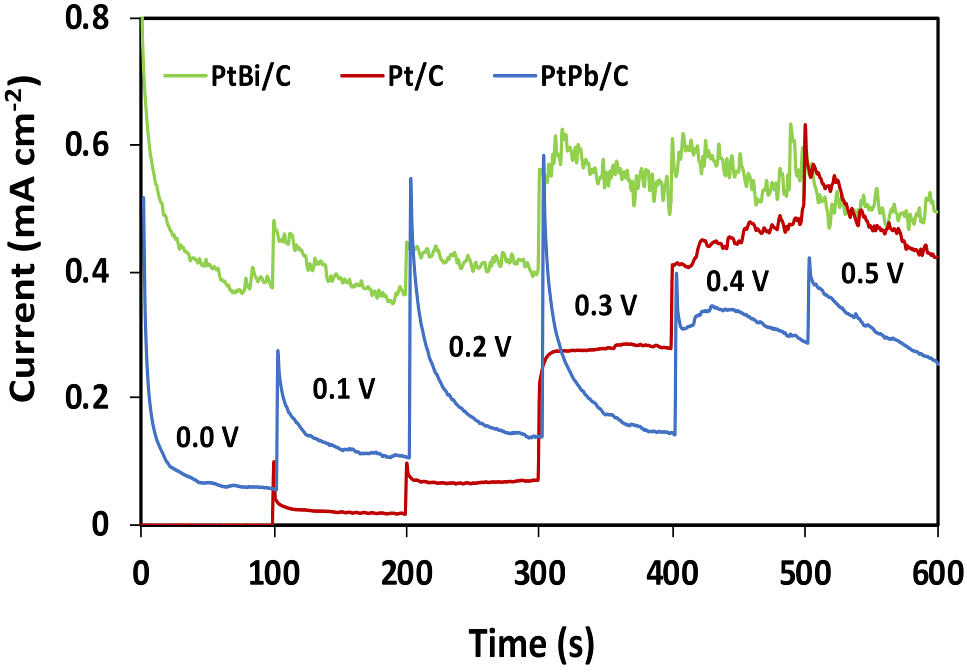

Figure 6.7: Staircase chronoamperometry curves at the Pt/C, PtBi/C, and PtPb/C catalysts at (0 V to 0.5 V vs SCE) in 0.1 M formic acid and 0.5 M H_2SO_4 (aq).

However, they converged at higher potentials, and the currents for PtPb/C fell below those for Pt/C at 0.3 V. It is also notable that the rate of the current decay at each potential was minimal at PtBi/C, while at PtPb/C the current dropped rapidly and then became relatively stable. In contrast, the current at the Pt/C catalyst increased over time from 0.2 to 0.4 V. Additionally, the currents at 0.5 V were similar for the PtBi/C and Pt/C catalysts. Together, these observations indicated that there was little accumulation of CO_{abs} on the PtBi/C catalyst, and less/slower accumulation on PtPb/C relative to Pt/C.

Figure 6.8 represents pulse chronoamperometry curves for formic acid oxidation at the Pt/C, PtBi/C, and PtPb/C catalysts. The chronoamperometric currents were recorded consecutively (from 0 V to 0.5 V in 0.1 V steps) with short (5 s) pulses to a high potential (+0.7 V) before each new potential was applied. It is seen that the current at the PtBi/C catalyst was almost constant from 0.2 to 0.4 V. In contrast, the current decreased over time at both the Pt/C and PtPb/C catalysts. This indicates that even though the surface was cleaned before every step, the CO_{ads} poison formed more rapidly on the Pt/C and PtPb/C catalysts relative to PtBi/C.

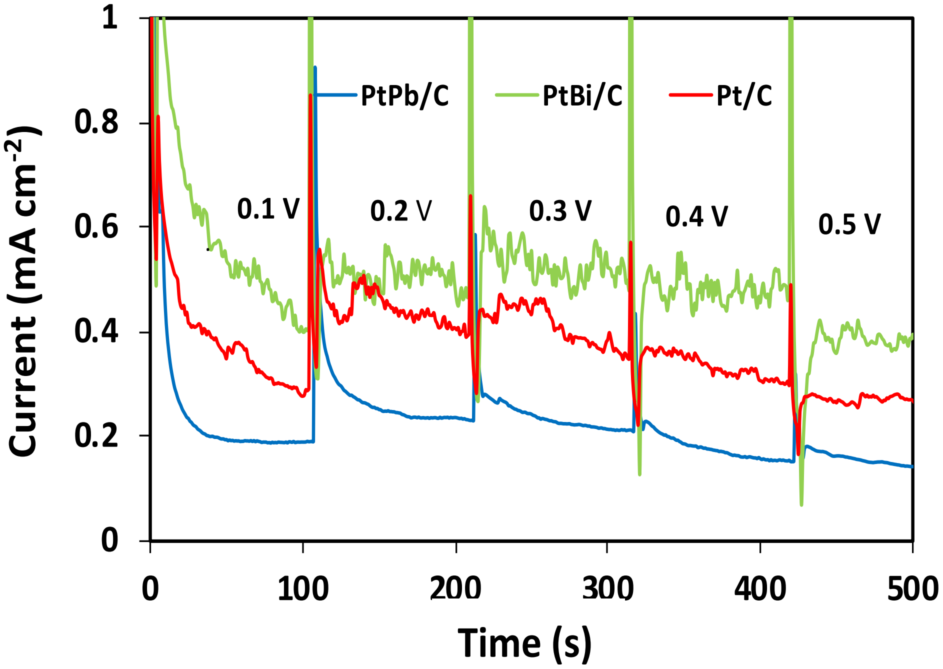

Figure 6.8. Pulse chronoamperometry curves at the Pt/C, PtBi/C, and PtPb/C catalysts at (0 V to 0.5 V vs SCE) in 0.1 M formic acid and 0.5 M H_2SO_4 (aq).

6.3.3 Methanol oxidation

Figure 6.9 exhibits cyclic voltammograms at the Pt/C, PtBi/C, and PtPb/C catalysts in 0.5 M H_2SO_4 (aq) and 0.1 M methanol. It is clearly seen that both the PtPb/C and Pt/C catalysts show typical voltammetric profiles for methanol oxidation. There are methanol oxidation peaks on both the forward and backward scans. However, in the case of the PtBi/C catalyst, the peak on the forward scan exhibited a distinct shoulder at ca. 0.4 V, and during the reverse scan there was a cathodic peak at ca. 0.5 V prior to the anodic peak. The cathodic peak was presumably due to reduction of bismuth oxide, which coincides with the PtOH reduction peak in the background CV, as shown in Figure 6.5. The second anodic peak on the forward scan at ca. 0.67 V can then be assigned to the oxidation of bismuth oxide, since it corresponds to the peak for this process in Figure 6.5.

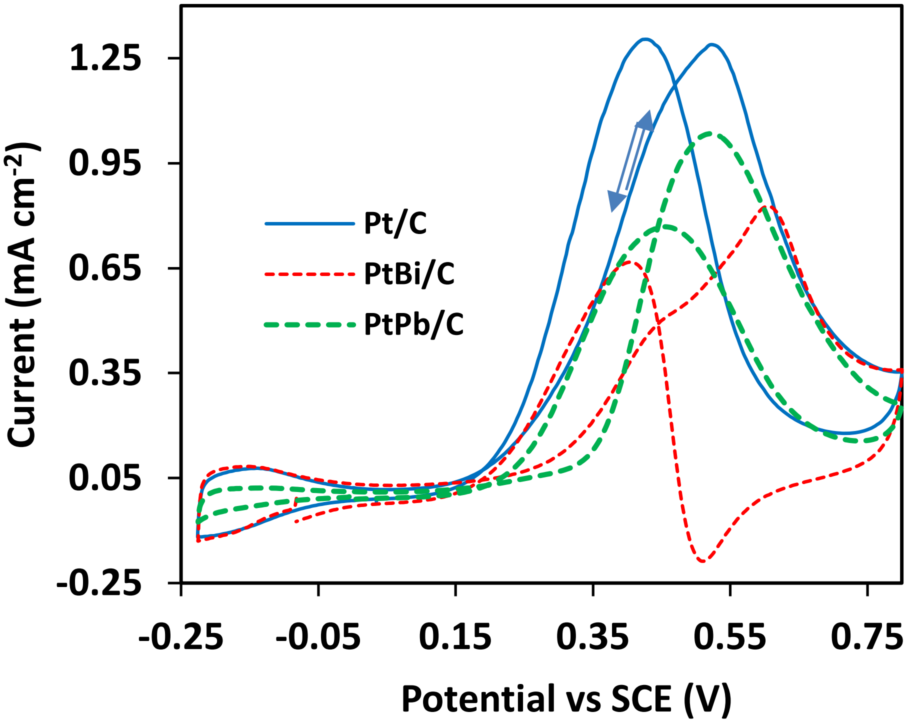

Figure 6.9. Cyclic voltammograms of the Pt/C, PtBi/C, and PtPb/C catalysts in 0.5 M H_2SO_4 (aq) and 0.1 M methanol at a scan rate of 10 mV s^{-1}

The onset potentials for methanol oxidation were more positive at the PtBi/C (0.24 V) and PtPb/C (0.32 V) catalysts than at Pt/C (0.20 V), indicating that the presence of both Bi and Pb adatoms inhibited methanol oxidation. Also, relative to Pt/C, both PtBi/C and PtPb/C produced considerably lower peak current densities. The lower currents cannot be attributed to blocking of active sites on the Pt surface by the Bi and Pb adatoms, since they have been corrected based on the active Pt areas. Together with the changes in the onset potential, the lower currents therefore suggest that electronic and/or third body effects inhibit methanol adsorption. The third body effect inhibits methanol oxidation because it limits the numbers of adjacent Pt atoms (ensembles) available for dissociative adsorption.

6.3.4 Ethanol oxidation

Figure 6.10 exhibits cyclic voltammograms at the Pt/C, PtBi/C, and PtPb/C catalysts in 0.5 M H_2SO_4 (aq) and 0.1 M ethanol. The shapes of the voltammograms were similar for all three catalysts, although the currents were lower for the PtBi/C and PtPb/C catalysts relative to Pt/C. As for methanol oxidation, the lower currents can be attributed to the decreased number of Pt ensembles available for ethanol adsorption [24]. However, at potentials below ca. 0.25 V (inset of Figure 6.10), the presence of Bi did appear to have a significant activating effect, suggesting that it provided a beneficial electronic effect.

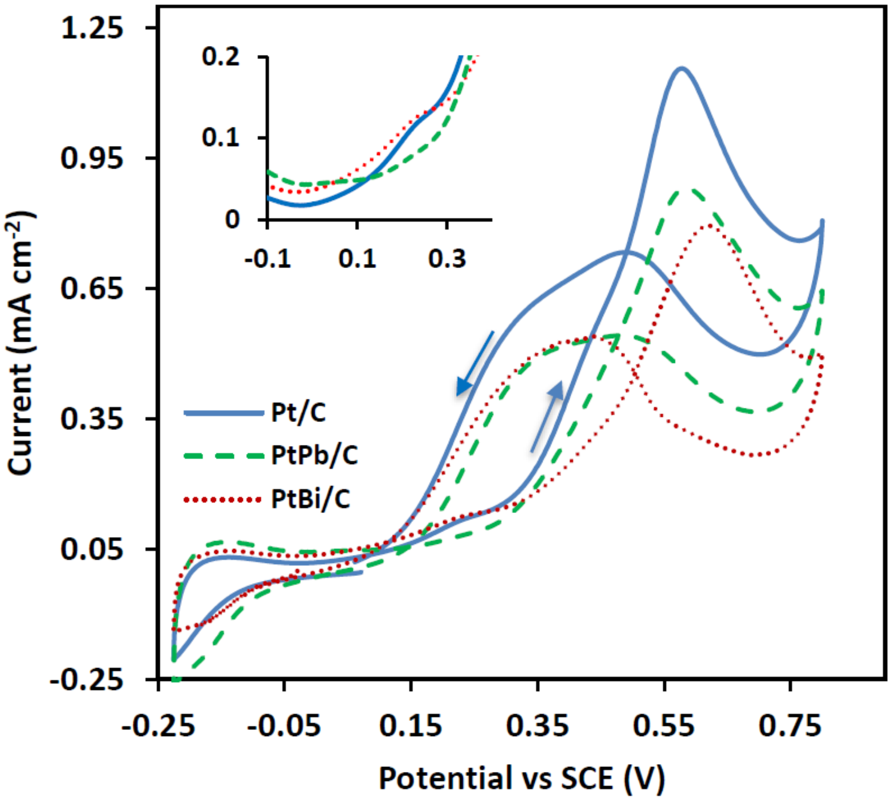

Figure 6.10. Cyclic voltammograms at the Pt/C, PtBi/C, and PtPb/C catalysts in 0.1 M ethanol and 0.5 M H_2SO_4 (aq) at a scan rate of 10 mV s^{-1}. The inset shows an enlargement of the low potential region.

6.4 Conclusions

Surface modification of a commercial Pt/C catalyst with Bi or Pb significantly enhances its catalytic activity for formic acid oxidation at low potentials. This can be attributed primarily to a third body effect, which inhibits the formation of adsorbed CO, and allows the oxidation of formic acid to occur primarily through a direct pathway. In contrast, the main effect of Bi or Pb was to inhibit the oxidation of methanol and ethanol, since these reactions requires ensembles of adjacent Pt sites. However, differences in the effects of Bi vs Pb on ethanol at low potentials suggest that Bi may provide a beneficial electronic effect. Although further work is required to fully explore these differences, it is clear that variation of both the modifying element and molecule being oxidized can provide useful information on the roles of third body, electronic, and other effects.

6.5 References

1. Adžić, R. R., Tripković, A. V., & Vesšović, V. B. (1986). Structural effects in electrocatalysis: oxidation of formic acid and hydrogen adsorption on platinum single-crystal stepped surfaces. Journal of Electroanalytical Chemistry and Interfacial Electrochemistry, 204, 329-341.
2. Busó-Rogero, C., Perales-Rondón, J. V., Farias, M. J., Vidal-Iglesias, F. J., Solla-Gullon, J., Herrero, E., & Feliu, J. M. (2014). Formic acid electrooxidation on thallium-decorated shape-controlled platinum nanoparticles: an improvement in electrocatalytic activity. Physical Chemistry Chemical Physics, 16, 13616-13624.
3. Climent, V., Herrero, E., & Feliu, J. M. (1998). Electrocatalysis of formic acid and CO oxidation on antimony-modified Pt (111) electrodes. Electrochimica Acta, 44, 1403-1414.
4. Smith, S. P., & Abruña, H. D. (1999). Structural effects on the oxidation of HCOOH by bismuth modified Pt (111) electrodes with (110) monatomic steps. Journal of Electroanalytical Chemistry, 467, 43-49.
5. Lei, H. W., Hattori, H., & Kita, H. (1996). Electrocatalysis by Pb adatoms of HCOOH oxidation at Pt (111) in acidic solution. Electrochimica Acta, 41, 1619-1628.
6. Kim, J., & Rhee, C. K. (2010). Ensemble size estimation in formic acid oxidation on Bi-modified Pt (111). Electrochemistry Communications, 12, 1731-1733.

7. Choi, M., Ahn, C. Y., Lee, H., Kim, J. K., Oh, S. H., Hwang, W., & Shin, W. (2019). Bi-modified Pt supported on carbon black as electro-oxidation catalyst for 300 W formic acid fuel cell stack. Applied Catalysis B: Environmental, 253, 187-195.
8. Herrero, E., Fernandez-Vega, A., Feliu, J. M., & Aldaz, A. (1993). Poison formation reaction from formic acid and methanol on Pt (111) electrodes modified by irreversibly adsorbed Bi and As. Journal of Electroanalytical Chemistry, 350, 73-88.
9. Bełtowska-Brzezinska, M., Heitbaum, J., & Vielstich, W. (1985). The influence of UPD-lead on the adsorption of formaldehyde, formic acid and methanol on Pt in acid solution. Electrochimica Acta, 30, 1465-1471.
10. Figueiredo, M. C., Santasalo-Aarnio, A., Vidal-Iglesias, F. J., Solla-Gullon, J., Feliu, J. M., Kontturi, K., & Kallio, T. (2013). Tailoring properties of platinum supported catalysts by irreversible adsorbed adatoms toward ethanol oxidation for direct ethanol fuel cells. Applied Catalysis B: Environmental, 140, 378-385.
11. Li, G., & Pickup, P. G. (2006). The promoting effect of Pb on carbon supported Pt and Pt/Ru catalysts for electro-oxidation of ethanol. Electrochimica Acta, 52, 1033-1037.
12. Tripković, A. V., Popović, K. D., Stevanović, R. M., Socha, R., & Kowal, A. (2006). Activity of a PtBi alloy in the electrochemical oxidation of formic acid. Electrochemistry Communications, 8, 1492-1498.
13. Volpe, D., Casado-Rivera, E., Alden, L., Lind, C., Hagerdon, K., Downie, C., & Abruna, H. D. (2004). Surface treatment effects on the electrocatalytic activity and characterization of intermetallic phases. Journal of Electrochemical Society, 151, A971.
14. Yu, X., & Pickup, P. G. (2011). Carbon supported PtBi catalysts for direct formic acid fuel cells. Electrochimica Acta, 56, 4037-4043.

15. Kang, S., Lee, J., Lee, J. K., Chung, S. Y., & Tak, Y. (2006). Influence of Bi modification of Pt anode catalyst in direct formic acid fuel cells. Journal of Physical Chemistry B, 110, 7270-7274.

16. Kim, B. J., Kwon, K., Rhee, C. K., Han, J., & Lim, T. H. (2008). Modification of Pt nanoelectrodes dispersed on carbon support using irreversible adsorption of Bi to enhance formic acid oxidation. Electrochimica Acta, 53, 7744-7750.

17. Lović, J. D., Obradović, M. D., Tripković, D. V., Popović, K. D., Jovanović, V. M., Gojković, S. L., & Tripković, A. V. (2012). High activity and stability of Pt_2Bi catalyst in formic acid oxidation. Electrocatalysis, 3, 346-352.

18. De-los-Santos-Alvarez, N., Alden, L. R., Rus, E., Wang, H., DiSalvo, F. J., & Abruna, H. D. (2009). CO tolerance of ordered intermetallic phases. Journal of Electroanalytical Chemistry, 626, 14-22.

19. Jiang, J., & Kucernak, A. (2005). Solid polymer electrolyte membrane composite microelectrode investigations of fuel cell reactions. II: voltammetric study of methanol oxidation at the nanostructured platinum microelectrode| Nafion® membrane interface. Journal of Electroanalytical Chemistry, 576, 223-236.

20. Jarvi, T. D. and Stuve, E. M. in Electrocatalysis, Frontiers of Electrochemistry, Lipkowski, J. and Ross, P. N. (1998). Editors, 75-154, Wiley–VCH, New York.

21. Luque, G. C., de Chialvo, M. R. G., & Chialvo, A. C. (2017). Kinetic study of the formic acid oxidation on steady state using a flow cell. Journal of Electrochemical Society, 164, H748.

22. Kim, B. J., Kwon, K., Rhee, C. K., Han, J., & Lim, T. H. (2008). Modification of Pt nanoelectrodes dispersed on carbon support using irreversible adsorption of Bi to enhance formic acid oxidation. Electrochimica Acta, 53, 7744-7750.
23. Garsany, Y., Baturina, O. A., Swider-Lyons, K. E., & Kocha, S. S. (2010). Experimental methods for quantifying the activity of platinum electrocatalysts for the oxygen reduction reaction. Analytical Chemistry. 82, 6321-6328.
24. Xia, X. H., Liess, H. D., & Iwasita, T. (1997). Early stages in the oxidation of ethanol at low index single crystal platinum electrodes. Journal of Electroanalytical Chemistry, 437, 233-240.

Chapter 7

Summary and future work

7. Summary and future work

7.1 Summary

In this research, our primary goal was to explore sustainable electrochemical techniques, including electrosynthesis and fuel cells. One of our studies focused on investigating the electrochemical coreduction of nitrite and carbon dioxide, which has become a promising method to sustainably produce fuels, chemicals, and fertilizers while addressing environmental concerns. Specifically, we explored the potential of iron-based phthalocyanine catalysts for producing ammonia and urea via CO_2 and NO_2^-electrolysis.

In Chapter 3, we focused on the electrochemical coreduction of CO_2 and NO_2^- at carbon-supported iron phthalocyanine (FePc/C) electrodes to accurately determine the production of ammonia and urea. The commonly used salicylate spectrophotometric method for quantifying both products can be susceptible to numerous interferences and matrix effects, leading to inaccurate determinations. Therefore, we used the standard addition technique to measure both ammonia and urea concentrations. We found that the average recovery of six replicate measurements of a mixture of 60 µM ammonia and 40 µM urea standard in the electrolyte was 60.0 ± 1.0 and 41.0 ± 1.6 µM for ammonia and urea, respectively.

While the diacetyl monoxime (DAM) spectrophotometric method has a low urea detection limit compared to the salicylate method, it cannot be used to measure urea in the presence of nitrite. To overcome this limitation, we used mixed-bed ion exchange resin to remove NO_2^- from the electrolysis samples, which enabled us to use the DAM method to measure urea concentrations in the presence of NO_2^- in the sample. With this method we found that the average recovery of five replicate measurements of 10 µM of urea standard in electrolyte solution was 10.6 ± 0.4 µM. We validated the accuracy of our measurements using liquid-chromatography-mass spectrometry. Our results demonstrate that the salicylate method can accurately analyze both ammonia and urea when a standard addition method is employed, reaction conditions are carefully controlled, and the accuracy of calibration slopes is verified.

In Chapter 4 of our research, we explored the use of carbon-supported sulfonated iron(III) phthalocyanine (FeTSPc/C) as a catalyst for producing urea from the coreduction of CO_2 and NO_2^-. Our findings indicate that the catalyst exhibited high selectivity for the coreduction of CO_2 and NO_2^- to urea, with a maximum faradaic efficiency of 54% at +0.053 V vs RHE and 25% co-production of NH_3. Moreover, we observed that electrodes prepared with a carbon black (CB) support and Nafion binder exhibited good stability in the 0.1 M $NaHCO_3$ electrolyte. Additionally, we observed that the urea yield rate was improved when optimizing the FeTSPc and CB ratio in the electrode. Our research suggests that FeTSPc/C has significant potential as a catalyst for urea production via the coreduction of CO_2 and NO_2^- at low overpotentials.

In Chapter 5, we investigated the selectivity and performance of urea production via the coreduction of CO_2 and NO_2^- in a proton-exchange membrane electrolysis cell (PEM cell) at a 5 cm^2 FePc/C electrode. Our results indicated that the faradaic efficiency of urea production increased from 2.8% to 15.9% compared to the normal three-electrode cell, highlighting the potential of the PEM cell for improving urea production efficiency.

In addition, we also examined the potential of carbon-supported MoS_2 (MoS_2/C) as a catalyst for urea production via the coreduction of N_2 and CO_2 in a PEM cell. However, we found that the MoS_2/C catalyst was unable to produce a measurable quantity of urea in water. Nonetheless, we discovered that trace amounts of urea were produced at MoS_2/C in 0.1M H_2SO_4 when both reagent gases N_2 and CO_2 were present in the gas phase.

Moreover, we conducted several experiments to evaluate the impact of different electrolyte solutions and reagent gas flow combinations on electrochemistry. Our findings showed that the performance of the PEM decreased over time when exposed to $NaHCO_3$ electrolyte, making it unsuitable for use in PEM electrolysis cells.

In the Chapter 6, our research focused on developing electrocatalysts for fuel cell applications. We compared the catalytic activities of PtBi/C and PtPb/C catalysts, which were prepared by the surface decoration of a commercial Pt/C catalyst, with the catalytic activity of unmodified Pt/C catalyst for electrochemical oxidation of formic acid, methanol, and ethanol. The results indicated that the addition of Bi or Pb significantly increased the catalytic activity of the Pt/C catalyst for formic acid oxidation at low potentials, with Bi having a greater effect. The PtBi/C catalyst was also found to have more stable activity than PtPb/C. Additionally, the PtBi/C catalyst demonstrated slightly higher ethanol oxidation activity at low potentials than unmodified Pt/C.

7.2 Future work

There are several aspects of this project that hold promise for further exploration. Although carbon-supported iron phthalocyanine (FePc/C) has been shown to be effective as a catalyst for the coreduction of NO_2^- and CO_2 to produce urea at low overpotentials, the selectivity of urea production using FePc/C as a catalyst has been found to be low. One promising approach to address this issue is to explore modification techniques for FePc catalysts. Research studies have suggested that different transition metals have the potential to produce urea through the coreduction of NO_2^- and CO_2 [1]. By modifying FePc with different transition metals using techniques such as surface modification or co-deposition, the electronic properties can be enhanced, and the number of active sites for coreduction can be increased. This could lead to an increase in the selectivity of urea production.

Ionic liquids have also shown great potential in both N_2 and CO_2 reduction processes [2, 3]. Our group investigated the use of ionic liquids as a binder to modify various carbon-supported metal phthalocyanines and found that they improved the selectivity of urea production from the coreduction of NO_2^- and CO_2. Further exploration of the potential of ionic liquids as an electrolyte for producing urea through the coreduction of NO_2^- and CO_2 is promising. Ionic liquids have high solubility for CO_2, which can enhance the mass transport of CO_2 to the electrode surface and improve the overall efficiency of the coreduction process.

In addition, carbon-supported iron(III) tetrasulfophthalocyanine (FeTSPc/C) has been found to be a highly active catalyst for NO_2^- and CO_2 coreduction to produce urea at low overpotentials. Although FeTSPc/C significantly promotes the selectivity of urea production, the yield rate of urea is low. Further work on electrode design and composition is needed to improve the rate of urea production and ensure its durability.

In this study, the potential of carbon-supported MoS_2 nanoparticles (MoS_2/C) as a catalyst for urea production through the coreduction of N_2 and CO_2 was explored. The results showed that trace amounts of urea could be produced at MoS_2/C when both reagent gases were in the gas phase. However, further investigation into different crystal structures of MoS_2, such as 2H-MoS_2 (hexagonal phase) and 1T-MoS_2 (trigonal phase), could yield promising results for urea production [3, 4]. Research has shown that various structures of MoS_2 catalysts have been effective for independent N_2 and CO_2 reduction to ammonia and alcohol, respectively, indicating the potential of MoS_2 as a versatile catalyst [5, 6].

A significant challenge we faced in this study was quantifying trace amounts of urea. Developing highly sensitive and interference-free detection methods is crucial in such cases. One potential solution is to explore the use of appropriate chemical derivatization techniques to improve the detection limit of urea in LC-MS analysis. Additionally, online mass spectrometry methods could also be investigated to quantify trace amounts of urea accurately.

Furthermore, it may be worthwhile to screen other types of membranes, such as anion exchange or a mixture of both, to improve the productivity of urea. Several studies have reported that a mixture of cation and anion membranes improves CO_2 reduction selectivity [9].

Overall, the thesis delves into sustainable electrochemical techniques that hold immense potential for making a substantial impact in the future. It focuses on key areas such as achieving carbon neutrality, promoting sustainable chemical production, and advancing energy storage solutions. By actively contributing to these critical domains, the thesis lays the foundation for a more sustainable and prosperous future.

7.3 References

1. Shibata, M., Yoshida, K., & Furuya, N. (1998). Electrochemical synthesis of urea at gas-diffusion electrodes: III. Simultaneous reduction of carbon dioxide and nitrite ions with various metal catalysts. Journal of Electrochemical Society, 145, 595.
2. Rosen, B. A., Salehi-Khojin, A., Thorson, M. R., Zhu, W., Whipple, D. T., Kenis, P. J., & Masel, R. I. (2011). Ionic liquid–mediated selective conversion of CO_2 to CO at low overpotentials. Science, 334, 643-644.

3. García Rey, N., & Dlott, D. D. (2015). Structural transition in an ionic liquid controls CO_2 electrochemical reduction. The Journal of Physical Chemistry C, 119, 20892-20899.
4. Gupta, D., Chauhan, V., & Kumar, R. (2020). A comprehensive review on synthesis and applications of molybdenum disulfide (MoS_2) material: Past and recent developments. Inorganic Chemistry Communications, 121, 108200.
5. Li, X., & Zhu, H. (2015). Two-dimensional MoS_2: Properties, preparation, and applications. Journal of Materiomics, 1(1), 33-44.
6. Pin-Chao, G., Kai-Liang, Z., Yu-Lin, F., Fang, W., Yin-Ping, M., Ye-Mei, H., & Han-Xia, Z. (2016). Recent progress of two-dimensional layered molybdenum disulfide. Acta Physica Sinica, 65
7. Li, X., Li, T., Ma, Y., Wei, Q., Qiu, W., Guo, H., & Sun, X. (2018). Boosted electrocatalytic N_2 reduction to NH_3 by defect-rich MoS_2 nanoflower. Advanced Energy Materials, 8, 1801357.
8. Francis, S. A., Velazquez, J. M., Ferrer, I. M., Torelli, D. A., Guevarra, D., McDowell, M. T., & Lewis, N. S. (2018). Reduction of aqueous CO_2 to 1-propanol at MoS_2 electrodes. Chemistry of Materials, 30, 4902-4908.

Appendix A:

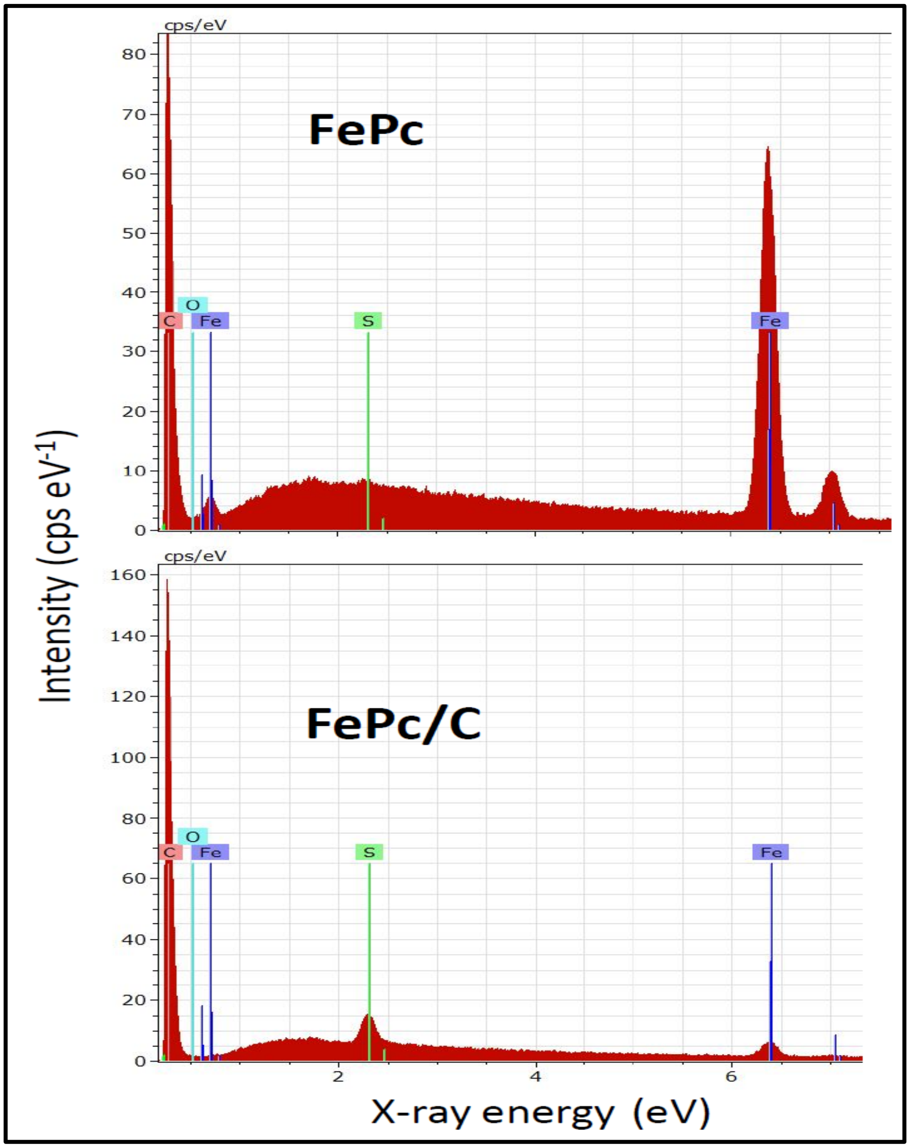

Figure A1. Energy dispersive X-ray emission spectra of the FePc and the FePc/C catalyst measured with an FEI Quanta 400 scanning electron microscope (SEM). The samples were dispersed in a mixture of water and 2-propanol for application to the carbon SEM tabs. The C:Fe ratio measured for the FePc samples was used to correct the mass% for Fe obtained for the FePc/C sample.

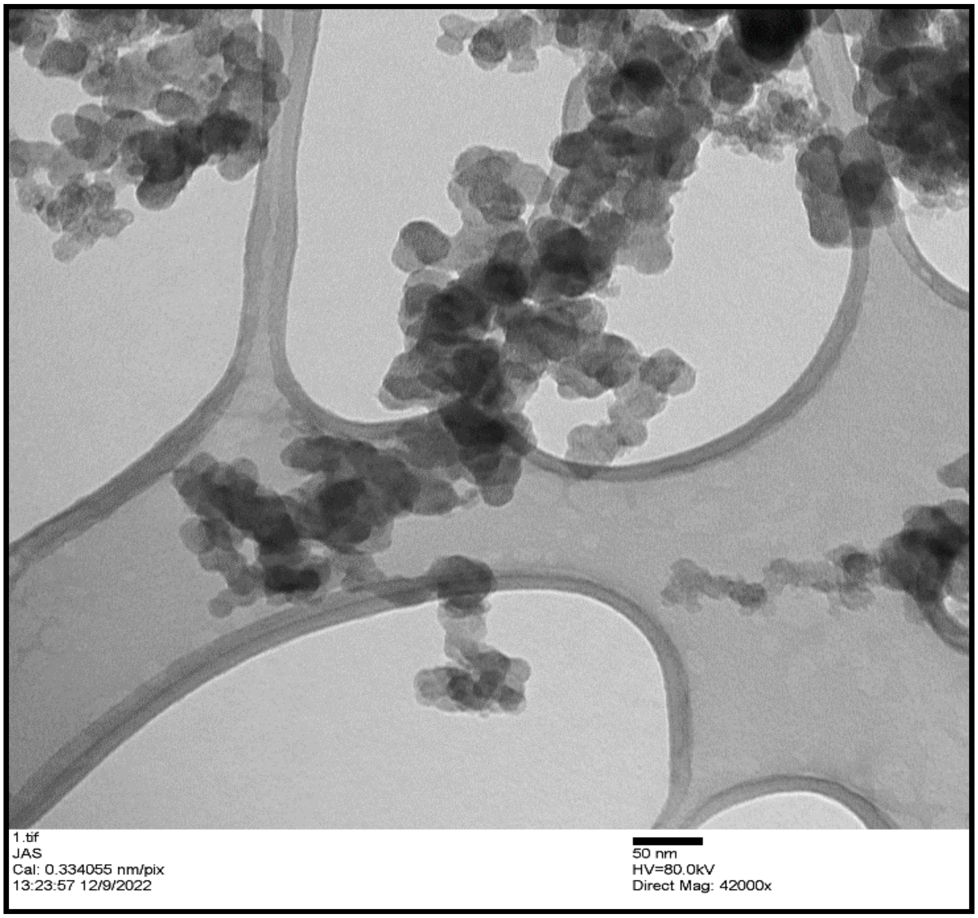

Figure A2. Transmission electron microscopy image of the FePc/C catalyst obtained with a Tecnai TM Spirit transmission electron microscope (Faculty of Medicine at Memorial University).

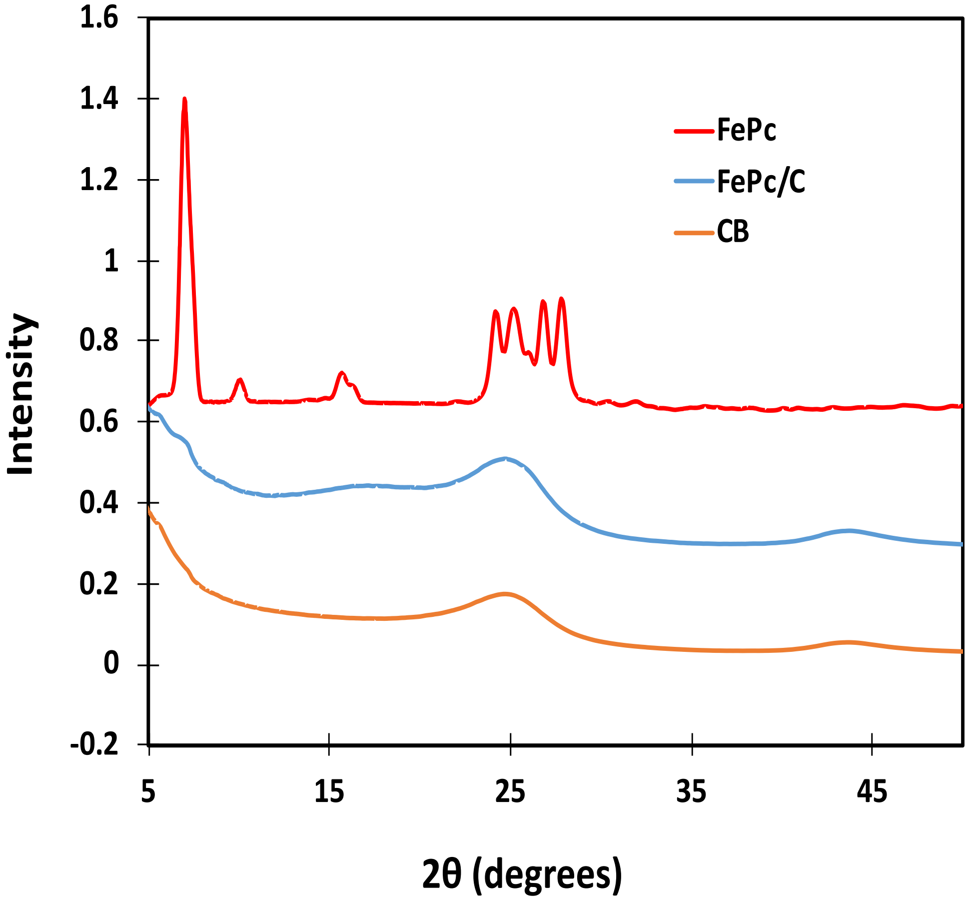

Figure A3. X-ray diffraction patterns for FePc, Vulcan carbon black, and the FePc/C catalyst obtained with a Rigaku Ultima IV X-ray diffractometer with a Cu Kα radiation source (0.154 nm).

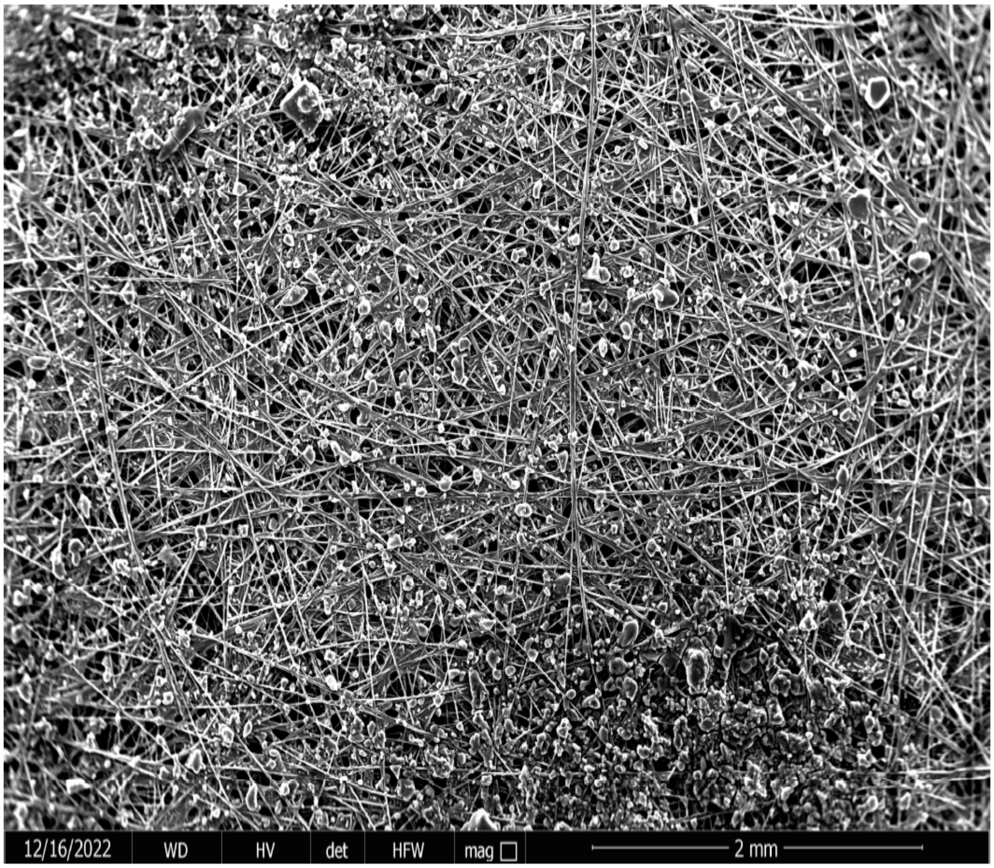

Figure A4. Scanning electron microscopy image of a FcPc/C/CFP electrode obtained with an FEI Quanta 400 scanning electron microscope.

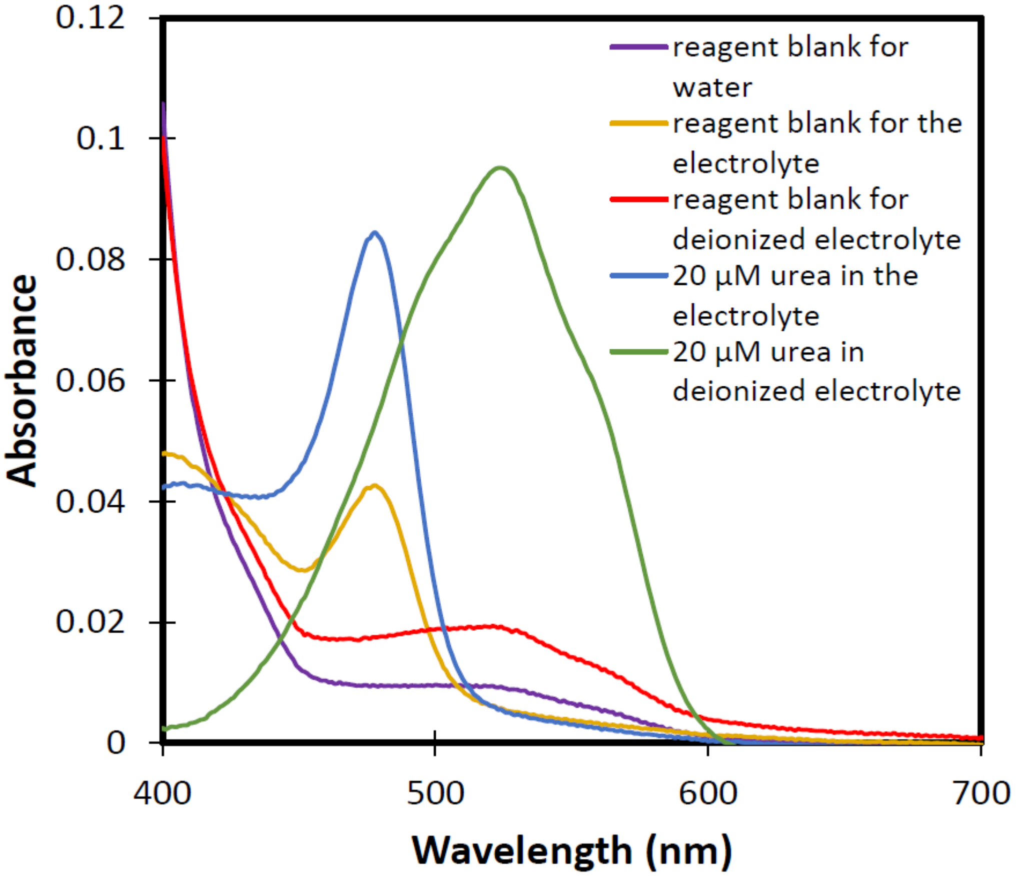

Figure A5. Spectra for analysis of urea by the DAM method in 0.1 M $NaHCO_3$ + 5 mM $NaNO_2$ (electrolyte) before and after deionization with a mixed bed ion-exchange resin, and reagent blanks obtained in the absence of urea. Water was used in the reference beam except for the deionized 20 µM urea sample, where the reagent blank for the deionized electrolyte was used.

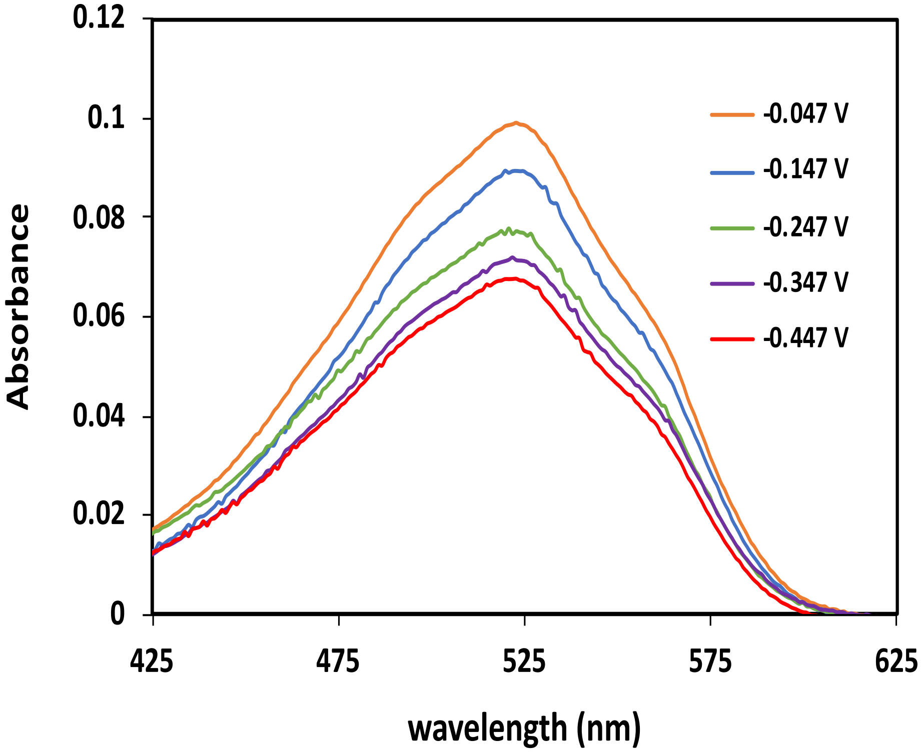

Figure A6. UV-Vis spectra for analysis of urea (DAM method) from electrolysis of 5 mM $NaNO_2$ in 0.1 M $NaHCO_3$ under CO_2 at FePc/C electrodes for 2 h.

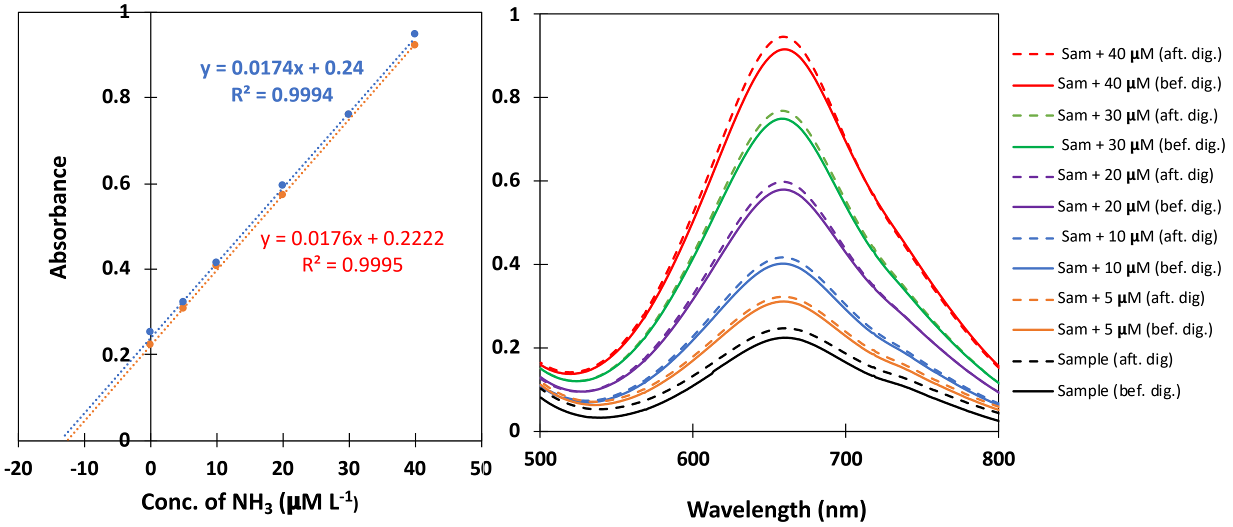

Figure A7: Standard addition curve and UV-Vis spectra for analysis of ammonia and urea by salicylate method for electrolysis of 5 mM $NaNO_2$ in 0.1 M $NaHCO_3$ under CO_2 @ -0.047 V at FePc/C electrode for 2 h. The labels "aft." and "bef." represent after and before, respectively, while "Sam" and "dig." refer to sample and digestion, respectively.

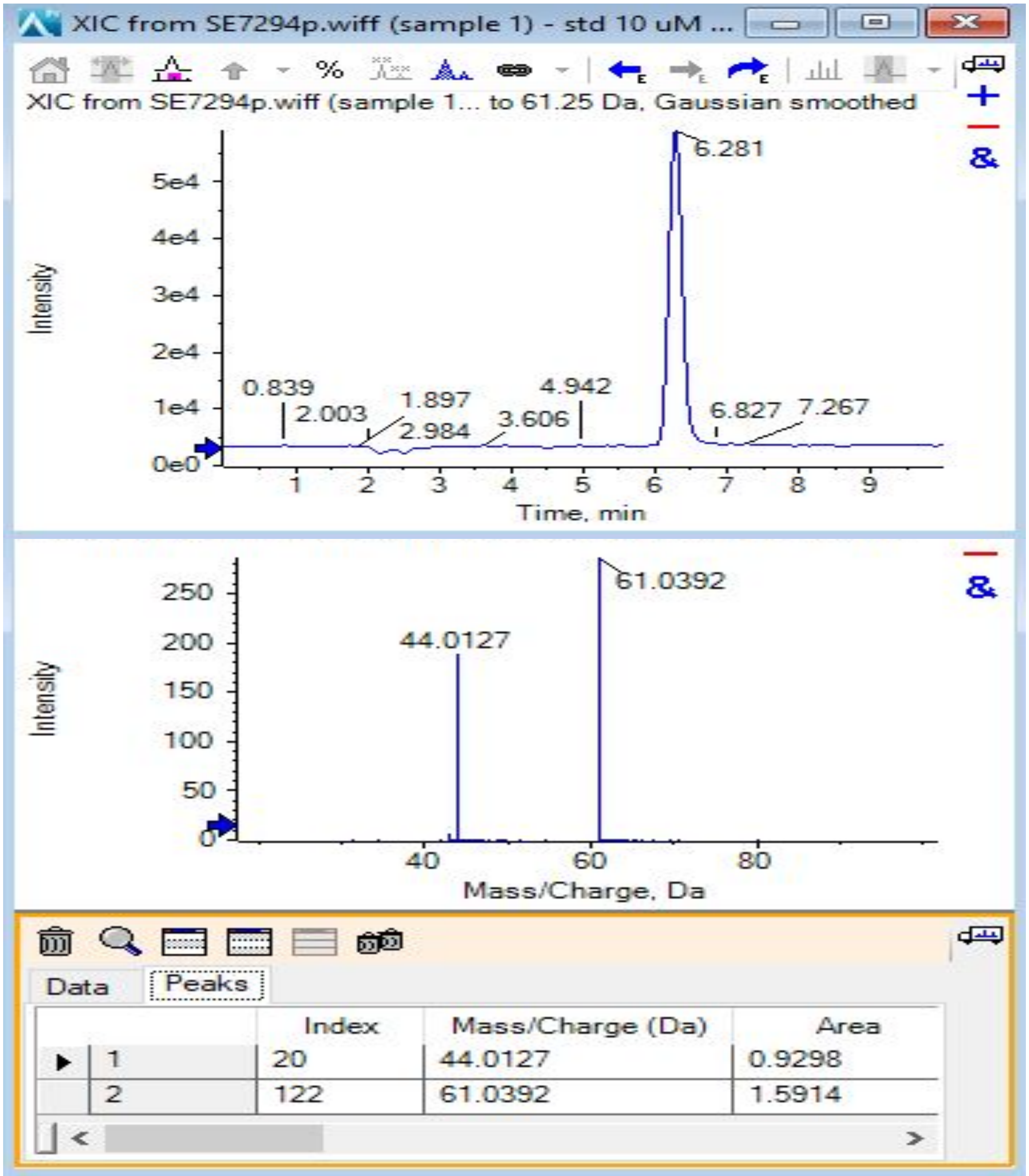

XIC from SE7294p.wiff (sample 1) - std 10 uM ...

XIC from SE7294p.wiff (sample 1... to 61.25 Da, Gaussian smoothed

	Index	Mass/Charge (Da)	Area
1	20	44.0127	0.9298
2	122	61.0392	1.5914

Figure A8. LC-MS/MS chromatogram for urea standard in 0.1 M $NaHCO_3$ and 5 mM $NaNO_2$ solution after deionized with mixed bed ion exchange resin. (Top: LC chromatogram, bottom: urea precursor ion and fragment ion, and their respective peak areas).

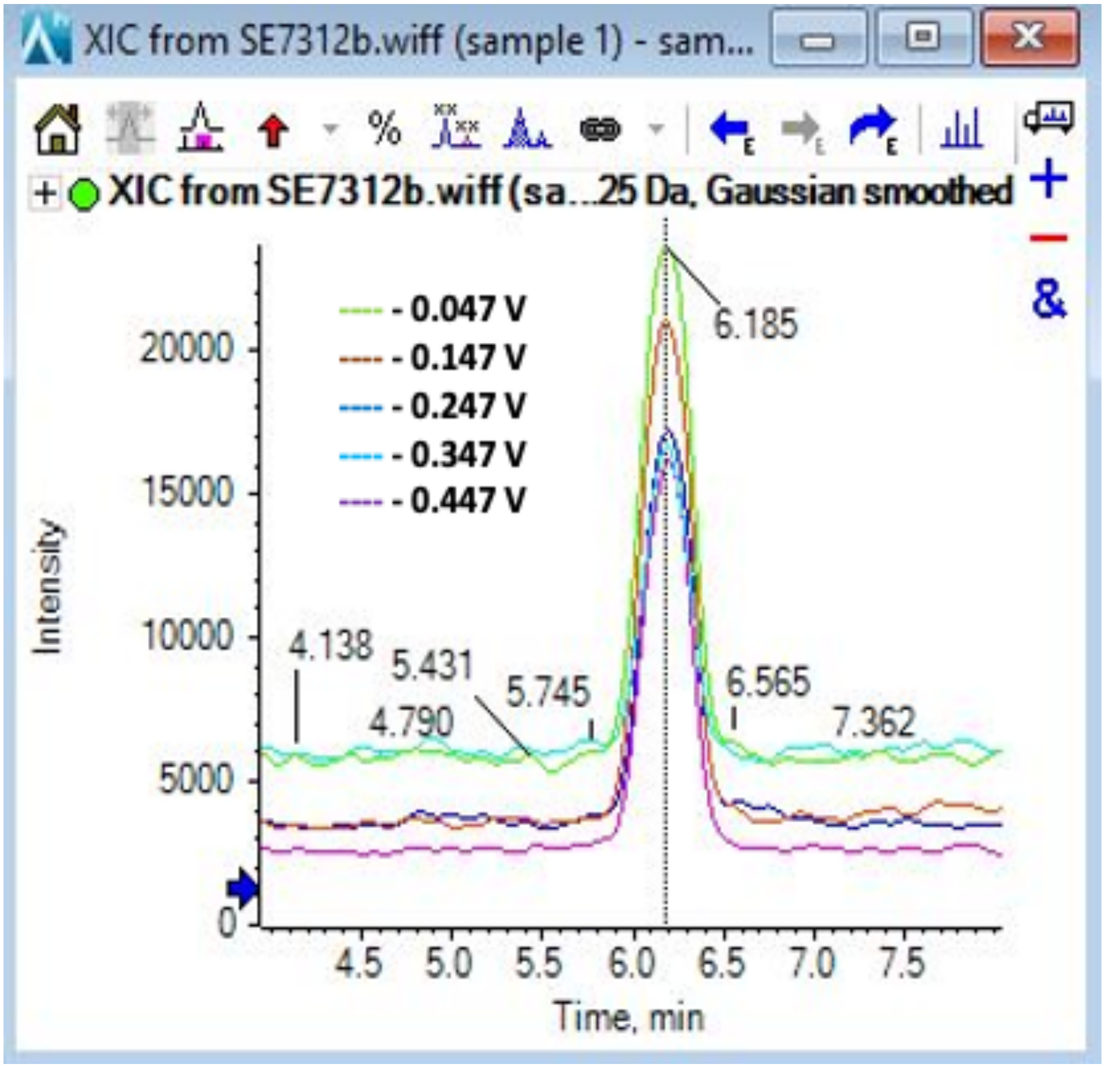

Figure A9. LC-MS chromatogram for analysis of urea from electrolysis of 5 mM $NaNO_2$ in 0.1 M $NaHCO_3$ under CO_2 at FePc/C electrodes for 2 h.

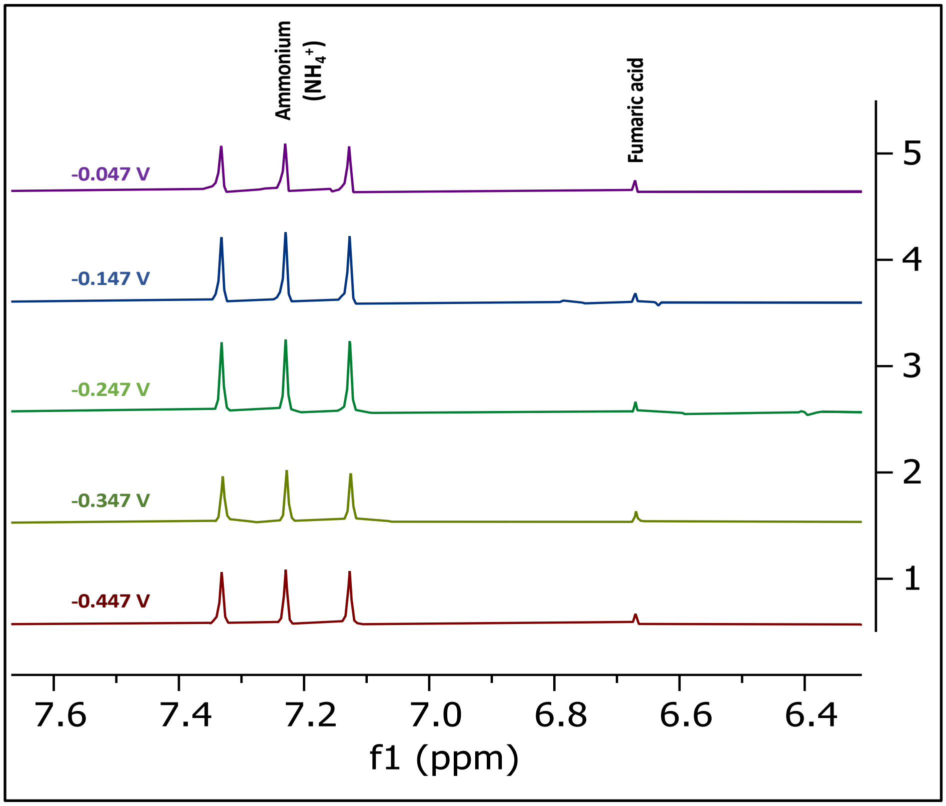

Figure A10. ^{1}H-NMR spectra for analysis of ammonia from electrolysis of 5 mM $NaNO_2$ in 0.1 M $NaHCO_3$ under CO_2 at FePc/C electrodes for 2 h.

Table A1. Average rates of urea and ammonia formation from electrolysis of 5 mM $NaNO_2$ in 0.1 M $NaHCO_3$ under CO_2 at FePc/C electrodes over 2 h.

Potential vs RHE (V)	**Rate of formation (µM h^{-1} cm^{-2})**	
	Urea	**Ammonia**
-0.047	0.157	3.76
-0.147	0.141	3.35
-0.247	0.122	4.97
-0.347	0.115	4.74
-0.447	0.106	3.27

Table A2: Standard addition analysis of ammonia and urea for six replicate samples (a mixture of 60 µM NH_4Cl and 40 µM urea in 0.1 M $NaHCO_3$ + mM $NaNO_2$) using the salicylate method.

Sample ID		**Slope**	**Intercept**	**Conc. of NH_3 (µM)**	**Conc. of urea (µM)**
Set-1	Before digestion	0.0175	0.104	59.43	41.04
	After digestion	0.0172	0.2434	141.51	
Set-2	Before digestion	0.0178	0.1049	58.93	40.36
	After digestion	0.0172	0.2402	139.65	
Set-3	Before digestion	0.0172	0.1044	60.70	40.96
	After Digestion	0.0172	0.2453	142.61	
Set-4	Before digestion	0.0173	0.1026	59.30	42.86
	After digestion	0.0173	0.2509	145.03	
Set-5	Before digestion	0.0177	0.1057	59.72	38.32
	After digestion	0.0176	0.2402	136.36	
Set-6	Before digestion	0.0171	0.1055	61.70	42.56
	After digestion	0.0170	0.2496	146.82	

Table A3: Concentrations of ammonia and urea for three replicate electrolysis samples (@ -0.047 V at FePc/C) using the salicylate method.

Sample ID **FePc/C @ -0.047 V**		**Slope**	**Intercept**	**Conc. of NH_3 (µM)**	**Conc. of urea (µM)**
Electrolysis -1	Before digestion	0.0176	0.2210	502.27	21.62
	After digestion	0.0174	0.2373	545.52	
Electrolysis -2	Before digestion	0.0176	0.2222	505.0	23.36
	After digestion	0.0174	0.240	551.72	
Electrolysis -3	Before digestion	0.0176	0.2207	501.59	22.65
	After digestion	0.0174	0.2379	546.89	

Appendix B:

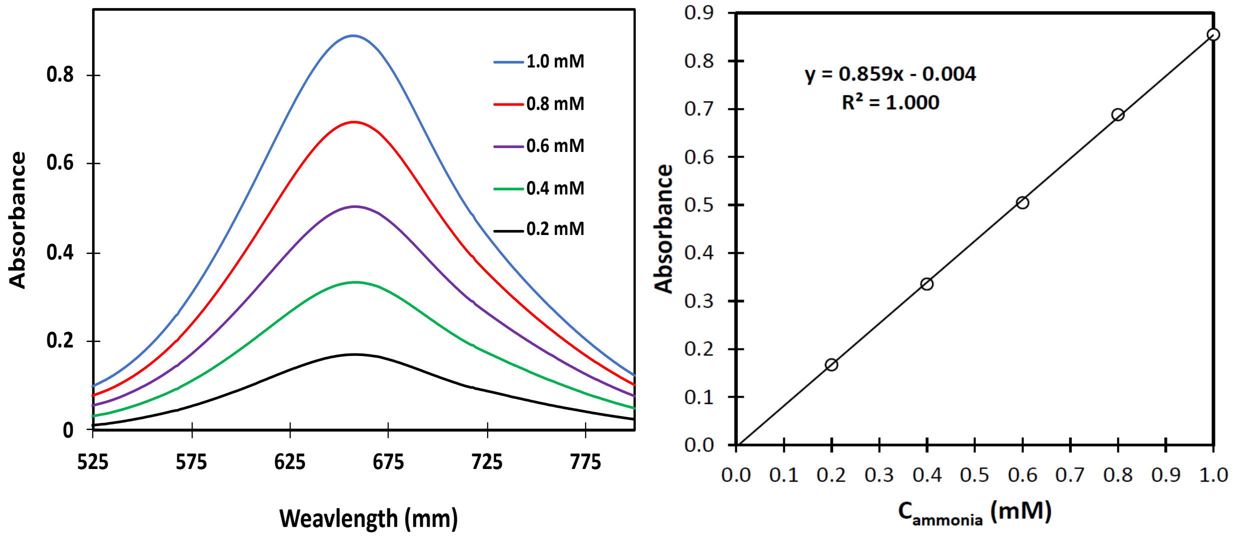

Figure B1. UV-Vis spectra (0.2- 1.0 mM of NH_4Cl) and calibration curve for analysis of ammonia in 0.1 M $NaHCO_3$ + 5 mM $NaNO_2$ by the salicylate method.

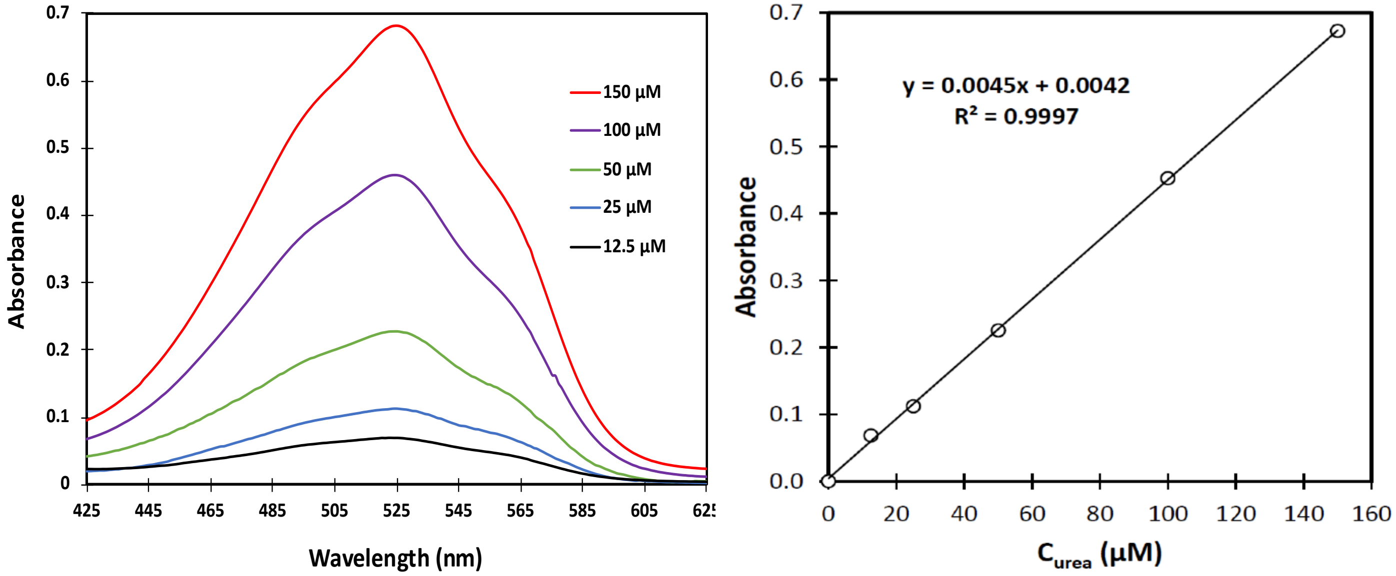

Figure B2. UV-Vis spectra (12.5-150 µM of urea) and calibration curve for analysis of urea in 0.1 M $NaHCO_3$ + 5 mM $NaNO_2$ by the DAM method following deionization with a mixed bed ion-exchange resin.

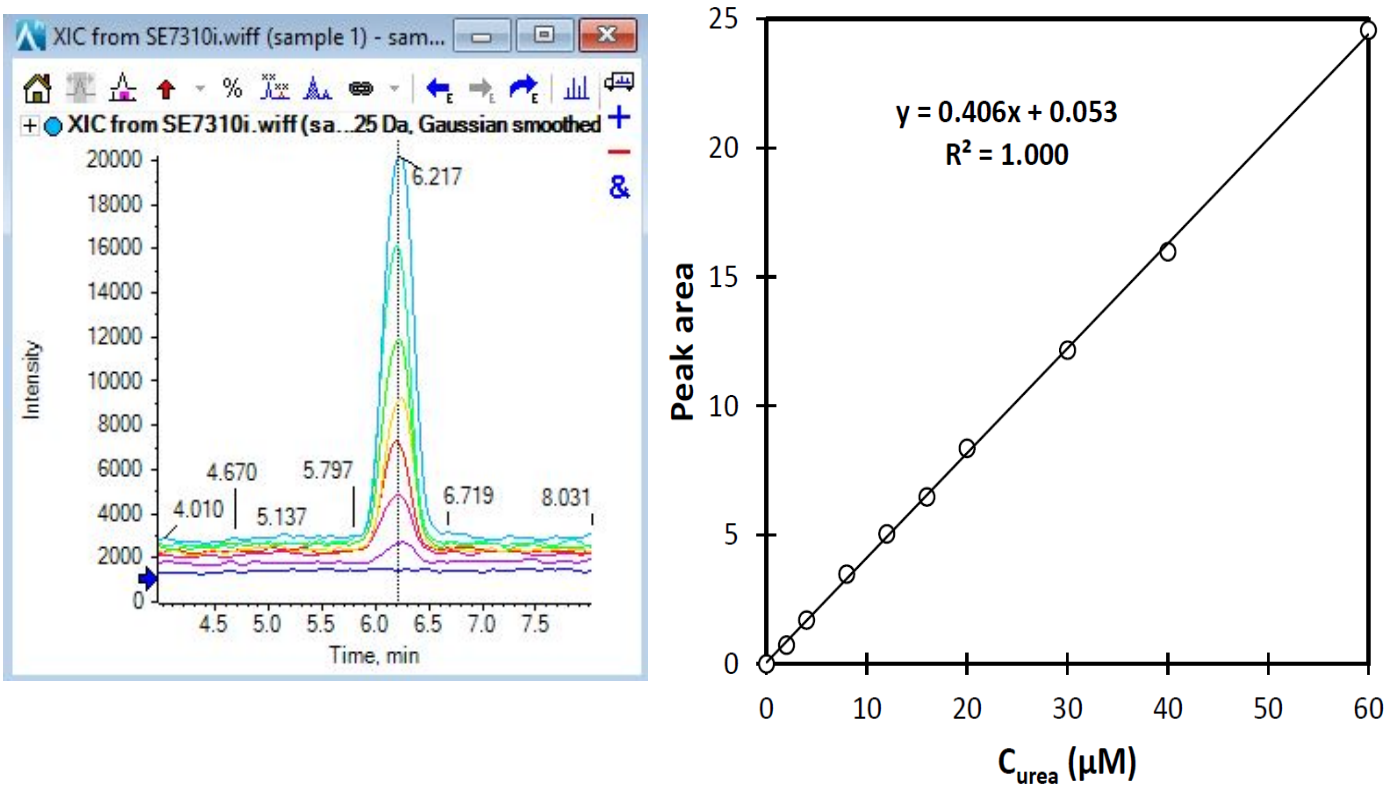

Figure B3. LC chromatograms (0-60 µM of urea standard) and calibration curve for analysis of urea in 0.1 M $NaHCO_3$ + 5 mM $NaNO_2$ by the LC-MS method following deionization with a mixed bed ion-exchange resin.

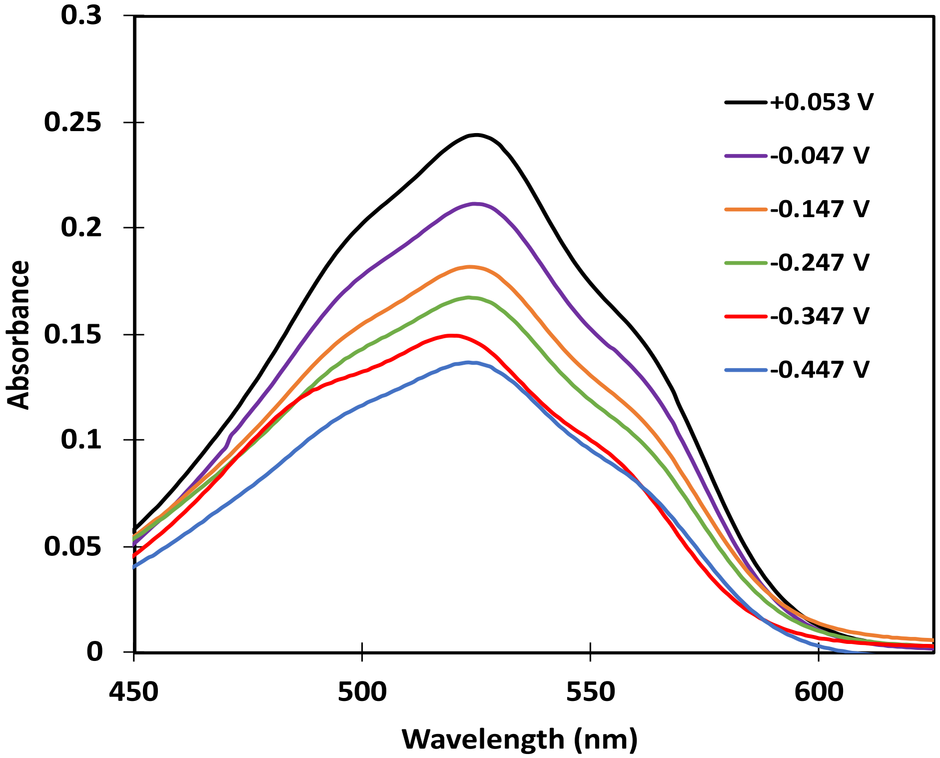

Figure B4. UV-Vis spectra for analysis of urea (DAM method) from electrolysis of 5 mM $NaNO_2$ in 0.1 M $NaHCO_3$ under CO_2 at 3% FeTSPc/C electrodes for 2 h.

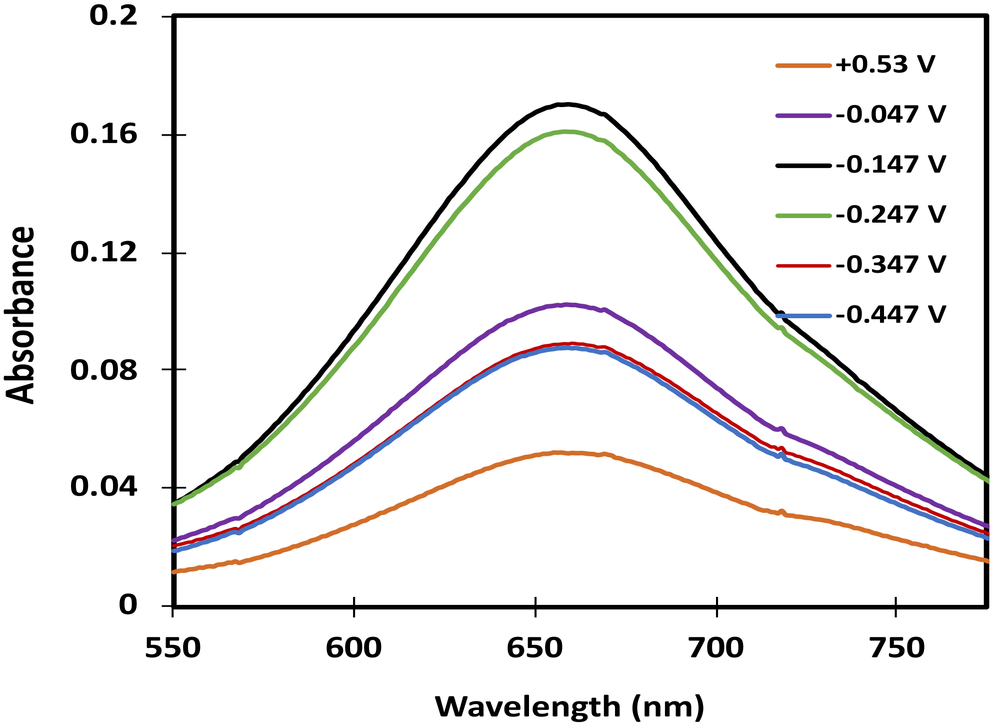

Figure B5. UV-Vis spectra for analysis of ammonia (salicylate method) from electrolysis of 5 mM $NaNO_2$ in 0.1 M $NaHCO_3$ under CO_2 at 3% FeTSPc/C electrodes for 2 h.

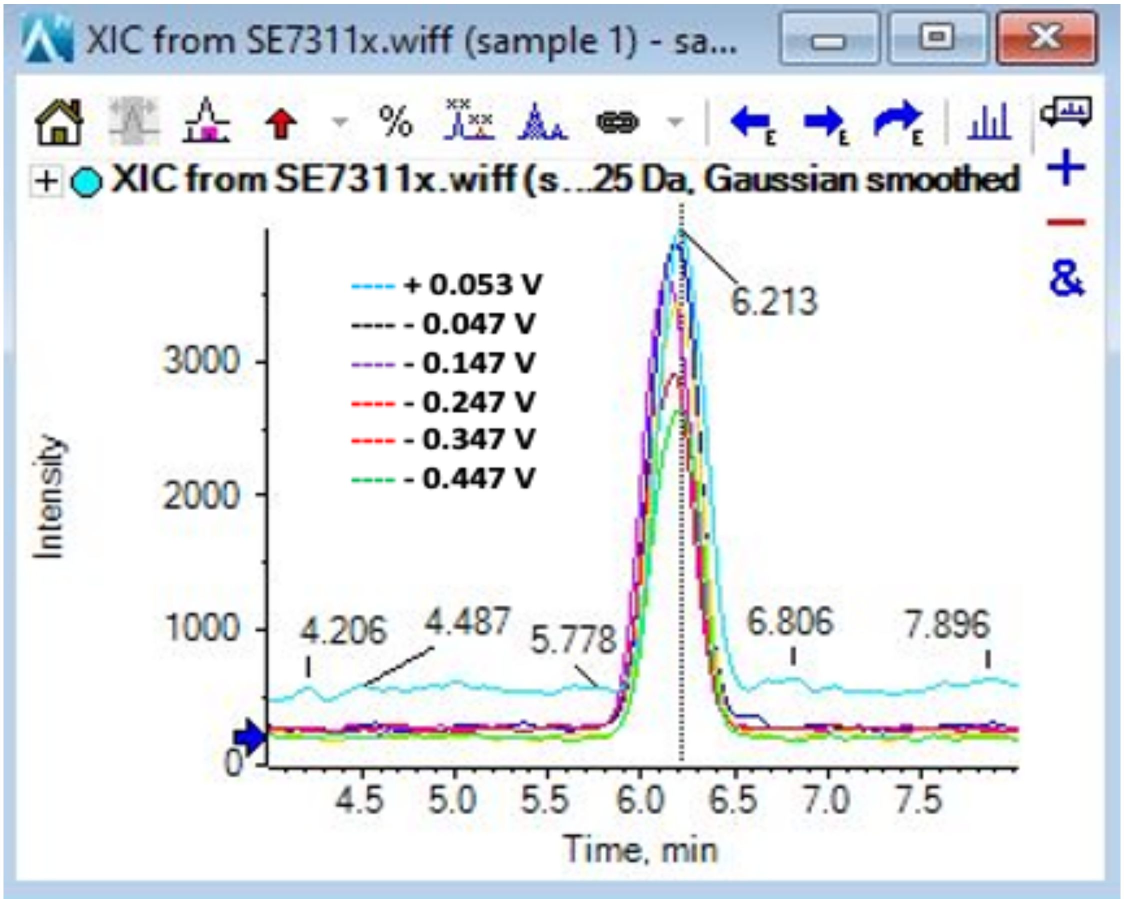

Figure B6. LC-MS chromatogram for analysis of urea from electrolysis of 5 mM $NaNO_2$ in 0.1 M $NaHCO_3$ under CO_2 at 3% FeTSPc/C electrodes for 2 h.

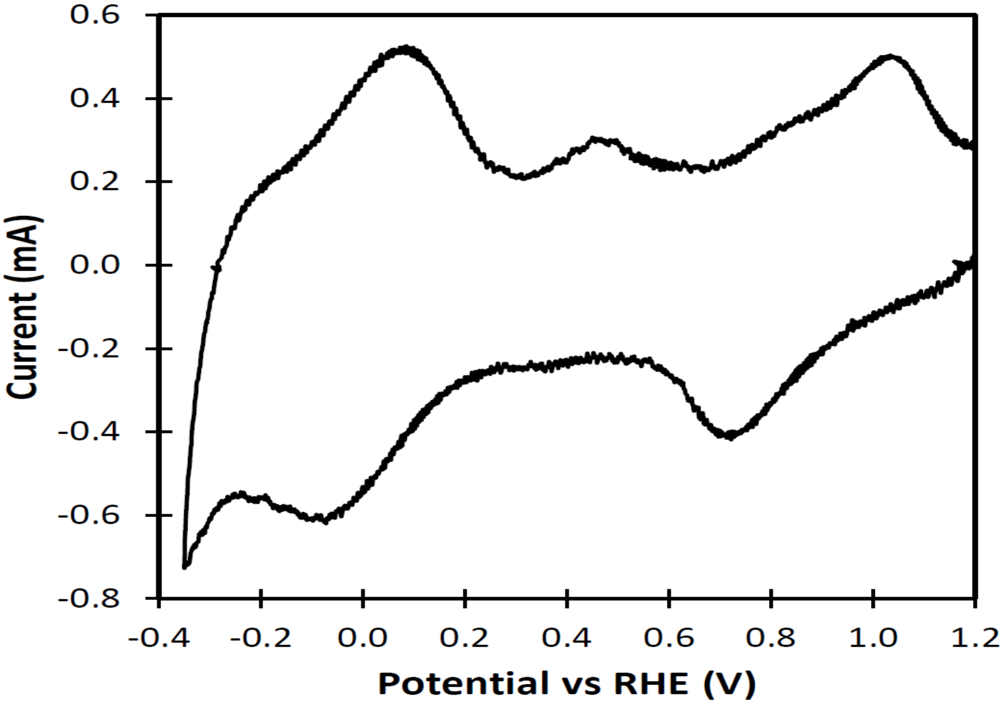

Figure B7. Cyclic voltammogram (10 mV s^{-1}) for a FePc/C electrode in 0.1 M $NaHCO_3$ under N_2.

Appendix C:

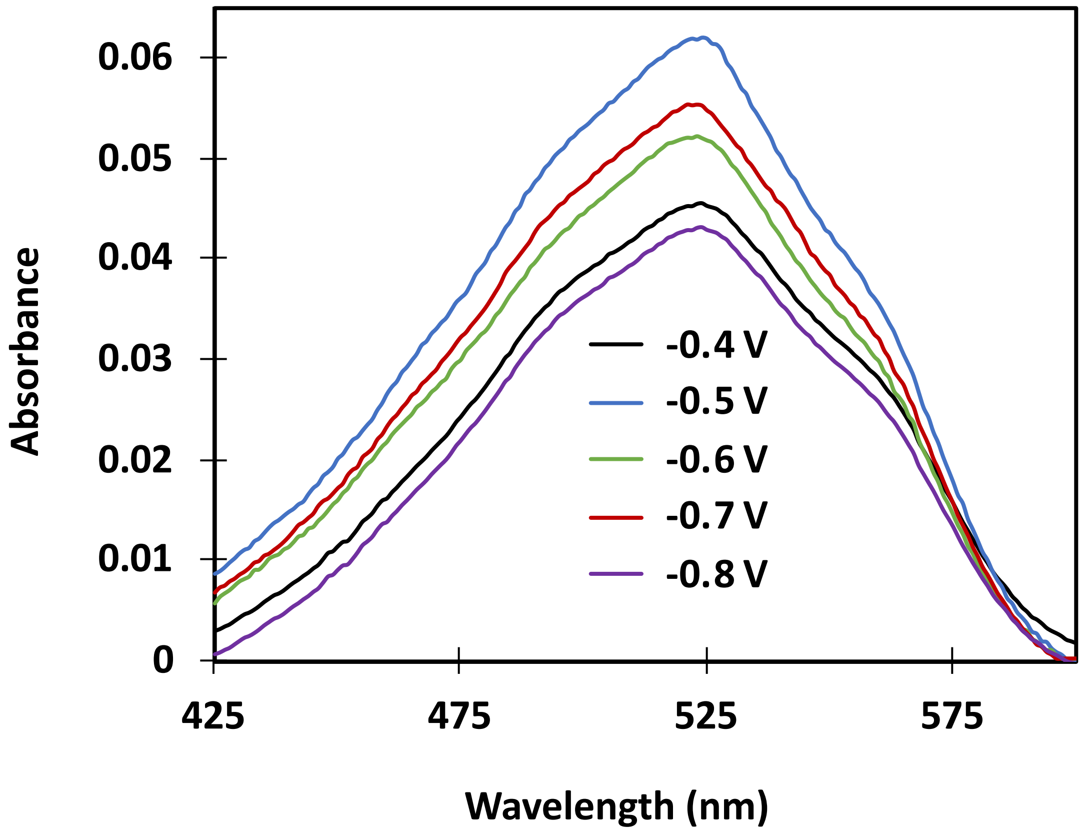

Figure C1. UV-Vis spectra for analysis of urea (DAM method) from electrolysis of 1 mM $NaNO_2$ and CO_2 in H_2O at a 5 cm^2 FePc/C electrode for 2 h.

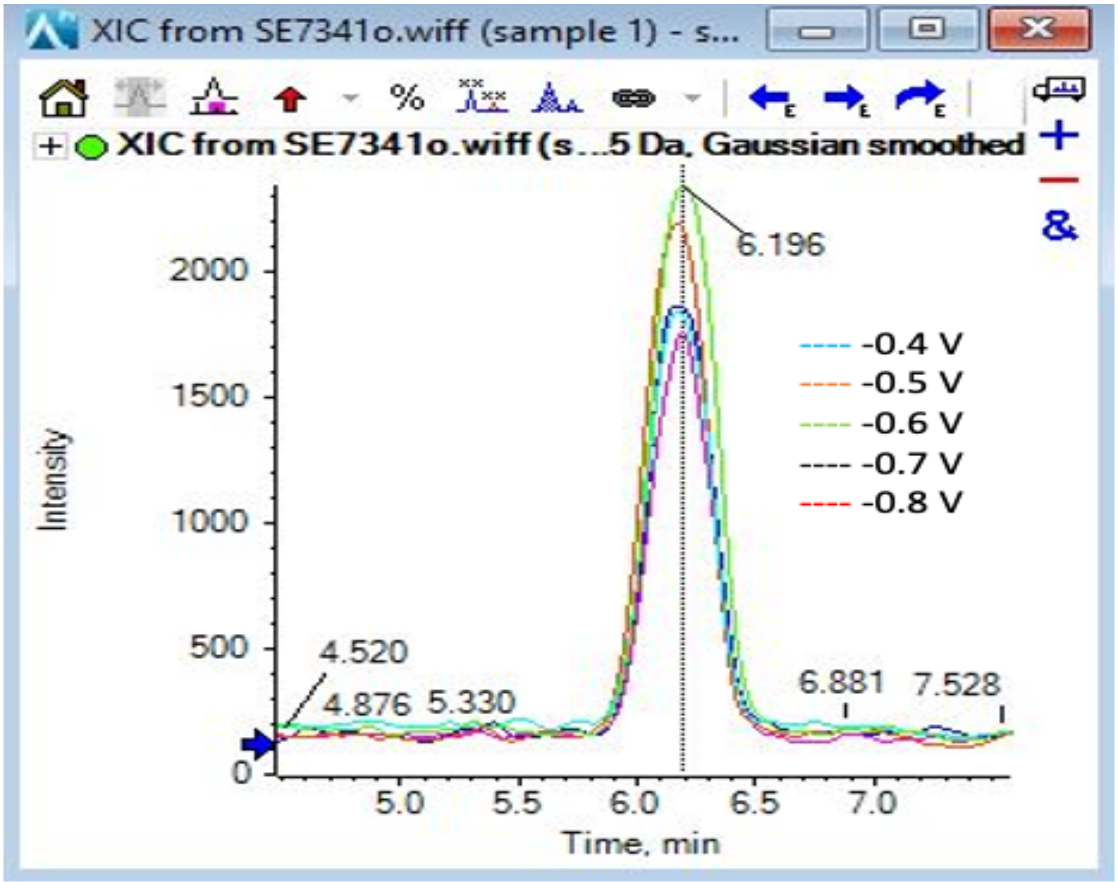

Figure C2. LC-MS chromatogram for analysis of urea from electrolysis of 1 mM $NaNO_2$ and CO_2 in H_2O at a 5 cm^2 FePc/C electrode for 2 h.

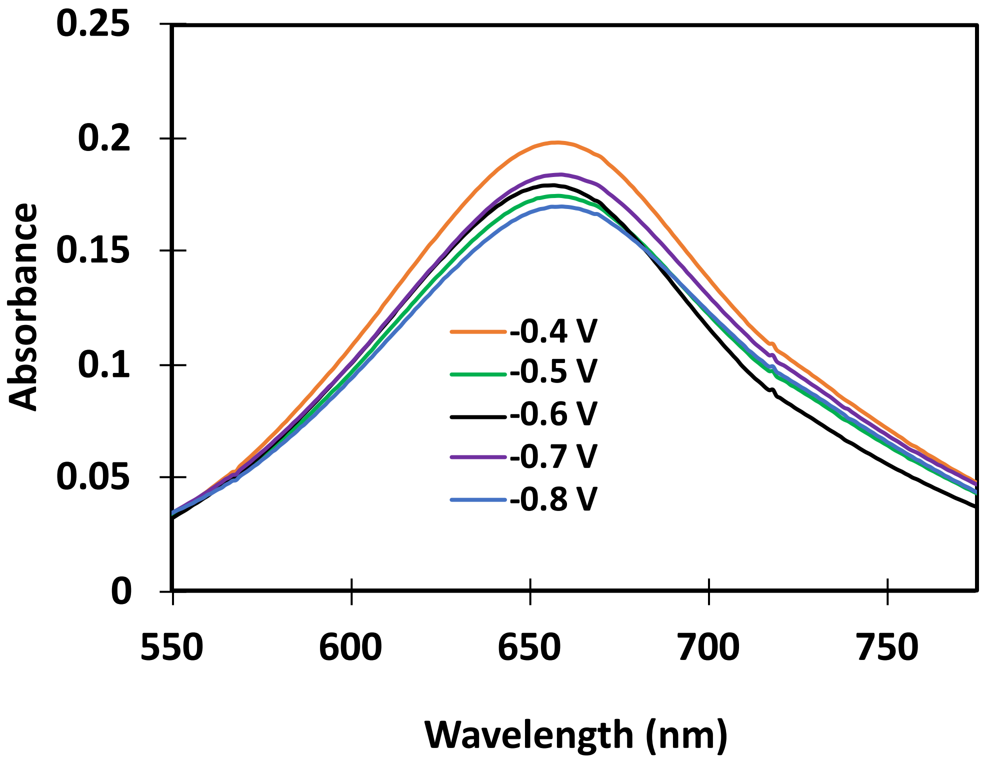

Figure C3. UV-Vis spectra for analysis of ammonia (salicylate method) from electrolysis of 1 mM $NaNO_2$ and CO_2 in H_2O at a 5 cm^2 FePc/C electrode for 2 h.

Appendix D:

List of chemicals and materials

Iron(II) phthalocyanine (FePc; Aldrich), Fe(III) tetrasulfophthalocyanine (iron(III) phthalocyanine-4,4′,4″,4‴-tetrasulfonic acid, compound with oxygen, monosodium salt hydrate; Sigma-Aldrich), MoS_2 (Sigma-Aldrich), Pt/C (Pt 70% on high surface area carbon, HiSPEC 13100, Alfa Aesar), carbon black (Vulcan XC-72; Cabot), 5% Nafion^{TM} solution (Dupont), 2-propanol (Caledon), 1-propanol (Sigma-Aldrich), formic acid (Sigma-Aldrich), methanol (Sigma-Aldrich), ethanol (Sigma-Aldrich), carbon fiber paper (CFP; Toray), sodium hydrogen carbonate (BDH), sodium nitrite (BDH), ammonium chloride (BDH), sodium hypochlorite (Sigma-Aldrich), salicylic acid (Sigma-Aldrich), sodium citrate (Sigma-Aldrich), sodium borohydride (BDH chemicals), $Bi(NO_3)_3.5H2O$ (Sigma-Aldrich), $Pb(NO_3)_2$ (Sigma-Aldrich), sodium hydroxide (BDH), sodium nitroprusside (Sigma-Aldrich), urea (99.0-100.5%; Sigma-Aldrich), diacetyl monoxime (DAM, 2,3-butanedione monoxime, Sigma-Aldrich), thiosemicarbazide (TSC; Sigma-Aldrich), iron(III) sulfate hydrate ($Fe_2(SO_4)_3$; Sigma-Aldrich), sulfuric acid (Fisher Scientific), AG 501-X8 mixed bed resin (Bio-Rad Laboratories), acetonitrile (99.9% HiPerSolv CHROMANORM®, BDH), ammonium acetate (Sigma-Aldrich), acetic acid (Fisher Scientific), HPLC-grade water (Fisher Scientific), dimethyl sulfoxide-d_6 (DMSO-d_6, Cambridge Isotope Laboratories, Inc), CO_2 (CD-50, Airgas), nitrogen (Praxair, UHP, NI 5.0UH-T), and urease (supplied as a glycerol solution, specific activity 500-800 units/mL; Sigma-Aldrich). Deionized (DI) water having a resistivity of $\geq$17.9 MΩ.cm was used for the experiments.